Investigation of Materials for Photochemical and Electrochemical Reduction of H_2O and CO_2, and Chemical Modifications of Antimonene and TiO_2

A Thesis submitted for the degree of

Doctor of Philosophy

by

Mohd Monis Ayyub

New Chemistry Unit
Jawaharlal Nehru Centre for Advanced Scientific Research
(A Deemed University)
Bangalore, India

March 2022

Dedicated to my parents and teachers

Declaration

I hereby declare that the matter embodied in this thesis entitled "**Investigation of Materials for Photochemical and Electrochemical Reduction of H_2O and CO_2, and Chemical Modifications of Antimonene and TiO_2**" is the result of investigations carried out by me under the supervision of Prof. C. N. R. Rao, FRS at the New Chemistry Unit, Jawaharlal Nehru Centre for Advanced Scientific Research, Bangalore, India and that it has not been submitted elsewhere for the award of any degree or diploma.

In keeping with the general practice in reporting scientific observations, due acknowledgement has been made whenever the work described is based on the findings of other investigators. Any oversight due to error of judgement is regretted.

Mohd Monis Ayyub

Certificate

I hereby certify that the matter embodied in this thesis entitled "**Investigation of Materials for Photochemical and Electrochemical Reduction of H_2O and CO_2, and Chemical Modifications of Antimonene and TiO_2**" has been carried out by Mr. Mohd Monis Ayyub at the New Chemistry Unit, Jawaharlal Nehru Centre for Advanced Scientific Research, Bangalore, India under my supervision and it has not been submitted elsewhere for the award of any degree or diploma.

(Prof. C. N. R. Rao)

(Research Supervisor)

Acknowledgements

First and foremost, I express my sincere gratitude to my research supervisor, Prof. C. N. R. Rao, FRS, for guiding me throughout my PhD. I consider myself privileged to have worked under his supervision, guidance, and mentorship. The values he has instilled in me helped me become more informed and positive towards science and life at large. His unending source of motivation has encouraged me to value the importance of hard work. His “no substitute for hard work” philosophy will remain ingrained in me and will be followed throughout my life. His unique methodology to manage his students and bring out the best of them has indeed helped me in my PhD works to learn more and improve myself. He has always encouraged me to pursue good science, to have an innovative outlook while solving challenging problems and be able to think unique. I am grateful to him for introducing me to the fascinating and vast field of materials chemistry. Not only has he been a great teacher, but also a valuable moral support on the personal front. It has been a fulfilling experience, a lifetime opportunity for me to work under his full spirited guidance.

I express my sincere gratitude to Prof. Subi J George, Chariman NCU, for his immense help and support in various aspects throughout my PhD.

I am extremely fortunate to have Prof. U. V. Waghmare (JNCASR) and Prof. S.V. Bhat (IISc) as my collaborators and for their invaluable discussions and timely guidance. I acknowledge Dr. C.P. Vinod for his immense help in XPS measurements. I acknowledge Prof. Sridhar Rajaram for various scientific discussions.

The courses offered by Prof. A Sundaresan, Prof. S Narasimhan, Prof. K Biswas, Prof. S. C. Peter, Prof R. Dutta, Prof S Sampath and Dr. C Ranjan has played an instrumental part in initiating my research career. I am indebted to them for the same.

I am thankful to chairmen of NCU, CPMU and ICMS for allowing me to use the various departmental facilities.

The contributions from Dr. S.R Lingampalli and Dr. Manjeet Chhetri for mentoring me during my initial days of research has been instrumental. I will forever be indebted to them.

The contributions from my co-workers have been indispensable and without them most of the works would have been incomplete. The assistance of Dr. S.R Lingampalli, Dr. Manjeet Chhetri, Dr Pramoda, Dr. Anand Roy, Dr. Uttam Gupta, Dr. Manjunath K, Dr, Suchitra Prasad, Manaswee Barua and Dr Shashidhara Acharya has been immense in completing my PhD work.

I am thankful and shall remain ever indebted to all my past and present lab mates especially Dr. Sunita Dey, Dr. Pramoda K., Dr. Uttam Gupta, Dr. Manjodh Kaur, Dr. K. Gopalakrishnan, Dr. S.R. Lingampalli, Dr. Sreedhara M. B, Dr. Anand Roy, Dr.Pratap Vishnoi, Dr. K Manjunath, Manaswee, Reetendra, Rohit, Amit, Swaraj, Navin, Devesh and Aditi for providing a very healthy atmosphere in lab and their helps in various occasions.

I acknowledge the assistance of technical staff at JNCASR; Ms. N. R. Selvi, Mrs. T. Usha, Dr. J. Ghatak, Mr Mahesh, Mr. A. Srinivas, Ms Meenakshi, Mr Sachin, Mr. Nandkishor, Mr Rajakumar and Mr. Anil. I thank, Mrs.Sudha, Mrs.Shashi, Mr.Gowda and Mr. Victor for their help in various ways. I also thank NCU and ICMS office staff Melissa, Ramya, Naveen and Nandesh.

I thank CSIR and Sheik Saqr laboratory for providing fellowships. I thank JNCASR and IISc for research facilities. The hostel, admin staff, academic staff, complab staff and Dhanvantari for all their help during my stay in JNCASR.

My deepest thanks to Mrs.Indumati Rao and Mr. Sanjay for their love, affection and hospitality extended to me during my association with them.

In addition to those who had a scientific impact on my graduate school career, I'm thankful for the presence of the many people who supported me on a personal level throughout. Thanks to all my PhD. batch mates with whom I started my life at this centre and whose cheerful company made these years of life so memorable. I specially acknowledge Momin, Dr. Mehraj, Ashutosh, Manaswee and Veenu for always being there for me and for all the memorable moments. I acknowledge and thank Dr. Kausar for guiding me during the early years of my PhD and for being there as a mentor and an elder brother. I thank all my friends Abdul, Dr. Shadab, Dr. Sajjad, Jabed, Shashank, Nijita, Surishi, Dr. Arjun and Reetendra. I especially thank my friends during B.Sc. and M.Sc.; Shivam, Vishal, Tarun, Jagpreet, Aayushi, Akram, Dr Naim, Aasif, Waqar and Jahangeer for the enriching experiences I had with them which motivated me to pursue PhD.

I thank my friends at JNCASR with whom I indulged in various sports activities, especially the football and cricket group.

I express my deep gratitude to all my teachers from Hermann Gmeiner School, S.G.T.B Khalsa college and Jamia Millia Islamia. Their contributions to my completion of PhD have been enormous. Special thanks to Prof. Tokeer Ahmed for guiding me during my MSc at Jamia Millia Islamia. I will always be indebted to him for his support.

This thesis is a humble offering to all my teachers from kindergarten to PhD.

I would like to thank and acknowledge my family, my parents, siblings, and relatives. Their understanding and supportive nature has always motivated me to pursue my own path. I’m fortunate to have a relatively large extended family who have helped keep me on track through the challenges of the last six years.

Above all, I acknowledge and praise Allah the Almighty, the most Gracious and the Most Merciful for bestowing upon me his endless blessings, for my good health and giving me the aptitude for pursuing a career in science.

Mohd Monis Ayyub

Prologue

In view of the unprecedented rise in anthropogenic CO_2 emissions and the extreme climatic changes that follows, it has become imperative to reduce the emissions and utilise renewable energy to produce high energy density fuels. The utilization of renewable energy such as solar or hydro energy as energy source for the synthesis of value-added fuels by the reduction of water and carbon dioxide is an effective strategy that offers a potential solution that simultaneously addresses both energy supply and storage and to further dissuade the humankind off fossil fuel dependence. This thesis is focussed on synthesizing and studying different types of materials for energy related applications.

Part I of the thesis is focussed on materials for photochemical and electrochemical reduction of water and carbon dioxide.

Chapter 1 introduces photochemical and electrochemical reduction of water and carbon dioxide. The chapter discusses the fundamental mechanism along with methods and brief discussion on catalyst materials choices.

Chapter 2 focusses on the photochemical reduction of carbon dioxide. Photoreduction of CO_2 using solar energy is an important problem of great relevance, and it is necessary to explore different types of semiconductor structures for the purpose. In the present study, we demonstrate the advantage of using heterostructures of the type ZnO/M/CdS (M = Ag, Au, $Ag_{1-x}Au_x$, $Ag_{1-x}Cu_x$) for the photoreduction of CO_2 in the liquid phase. In particular, use of alloys such as $Ag_{1-x}Cu_x$ favors the reduction. It is noteworthy that we have observed photoreduction of CO_2 in gas phase as well. Heterostructures are employed to enhance the charge carrier separation and metal nanoparticles act as co catalyst. In the case of $ZnO/Ag_{1-x}Cu_x/CdS$, CO production activity reaches a high value of 327.4 μmol $h^{-1}g^{-1}$.

Chapter 3 focusses on the electrochemical reduction of carbon dioxide (ECO_2RR) by carbon-based materials. The work involves the study of borocarbonitrides as electrocatalyst material for ECO_2RR in aqueous bicarbonate electrolyte. BCN exhibits higher selectivity for CO_2-to-CO conversion than N-doped carbon with $BC_{1.2}N_{0.8}$ (~26% N content) reaching CO faradaic efficiency of 98% at -0.45V (vs RHE). Thus, we have tuned the composition of $B_xC_yN_z$ to study the effects of incorporating B and N in carbon lattice. This work provides insights into the effects of heteroatom doping in carbon lattice on the surface area, CO_2 uptake and electrochemical reduction of CO_2. A linear correlation was observed between FE_{CO} and N content, specifically pyridinic N content, shedding light on the active center for ECO_2RR.

Chapter 4 involves studying the effects of covalent crosslinking nanosheets of MoS_2 with BCN on the hydrogen evolution activity. We have exploited the presence of different functional groups on the surfaces of BN (NH_2) and graphene (COOH) domains of the borocarbonitride, to functionalize with MoS_2. We have thus obtained two nanocomposites functionalized by amide linkages to differing domains in the lattice, designated as BN/BCN−MoS_2 and G/BCN−MoS_2. The composite where the graphene domains are cross-linked to MoS_2 nanosheets, G/BCN−MoS_2 (1:2), exhibits outstanding electrochemical HER activity with an onset potential of −30 mV (vs RHE) and a current density of 10 mA cm^{-2} at an overpotential of −35 mV. The physical mixture of BCN and MoS_2, on the other hand, does not display any notable HER activity. The BCN−MoS_2 composites also exhibit good photochemical activity. It is noteworthy that 2H-MoS_2, which does not exhibit significant catalytic activity, can be rendered highly active by cross-linking with BCN. The present study demonstrates the advantages of cross-linking of catalytically

active heterolayers BCN and MoS_2 for the HER reaction. The enhanced HER activity in cross-linked composites arises from the increased charge-transfer rates as well as from the more exposed catalytically active sites.

Chapter 5 deals with the utilization of seawater for photocatalytic water splitting. The abundant presence of water in oceans offers an important alternative approach for water splitting using seawater. In this work, we study various semiconductor catalyst already reported from our group and their photocatalytic water splitting activity towards efficiently reducing seawater under visible light irradiation. To our surprise we find that for simple semiconductor and complex heterostructure based photocatalyst, the performance is slightly better in seawater than in pure water when we use inorganic sacrificial agents such as Na_2S/Na_2SO_3. The results suggest that by a suitable choice of catalysts, one can split seawater without any prior treatment. This study might be a crucial step in solving the energy problem to some extent.

Part II is focusses on aliovalent anion substitution in TiO_2 and is based on the fact that such substitution in inorganic materials brings about marked changes in properties. In view of the important properties of TiO_2, we have attempted to prepare TiNF by employing an entirely new procedure involving the reaction of TiN with TiF_4. Partial substitution of oxygen in TiO_2 by N and F reduces the band gap, but complete substitution increases the band gap comparable to that of the oxide. A detailed first-principles calculations has been carried out on structural and electronic properties of N, F-TiO_2 and the TiNF phases. This has enabled us to understand the effects of N, F substitution in TiO_2 in terms of the crystal structure, electronic structure, and optical properties. Based on the analysis of conduction and valence band edges, we predict TiNF to be suitable for photocatalytic water splitting

reaction and preliminary results show that TiNF is catalytically more active than TiO_2 for photocatalytic water splitting.

Part III focusses on the synthesis and chemical functionalization of Antimonene, a member for group 15 pnictogens. In this work, band edge emission of liquid exfoliated antimonene nanosheets is observed at ~2.23 eV. The presence of lone pair on antimony makes the surface reactive and susceptible to surface functionalization. Modification of antimonene by chemical functionalization can serve as a suitable approach towards tuning its electronic properties. To this effect we have studied covalent and non-covalent functionalization of antimonene nanosheets.

Spontaneous covalent functionalization of antimonene nanosheets with diazonium salt proceeds with the transfer of lone pairs from Sb to the diazonium salts forming organic moieties on the surface attached predominantly via Sb-C bonds. Interestingly, band edge can be tailored upon functionalization to 2.18 eV. Non-covalent functionalization of antimonene nanosheets is achieved by reaction with Group 13 Lewis acids (BCl_3, $AlCl_3$, $GaCl_3$ and $InCl_3$) and group 12 Lewis acids ($ZnCl_2$ and $CdCl_2$). Lone pair of electrons on antimonene acts as Lewis bases and forms Lewis acid-base adducts. Interestingly, we observe a blue shift in emission spectra of antimonene after non-covalent functionalization. This study demonstrates the efficacy of chemical functionalization on tuning properties of 2D materials.

Table of Contents

Part I

Photochemical and Electrochemical Reduction of H_2O and CO_2

Chapter 1

Fundamentals of Photochemical and Electrochemical Reduction of CO_2 and H_2O

Summary

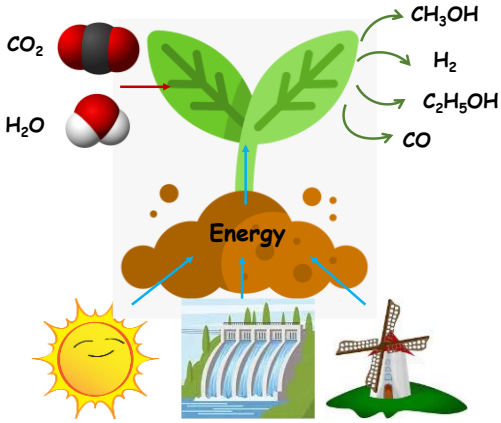

Humans depend greatly on fossil fuels for energy needs. Utilization of fossil fuels has led to an unprecedented rise in anthropogenic emission of harmful greenhouse gases such as carbon dioxide, nitrous oxide, etc. which has caused drastic climatic changes. Reducing the emissions and existing levels of greenhouse gases from the atmosphere is extremely crucial to stop further deterioration of earth's climate. A possible solution is the utilization of abundant sources of renewable energy such as solar or wind energy to convert carbon dioxide and water into high energy density fuels which solves both the problems of reducing CO_2 emissions and to reduce our dependance on fossil fuels. This chapter is based on understanding the fundamental concepts of production of hydrogen from water splitting reaction and production of value-added fuels from the reduction of carbon dioxide. The discussion describes the mechanism of electrochemical and photochemical reduction of carbon dioxide and water, along with experimental techniques and measurement parameters.

Paper based on this work has appeared in *ACS Omega* **2017**, 2,6, 2740-2748; *Mater. Horiz.*, **2021**, 8, 2420-2443.

1.1 Introduction

Human influence on earth's climate is unprecedented. Critical and widespread damage to human and natural systems are being driven by human-induced climate changes with growing frequency, intensity and duration of extreme weather events which includes droughts, wildfires, terrestrial and marine heatwaves, cyclones, and flood. Over the period of 1992-2011, there has been a substantial decrease in glacial ice resulting in a global mean sea level rise of 0.19 m. The observed global mean surface temperature has increased to 0.87^{o}C for the period of 2006-2015 (**Figure 1a**). The impact of these change on climate is clearly observed in natural systems, with changing precipitation, melting of ice, altering the hydrological systems. There has been an unprecedented increase in anthropogenic greenhouse gas emissions of CO_2, CH_4 and N_2O. Cumulative CO_2 emissions from 1876 to 2010 were 1,930 $GtCO_2$ and increased to 2,220 $GtCO_2$ by 2017. The yearly rise in CO_2 levels was 49±4.5 $GtCO_2$-eq/yr in 2010 which is expected to increase to 52-58 $GtCO_2$-eq/yr in 2030. Figure 1b shows the effect of rise of rise in CO_2 emissions on surface temperatures. Global warming is likely to reach 1.5^{o}C between 2030 and 2052 if it continues to increase at the current rate and its impacts on human and natural systems will be catastrophic and some will be irreversible (**Figure 1b**).[1,2]

Reducing the emissions and existing levels of greenhouse gases from the atmosphere is extremely crucial to stop further deterioration of earth's climate. Various technologies have been studied towards these goals. A possible solution is the utilization of abundant sources of renewable energy such as solar or wind energy. The energy produced from these renewable sources can be utilized to convert carbon dioxide and water into high energy density fuels such as hydrogen, methanol, etc. which solves both the

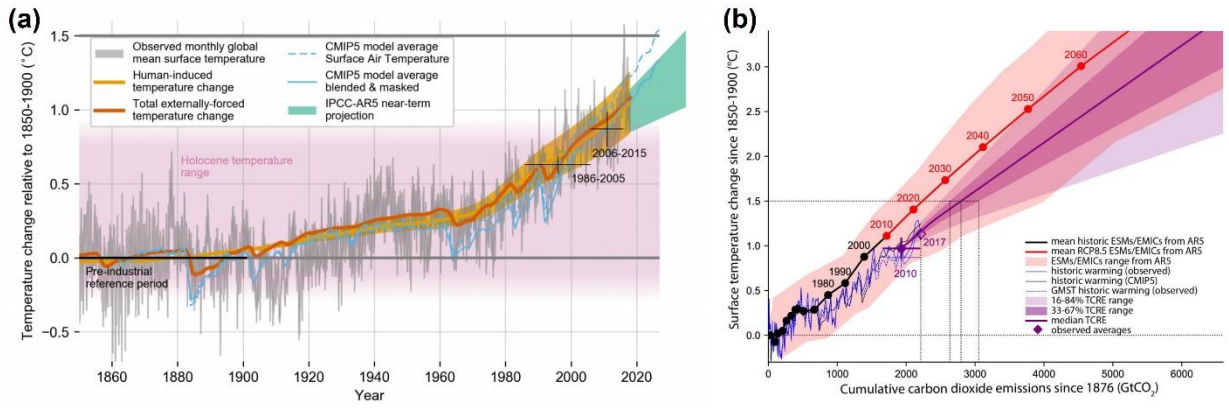

Figure 1. (a) Evolution of global mean surface temperature (GMST) over the period of instrumental observations. (b) Temperature changes from 1850–1900 versus cumulative CO_2 emissions since 1st January 1876. Reproduced with permission from ref 1 and 2.

problems of reducing CO_2 emissions and to reduce our dependance on fossil fuels. CO_2 can be utilized in several ways: (a) as a starting material for synthesis of chemicals such as urea, salicylic acid, inorganic carbonates, organic carbonates, formic acid, carbamates, acrylates, etc., (b) production of fuels by electrochemical, photochemical, photoelectrochemical and thermochemical reduction of CO_2 , (c) biotechnological conversion of CO_2 where enzymes such as formate dehydrogenase, formaldehyde dehydrogenase and alcohol dehydrogenase can reduce CO_2 in water at ambient temperature to produce methanol[3] and (c) direct utilization of CO_2 for example as a substitute for chemicals such as chlorofluorocarbons since it has a low climate change impact. Among these approaches the photochemical and electrochemical conversion of CO_2 and water are very interesting and attractive because of their environmental compatibility coupling with renewable energy resources (solar, tidal, and wind), ambient operating conditions and precise control over reaction by adjusting external parameters. The subsequent sections

discuss the fundamental principles the photochemical and electrochemical reduction of carbon dioxide and water.

1.2 Electrochemical reduction of CO_2

Reduction of CO_2 is a thermodynamically uphill reaction, demanding significant energy input to break the strong C=O bond (750kJ mol^{-1})[4]. CO_2 molecule has a linear geometry with $D_{\infty h}$ symmetry and a closed shell electronic configuration which makes it chemically inert. The adsorption of CO_2 on the catalyst surface followed by the first electron transfer forms a bent $CO_2^{\bullet-}$ which requires high energy since it breaks the symmetry and increases the repulsion between free electrons in bent molecule. This single electron transfer requires a high potential of -1.90 V (vs SHE), which poses a substantial overpotential and is generally the rate determining step.[5] In subsequent steps the adsorbed CO_2 radical anion takes up multiple protons and electrons, known as proton coupled electron transfer (PCET) reaction, to form various products. **Table 1** and **Figure 2** illustrates the various possible pathways for the reduction of CO_2 involving multiple electron and proton transfer.[5] The potential for the reduction of protons to form hydrogen lies very close to the reduction potentials for CO_2 which therefore acts as a competing reaction. Reduction of CO_2 follows complex reaction pathways with several intermediates and electron transfers making the kinetics very sluggish. CO_2 reduction reactions which are otherwise thermodynamically feasible than proton reduction becomes more difficult since the latter is a one electron transfer with low overpotentials. Therefore, proton reduction competes with ECO2RR and is a major deterring factor for many electrodes.[6]

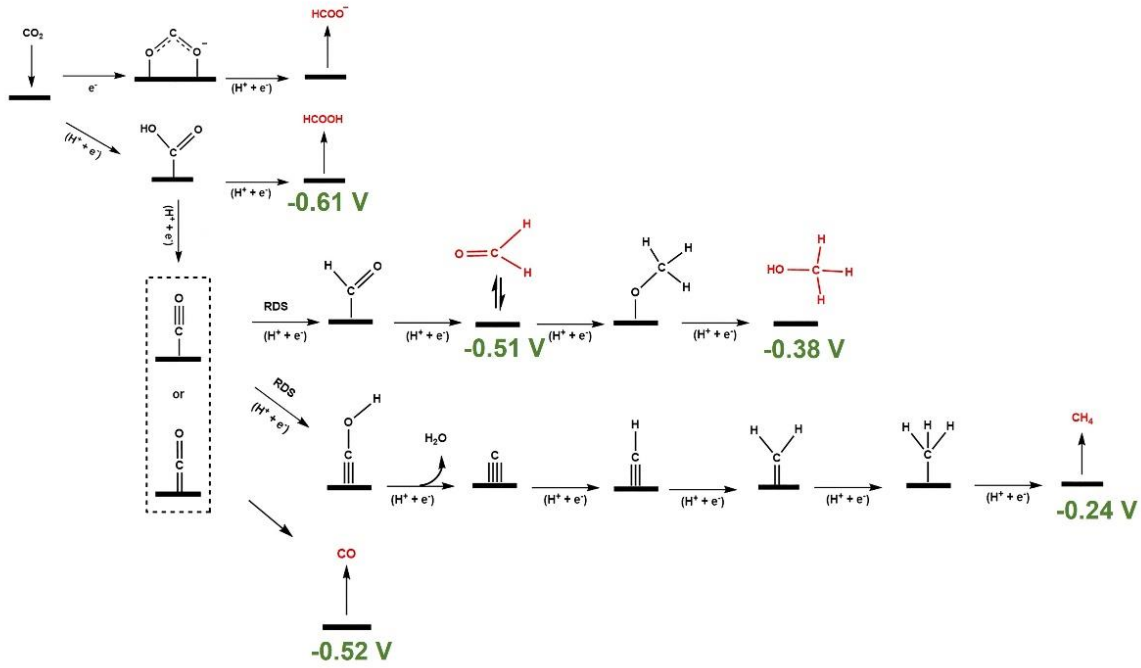

Figure 2. Electrochemical reduction of CO_2 on a catalyst surface with standard reduction potentials of products mentioned in green (vs RHE at pH = 7). Adapted with permission from ref 5, Copyright 2017, with permission from Elsevier.

Electrolytic cells convert electrical energy into chemical energy by applying voltage between a pair of electrodes and carrying out redox reactions. The two electrodes, cathode, and anode, facilitates the reduction and oxidation reactions by the transfer of electrons to and from the reactive species in the solution, respectively (**Figure 3**). Electrocatalysts are employed to participate in the electrochemical CO_2 reduction reaction (ECO2RR) and increase the rate of reaction at a potential close to equilibrium potential. Apart from reducing the overpotential, an electrocatalyst should exhibit high catalytic selectivity of the reaction products and chemical stability. The nature and properties of the electrocatalyst play a crucial role. Formation of the products depends greatly on the adsorption of CO_2 molecules and reaction intermediates on the catalyst surface. The

Table 1. Equilibrium reduction potential of CO_2 in aqueous solutions at Ph = 7 vs RHE.

Half-cell electrochemical reaction	Equilibrium potential (vs RHE)
$2H^+ + 2e^- \rightarrow H_2$	-0.42
$CO_2 + 2H^+ + 2e^- \rightarrow HCOOH$	-0.61
$CO_2 + 2H^+ + 2e^- \rightarrow CO + H_2O$	-0.52
$CO_2 + 4H^+ + 4e^- \rightarrow HCHO + H_2O$	-0.51
$CO_2 + 6H^+ + 6e^- \rightarrow CH_3OH + H_2O$	-0.38
$CO_2 + 8H^+ + 8e^- \rightarrow CH_4 + 2H_2O$	-0.24
$2CO_2 + 12H^+ + 12e^- \rightarrow C_2H_4 + 4H_2O$	-0.34
$CO_2 + e^- \rightarrow CO_2^-$	-1.9

Equilibrium potentials are related to thermodynamic redox potential of the reactions and can be calculated by the Nernst equation.

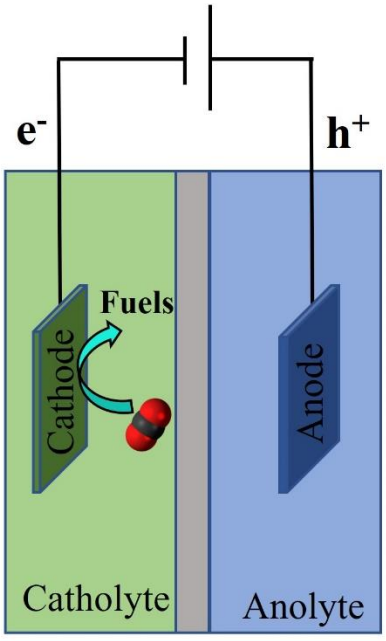

Cathode:

$CO_2(g) + e^- + H^+ \rightarrow$ Reduced products

(CO, HCOOH, CH_4, etc.)

$H^+ + e^- \rightarrow H_2$ (g)

Anode:

$2H_2O$ (l) $\rightarrow O_2 + 4\,H^+ + 4e^-$

Figure 3. Schematic illustration of an electrochemical cell with redox reactions at electrodes.

optimal adsorption of a molecule on a catalyst surface is generally defined by the Sabatier principle, which states that an efficient catalyst binds neither too strongly nor too weakly.[7] A multiple electron transfer reduction process includes more than one reaction intermediate, and the binding energies of the adsorbed intermediates might be correlated.[8][9] Theoretical calculations have revealed that there exists an energetic scaling relation between *CO and *CHO intermediates which leads to an overpotential for the reduction of CO_2 to methane or methanol.[10]

It is obvious from the above discussion that electrochemical reduction of CO_2 (ECO2RR) is a thermodynamically uphill reaction, the stable CO_2 molecule and complex reaction pathways makes the reaction kinetically sluggish with low product selectivities at times. The design and synthesis of efficient electrocatalysts for ECO2RR are needed to overcome these challenges. An extensive understanding of the underlying fundamental principles of the ECO2RR is necessary for the design of electrocatalysts and extensive efforts have been made to elucidate the mechanism of ECO2RR on different metal catalyst electrodes. The advent of the ECO2RR was marked by the seminal work by Rysselberghe,[11,12] Hori and Suzuki.[13] Rysselberghe et al.[11,12] was the first to demonstrate reduction of carbon dioxide at the dropping mercury cathode. Hori et al.[13] observed the production of gaseous products like CO, CH_4 and H_2 from the ECO2RR in aqueous bicarbonate solutions at various metal electrodes. Product formation was found to be cathode dependent where formate was the major product for Cd, Sn, Pb, In and Zn, CO was the major product for Ag and Au, CH_4 was the major product for Cu, and H_2 was the major product for Ni and Fe.[14] These pioneering studies laid the foundation for a surge in research for finding an efficient, selective, and stable electrocatalyst for CO_2 reduction.

More recent results also show that transition metals Ag, Zn, Au, Ni, Fe, Pt and Cu all produce methane, methanol, or both as the products of the CO_2 reduction reaction in aqueous bicarbonate solutions.[15] The activities of these metals are closely related to their CO binding abilities, where weak binding Au, Ag and Zn exhibit high current efficiencies and strong binding Ni, Fe and Pt exhibit higher HER efficiencies. Cu with moderate binding energy of CO exhibits a high efficiency but less compared to Au, Ag, or Zn.

1.2.1 Reaction Pathways

Understanding the mechanism of CO_2 reduction over a catalyst surface is crucial in designing better catalysts. ECO2RR follows three basic steps:

(i) adsorption of CO_2 molecules on the electrocatalyst surface,

(ii) a series of proton coupled electron transfer reactions involving various reaction intermediates and

(iii) reorganization of the adsorbed product followed by desorption from the surface.

Theoretical studies provide an elegant approach to model electrochemical reactions using a computational hydrogen electrode (CHE) model which when coupled with the adsorption energies from density functional theory (DFT) gives a complete picture of electrochemical reaction pathways and the voltage requirements.[16] Other models, namely water solvated and shuttling models, are also employed for extensive understanding.[17] Experimental studies have shown that the actual reduction of CO_2 does not occur at the thermodynamic potential (**Table 1**) but requires an overpotential which can be studied by the CHE model. Limiting potential, the potential at which the reaction pathway becomes exergonic, is a measure of the onset potential of different electrochemical reaction

pathways. The reaction step with the most negative limiting potential (U_L) is the potential determining step (PDS) and the difference between U_L and U_o (standard reduction potential) gives the thermodynamic overpotential required for PDS.

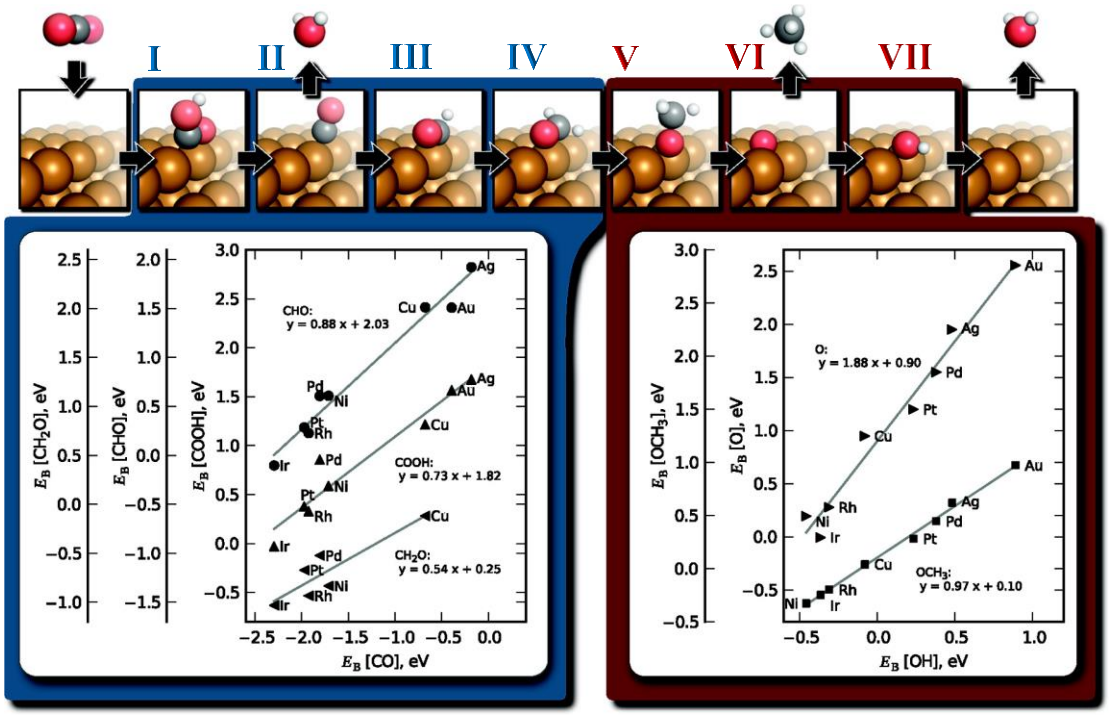

Figure 4. Free energy diagram for the proposed reaction pathway of CO_2 to CH_4 on Cu. Intermediates: I = HCOO, II= CO, III= HCO, IV=H_2CO, V=H_3CO, VI= O, VII=OH. Reprinted with permission from ref. 10, Copyright 2012, American Chemical Society.

In this section, we discuss a well-studied and understood mechanism of ECO2RR on Cu cathodes. The steps of ECO2RR on Cu are depicted in **Figure 4** which shows eight proton-electron transfer reactions forming methane, involving seven adsorbed intermediates.[18,19] The first reaction pathway(competing) is the reduction of H^+ to H_2, which starts at -0.03 V (vs. RHE) on a Cu (211) surface. The second reaction pathway is the formation of formic acid (HCOOH), where transfer of a proton-electron pair to adsorbed CO_2 forms carboxyl species and is the potential limiting step requiring -0.41 V

(vs. RHE). A subsequent addition of a proton-electron pair leads to the formation of HCOOH. Another reaction pathway that requires a similar potential of -0.41 V (vs. RHE) is the formation of CO. After the potential limiting step of carboxyl formation, the energy pathway is exergonic to remove water and form adsorbed CO. The weakly bound CO at this stage leads to the production of CO gas. The adsorbed CO is a very important intermediate for the subsequent reduction to form hydrocarbons such as CH_4, C_2H_4, etc. The limiting potential for the hydrogenation of CO to form adsorbed CHO is -0.74 V (vs. RHE). Addition of proton-electron pairs to CHO leads to the formation of adsorbed formaldehyde (H_2CO). Further protonation forms adsorbed methoxy (OCH_3). A proton from the solution takes away the methyl group as methane and the remaining adsorbed oxygen forms water. The CHE model predicts several pathways for ethylene formation, all of which go through adsorbed CHO. The formation of a C-C bond occurs in a non-electrochemical step. Thus, the key step for the formation of hydrocarbons is the formation of adsorbed CHO where its stability relative to adsorbed CO will significantly reduce the overpotential. Catalysts with weak CO binding will predominantly form CO gas whereas catalysts that bind CHO strongly will lead to the formation of hydrocarbons.

The seven intermediates on the Cu surface interact with the catalyst surface through carbon or oxygen atoms. A correlation among the adsorption energies of the intermediates bound through the C atom or O atom exists for all intermediates (**Figure 4**).[10] For example, the binding energy (E_b) of CHO varies linearly with the binding energy of CO:

$$E_b\,[CHO] = 0.55\ E_b\,[CO] + 2.03\ eV \qquad (1)$$

These linear scaling relationships make it possible to relate the limiting potential of elementary steps as a function of E_B[CO] or E_B[OH] and a volcano plot emerges for the

overpotential of the CO_2RR to CH_4 on different metal electrodes (**Figure 5**). Limiting potential (U_L) with respect to the equilibrium potential gives an estimate for the potential required for a reaction step. The lines for CO* → CHO* and CO_2 → COOH* have the

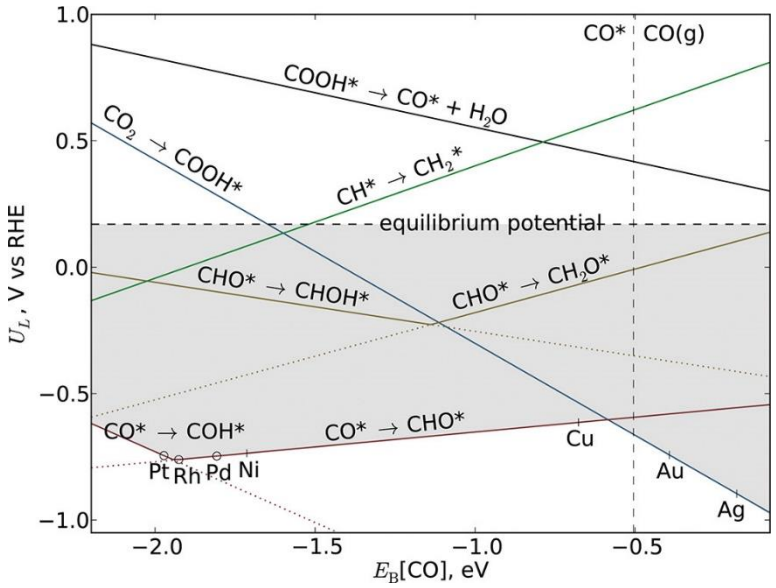

Figure 5. Limiting potentials (U_L) for elementary proton-transfer steps for the mechanism of figure 4. Reprinted with permission from ref. 10, Copyright 2012, American Chemical Society.

most negative U_L, and hence would determine the overpotential of the reaction. The U_L lines for the oxygen bound species are much less negative compared to carbon bound species, which implies that for most catalysts, the potential limiting step will be CO* → CHO*. Moreover, the U_L line for this step is nearly horizontal, which can be explained by equation (1) suggesting that the binding energies of CO and CHO are closely correlated and a catalyst surface that stabilizes the intermediate CHO will also stabilize CO with similar binding energy. There are other pathways possible and **Figure 5** shows a few of them, which proceed *via* a CO* intermediate. A dotted vertical equilibrium line shows binding energies at which CO is more stable than CO* and therefore catalysts on the right

side of the line would liberate CO. Solid lines in the plot depict the most favorable reaction at any value of E_B[CO] and therefore trends in CO_2 reduction for a transition metal catalyst can be predicted. Au and Ag which are present on the right of the CO desorption line predominantly produce CO as the major product. Cu is present at the top of the volcano while still requiring a large overpotential for the CO* → CHO* step. Catalysts marked with open circles indicate those where the HER would dominate over CO_2 reduction.[18,19] Improvement of the catalytic activity of electrocatalysts is limited by the linear scaling relations of intermediates; for example, the reduction of CO_2 to CO will be fast if the adsorption of COOH is strong and adsorption of CO is weak. This requirement is not fulfilled since the binding energies of intermediates scale linearly. Moreover, the reduction beyond CO goes through a PCET to form CHO and again the binding energies of CO and CHO scale linearly. Hence, the intermediates COOH and CHO cannot be independently stabilized without CO, thereby limiting the overpotential for the reaction.

Experimental studies of CO_2 reduction on the Cu surface by the Jaramillo group stresses on the complex nature of the reduction mechanism at catalyst surfaces.[20] A total of 16 different products were detected, out of which 12 were C2 or C3 species. Hydrogen, CO, and formate were the major products at lower potentials and as the potential is increased to more negative values, formation of C1–C3 products is observed. A later study on various transition metals Ag, Zn, Au, Ni, Fe, Pt and Cu shows that all of them produce methane, methanol, or both.[15] The above experimental results show that at lower overpotentials, the products formed only require two electrons while more reduced products are formed only at higher overpotentials. These results are consistent with the theoretical mechanistic discussion where it was concluded that the formation of CO and

formate has low kinetic barrier and the conversion of CO to hydrocarbons goes through a rather difficult CO* - CHO* step, hence requiring higher overpotentials. Formation of all the C2 and C3 products as a function of potential follows the same trend indicating that they follow a similar mechanistic pathway. Initially, the C–C coupling rate increases with increasing potential and then starts to decrease which could be due to more favorable proto-electron transfer to from methane at such negative potentials. At such high potentials, the probability of two adsorbed C1 species encountering each other decreases.

The above discussion on the mechanistic aspect of CO_2 reduction sheds light on various potential limiting reaction steps. Protonation of adsorbed CO* to adsorbed CHO* and a poor activity for the HER are the necessary requirements for efficient CO_2 reduction to higher products (more reduced than CO) on a catalyst surface. Linear scaling relationships between reaction intermediates increase the overpotential and therefore decoupling the binding energies could be a way to overcome this problem.

1.2.2 Measurement parameters, electrochemical cell design and electrolyte

Activity descriptors: Electrochemical reduction of CO_2 (ECO2RR) becomes thermodynamically favorable at the potentials mentioned in the equations in Table 1, but these reactions initiate at more negative potentials due to kinetic limitations. The potential at which the thermodynamic and kinetic barrier becomes downhill and reduction reaction commences is defined as the onset potential. Experimental determination of the onset potential is ill defined and various methods are used in the literature. Two of the most common ways to determine it are, first, the intersection point of the tangent of exponential increase in current and background current and second, the linear extrapolation of the exponential rise in current at increasing potential. The extra potential required to overcome

the kinetic barrier, the difference between thermodynamic potential and onset potential, is defined as overpotential. Current densities are also an important parameter which indicates the performance of the catalyst and the electrochemical setup as it is a measure of total rate of reaction. Current obtained at an overpotential normalized over the surface area of the catalyst is defined as the current density (j). It is essential to normalize the current with electrochemically active surface area (ECSA) rather than geometric area of the electrode to determine if the higher currents are due to high surface area or enhanced intrinsic activity. A higher current density could be due to better catalytic activity, increased electrochemically active sites and an efficient electrochemical cell setup. The efficiency of the catalyst is defined in terms of faradaic efficiency, which is a direct parameter to show the selectivity of a catalyst. To elucidate the reaction mechanism a plot of overpotential vs. logarithm of current density is plotted, known as the Tafel plot. The slope of this plot in the kinetically controlled region is known as the Tafel slope which is an indicator of reaction mechanism and rate determining steps. The Tafel slope is a useful tool although it should be used with caution due to the limitations of its applicability. The experimental data, current vs. overpotential plot, requires more than two order of magnitude current range with mass transport limitations, Ohmic drop, and background current being nullified or considered.[21] Similarly, when more than one product is formed, partial current density should be used instead of total current density.

Electrochemical cell configuration: ECO2RR studies depend greatly on the configuration of the electrochemical cell. An electrochemical H-cell is the most widely used cell configuration for catalyst and electrolyte evaluation. In a typical H-cell configuration, the working electrode and reference electrode are placed in the cathodic compartment and the

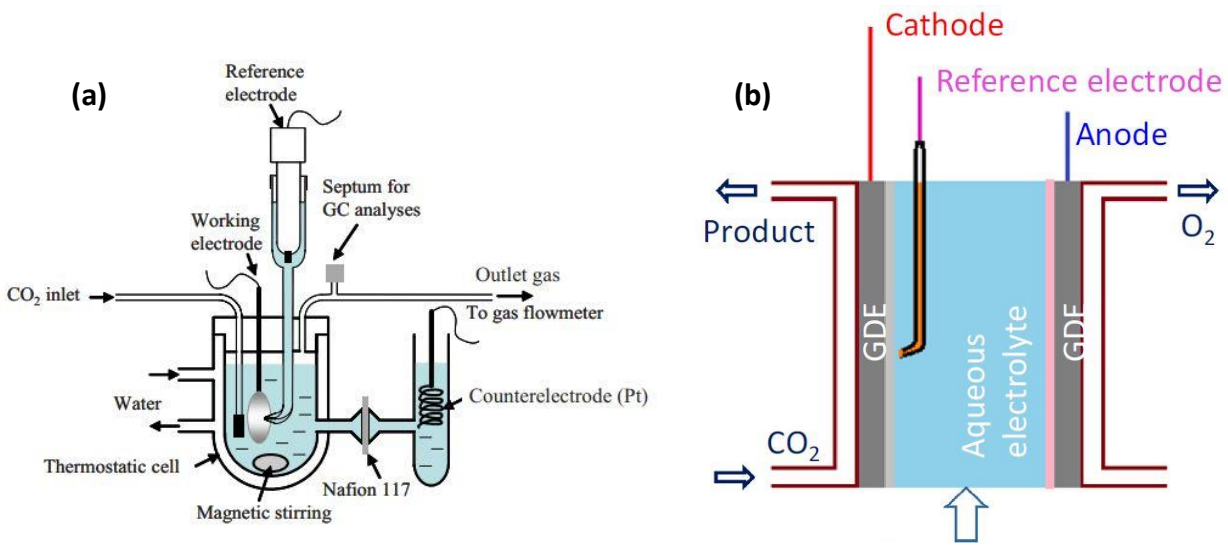

Figure 6. Schematic representation of electrochemical cell configuration (a) H-cell and (b) Microfluidic cell. Reproduction with permission from ref. 22, Copyright 2010, The Electrochemical Society and Reproduction with permission from ref. 23, Copyright 2020, Elsevier.

counter electrode is placed in the anodic compartment. The cathodic and anodic compartments are separated by an ion-exchange membrane which supports ionic conductivity and suppresses diffusion of products and species to and from both compartments. CO_2 gas is bubbled in the cathodic compartment and is fed to a gas chromatograph instrument for product analysis (**Figure 6a**).[22] Evaluation of the CO2RR activity can be extended using a microfluidic flow cell system which uses a gas diffusion electrode (GDE). The cathode and anode are separated by a thin channel (<1 mm) of flowing liquid electrolyte and gaseous CO_2 enters the system from the back of the cathode thus eliminating the solubility limitation. The mass transport limitation is lifted due to this gas phase diffusion of CO_2 at the GDE electrode/electrolyte interface (**Figure 6b**).[23]

Electrolyte: Selection of a suitable electrolyte with high conductivity and sufficient CO_2 solubility is of utmost importance for selective and efficient ECO2RR. The most used electrolytes are aqueous solutions of sodium and potassium bicarbonate which have a pH

value of 7 when saturated with CO_2 and act as buffers during the ECO2RR. Due to the formation of hydroxide species during the ECO2RR and HER, the local pH near the electrode is higher than the bulk electrolyte thus requiring buffer electrolytes to reduce this effect.[24]

Low CO_2 solubility and high proton concentration assisting competing HER prompts for the use of non-aqueous electrolytes such as dimethyl formamide, acetonitrile and methanol. These non-aqueous electrolytes have higher CO_2 solubility, and the concentration of water can be precisely regulated to suppress the competing HER. Furthermore, ECO2RR in nonaqueous solvents is sensitive to the presence of water, where it can change the reaction pathways leading to different product selectivity in the presence of trace amounts of water.[25] Furthermore, the presence of water in a non-aqueous electrolyte has a strong promoting effect due to the stabilization of CO_2[26] and to participate in PCET reactions to form C–H bonds. Nonaqueous solvents generally have low faradaic efficiencies thereby limiting their wide-scale applications.[27] Ionic liquid (IL) electrolytes are another alternative because of their high electrical conductivities and high solubility of CO_2.[28] Imidazolium based ILs have been shown to lower the free energy of formation of CO_2 by complexing with CO_2 molecules, thus reducing the overall barrier for the ECO2RR.[29,30] ILs despite their low overpotentials for the ECO2RR exhibit low current density, are very costly and unstable in the presence of water are not an obvious choice for an electrolyte. Briefly, the aqueous bicarbonate solutions are still the most practical and reliable electrolyte choice for the ECO2RR.

1.3 Photochemical reduction of water and carbon dioxide

Sun is an inexhaustible source of energy which can be utilized to meet the energy demands. Photoexcitation of a light absorbing material from sunlight is therefore an attractive approach to generate highly energetic electrons capable of driving H_2O/CO_2 reduction. Honda and Fujishima were the first to demonstrate splitting of water under UV illumination from TiO_2 photoelectrodes.[31] Splitting of water/CO_2 is possible by light, wherein a light harvesting material such as a dye or a semiconductor absorbs the radiation, and the excitation energy is eventually transmitted to water/CO_2 for the reduction and oxidation. There are two approaches towards overall photocatalytic water/CO_2 splitting: (a) using a single photocatalyst for reduction and oxidation and (b) approach based on natural photosynthesis (Z-scheme) in which two photocatalysts are employed for the reduction and oxidation.[32,33] Photogenerated electrons are utilized for the reduction of water, which is a one electron transfer reaction and reduction of CO_2 involving multiple electron-proton transfer, as already discussed in previous section. On the other hand, the photogenerated holes are utilized for oxidation of water to oxygen. Sunlight can be captured by using a light harvesting material such as a dye or a semiconductor. Semiconductors are an interesting type of materials for light harvesting because of their tuneable band gaps. The next section discusses the mechanism of photocatalytic reduction of H_2O/CO_2 involving semiconductor materials.

1.3.1 Reaction Pathways

The process of photocatalytic reduction of H_2O/CO_2 on a semiconductor photocatalyst involves three basic steps as illustrated in **figure 7a**:

(i) absorption of light,

(ii) separation of charge carriers

(iii) redox reactions at the surface

Upon illumination of light the semiconductor photocatalyst absorbs light, which excites the electrons from valence band (VB) to the conduction band (CB), leaving behind holes in the VB. After the formation of photogenerated electron and holes, the next crucial step is their spatial separation to reach the surface of semiconductor for efficient utilization in redox reactions. The final step is the redox reaction at the catalyst surface which depends on the presence of active sites and surface area. The photogenerated charge carriers can undergo several reactions involving redox reactions at the catalyst surface and recombination (**Figure 7b**). Recombination of charge carriers has detrimental effect on the

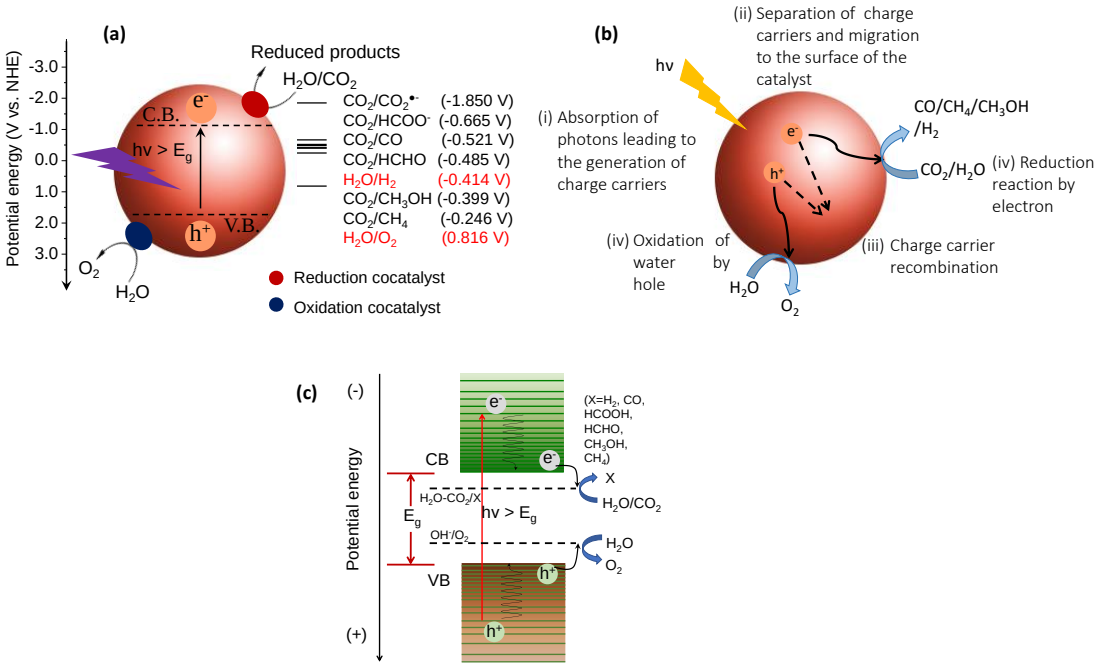

Figure 7. (a) Schematic illustration of mechanism of photocatalytic H_2O and CO_2 reduction on semiconductor photocatalyst, (b) various possible surface reactions of photogenerated charge carriers and (c) thermodynamic requirements of a semiconductor for photocatalytic H_2O and CO_2 reduction. Reproduced with permission from ref 33, Copyright 2017, American Chemical Society.

overall photocatalytic efficiency of photocatalyst. The competition between charge carrier recombination and separation depends on the relative timescale of the two processes and the recombination rate which is affected by a complex interplay of structural parameters such as material crystallinity, particle dimension and surface properties.[34]

From a thermodynamic standpoint, the levels of conduction band minima and valence band maxima are crucial to determine the feasibility of reduction and oxidation reactions, respectively. It is essential that the potential of the valence band maximum (VBM) and the conduction band minimum (CBM) of the semiconductor should match with the oxidation and reduction potentials of the adsorbate, respectively. The CBM should be more negative than the reduction potential (**Table 1**) while the VBM should be more positive than the water oxidation potential (0.82V vs NHE at pH 7) (**Figure 7c**). If the above conditions are satisfied, transfer of electrons from the CB to H_2O/CO_2 as well as from water to the VB becomes thermodynamically favorable. The semiconductor photocatalyst should possess a band gap that straddles the reduction and oxidation potentials of H_2O/CO_2 and water, respectively. From the kinetic viewpoint, it is crucial to provide an overpotential to overcome kinetic barriers and achieve a high reaction rate.[35,36] The overall efficiency of the system depends on the cumulative effect of efficiencies of all the processes namely, light absorption, charge separation and migration, transport efficiency and utilization of electrons for reduction reaction. Maintaining a balance of thermodynamic and kinetic limitations, which depend upon electronic and surface properties, is essential. Therefore, all the effects need to be optimized to design an efficient photocatalyst. Additionally, the redox potentials for CO_2 reduction are very close to water reduction potential which further complicates the selectivity of the catalyst. Reduction of

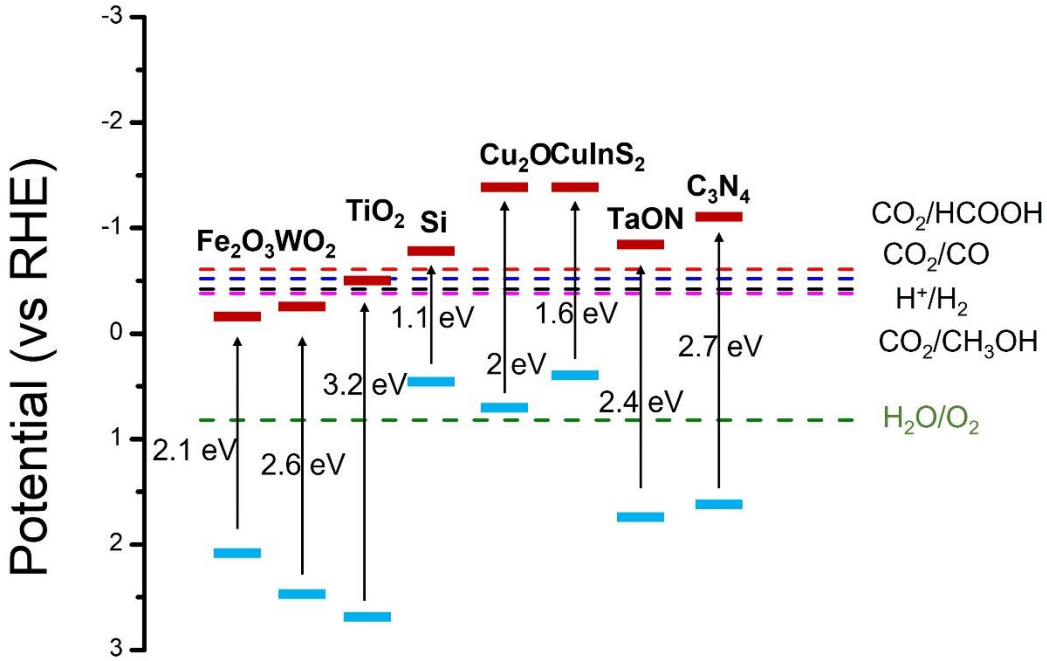

Figure 8. Band position of some semiconductors in comparison with water and carbon dioxide reduction potentials (vs RHE at pH=7). Adapted with permission from Royal Society of Chemistry, ref 37; permission conveyed through Copyright Clearance Center, Inc.

CO_2 proceeds via several steps involving transfer of electron-proton pairs and formation of various intermediates which increases the kinetic barrier and hence requires a high overpotential compared to water reduction. **Figure 8** shows the relative position of water reduction and CO_2 reduction potentials of some semiconductors.[37] This band alignment and kinetic barriers suggest that water reduction always competes with CO_2 reduction.[38]

Co-catalysts are generally introduced to increase the number of active sites for redox reactions and to decrease charge carrier recombination. The photogenerated charge carriers are transferred to the adsorbed cocatalyst, which acts as an electron or hole sink.[39] For example, metal nanoparticles supported on semiconductor can efficiently separate the charge carriers. Fermi level (E_f) of metal lies below CB level which facilitates the transfer

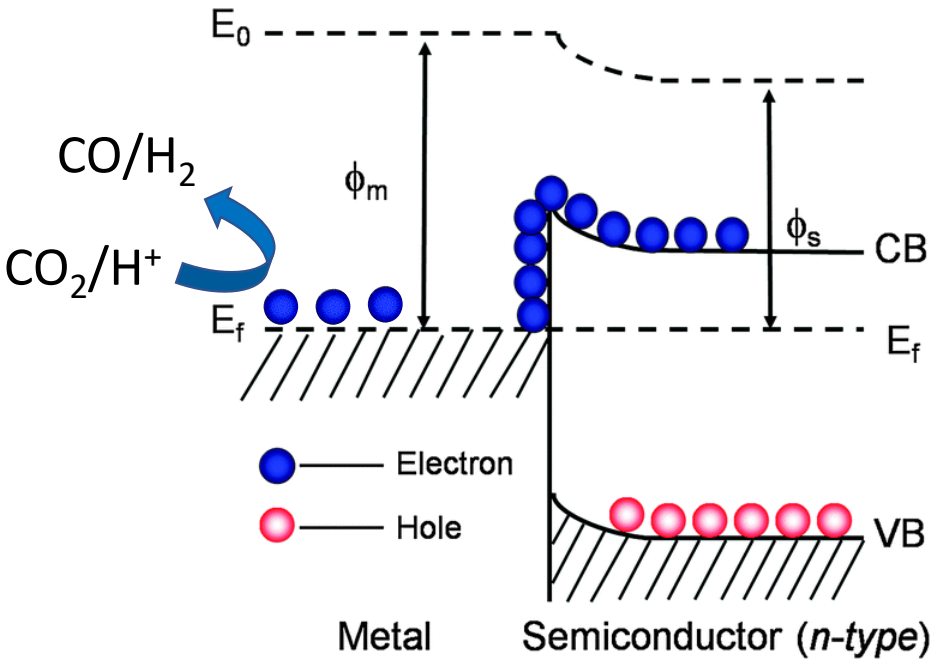

Figure 9. Schematic illustration of mechanism of photocatalytic H_2O and CO_2 reduction on semiconductor loaded with a metal cocatalyst. Adapted with permission from Royal Society of Chemistry, ref 39; permission conveyed through Copyright Clearance Center, Inc.

of electrons from semiconductor CBM to metal E_f (**Figure 9**). The electrons are accumulated in the metal while the holes in semiconductor, effectively forming a Schottky barrier at the metal-semiconductor interface. Therefore, basic function of a semiconductor in photocatalysis is to absorb incident photons to generate electron–hole pairs and enable its separation to the reactive site. Introduction of a cocatalyst on the surface of semiconductor at this stage considerably expedites the interfacial electron transfer rates.

1.3.2 Screening of photocatalysts, activity parameters and experimental setup

A suitable photocatalyst must possess a band gap that sufficiently absorbs a large part of solar spectrum. It should possess suitable band edge positions that straddle the reduction and oxidation potentials to ensure thermodynamically feasible reaction. To ensure efficient

separation of photo-generated charge carriers the photocatalyst should have high crystallinity, which eliminates crystal imperfections that act as recombination centers.

Particle size also affects the charge carrier separation, where a small size allows the carriers to quickly diffuse to the surface thus decreasing the recombination probability. Although, a very small size will lead to insufficient light absorption. Morphology also affects the photocatalytic activity where it affects the anisotropic charge distribution, due to which reaction sites can be spatially separated.[40,41] The current bottleneck of photocatalyst systems is the charge carrier recombination which results in low quantum yields. Various possible strategies such as band gap engineering, micro/nano engineering, bionic engineering, cocatalyst engineering, surface engineering, interface engineering has been employed to enhance the efficiency of photocatalysts.[34,38]

Correct measurement of the catalytic efficiencies is very crucial and therefore conditions under which the efficiency is measured must be carefully determined.[42] Evaluation of photocatalytic activity can be done by measuring the amount of product (gas or liquid) formed during reaction. The product formation depends greatly on the experimental setup and reaction conditions. So, to compare the activity it is important to calculate overall quantum yield (QY) or apparent quantum yield (AQY).

QY (%) = Number of reacted electrons/Number of absorbed photons * 100

AQY (%) = Number of reacted electrons/Number of incident photons * 100

It is common practice to use sacrificial electron donors to expedite the rate of oxidation reaction, which makes it convenient to study only the reduction half of the reaction. However, the oxidation products of sacrificial donors often contribute to the yield

of reduction products, thereby creating inaccuracies in the quantification of reduction products. The sacrificial donors generally employed for photocatalysis are alcohols, triethanolamine, ascorbic acid, EDTA, etc. which are rich in carbon and hydrogen, and produce hydrogen and C1 products after oxidation.[43] Sacrificial donors can also participate indirectly in the reduction reaction. For example, oxidation of alcohols forms alkoxy radicals which can inject electrons in the semiconductor, hence participating indirectly in the reduction reaction (**Figure 10**). It is therefore imperative to carefully analyze the role of sacrificial donors in every photocatalytic system and determine their contribution to the overall yield of reduction products.[44]

Methods of photocatalytic H_2O reduction: Reduction of water can be carried out in liquid phase with the catalyst dispersed in an aqueous solution containing additives such as sacrificial electron donors. The most used reaction setup consists of a reaction cell (quartz

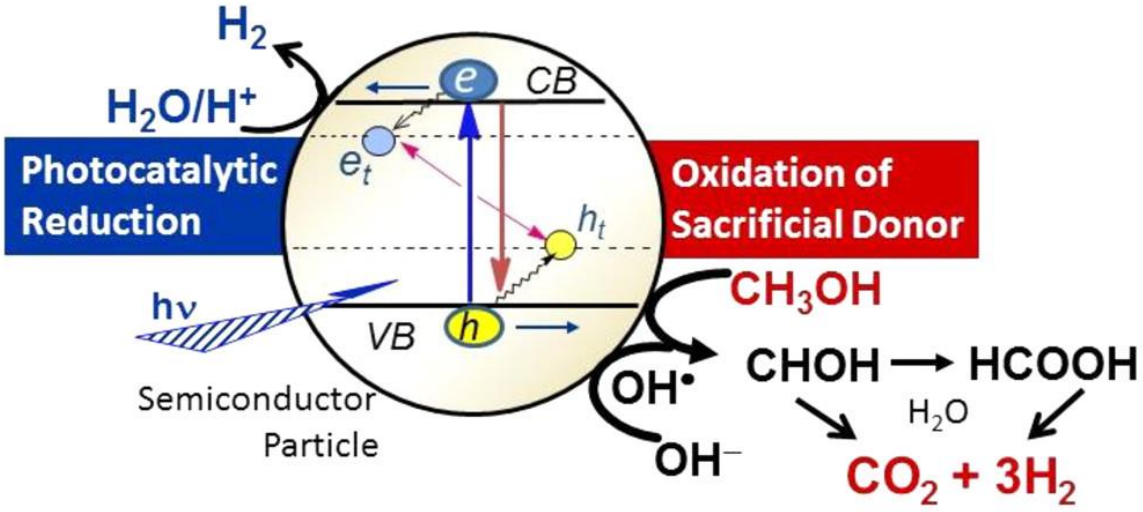

Figure 10. Schematic illustration of the photocatalytic reduction of water in the presence of methanol. The oxidation of methanol (sacrificial donor) in this example by photogenerated holes and hydroxyl radicals could result in the formation of H_2 and other intermediates. Reproduced with permission from ref 44, Copyright 2018, American Chemical Society.

or glass), vacuum pump, light source (generally a Xe-lamp with power in the range of 300–400 W), and gas chromatography instrument. Prior to the light irradiation, reaction cell with photocatalyst dispersion should be purged with the inert gas (N_2 or Ar) to remove the dissolved oxygen and the cell should be airtight. Evolved O_2 and H_2 gases can be measured using gas sensors or volumetric methods. It is essential to study the stability of photocatalyst over long durations and ensure that it retains its chemical and structural stability during the reaction.

Methods of photocatalytic CO_2 reduction: Reduction of CO_2 can be carried out in liquid phase or gas phase. In the liquid-phase reaction, reduction of CO_2 is carried out with a saturated aqueous solution of CO_2. CO_2 has limited solubility in water which can be improved by using additives such as NaOH, $NaHCO_3$, or Na_2CO_3. These additives enhance the CO_2 solubility, though the reduction of bicarbonate and carbonate species is more difficult. Surface adsorption of H_2O is preferable over CO_2 in the liquid phase, and thus the reduction of water is favorable. On the other hand, gas-phase reactions are carried out with humidified CO_2. To explore the effect of the method of evaluation on activities, Xie et al.[45] have employed TiO_2 and Pt-TiO_2 as photocatalysts and studied the reduction of CO_2 in both the liquid phase and gas phase. CH_4 production activity is nearly 3 times more, whereas hydrogen production is less in gas-phase compared to liquid phase reactions. Nearly 3−4 times more selectivity in CO_2 reduction over water reduction is observed in the gas phase.

The activity in the liquid phase is also affected by the pH of the reaction medium, surface hydroxyl groups, solvent, and additives. The increase in pH increases the rate of the reaction

CO_2 (aq) + OH^- ⇄ HCO_3^-

This leads to different concentrations of species (CO_3^{2-}, HCO_3^-, and CO_2) at different pH.[46] Thus, addition of NaOH could improve the dissolution of CO_2, thereby increasing the efficiency of photoreduction of CO_2 on TiO_2-supported Cu catalysts. In the gas phase, photocatalytic activity is affected by the surface properties of the photocatalysts, CO_2−H_2O ratio, and feed pressure, temperature, etc. It is often customary to use sacrificial reagents to consume the holes. The addition of a sacrificial reagent to the reaction mixture enhances photocatalytic reduction.

1.4 Conclusion

The above discussion highlights the importance and fundamentals of electrochemical and photochemical reduction of CO_2 and H_2O. Great amount of research has been carried out to design catalysts efficient enough for practical applications. Although a plethora of materials, reaction media and electrochemical cell designs have been studied, the problem is still at large. The complete understanding of the reduction mechanism is a necessary piece of the puzzle. There are many challenges that lie ahead in developing highly efficient catalyst systems, there has been progress towards achieving this goal. In the following chapters, we explore various types of materials for the electrochemical and photochemical reduction of carbon dioxide and water.

1.5 References

[1] H. O. Pörtner, D. C. Roberts, M. Tignor, E. S. Poloczanska, K. Mintenbeck, A. Alegria, M. Craig, S. Langsdorf, S. Löschke, V. Möller, A. Okem, B. Rama, "IPCC, 2022: Climate Change 2022: Impacts, Adaptation, and Vulnerability. Contribution of Working Group II to the Sixth Assessment Report of the Intergovernmental Panel on Climate Change,"

[2] V. Masson-Delmotte, P. Zhai, H.-O. Pörtner, D. Roberts, J. Skea, P. Shukla, A. Pirani, W. Moufouma-Okia, C. Péan, R. Pidcock, S. Connors, J. Matthews, Y. Chen, X. Zhou, M. Gomis, E. Lonnoy, T. Maycock, M. Tignor, T. Waterfield, *IPCC, 2018: Summary for Policymakers. In: Global Warming of 1.5°C. An IPCC Special Report on the impacts of Global Warming of 1.5°C above Pre-Industrial Levels and Related Global Greenhouse Gas Emission Pathways, in the Context of Strengthening the Global Response to the Threat of Climate Change, Sustainable Development, and Efforts to Eradicate Poverty*, **2018**.

[3] R. Obert, B. C. Dave, *Ind. Eng. Chem. Res* **1998**, *37*, 12192.

[4] D. D. Wagman, W. H. Evans, V. B. Parker, *Supplement Journal of Physical and Chemical Reference Data* **1989**, *18*, 783.

[5] Z. Sun, T. Ma, H. Tao, Q. Fan, B. Han, *Chem* **2017**, *3*, 560.

[6] D. T. Whipple, P. J. A. Kenis, *J. Phys. Chem. Lett* **2010**, *1*, 3451.

[7] M. Duca, M. T. M. Koper, *Surface Interf. Sci.* **2020**, 773.

[8] F. Abild-Pedersen, J. Greeley, F. Studt, J. Rossmeisl, T. R. Munter, P. G. Moses, E. Skúlason, T. Bligaard, J. K. Nørskov, *Phys. Rev. Lett.* **2007**, *99*, 016105.

[9] F. Calle-Vallejo, J. I. Martínez, J. M. García-Lastra, J. Rossmeisl, M. T. M. Koper, *Phys. Rev. Lett.* **2012**, *108*, 116103.

[10] A. A. Peterson, J. K. Nørskov, *J. Phys. Chem. Lett* **2012**, *3*, 21.

[11] P. van Rysselberghe, G. J. Alkire, *J. Am. Chem. Soc.* **1944**, *66*, 1801.

[12] T. E. Teeter, P. van Rysselberghe, *J. Chem. Phys.* **1954**, *22*, 759.

[13] Y. Hori, K. Kikuchi, S. Suzuki, *Chem. Lett.* **1985**, *14*, 1695.

[14] Y. Hori, K. Kikuchi, A. Murata, S. Suzuki, *Chem. Lett.* **1986**, 897.

[15] K. P. Kuhl, T. Hatsukade, E. R. Cave, D. N. Abram, J. Kibsgaard, T. F. Jaramillo, *J. Am. Chem. Soc.* **2014**, *136*, 14107.

[16] S. Xu, E. A. Carter, *Chem. Rev.* **2018**, *119*, 6631.

[17] Y. Li, S. H. Chan, Q. Sun, *Nanoscale* **2015**, *7*, 8663.

[18] A. A. Peterson, F. Abild-Pedersen, F. Studt, J. Rossmeisl, J. K. Nørskov, *Energy Environ. Sci.* **2010**, *3*, 1311.

[19] W. J. Durand, A. A. Peterson, F. Studt, F. Abild-Pedersen, J. K. Nørskov, *Surface Sci.* **2011**, *605*, 1354.

[20] K. P. Kuhl, E. R. Cave, D. N. Abram, T. F. Jaramillo, *Energy Environ. Sci.* **2012**, *5*, 7050.

[21] A. P. Murthy, J. Theerthagiri, J. Madhavan, *J. Phys. Chem. C* **2018**, *122*, 23943.

[22] C. Delacourt, P. L. Ridgway, J. Newman, *J. Electrochem. Soc.* **2010**, *157*, B1902.

[23] R. A. Tufa, D. Chanda, M. Ma, D. Aili, T. B. Demissie, J. Vaes, Q. Li, S. Liu, D. Pant, *Appl. Energy* **2020**, *277*, 115557.

[24] M. T. M. Koper, *Chem. Sci.* **2013**, *4*, 2710.

[25] A. Aljabour, H. Coskun, D. H. Apaydin, F. Ozel, A. W. Hassel, P. Stadler, N. S. Sariciftci, M. Kus, *Appl. Catal. B Environ.* **2018**, *229*, 163.

[26] A. v. Rudnev, U. E. Zhumaev, A. Kuzume, S. Vesztergom, J. Furrer, P. Broekmann, T. Wandlowski, *Electrochim. Acta* **2016**, *189*, 38.

[27] F. Zhang, H. Zhang, Z. Liu, *Curr. Op. Green Sustain. Chem.* **2019**, *16*, 77.

[28] C. Cadena, J. L. Anthony, J. K. Shah, T. I. Morrow, J. F. Brennecke, E. J. Maginn, *J. Am. Chem. Soc.* **2004**, *126*, 5300.

[29] S. Wang, X. Wang, *Angew. Chem. Int. Ed.* **2016**, *55*, 2308.

[30] B. A. Rosen, A. Salehi-Khojin, M. R. Thorson, W. Zhu, D. T. Whipple, P. J. A. Kenis, R. I. Masel, *Science* **2011**, *334*, 643.

[31] A. Fujishima, K. Honda, *Nature* **1972**, *238*, 37.

[32] K. Maeda, K. Domen, *J. Phys. Chem. Lett.* **2010**, *1*, 2655.

[33] S. R. Lingampalli, M. M. Ayyub, C. N. R. Rao, *ACS Omega* **2017**, *2*, 2740.

[34] J. Wu, Y. Huang, W. Ye, Y. Li, J. Wu, Y. Huang, W. Ye, Y. Li, *Adv. Sci.* **2017**, *4*, 1700194.

[35] A. Kudo, Y. Miseki, *Chem. Soc. Rev.* **2008**, *38*, 253.

[36] X. Li, J. Yu, J. Low, Y. Fang, J. Xiao, X. Chen, *J. Mater. Chem. A* **2015**, *3*, 2485.

[37] P. D. Tran, L. H. Wong, J. Barber, J. S. C. Loo, *Energy Environ. Sci.* **2012**, *5*, 5902.

[38] J. K. Stolarczyk, S. Bhattacharyya, L. Polavarapu, J. Feldmann, *ACS Catal.* **2018**, *8*, 3602.

[39] H. Wang, L. Zhang, Z. Chen, J. Hu, S. Li, Z. Wang, J. Liu, X. Wang, *Chem. Soc. Rev.* **2014**, *43*, 5234.

[40] S. Chen, T. Takata, K. Domen, *Nat. Rev. Mater.* **2017**, 2.

[41] H. Kato, K. Asakura, A. Kudo, *J. Am. Chem. Soc.* **2003**, *125*, 3082.

[42] J. M. Buriak, P. V. Kamat, K. S. Schanze, *ACS Appl. Mater. Interfaces* **2014**, 6, 15...

[43] J. Schneider, D. W. Bahnemann, *J. Phys. Chem. Lett.* **2013**, *4*, 3479.

[44] J. Schneider, D. W. Bahnemann, Y. Maeda, A. Fujishima, K. Honda, J. M. Buriak, P. v Kamat, K. S. Schanze, M. Qureshi, K. Takanabe, K. Rajeshwar, A. Thomas, C. Janákyjanáky, R. Chen, *ACS Energy Lett.* **2018**, *3*, 622.

[45] S. Xie, Y. Wang, Q. Zhang, W. Deng, Y. Wang, *ACS Catal.* **2014**, *4*, 3644.

[46] M. Gattrell, N. Gupta, A. Co, *J. Electroanal. Chem.* **2006**, *594*, 1.

Chapter 2

Photocatalytic reduction of CO_2 by employing $ZnO/Ag_{1-x}Cu_x/CdS$ and related heterostructures

Summary

In view of the great importance of finding ways to reduce CO_2 by using solar energy, we have examined the advantage of employing heterostructures containing bimetallic alloys for the purpose. This choice is based on the knowledge that metals such as Pt reduce CO_2, although the activity may not be considerable. Heterostructures are employed to enhance the charge carrier separation and metal nanoparticles act as co catalyst. Our studies on the reduction of CO_2 by ZnO/M/CdS (M = Ag, Au, $Ag_{1-x}Au_x$, $Ag_{1-x}Cu_x$) heterostructures in liquid phase have shown good results specially in the case of $ZnO/Ag_{1-x}Cu_x/CdS$, reaching a CO production activity of 327.4 µmol $h^{-1}g^{-1}$. The heterostructures also reduce CO_2 in the gas-phase although the production activity of CO is not high. Some of the heterostructures exhibit reduction of CO_2 even in the absence of a sacrificial reagent.

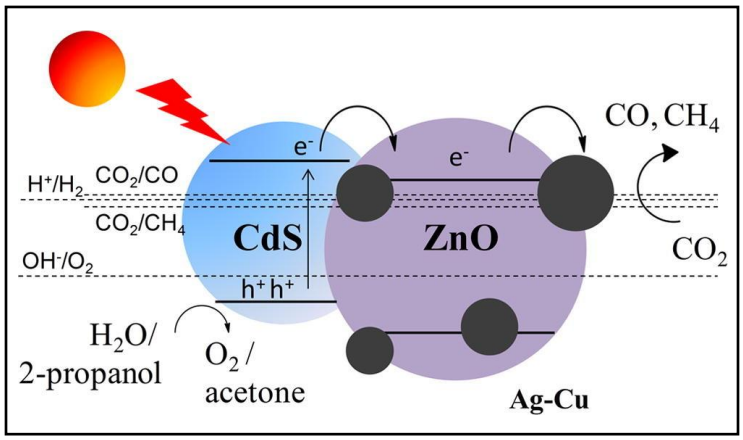

Paper based on this work has appeared in *Chem, Phys. Lett.* **2018**, 691, 28-32.

2.1 Introduction

Drastic reduction of CO_2 in the atmosphere has become imperative to save the environment. One way of accomplishing this objective is to use solar energy for the conversion of CO_2 to useful chemicals. Photocatalytic reduction of CO_2 on suspended semiconductor-powders was reported some years ago by Fujishima et al.[1] A variety of semiconductor based photocatalyst have been studied for the photocatalytic reduction of CO_2.[2–5] The current bottleneck towards achieving high efficiency in photocatalytic systems is the quick recombination of photogenerated electrons and holes which reduces the photocatalytic activity drastically. Various strategies are being studied to enhance the separation of photogenerated electrons and holes. For example, coupling of two semiconductors with band alignment in such a way that valence band maxima (VBM) and conduction band minima (CBM) of semiconductor A is higher than the VBM and CBM of semiconductor B (**Figure 1**). The bands bend at the interface and produces a field that drives the photogenerated electrons and holes in opposite directions, thereby enhancing the charge carrier separation.[6] This type of heterostructures is known as Type II heterostructures and can enhance the photocatalytic activity. It has been observed that prolonged life-times of charge carriers in Type II heterostructures over individual components results in superior photocatalytic activity.[7] ZnO/Pt/CdS type heterostructures wherein Pt is present on ZnO are known to exhibit excellent photocatalytic hydrogen evolution activity.[8] CdSe/Pt/TiO_2 has been employed for the reduction of CO_2 to CH_4 in the gas-phase under visible-light irradiation,[9] although Pt often gets poisoned by CO.[10] Ag, on the other hand, shows superior activity compared to Pt due to weaker binding of CO.[10] Cu also possesses good reactivity towards CO_2 reduction, but Cu nanoparticles easily get oxidized. There is considerable effort to stabilize Cu nanoparticles by making

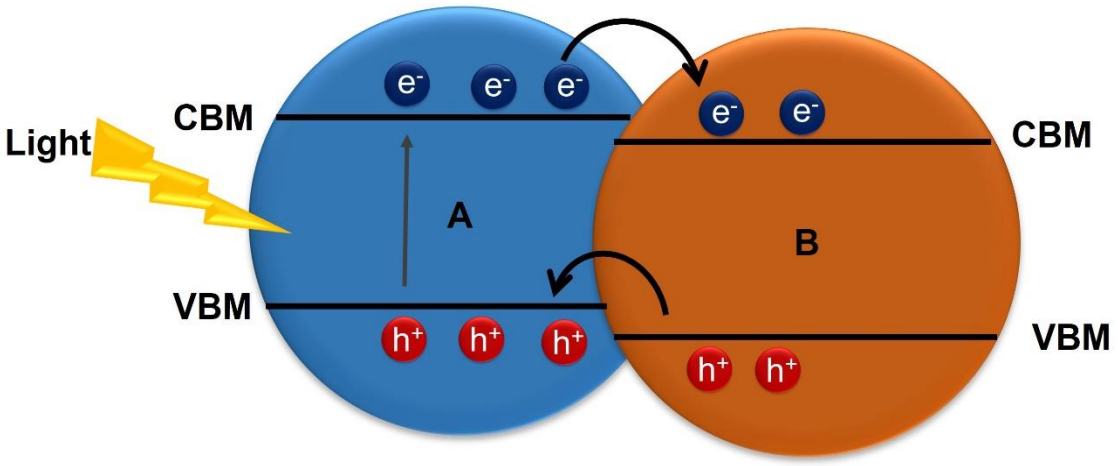

Figure 1. Schematic illustration of charge carrier separation in Type II heterostructures.

alloys with other metals, but their use in ZnO/Pt/CdS type heterostructures has not been explored.

Catalytic activity of transition metal co-catalyst depends on the adsorption energy of intermediates on the metal surface since the activation energy of the elementary surface reactions are strongly correlated with them. Adsorption energies depend on the electronic structure of the adsorbent and their interaction with metal d-states for transition metal catalysts. **Figure 2a** shows a schematic illustration of typical density of states for a transition metal having a broad s band and a narrow d-band. The interaction of d-band with absorbate states give rise to bonding and antibonding states (**Figure 2b**). A shift in d-band center upwards towards fermi level leads to the formation of antibonding states above the fermi level (**Figure 2c**). Since these antibonding states are above the fermi level and unoccupied, the bond becomes stronger as the number of empty states increases.[11] In general, the higher the d-states are relative to fermi level the stronger the interaction will be with adsorbate states.[12,13] Moreover, the electronic structure or the position d-band

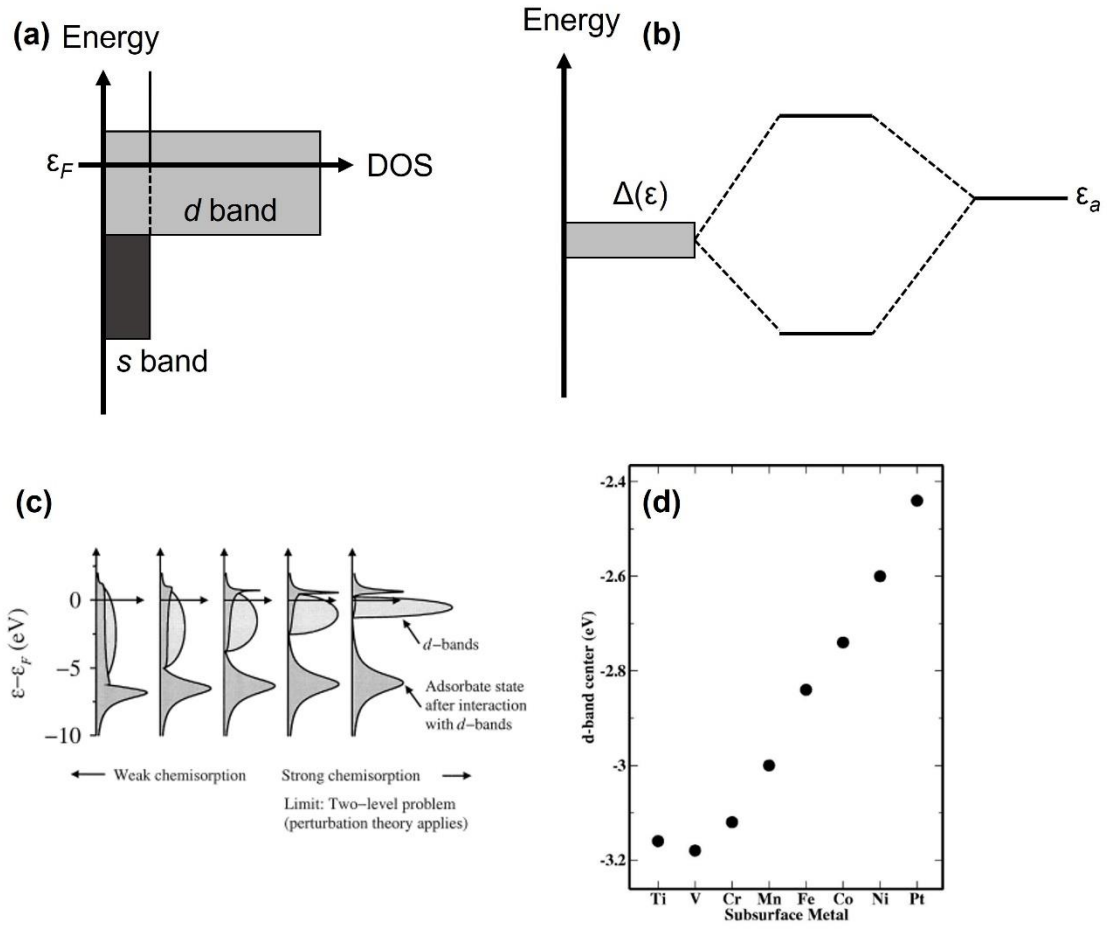

Figure 2. Schematic illustration of (a) density of states of a transition metal, (b) interaction of d-band of transition metal with the adsorbate state forming bonding and antibonding states, (c) interaction of d-band with adsorbate states, formation of antibonding states above the fermi level with the shift of d-band center towards fermi level, and (d) variation of d-band center of Pt containing various transition metals. Reproduced with permission from ref 11, Copyright (2000), with permission from Elsevier; Used with permission of Royal Society of Chemistry ref 13 and American Institute of Physics ref 16; permission conveyed through Copyright Clearance Center, Inc.

center can be altered by inserting another metal in the lattice as evidenced by the incorporation of metal layer in Pt lattice (**Figure 2d**).[14–16]

Therefore, the incorporation of a second metal helps in tailoring the electronic and geometric structures which enhances the catalytic activity and selectivity. Yang *et al*. demonstrated that the Au-Cu exhibits enhanced catalytic activity towards electrochemical CO_2 reduction. This enhanced activity is due to changes in the electronic structure and the local configuration of active sites which have a large effect on binding energy of intermediates.[17] Moreover, the presence of Au in the lattice stabilizes Cu from surface oxidation.[18] Similar enhancement of activity was also observed for Ag-Cu alloys.[19]

2.2 Scope of present investigation

Herein, we present our investigations involving bimetallic alloys of Ag and Cu in heterostructures of the type ZnO/M/CdS (M =$Ag_{1-x}Cu_x$) for the reduction of CO_2 under visible-light irradiation. We have extended these investigations to heterostructures containing Au, Pt and $Ag_{1-x}Au_x$ alloys as well, but found the best photocatalytic activity with the heterostructures containing $Ag_{1-x}Cu_x$ alloys. These photocatalysts exhibit activity in the gas-phase as well with water as the reducing agent and appear to reduce CO_2 to methanol in the presence of sacrificial agent Na_2SO_3.

2.3 Experimental

Materials: $Zn(CH_3COO)_2.2H_2O$ (SD Fine Chem Ltd, India, 99.5 %), KOH (SD Fine Chem Ltd, India, 85.5 %), $AgNO_3$ (Sigma-Aldrich, 99%), H_2PtCl_6 (Sigma-Aldrich, 37.5 % Pt basis), $HAuCl_4$ (Sigma-Aldrich, 49% Au basis), $Cd(CH_3COO)_2.2H_2O$ (SD Fine Chem Ltd, India, 99.0 %), 2-propanol (Company, Purity), CO_2 (Chemix gases, 99.995%), methanol (Spectrochem, India, 99.9 %), $Na_2S.xH_2O$ (SD Fine Chem Ltd, India), Na_2SO_3 (SD Fine

Chem Ltd, India, 97 %), water (Millipore, 18.2 MΩ.cm) are used without any further purification.

Synthesis: ZnO/$Ag_{1-x}Cu_x$/CdS heterostructures were prepared by a method reported for the synthesis of ZnO/Pt/CdS.[8] In a typical procedure, alloy nanoparticles and CdS were sequentially deposited on preformed ZnO.

Synthesis of ZnO nanoparticles: Zn $(CH_3COO)_2.2H_2O$ (4 mmol) was dissolved in methanol (70 mL) and the temperature of the solution was raised to 60 °C. KOH dissolved in methanol (8 mmol in 10 mL of methanol) was drop-wise added to the zinc acetate solution and the resulting solution was kept at 60 °C for 2h with a constant stirring at 1500 rpm. The solution color slowly transformed to white turbid due to the formation of ZnO nanoparticles. After 2 h, 5 mL of H_2O was added to the reaction solution and was stirred for additional 10 min. The product was separated by centrifugation (5000 rpm, 3 min) and washed with methanol and dried at room temperature. These ZnO nanoparticles were used as precursor for the synthesis of heterostructures.

Deposition of metal and alloy nanoparticles on ZnO: ZnO/M/CdS (M = Ag, Pt, Au, $Ag_{1-x}Au_x$ and $Ag_{1-x}Cu_x$) were synthesized by the photo-deposition of metal nanoparticles (Ag, Pt and Au) on ZnO and subsequent deposition of CdS on metal deposited ZnO. In a typical synthesis process, aqueous solutions of $AgNO_3$ (10 mM), H_2PtCl_6 (10 mM) and $HAuCl_4$ (10 mM) were used as precursors for Ag, Pt and Au respectively. For monometallic deposition, ZnO (1 mmol) was dispersed in water (70 mL) containing 10 vol% of methanol and an aqueous solution of metal precursors (10 mM, 1 mL) were added to the ZnO dispersions and sonicated under dark for few minutes. Similarly, for alloy nanoparticle deposition, an aqueous solution containing 10mM each of the constituent

metal (for example 10mM $AgNO_3$ and 10mM $CuSO_4.5H_2O$) was added to the dispersion of ZnO. These solutions were irradiated with UV-visible irradiation (400 W Xe) for 30 min. Photo-deposition of the metals is evident from the change in color of the solution. ZnO/M (M = Ag, Pt, Au, $Ag_{1-x}Au_x$ and $Ag_{1-x}Cu_x$) nanoparticles were collected by centrifugation, washed with water, and re-dispersed in methanol solution. Methanolic solutions of cadmium acetate (0.2 mmol) and sodium sulfide (0.2 mmol) solutions were drop-wise added to the ZnO/M (Ag, Pt and Au) solution. After CdS deposition, ZnO/M/CdS heterostructures were collected by centrifugation and washed with water and dried at 60 °C for overnight. The product obtained was ground well and subjected for further characterization.

Physical Characterization:

X-ray diffraction patterns (XRD) of the products were recorded with Bruker D8 Diffraction System using a Cu Kα source (λ= 0.154178 nm). UV-Vis absorption spectra were taken with Perkin Elmer Model Lambda 900 spectrometer. CO_2 reduction products in the gas-phase were identified and estimated by the Perkin Elmer gas-chromatograph (Perkin Elmer, Clarus 580). Liquid products were identified and quantified by using sodium acetate as in internal standard in NMR.

Photocatalytic reduction of carbon dioxide

Photocatalytic reduction of CO_2 was evaluated in two different experimental conditions, former being the liquid-phase and latter being the gas-phase reaction. In a typical liquid phase process, 20 mg of the photocatalysts was dispersed in 80 mL of water containing 10 vol% of 2-propanol and $NaHCO_3$ (0.4 M). The reaction mixture was

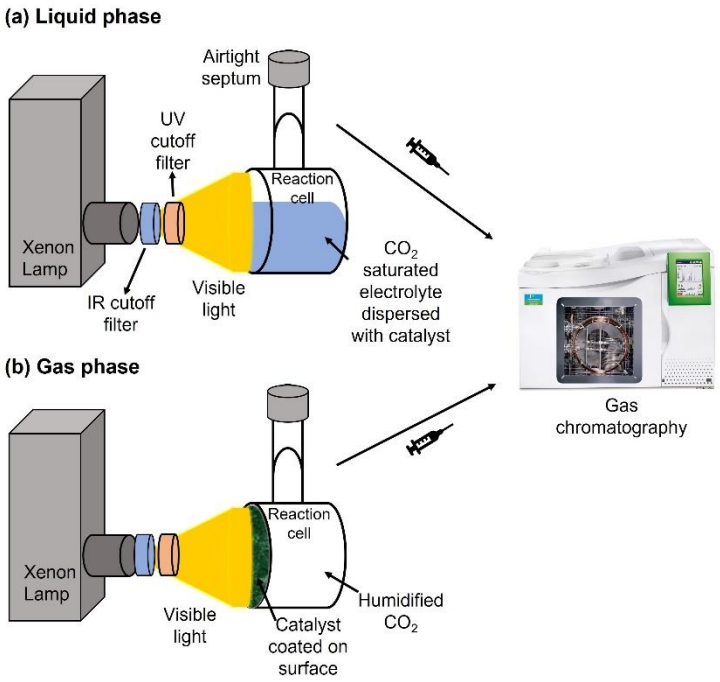

Scheme 1. Schematic illustration of (a) liquid phase and (b) gas phase photocatalytic CO_2 reduction setup.

transferred to a glass-cell with a total volume of 130 mL. The photocatalytic reaction cell design was modeled to expose the flat faces perpendicular to the collimated light beam (**Scheme 1a**). The solution was saturated with CO_2 by bubbling CO_2 for 30 minutes. To remove common trace impurities such as CH_3OH, the CO_2 gas was purged through NaOH solution, prior to its introduction in the reaction cell. Then, CO_2 saturated reaction mixture was exposed to visible-light irradiation ($\lambda > 395$ nm, 400 W Xe, Newport). A water filter was used to cut-off the IR radiation and a 395 nm cut-off filter was used to absorb the UV radiation. The intensity of the radiation was measured by an irradiance meter (Newport). Gas samples were collected and tested at equal time intervals with gas-chromatograph (Perkin Elmer, Clarus 580). Liquid samples were collected and added to D_2O solution

containing sodium acetate as an internal standard to evaluate the liquid products through 1H-NMR.

Gas-phase CO_2 reduction reactions were evaluated in a reaction flask with a total volume of 160 mL. 10 mg of the photocatalysts were deposited on flat face of the cell. Glass cell was evacuated and filled with CO_2 and water vapor sequentially for five times. CO_2 was filled in the cell through a water bubbler to create humidified CO_2. The cell was irradiated with either sunlight or visible light (**Scheme 1b**). The gas samples were collected and tested with gas-chromatograph for the detection of CO, CH_4 and H_2.

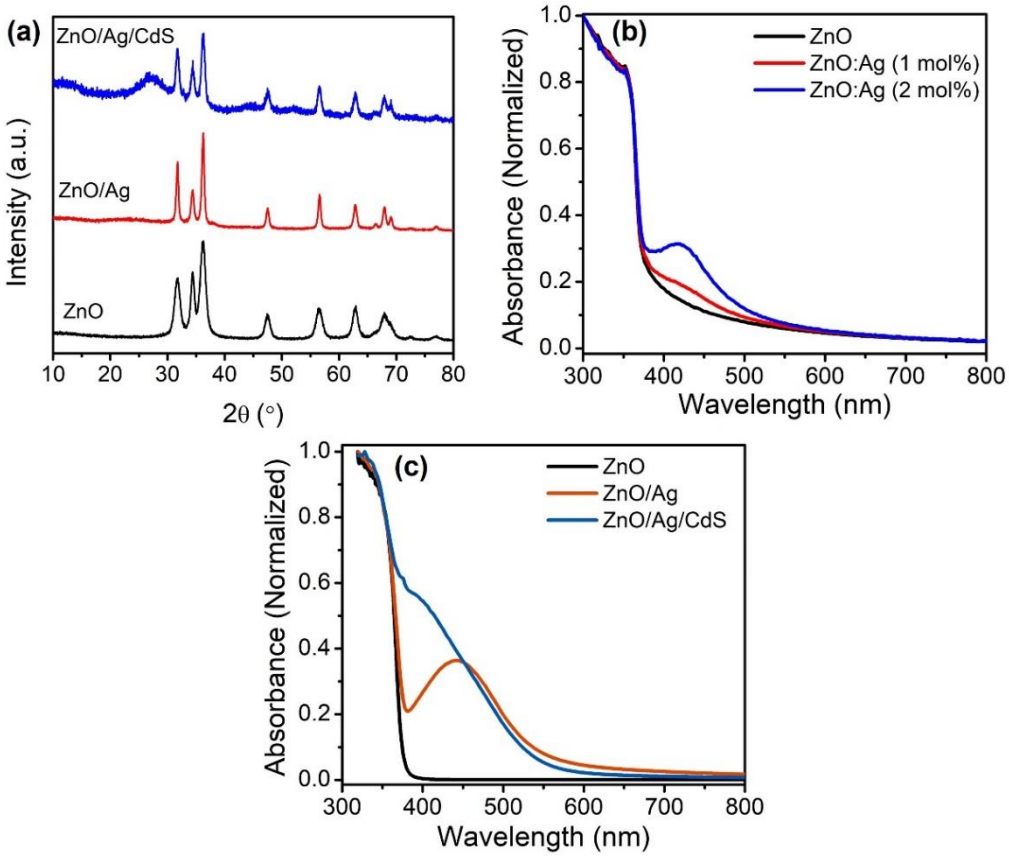

Figure 3. (a) X-ray diffraction patterns of ZnO, ZnO/Ag and ZnO/Ag/CdS. Comparison of absorption spectra of (b) ZnO, ZnO/Ag (1mol%) and ZnO/Ag (2 mol%) and (c) ZnO, ZnO/Ag and ZnO/Ag/CdS.

2.4 Results and Discussion

Phase purity as well as crystal structures of the components of the heterostructures were determined by X-ray diffraction (XRD). **Figure 3a** shows the X-ray diffraction patterns of ZnO, ZnO/Ag and ZnO/Ag/CdS. It is evident from the XRD patterns that ZnO exists in the wurtzite structure (space group $P6_3mc$, a = 3.24 Å, c = 5.22 Å) in the heterostructures. No signature of Ag is observed in the diffraction patterns of ZnO/Ag and ZnO/Ag/CdS, the average crystallite sizes of ZnO and CdS being 10 and 3 nm respectively. ZnO is a wide band gap (3.2 eV) semiconductor and absorbs light only in the region below λ = 387 nm. However, ZnO/Ag has visible absorption due to the surface-plasmon-resonance (SPR) band of Ag nanoparticles in addition to the absorption due to ZnO. **Figure 3b** shows the absorption spectrum of ZnO/Ag with varying amounts of Ag. The absorption intensity of the SPR band of Ag increases with increasing the Ag content. The spectrum of ZnO/Ag/CdS (**Figure 3c**) has contributions from both CdS and Ag in the visible region.

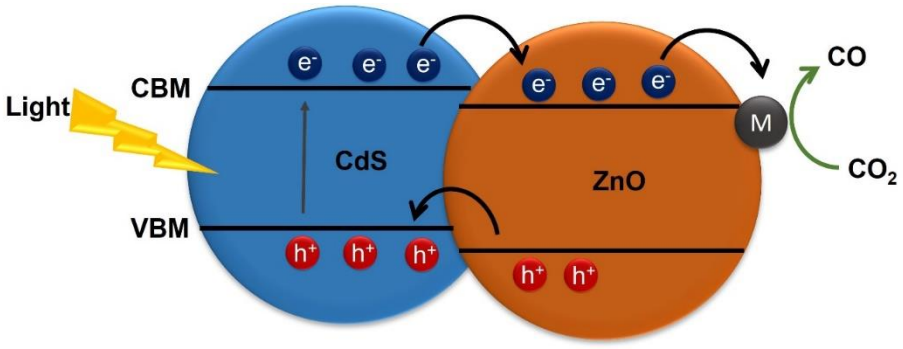

Scheme 2. Schematic illustration of photocatalytic CO_2 reduction on co-catalyst loaded ZnO/CdS heterostructure. M= Pt, Ag, Au.

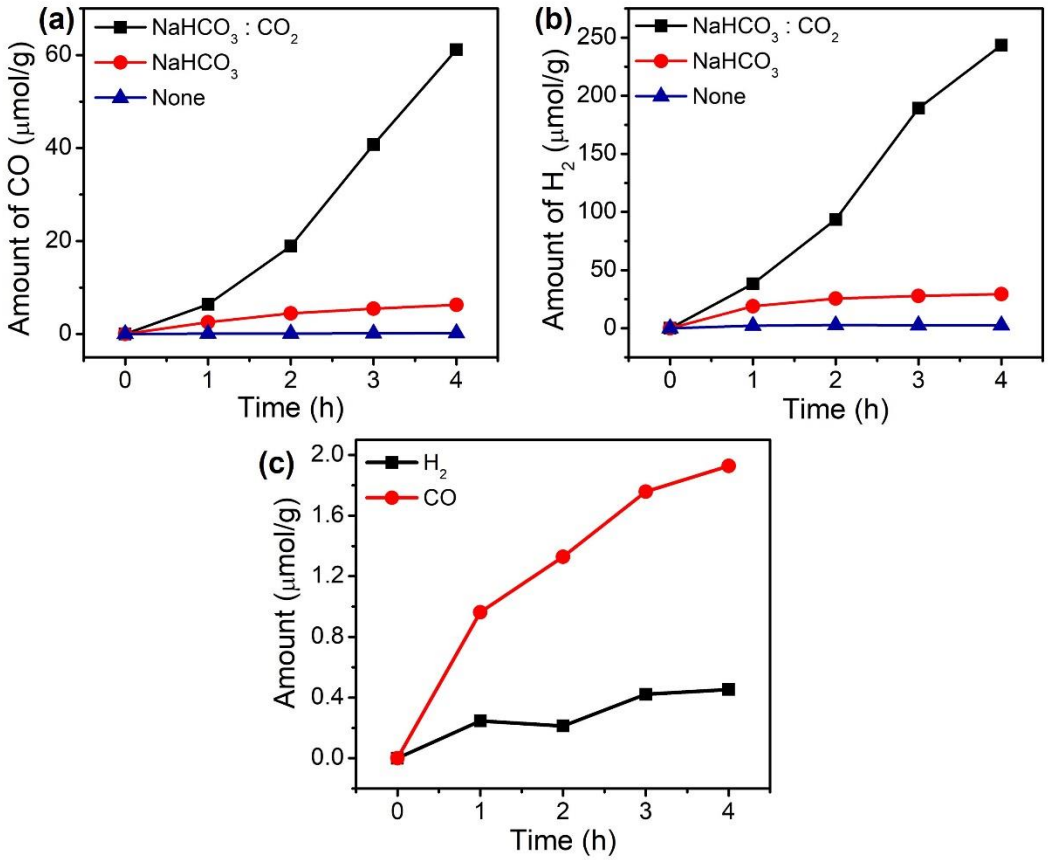

Figure 4. Photocatalytic reduction of CO_2 on ZnO/Ag/CdS heterostructures from the CO_2 saturated aqueous solution containing various electrolytes under visible-light irradiation (400 W Xe lamp, $\lambda \geq 395$ nm).

Scheme 2 gives a basic illustration of photocatalytic CO_2 reduction on ZnO/M/CdS heterostructures. Photocatalytic CO_2 reduction on these heterostructures was carried out in saturated aqueous solutions of CO_2 containing 2-propanol (10 vol %) and $NaHCO_3$ (0.4 M) (pH = ~12). Here, 2-propanol acts as a sacrificial electron donor which consumes holes and $NaHCO_3$ enhances the CO_2 uptake of the solution. In these studies, CO and CH_4 were obtained as major and minor reduction products, respectively and hydrogen was obtained as a competing photo-reduction product. ZnO/Ag/CdS heterostructure reduce CO_2 to CO at a rate of 21.1 μmol $h^{-1}g^{-1}$ under visible-light (**Figure 4**). Control experiments were

carried out to ensure that CO was the product of reduction of CO_2. In the absence of both CO_2 and $NaHCO_3$, we failed to observe production of CO, even though 2-propanol was present as the scavenger (**Figure 4**). Moreover, in a N_2 saturated electrolyte only hydrogen evolution was observed with no CO production. Clearly, the origin of CO is CO_2, the high pH favoring photocatalytic activity. We have also carried out photocatalytic CO_2 reduction with ZnO/Ag (**Figure 4c**). ZnO/Ag is a visible-light responsive photocatalyst, visible-light response originating from surface plasmon resonance (SPR) of Ag nanoparticles. ZnO/Ag also reduces CO_2 to CO under visible-light irradiation although the CO production rate is considerably lower than ZnO/Ag/CdS heterostructures. The enhanced activity of the heterostructure could be due to enhanced visible light absorption of CdS and efficient charge carrier separation in the heterostructure.

The ZnO/Pt/CdS heterostructure mainly produces hydrogen with H_2 evolution of 606 μmol $h^{-1}g^{-1}$ (**Figure 5**). It also reduces CO_2 to CO at a production rate of (5.8 μmol $h^{-1}g^{-1}$). Pt is highly selective to produce hydrogen.[2] The ZnO/Au/CdS heterostructure exhibits superior activity towards CO_2 reduction and shows good hydrogen production compared to both ZnO/Ag/CdS and ZnO/Pt/CdS (**Figure 5**). An 8-fold increment in CO production is observed with ZnO/Au/CdS compared to ZnO/Pt/CdS. Interestingly, heterostructure with Ag shows enhanced CO production (~ 5-fold) and considerably reduced H_2 production (~ 7-fold) compared to ZnO/Pt/CdS. We have further examined bimetallic alloys of Ag with Au expecting superior reduction activity towards CO_2. In Figure 5 c-d, we show photocatalytic activities of ZnO/$Ag_{0.5}Au_{0.5}$/CdS along with those of ZnO/Ag/CdS and ZnO/Au/CdS. ZnO/$Ag_{0.5}Au_{0.5}$/CdS exhibits CO production activity of 110 μmol $h^{-1}g^{-1}$ under visible-light irradiation which is nearly 4-fold and 2-fold larger

compared to ZnO/Ag/CdS and ZnO/Au/CdS respectively. Whereas H_2 production does not increase.

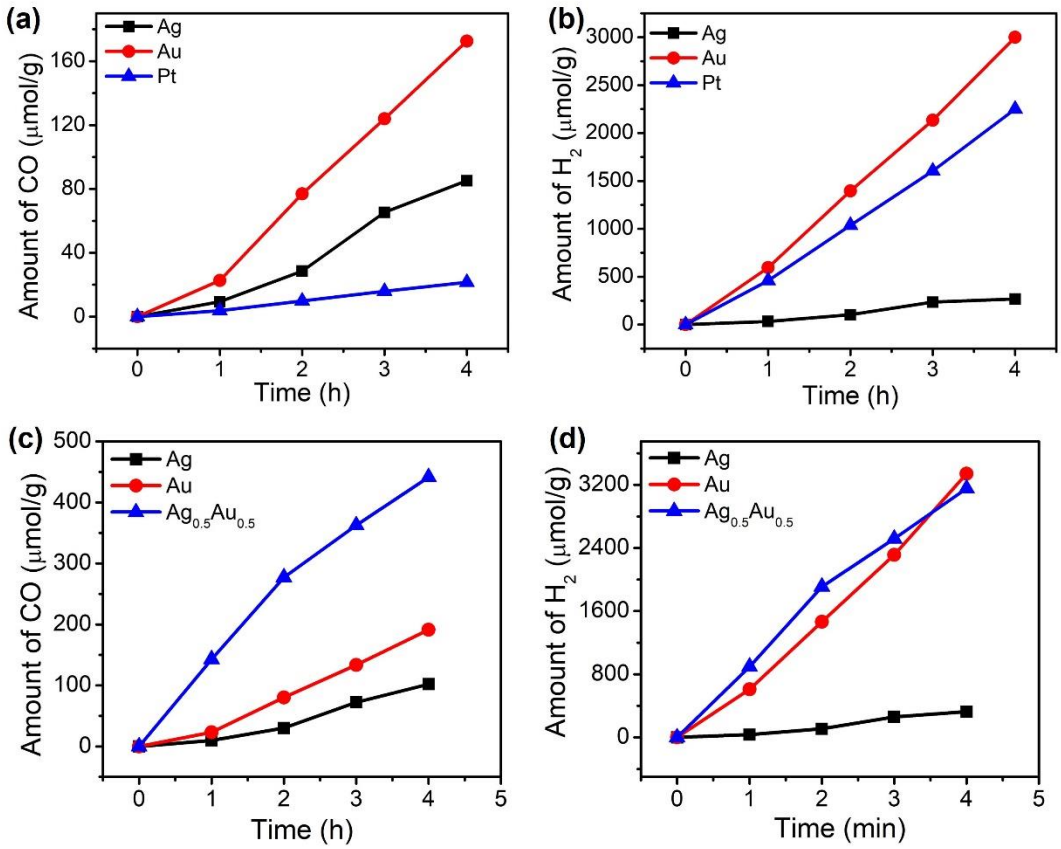

Figure 5. Comparison of photocatalytic activities of production (a) CO and (b) H_2 on heterostructures containing different metal (ZnO/M/CdS, where M = Ag, Au and Pt). Comparison of photocatalytic activities of production (c) CO and (d) H_2 on ZnO/$Ag_{0.5}Au_{0.5}$/CdS with ZnO/Ag/CdS and ZnO/Au/CdS. Photocatalytic studies are carried out in 75 ml of CO_2 saturated aqueous solution containing 20 mg of the photocatalyst, 10 vol% 2-propanol, $NaHCO_3$; under the irradiation of visible light (400 W Xe, $\lambda > 395$ nm).

The catalytic activity and stability of the Cu nanoparticles are improved by alloying of Cu with Au.[17,18] Xu *et al.*[18] demonstrated composition-dependent stability of Cu-Au bimetallic alloys, where the oxidation rate of alloy is minimum with highest Au content.

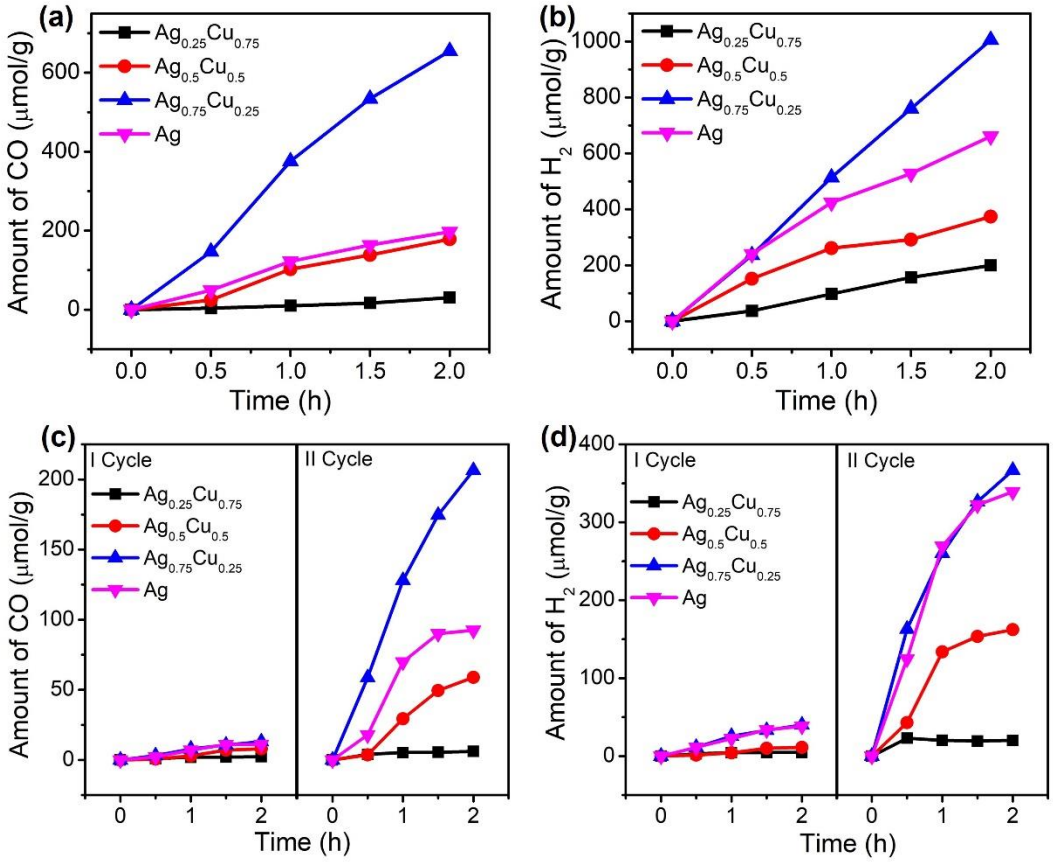

Figure 6. Photocatalytic activities of production (a) CO and (b) H_2 on heterostructures containing different compositions of Ag and Cu metal alloys in third cycle and (c) CO and (d) H_2 production in the first and second cycles. Photocatalytic studies are carried out in 75 ml of CO_2 saturated aqueous solution containing 20 mg of the photocatalyst, 10 vol% 2-propanol, $NaHCO_3$; under the irradiation of visible light (400 W Xe, $\lambda > 395$ nm).

More importantly, Au_2Cu shows lower over potential for the reduction of CO_2 compared Au or Cu. We believed that the use of binary alloys of Cu with Au and Ag in the heterostructures was a promising strategy for the reduction of CO_2. We, therefore, prepared heterostructures containing $Au_{0.5}Cu_{0.5}$ and $Ag_{0.5}Cu_{0.5}$ and found that ZnO/$Ag_{0.5}Cu_{0.5}$/CdS exhibits superior CO_2 reduction activity compared to ZnO/ $Au_{0.5}Cu_{0.5}$/CdS.

Prompted by above results, we prepared the heterostructures of ZnO/$Ag_{1-x}Cu_x$/CdS with varying the composition of the $Ag_{1-x}Cu_x$ (x = 0 – 0.75) alloy and examined their photocatalytic activities. Due to the instability of Cu nanoparticles, we could not evaluate the photocatalytic properties of the ZnO/Cu/CdS heterostructure. We, however, examined photocatalytic activity of heterostructures containing $Ag_{0.25}Cu_{0.75}$, $Ag_{0.5}Cu_{0.5}$, $Ag_{0.75}Cu_{0.25}$ and Ag. The photocatalytic activity increased in subsequent cycles with all the heterostructures **(Figure 6)**. ZnO/Ag/CdS exhibits a CO production activity of 98.6 μmol $h^{-1}g^{-1}$ in the third cycle, which is nearly twice, that of the activity in the second cycle. Partial substitution of Cu in Ag as in ZnO/$Ag_{0.75}Cu_{0.25}$/CdS yields nearly 327.4 μmol $h^{-1}g^{-1}$ of CO in the third cycle, which is nearly a three-fold improvement compared to the second cycle. Further increase in the Cu amount as in ZnO/$Ag_{0.5}Cu_{0.5}$/CdS yields only 89.3 μmol $h^{-1}g^{-1}$ of CO. CO production decreases to 15.2 μmol $h^{-1}g^{-1}$ with further increase in Cu content. From **Figure 6 a-b**, we see that both H_2 and CO production activities are higher with $Ag_{0.75}Cu_{0.25}$ and interestingly the relative production of CO is also maximum with ZnO/$Ag_{0.75}Cu_{0.25}$/CdS (**Figure 7**). The photocatalytic activity of ZnO/$Ag_{0.75}Cu_{0.25}$/CdS heterostructure under visible light irradiation is compared with the catalytic activities reported in the literature in **Table 1**. We see that the activity of ZnO/$Ag_{0.75}Cu_{0.25}$/CdS is superior or comparable to the best activities under similar conditions reported in the literature.

We have also examined photocatalytic activities of the alloy-based heterostructures under sunlight irradiation (**Figure 8**). Relative intensities at different wavelengths as well as the presence of a small fraction of UV in the sunlight seem to affect the photocatalytic activity, probably due to the presence of ZnO nanoparticles which are active under UV

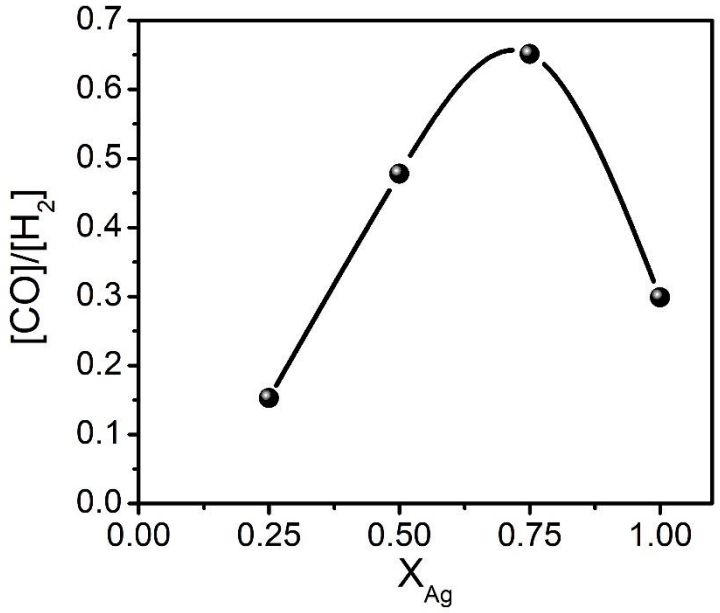

Figure 7. Ratio of CO and hydrogen production activity as a function of mole fraction of Ag in $Ag_{1-x}Cu_x$ alloys in third cycle.

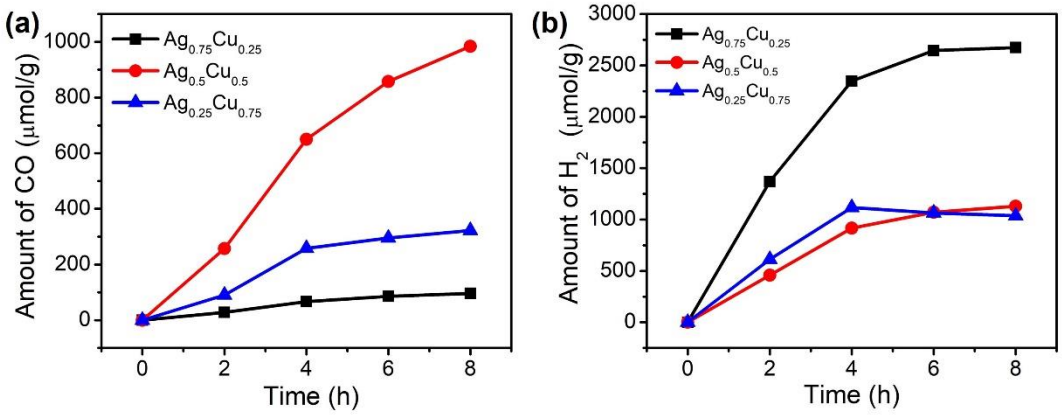

Figure 8. Photocatalytic activities for the production of (a) CO and (b) H_2 using heterostructures containing different compositions of $Ag_{1-x}Cu_x$ alloys under direct irradiation of sunlight in the third cycle. Photocatalytic studies are carried out in 75 ml of CO_2 saturated aqueous solution containing 20 mg of the photocatalyst, 10 vol% 2-propanol, $NaHCO_3$; under the irradiation of direct sunlight.

irradiation. The photocatalytic activity increases in subsequent cycles under sunlight as well. ZnO/$Ag_{0.5}Cu_{0.5}$/CdS exhibits superior photocatalytic activity with a CO production

rate of 162 μmol $h^{-1}g^{-1}$. It is interesting that this composition yields least hydrogen evolution. Further increase in Cu content as $ZnO/Ag_{0.25}Cu_{0.75}/CdS$ decreases the photocatalytic activity. The photocatalytic activities obtained under Xe lamp irradiation is generally larger due to the high intensity (~ 2 Sun).

Table 1. Comparison of photocatalytic CO_2 reduction yields obtained by various photocatalysts in liquid-phase reactions

Photocatalyst	**Light Source**	**Reaction medium**	**Weight (mg)**	**Products**	**Product Yields (μmol $h^{-1}g^{-1}$)**	**(μmol h^{-1})**	**References**
$ZnO/Ag_{0.5}Cu_{0.5}/CdS$	Sunlight	2-propanol and water	20	CO, CH_4, H_2	162 (CO)	3.24 (CO)	Present work
$ZnO/Ag_{0.75}Cu_{0.25}/CdS$	Visible	2-propanol and water	20	CO, CH_4, H_2	327 (CO)	6.54 (CO)	Present work
Pt: TiO_2	UV	H_2O	20	H_2, CH_4, CO	1.4 (CH_4)	0.028 (CH_4)	[3]
ZnS:Cd	UV (Xe)	2-propanol and water	-	HCOOH, H_2	-	10 (HCOOH)	[5]
CdS	Visible	2-propanol and water	0.14	HCOOH, CO, H_2	10 (HCOOH)	0.001 (HCOOH)	[19]
$ZnFe_2O_4/TiO_2$	UV	Cyclohexanol and water	10	HCOO-	22 ($HCOO^-$)	0.22 ($HCOO^-$)	[20]
Ru(II)-complex/C_3N_4	Visible	Methanol-DMA-water	8	CO	5.7 (CO)	0.045 (CO)	[21]
Ru(II)-complex/Ag/C_3N_4	Visible	K_2CO_3-EDTA-water	4	$HCOO^-$, H_2	83 ($HCOO^-$)	0.33 ($HCOO^-$)	[22]

We have further studied CO_2 reduction activity of ZnO/Ag/CdS in the presence of Na_2SO_3 as the sacrificial hole scavenger and the preliminary results show formation of methanol with a CH_3OH production activity of 62 μmol $h^{-1}g^{-1}$ (**Figure 9a**). It is possible that the large negative reduction potential of the Na_2SO_3/Na_2SO_4 redox couple may have caused the easy removal of holes from the photocatalyst. The production of methanol can arise from the high density of photoexcited electrons. Specific interaction of CO_2/bicarbonate/carbonate with the Na_2SO_3 on the photocatalysts surface, however, needs to be explored.

We have extended our study by studying the photocatalytic activity of these heterostructures in gas phase. In these experiments, we bubbled CO_2 through water as a gaseous feed without any sacrificial agent. The heterostructure reduces CO_2 mainly to CO (minor quantity of CH_4) with a CO production rate of ~2 μmol $h^{-1}g^{-1}$ under direct sun light-irradiation. Interestingly, we did not observe any reduction of water. The yield of CO obtained in the gas-phase reduction is rather low (**Figure 9b**).

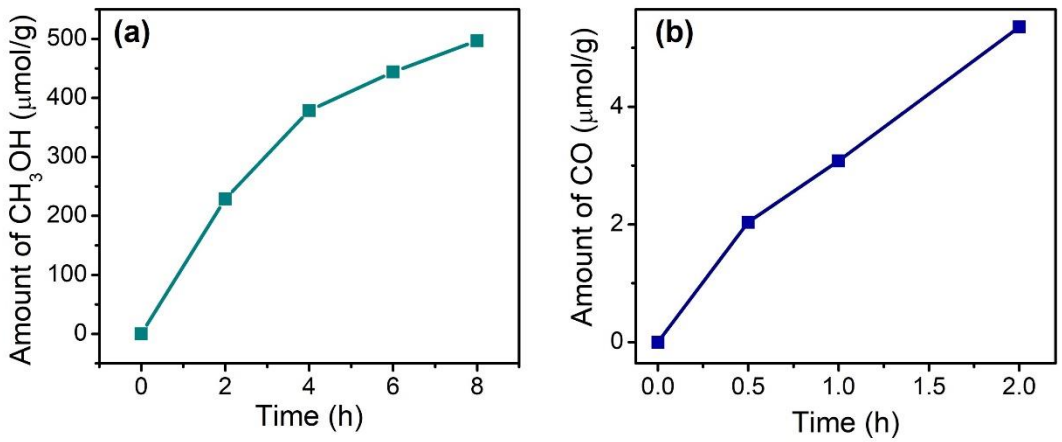

Figure 7. Photocatalytic reduction of CO_2 on ZnO/Ag/CdS from (a) CO_2 saturated aqueous solution containing $NaHCO_3$-Na_2SO_3 under visible light irradiation and (b) from humidified CO_2 in gas phase under the irradiation of sunlight.

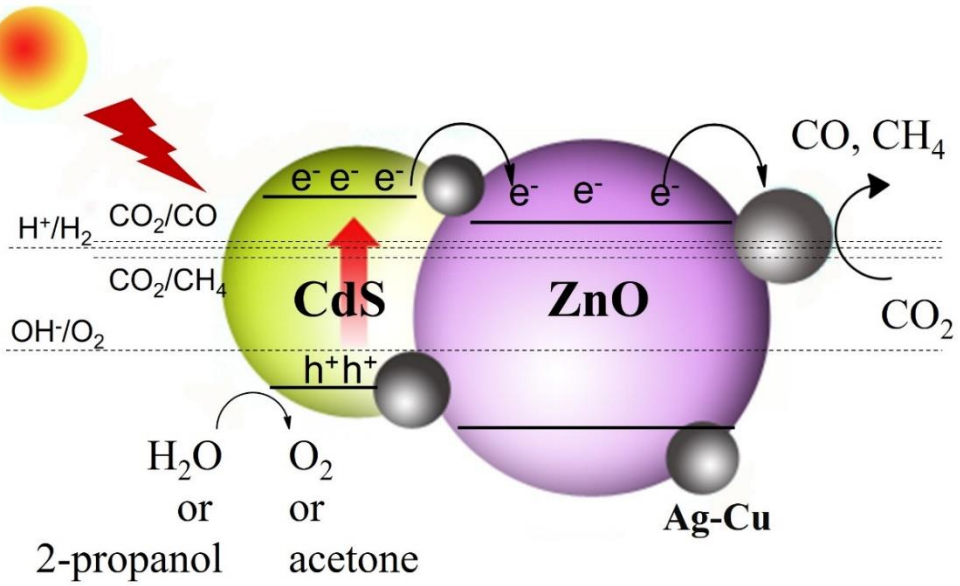

Figure 10. Mechanism of photocatalytic reduction of CO_2 by ZnO/M/CdS heterostructures (M = Ag, Au, Pt, Ag1-xAux and Ag1-xCux) under visible light irradiation.

Mechanism: Figure 10 shows a schematic illustration of the mechanism of reduction of CO_2 on ZnO/M/CdS type heterostructure. Upon visible-light irradiation, CdS in ZnO/M/CdS absorbs the light while upon UV-visible light irradiation, both ZnO and CdS absorb light and generate charge carriers. The ZnO/CdS interface causes injection of the excited electrons from CdS to ZnO, and holes from ZnO to CdS. Holes in the VB of CdS get consumed by 2-propanol to yield acetone and by water to yield oxygen. Metal or metal-alloy nanoparticles catalyze the reduction of CO_2 upon accepting electrons from the CB of ZnO.

Adsorption energy of intermediates on Cu surface is stronger than Ag since d-band center of Cu is higher than of Ag. This implies than with the introduction of Cu in Ag, the binding strength of intermediate should increase leading to a decreased CO production

activity. However, we observe that introduction of ~25% Cu in Ag leads to significant enhancement in the CO production. Therefore, the catalytic activity of alloy co-catalyst does not entirely depend upon the electronic structure but also on the local atomic arrangement of active sites.[20,21] Reports from other groups shows that incorporation of Cu in Au enhances the catalytic activity which is due to changes in the electronic structure as well as due to stabilization of *COOH intermediates by the oxygen affinitive Cu atoms.[20,22] Therefore, the presence of Cu in Ag might similarly stabilize the *COOH intermediate. A similar enhancement of catalytic activity with Ag-Cu alloys was also reported by other groups.[23,24]

2.5 Conclusions

Photoreduction of CO_2 is an important problem of great relevance, and it is necessary to explore different types of reducing semiconductor structures for the purpose. In the present study, we demonstrate the advantage of using heterostructures of the type ZnO/M/CdS (M = Ag, Au, $Ag_{1-x}Au_x$, $Ag_{1-x}Cu_x$) for the photoreduction of CO_2 in the liquid phase. In particular, use of alloys such as $Ag_{1-x}Cu_x$ favors the reduction. While the main product that we have obtained is CO, there is need for further study of heterostructures to obtain other reduction products. It is noteworthy that we have observed photoreduction of CO_2 in gas phase as well. While further efforts are necessary to explore under what conditions one can obtain better reduction activity in the gas phase, what is of interest is that sacrificial agents can be eliminated under certain conditions. The observation of a new photoluminescence band under irradiation has to be taken into account in explaining the mechanism of CO_2 reduction by these heterostructures.

2.6 References

[1] T. Inoue, A. Fujishima, S. Konishi, K. Honda, *Nature* **1979**, *277*, 637.

[2] W. Tu, Y. Zhou, Z. Zou, *Adv. Mater.* **2014**, *26*, 4607.

[3] S. Xie, Y. Wang, Q. Zhang, W. Deng, Y. Wang, *ACS Catal.* **2014**, *4*, 3644.

[4] B. J. Liu, T. Torimoto, H. Yoneyama, *J. Photochem. Photobiol. A*, **1998**, *115*, 227.

[5] H. Inoue, H. Moriwaki, K. Maeda, H. Yoneyama, *J. Photochem. Photobiol. A*, **1995**, *86*, 191.

[6] H. Wang, L. Zhang, Z. Chen, J. Hu, S. Li, Z. Wang, J. Liu, X. Wang, *Chem. Soc. Rev.* **2014**, *43*, 5234.

[7] X. Wang, G. Liu, Z. G. Chen, F. Li, L. Wang, G. Q. Lu, H. M. Cheng, *Chem. Commun.* **2009**, *0*, 3452.

[8] S. R. Lingampalli, U. K. Gautam, C. N. R. Rao, *Energy Environ. Sci.* **2013**, *6*, 3589.

[9] C. Wang, R. L. Thompson, J. Baltrus, C. Matranga, *J. Phys. Chem. Lett.* **2010**, *1*, 48.

[10] J. L. White, M. F. Baruch, J. E. Pander, Y. Hu, I. C. Fortmeyer, J. E. Park, T. Zhang, K. Liao, J. Gu, Y. Yan, T. W. Shaw, E. Abelev, A. B. Bocarsly, *Chem. Rev.* **2015**, *115*, 12888.

[11] B. Hammer, J. K. Nørskov, *Adv. Catal.* **2000**, *45*, 71.

[12] J. K. Nørskov, T. Bligaard, J. Rossmeisl, C. H. Christensen, *Nat. Chem.* **2009**, *1*, 37.

[13] B. Hammer, *Faraday Discuss* **1998**, *110*, 323.

[14] A. Ruban, B. Hammer, P. Stoltze, H. L. Skriver, J. K. Nørskov, *J. Mol. Catal. A. Chem.* **1997**, *115*, 421.

[15] B. Hammer, J. K. Nørskov, *Surf. Sci.* **1995**, *343*, 211.

[16] J. R. Kitchin, J. K. Nørskov, M. A. Barteau, J. G. Chen, *J. Chem. Phys.* **2004**, *120*, 10240.

[17] D. Kim, J. Resasco, Y. Yu, A. M. Asiri, P. Yang, *Nat. Commun. 2014 5:1* **2014**, *5*, 1.

[18] Z. Xu, E. Lai, Y. Shao-Horn, K. Hamad-Schifferli, *Chem. Commun.* **2012**, *48*, 5626.

[19] J. Huang, M. Mensi, E. Oveisi, V. Mantella, R. Buonsanti, *J. Am. Chem. Soc.* **2019**, *141*, 2490.

[20] S. Back, J. H. Kim, Y. T. Kim, Y. Jung, *ACS Appl. Mater. Inter.* **2016**, *8*, 23022.

[21] S. Ma, M. Sadakiyo, M. Heim, R. Luo, R. T. Haasch, J. I. Gold, M. Yamauchi, P. J. A. Kenis, *J. Am. Chem. Soc.* **2017**, *139*, 47.

[22] D. Kim, J. Resasco, Y. Yu, A. M. Asiri, P. Yang, *Nat. Commun.* **2014**, *5*, 1.

[23] J. Choi, M. J. Kim, S. H. Ahn, I. Choi, J. H. Jang, Y. S. Ham, J. J. Kim, S. K. Kim, *Chem. Eng. J.* **2016**, *299*, 37.

[24] Z. Chang, S. Huo, W. Zhang, J. Fang, H. Wang, *J. Phys. Chem. C* **2017**, *121*, 11368.

Chapter 3

Borocarbonitrides as metal-free electrocatalysts for the electrochemical reduction of CO_2

Summary

Majority of research for electrocatalyst development is focused on metal-based catalysts which suffer from drawbacks such as high cost, limited resource availability and competing hydrogen evolution. Herein, we study electrochemical reduction of CO_2 on metal-free borocarbonitride ($B_xC_yN_z$) catalysts in aqueous electrolyte. $BC_{1.2}N_{0.8}$ catalyst exhibits high selectivity for CO, reaching CO faradaic efficiency of 98% at -0.45V (vs RHE). Thus, we have tuned the composition of $B_xC_yN_z$ to study the effects of incorporating B and N in carbon lattice. This work provides insights into the effects of heteroatom doping in carbon lattice on the surface area, CO_2 uptake and electrochemical reduction of CO_2. A linear correlation was observed between FE_{CO} and N content, specifically pyridinic N content, shedding light on the active site for the electrochemical reduction of CO_2.

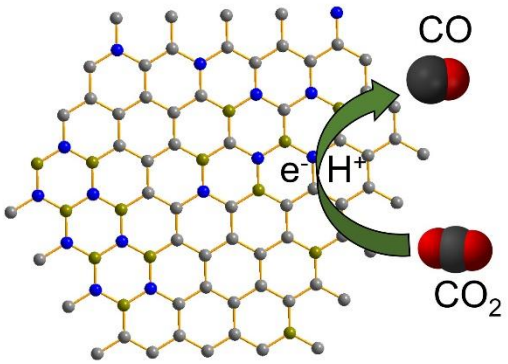

3.1 Introduction

Electrochemical reduction of CO_2 to produce value-added fuels has been regarded as an effective approach to reduce atmospheric CO_2 levels and to reduce further CO_2 emissions.[1] Electrochemical CO_2 reduction reaction (ECO2RR) at a catalyst surface involves adsorption of gaseous CO_2 molecule and its conversion to products via reduction reactions. CO_2 is a very stable molecule and the transfer of an electron to a linear CO_2 molecule to form bent CO_2 radical anion requires very high potential.[2] Moreover, the reduction of CO_2 at the catalyst surface competes with hydrogen evolution reaction which further complicates ECO2RR. Electrocatalyst development that facilitate efficient reduction of CO_2 with high selectivity and stability is being extensively carried out.[3] ECO2RR was first demonstrated on a dropping mercury electrode by Rysselberghe et. al.[4] Later studies showed that CO_2 can be reduced to carbon monoxide, methane, methanol, ethylene, etc. at metal electrodes.[2,5,6] Among the metal electrocatalyst, Cu, Ag and Au have been most widely studied.[7] Although these metal electrocatalyst efficiently reduce CO_2 to various value-added chemicals such as methanol, ethanol, etc. they suffer with drawbacks such as high cost and undesirable competing HER which restricts their large-scale applications. In this regard carbon based electrocatalyst have been studied for ECO2RR.[8] Carbon based materials have advantages such as natural abundance, tailorable structures, high surface area with good gas adsorption properties, quick penetration of electrolytes and are environmentally benign.[9] The tailorable nature of carbon materials makes them an attractive material for catalysis with the potential to eliminate the usage of metals. Carbon based materials have been extensively studied for various applications such

as hydrogen evolution reaction, oxygen evolution reaction and oxygen reduction reaction.[10–14]

Despite the excellent physical properties pristine carbon materials are inert towards ECO2RR due to the inability of neutral carbon atom to activate CO_2 molecule. However, the incorporation of heteroatoms such as B, N, F or S can significantly alter the electronic properties and enhance electrocatalytic activity rendering an otherwise inactive catalyst active towards ECO2RR.[15–17] Furthermore, CO_2 is a weak Lewis acid and the introduction of Lewis basic center in the carbon matrix by incorporation of heteroatom such as N can effectively enhance CO_2 adsorption.[8,18] N-doped carbon porous materials have been shown to effectively adsorb high amounts of CO_2.[19] B-doped graphene has also been shown to reduce CO_2 to HCOOH.[20] A crucial step in ECO2RR is the formation of *COOH intermediate and has a high energy barrier for undoped carbon which reduces with the introduction of heteroatom defect sites in lattice.[20,21] Catalytic activity of doped carbon materials can be further tuned by anchoring metal nanoparticles on the surface. Incorporation of metal in the lattice increases the active sites and the choice of metal offers the ability to tune selectivity for ECO2RR product.[17,22]

3.2 Scope of present investigation

Doping with two heteroatoms has been shown to be an efficient strategy to alter the properties of C lattice. Previous studies have shown that borocarbonitrides ($B_xC_yN_z$) exhibit high surface areas with excellent CO_2 adsorptive properties.[23,24] Borocarbonitrides were also shown to be efficient electrocatalyst for hydrogen evolution reaction under acidic conditions.[25] More recent results suggest that incorporation of two heteroatoms can

enhance the electrochemical activity. Liu et al[26] reported B, N doping in nanodiamond lattice to enhance production of C2 products. Pan et al[27] and Yang et al[17,28] reported S doping with N in carbon matrix to enhance the activity. Recently, Zhao et al[29] demonstrated ECO2RR from N, B dual doped 3D porous carbon to produce CO with a FE_{CO} of 83% at a low overpotential of 290mV. Thus far, there is a lack of systemic investigation towards understanding the catalytic activity of borocarbonitrides. This prompted us to study physical properties and ECO2RR of borocarbonitrides ($B_xC_yN_z$) and study the effect of changing/tuning the B, N content. In this article, we report our findings of ECO2RR employing borocarbonitrides in an aqueous bicarbonate electrolyte. Borocarbonitrides exhibit increased selectivity for CO production and improved stability under potentiostatic conditions. BCN-3 ($BC_{1.2}N_{0.8}$) exhibits highest FECO 98% at -0.45V. Catalytic activity of $B_xC_yN_z$ was found to be dependent on the N content, where FE_{CO} has a positive correlation of % N-content. The boron sites also assist in adsorption of CO_2, and the synergistic effect of B and N leads to better catalytic activity of $B_xC_yN_z$. Moreover, the synthesis procedure of $B_xC_yN_z$ facilitates incorporation of high amount of N and B in the lattice, along with high surface area which is beneficial for ECO2RR.

3.3 Experimental

Synthesis: $B_xC_yN_z$ were synthesized by a reaction of boric acid, urea and activated charcoal as reported earlier (**Figure 1**).[25] Briefly, boric acid, urea and activated charcoal were stepwise dissolved in 40mL Millipore water via ultrasonication. This homogenous dispersion was heated at 60^{o}C with continuous stirring till it dries completely. This precursor was ground and transferred to an alumina boat and heated in a tubular furnace at

930ºC for 10h under N_2 atmosphere. The product obtained after this was heated in NH_3 atmosphere at 960ºC for 4h. Different compositions of $B_xC_yN_z$ were synthesized by altering the relative amounts of boric acid, urea and activated charcoal (Table 1).

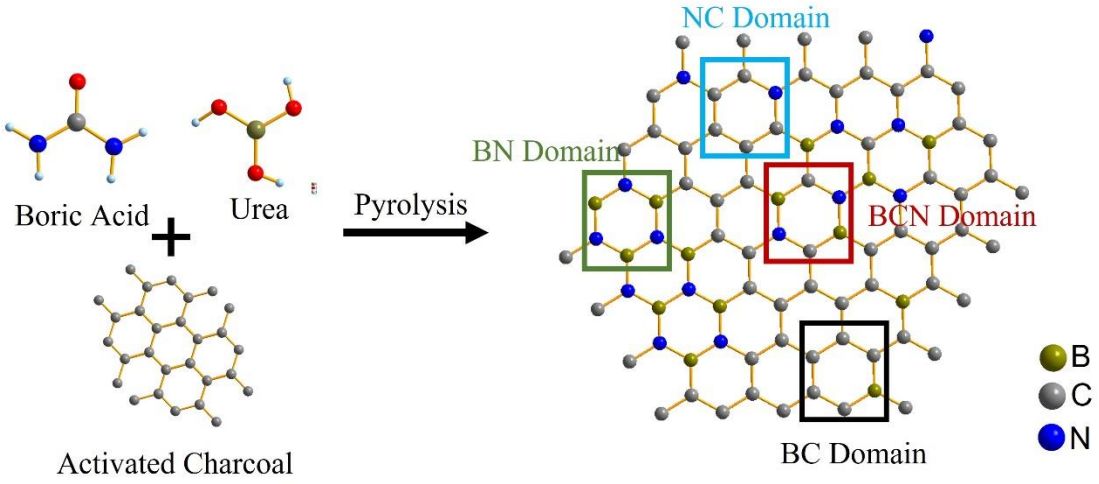

Figure 1. Schematic representation of synthesis procedure and structure of $B_xC_yN_z$

Table 1. Sample name, composition, and reactant ratios of materials under study

Sample	Composition	Boric Acid(g)	Activated Charcoal (g)	Urea (g)
BCN-1	$BC_{12.3}N_{0.9}$	0.1	1	3.6
BCN-2	$BC_{6.9}N_{0.8}$	0.3	1.5	3.6
BCN-3	$BC_{1.2}N_{0.8}$	0.3	1	3.6
BCN-4	$BC_{0.4}N_{0.8}$	0.3	0.5	3.6
NC	$C_{9.8}N_{0.02}$	-	1	3.6
BC		0.3	1	-
BN		0.3	-	3.6

Physical Characterization: Morphology of $B_xC_yN_z$ was studied by transmission electron microscopy, JEOL JEM 2100 plus 200kV. FTIR spectra were recorded with Perkin Elmer IR instrument. The atomic ratio of elements and the chemical nature of bonds were studied by X-ray photoelectron spectroscopy measurements, carried out on a Thermo K alpha+ spectrometer using monochromated Al Kα radiation. Surface area measurements were carried out in a MicrotracBEL Belsorp max II instrument. Scanning electron microscopy was carried out in a Zeiss Gemini SEM 500 instrument. Powder X-ray diffraction (PXRD) measurements were done at room temperature on a Rigaku Mini flex X-ray diffractometer with Cu Kα X-ray source(λ=1.5406Å), equipped with a position-sensitive detector.

Electrochemical Measurements: The electrochemical measurements were performed using an CHI760E electrochemical workstation with an air-tight borosil H-cell, where cathodic and anodic chambers were separated by an anion exchange membrane. Glassy carbon electrode (GCE) was used as working electrode, graphite rod was used as a counter electrode and Ag/AgCl(1M) was used as the reference electrode. All potentials were measured against Ag/AgCl and then converted to RHE scale using Nernst equation, E(vs RHE) = E(vs Ag/AgCl) + 0.229V + 0.0591*pH. Prior to the working electrode preparation, GCE was polished with alumina powder (CHI inc.). For the preparation of catalyst ink, 5mg of catalyst was ultrasonically dispersed in 1mL Nafion solution (Milli-Q water: Isopropanol:5wt% nafion = 800µL:200 µL:60 µL). 10 µL of this homogenous ink was drop coated on the polished GCE and allowed to dry under ambient conditions. A 0.25M $NaHCO_3$ (99.995%, Sigma Aldrich) was prepared in Milli-Q water and used an electrolyte. Linear sweep voltammetry was performed with a scan rate of 5mV/s. Cathodic chamber was purged with pure CO_2 (99.9%, Bhuruka Gases Ltd). or N_2 (99.9995%, Spec & Cal

Gases Pvt. Ltd.) gas for 30 minutes prior to and throughout every measurement at a rate of 10mL/min. The outlet gas from the cathodic chamber was directly injected into Perkin Elmer Gas chromatography instrument (Clarus 580) equipped with a TCD and FID. For the analysis of reduction products, chronoamperometry was performed for 30 mins and the effluent from the cathodic compartment were analyzed at 29th minute.

The Faradaic efficiency for gaseous products was calculated by using the following equations,

$$\text{FE (\%)} = \frac{zcVF}{i} * 100$$

Here, z is the number of electrons involved in the reduction reaction, c is the concentration of gaseous product determined by GC, F is faraday constant, V is the flow of CO_2 and *i* is current. The standard deviations of FE were calculated from measurements on three different electrodes. Electrochemical impedance spectroscopy (EIS) was performed near the onset potential from 10^5 to 10^{-2} Hz with an AC voltage of 5mV in CO_2 saturated 0.25 M $NaHCO_3$ and 0.5M H_2SO_4.

3.4 Results

Figure 1 shows the schematic of $B_xC_yN_z$ synthesis procedure. Transmission electron microscopy investigation of the synthesized $B_xC_yN_z$ revealed the formation of layered structure (**Figure 2a**). The Fourier-transform infrared spectroscopy (FTIR) of $B_xC_yN_z$ in comparison with undoped activated charcoal (AC), N-doped carbon (NC), B-doped carbon (BC) and boron nitride (BN) are shown in figure 1b. $B_xC_yN_z$ contains

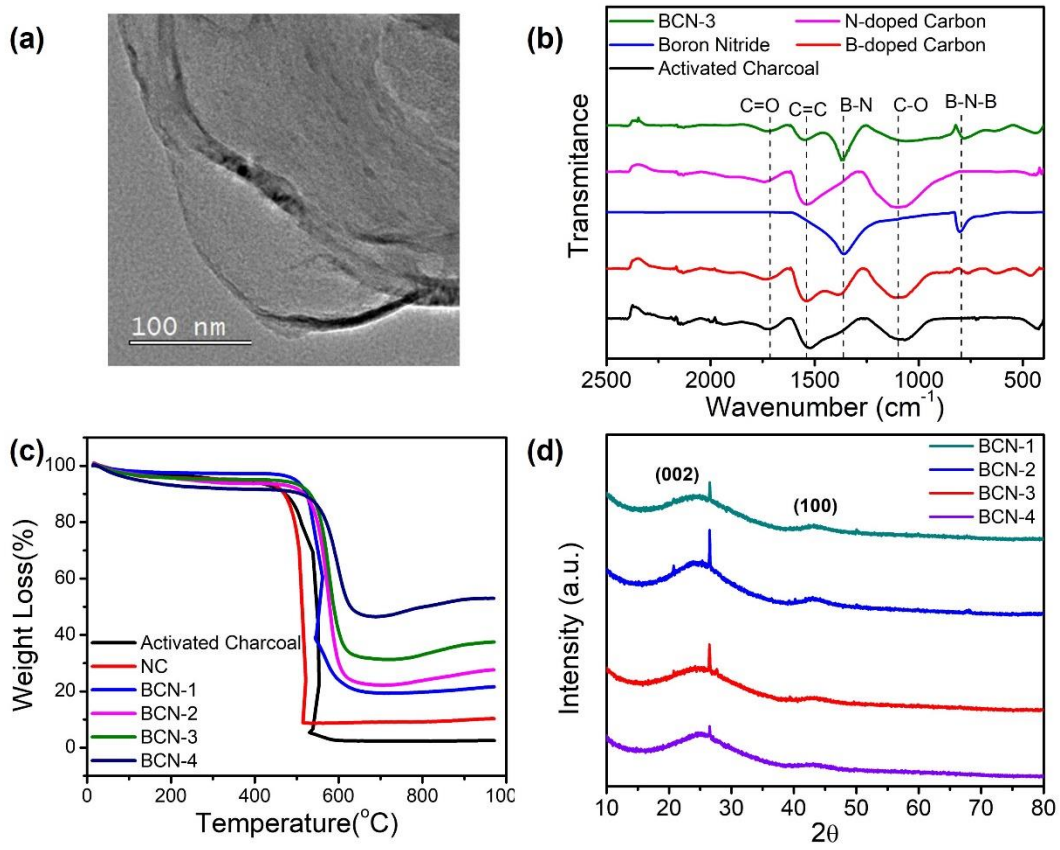

Figure 2. (a) TEM image of BCN-3, (b) FTIR spectra of BCN-3 in comparison with N-doped carbon, boron nitride, B-doped carbon and activated charcoal, (c) Thermogravimetric analysis of activated charcoal, N-doped carbon (NC) and BCN compositions and (d) X-ray diffraction of pattern of all BCN compositions

vibrations from C=O (1720 cm^{-1}), C=C (1540 cm^{-1}), B-N (1360 cm^{-1}), C-O (1095 cm^{-1}) and B-N-B (800 cm^{-1}) (**Figure 2b**). FTIR result reveals the formation of B-N domains in carbon lattice of $B_xC_yN_z$ along with graphene domains and the presence of carbonyl functional groups. Thermogravimetric analysis was carried out in oxygen atmosphere for all the $B_xC_yN_z$ compositions to get an estimate of carbon content. The TGA curves (**Figure 2c**) show a sharp dip in weight at around 500 ºC which is due to burning of C content in oxygen, indicating the %C content in $B_xC_yN_z$. It is observed that BCN-1 has highest carbon

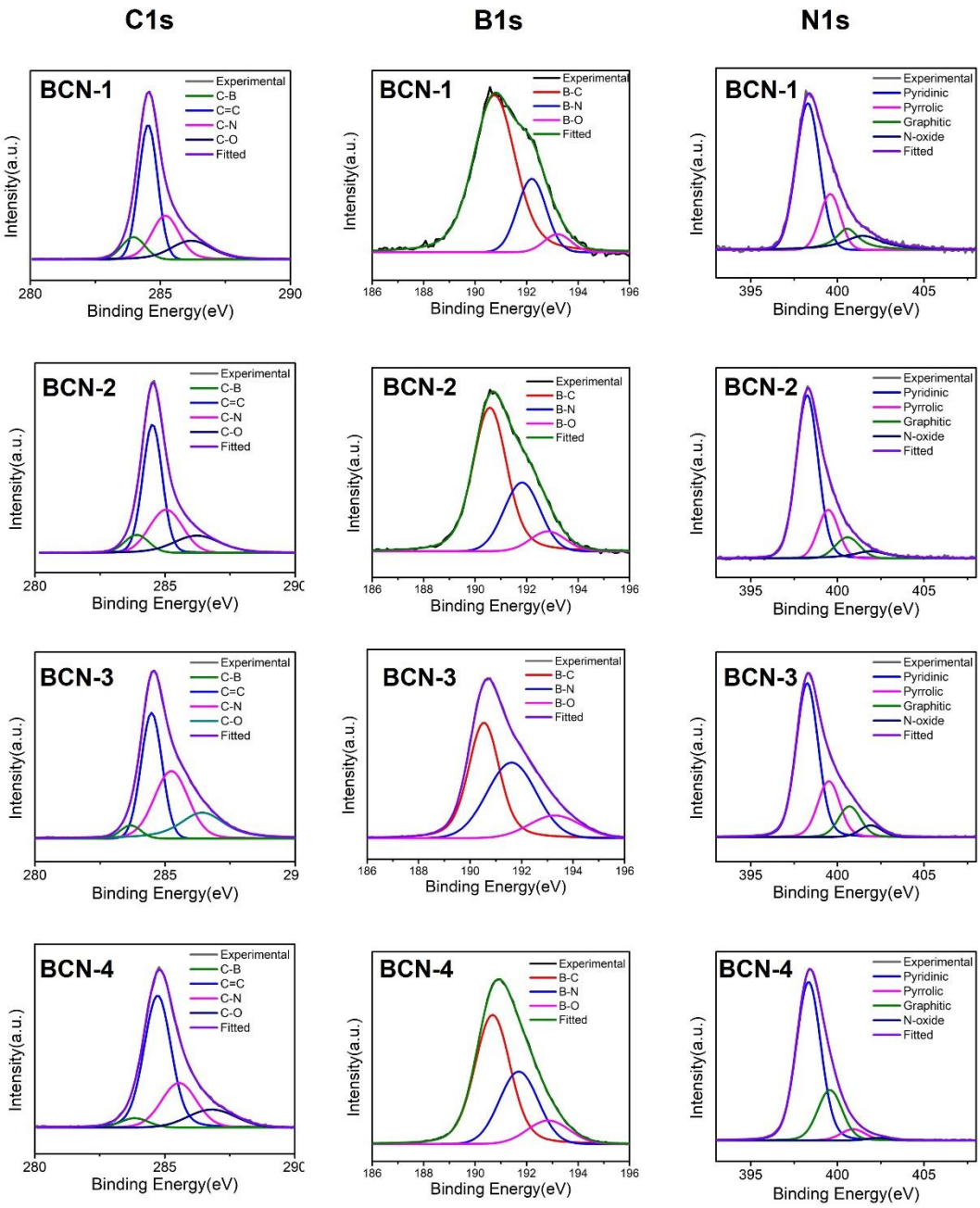

Figure 3. XPS C1s, B1s and B1s core level spectra of BCN-1, BCN-2, BCN-3 and BCN-4.

content followed by BCN-2, BCN-3, and BCN-4. X-ray diffraction patterns of $B_xC_yN_z$ (**Figure 2d**) shows two distinctive broad peaks at ~26° and ~43° (along with residual peaks

from glass sample holder), corresponding to (002) and (100) interlayer reflections, respectively.[24]

The chemical composition and the chemical nature of bonds was determined by X-ray photoelectron spectroscopy (XPS) (**Figure 3**). For activated charcoal, only carbon peak was observed, while an additional peak for N appears in N-doped carbon. For BCN, we observe the presence of B, C and N peaks in the survey spectrum. Core level C1s, B1s and N1s spectra for all $B_xC_yN_z$ compositions are given in **Figure 3**. C1s core level spectra could be deconvoluted into four peaks at 283.9, 284.5, 285.4 and 286.5 eV corresponding to C-B, sp^2-C, C-N and C-O species originating from surface functional groups, respectively (**Figure 3a**). The B1s core level spectra could be deconvoluted into three peaks at 190.7, 192.2 and 193.2 eV corresponding to B-C, B-N and B-O species, respectively (**Figure 3b**). The N1s core level spectra can be deconvoluted into four peaks at nearly 398.3, 399.1, 401.1 and 403.8 eV corresponding to pyridinic N, pyrrolic N, graphitic N and surface N-oxide species, respectively (**Figure 3c**). XPS analysis of the core level spectra clearly show the presence of various species such as B-C, B-N, C-N and C-C, which confirms the presence of graphene, boron nitride and borocarbonitride domains in BCN. Further, it also reveals the presence of functional groups such as -COOH/ -OH.

Surface area and pore size analysis of $B_xC_yN_z$ were estimated by the N_2 adsorption isotherm data (**Figure 4a**). Among all the samples, BN exhibits lowest specific surface area (597 m^2g^{-1}), followed by activated charcoal (1118 m^2g^{-1}), B-doped carbon (1138 m^2g^{-1}), BCN-1 (1624 m^2g^{-1}) and N-doped carbon (1672 m^2g^{-1}) (**Figure 4b**). It is evident from the above data that incorporation of B, N significantly increases specific surface area of activated charcoal. AC has a specific surface area of 1118 m^2g^{-1}, which increases to 1624

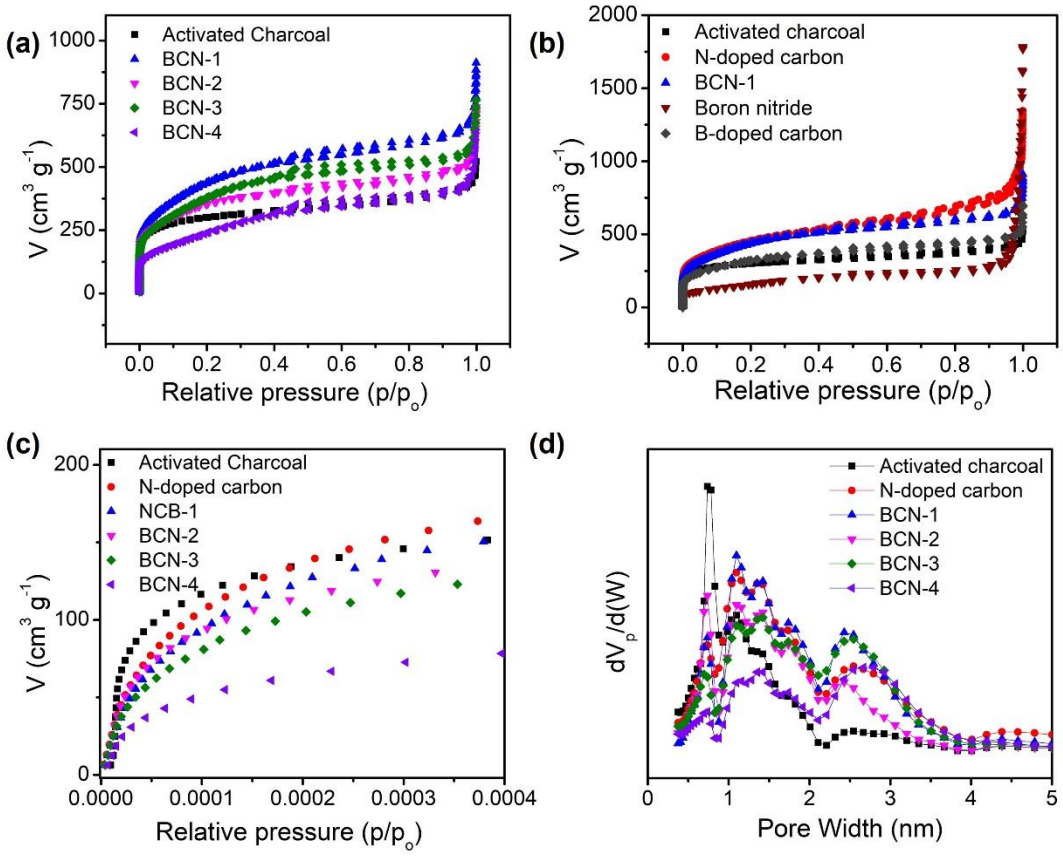

Figure 4. (a) N_2 adsorption isotherm of AC and composition of $B_xC_yN_z$, (b) comparison of N_2 adsorption isotherm of BCN-1 with AC, NC, BN and BC, (c) N_2 adsorption isotherm at low relative pressure range and (d) particle size distribution analysis from BET data.

m^2g^{-1} for BCN-1, followed by BCN-2 (1317 m^2g^{-1}), BCN-3 (1419 m^2g^{-1}) and BCN-4 (924 m^2g^{-1}). Specific surface area decreases with increasing B, N content in BCN, with BCN-4 exhibiting lower specific surface area than AC indicating that increase in BN content has a detrimental effect on the surface porosity. In comparison to AC, BCN has overall high nitrogen uptake over the whole relative pressure range except at very low relative pressures (up to $p/p_o = 10^{-4}$) (**Figure 4c**). This higher uptake of N_2 at lower relative pressure range suggest filling of pores < 1 nm. Particle size distribution (PSD) analysis also shows a higher density of micropores (< 1 nm) in AC as compared to BCN (**Figure 4d**). Majority of pores

in BCN are of 1.09 nm whereas in AC it is 0.74 nm which suggests the collapse of smaller micropores into bigger pores with doping N and B. A close observation of the adsorption isotherms shows that at low pressures the gas adsorption shows characteristic feature of microporous Type I isotherm whereas at higher relative pressures the isotherms deviate from the Type I nature and shows characteristic feature of type IVA which corresponds to mesoporous materials. This deviation from microporous to mesoporous increases gradually with increase in B, N content of BCN, where BCN-4 with the highest amount of B, N content deviates the most from the Type I feature and a clear hysteresis loop can be seen in the range of $0.40<p/p_o>0.90$. This observation is corroborated with the PSD analysis where the peak for pore size 2.4 nm increases for BCN in comparison to AC (**Figure 4d**).

Electrochemical CO_2 reduction performance of the BCN catalysts was measured in CO_2 saturated 0.25 M $NaHCO_3$ electrolyte with a standard H-cell three-electrode setup, with graphite as counter electrode and Ag/AgCl as reference electrode. **Figure 5a** shows linear sweep voltammograms of all catalysts in CO_2 saturated electrolyte indicating reduction of CO_2. Compared to AC, all the doped carbon catalyst exhibits lower onset potentials and increased currents. BCN-1 exhibits lowest onset potential of -0.53 V followed by BCN-3 (-0.56 V), BCN-2 (-0.55 V) and BCN-4 (-0.59 V) for current density of 2 mA cm^{-2}. Onset potential of BCN-1 lies very close to N-doped carbon (-0.52 V) but at higher potentials N-doped carbon overtakes BCN-1 and exhibits higher currents than all compositions of BCN which is due to higher H_2 production. LSV in an CO_2 saturated aqueous bicarbonate solution is not indicative of CO_2 reduction, since the onset of HER lies very close to CO_2 onset potential. Constant potential electrolysis was carried out in the potential range of -0.3 to -0.9 V with an interval of 0.05V for 30 minutes and gas from the

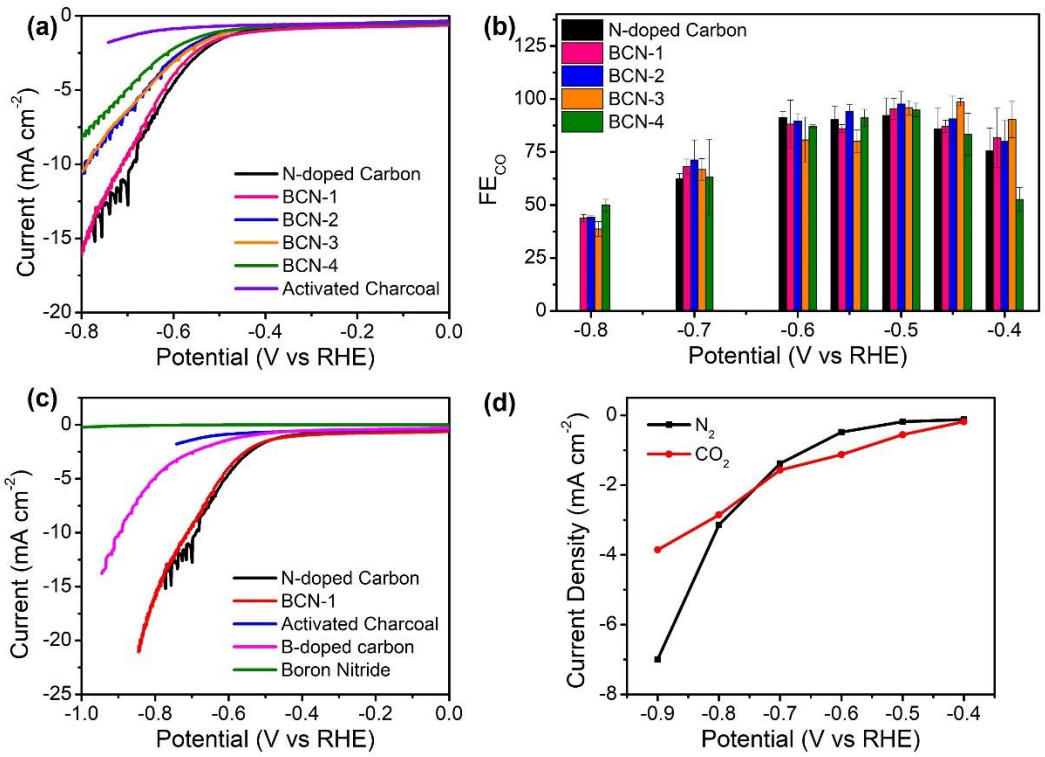

Figure 5. (a) Linear sweep voltammetry in CO_2 saturated 0.25M $NaHCO_3$, (b) faradaic efficiency of CO as a function of potential for $B_xC_yN_z$ and N-doped carbon, (c) Comparison of linear sweep voltammograms of N-doped carbon, B-doped carbon, Boron nitride, activated charcoal and borocarbonitride in CO_2 saturated 0.25M $NaHCO_3$ and (d) steady state currents for BCN-3 in N_2 and CO_2 saturated electrolyte. Catalyst ink (Milli-Q water: Isopropanol:5wt% nafion = 800µL:200 µL:60 µL). was dropcoated on glassy carbon electrode (0.7 mg/cm^2). Ag/AgCl (1M) and graphite rod were used as reference and counter electrode, respectively.

cathodic chamber was analyzed. Only CO was observed as the CO_2 reduction product over the whole potential range along with competing hydrogen.

Faradaic efficiencies of CO (FE_{CO}) were calculated and are plotted as a function of potential for all catalyst in **Figure 5b**. At potentials lower than -0.4 V no gas evolution was observed. CO was detected for all the samples at -0.4V, with highest FE_{CO} of ~90% for BCN-3. BCN-3 exhibits highest FE_{CO} at -0.45V of ~98%, whereas NC exhibits highest

FE_{CO} at -0.5V of ~92%. N-doped carbon, despite having a lower onset potential and higher currents exhibits lower FE_{CO} which suggest lower selectivity for CO_2 reduction and a higher contribution of competing HER. Moreover, comparing LSV of $B_xC_yN_z$ with N-doped carbon and B-doped carbon reveals that B-doped carbon exhibits higher onset potentials and very poor selectivity towards CO (**Figure 5c**). The poor activity and low selectivity of single N and B doped carbon along with a significant enhancement of FECO at lower potentials for $B_xC_yN_z$ substantiates that codoping of B and N in carbon lattice has a synergistic effect on improving the catalytic of $B_xC_yN_z$. To further confirm the reduction of CO_2 at the catalyst surface, the same potentiostatic experiments were repeated in a N_2-saturated electrolyte and no CO was detected by the GC at any potential. Steady state currents at each potential in CO_2 and N_2 saturated electrolyte were plotted as a function of potential and significantly higher currents were observed in the case of CO_2-saturated electrolyte at lower potentials clearly suggesting CO_2 reduction by BCN catalysts (**Figure 5d**).

Stability of the catalyst (BCN-3) under potentiostatic conditions was analyzed by running a constant potential electrolysis at -0.45V for 12 h and gas from the cathodic chamber was analyzed by GC at every hour. At -0.45 V, BCN-3 exhibits highest FE_{CO} and retains ~93% of its activity at the end of 12h with current density of 0.15 mA cm^{-2} (**Figure 6a**). Moreover, BCN-3 is stable in the potential range of -0.45 to -0.55 V, retaining ~90% activity at the end of 12h with CO partial current densities (j_{CO}) of ~0.5 mA cm^{-2}(**Figure 6b and 6c**). For comparison the same experiment was repeated for N-doped carbon which exhibits a faster decay in FE_{CO} (**Figure 6d**). To study the effect of long duration ECO2RR on the catalyst TEM and SEM-EDAX was done on the catalyst after the 12h stability run.

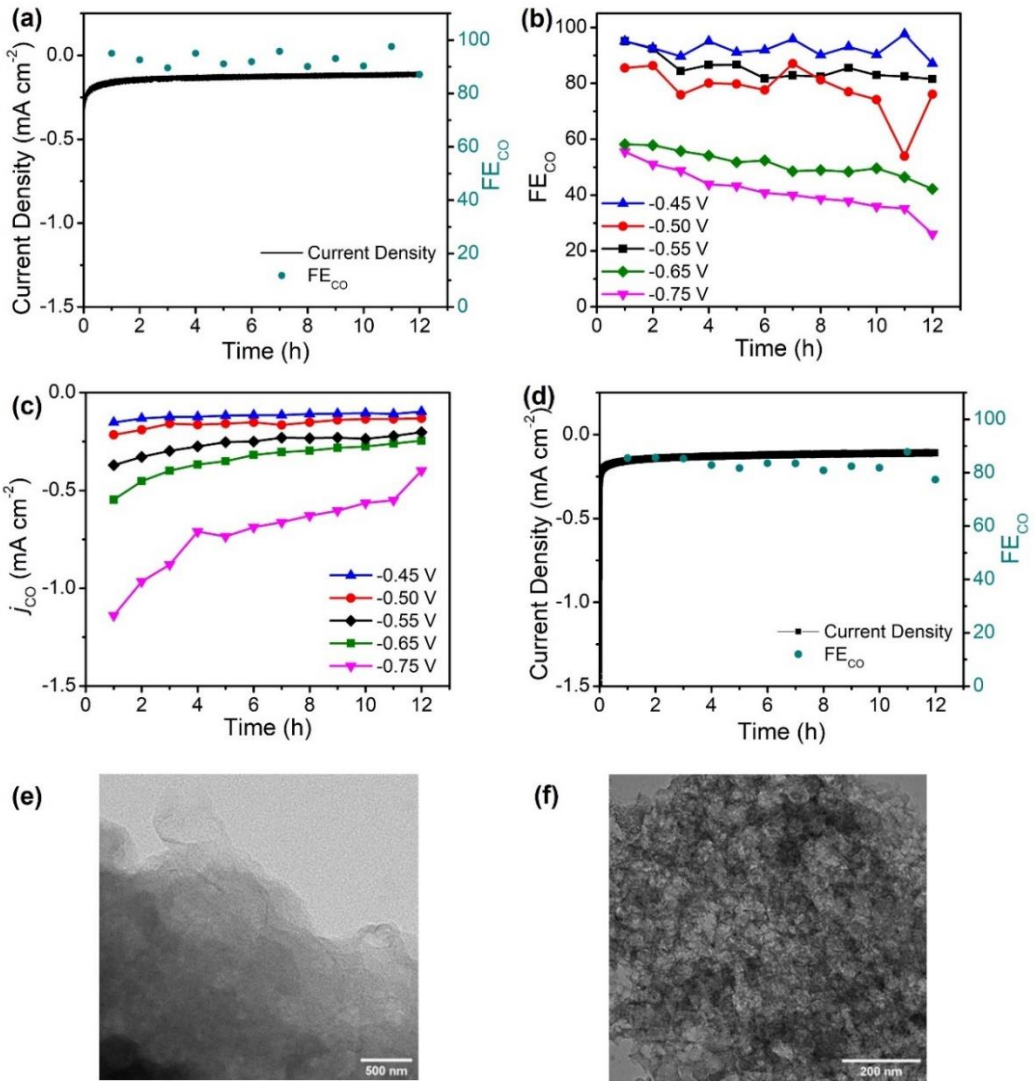

Figure 6. (a) Chronoamperometric i-t curve and the corresponding faradaic efficiency of CO (FE_{CO}) for (a) BCN-3 at -0.45 V and (d) N-doped carbon over a period of 12 hours, (b) FE_{CO} in the potential range of -0.45V to -0.75 V with (c) their corresponding CO partial current densities (j_{CO}) and TEM image of (e) BCN-3 and (f) N-doped carbon after chronoamperometric experiment. Ag/AgCl (1M) and graphite rod were used as reference and counter electrode, respectively.

TEM of BCN-3 confirms sheet like morphology with no structural damage whereas for NC a clear disruption of morphology can be seen (**Figure 6e and 6f**). The excellent stability

of $B_xC_yN_z$ under potentiostatic conditions could be due to the enhanced structural stability imparted by the BCN and BN domains.[30–32]

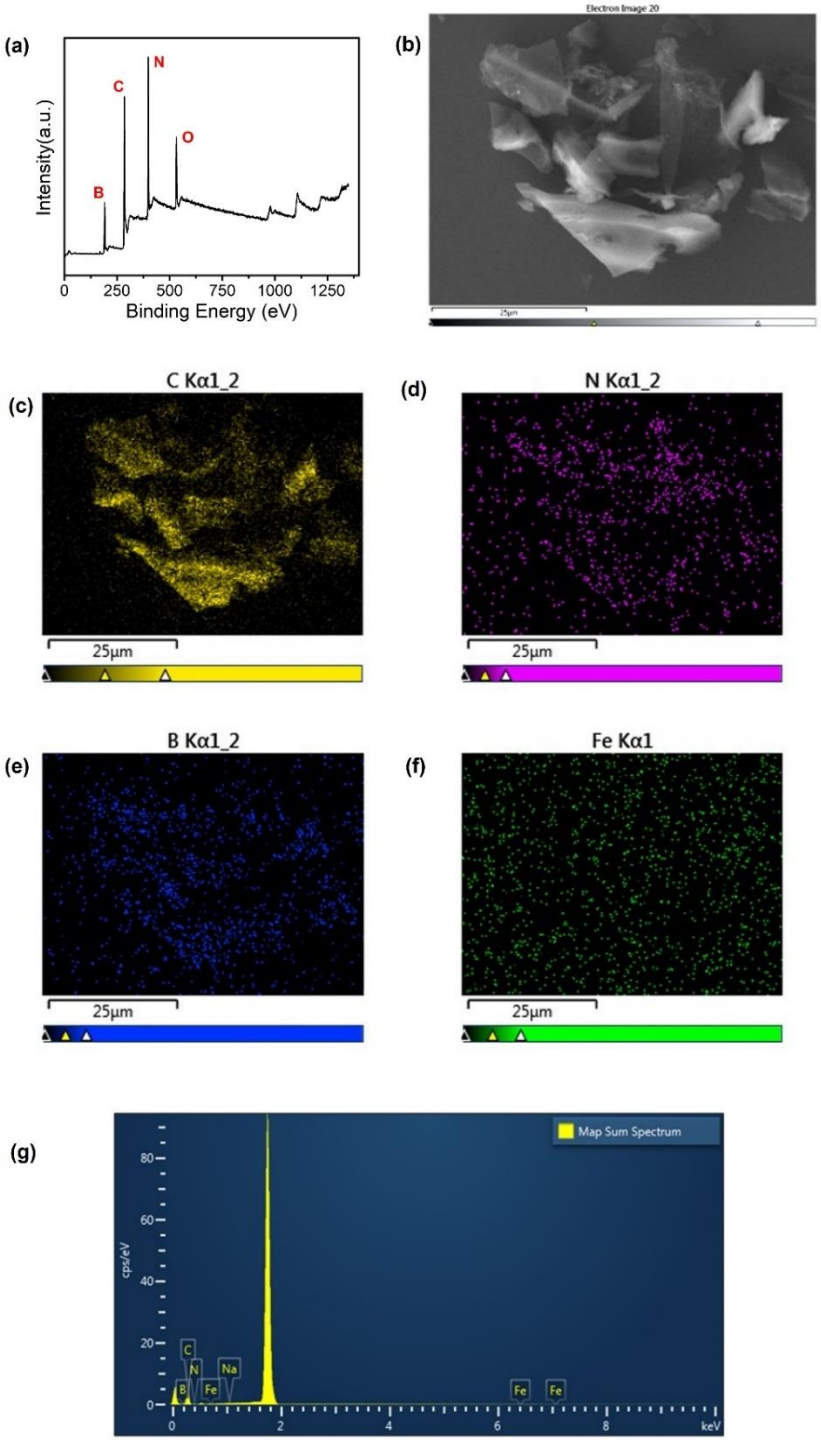

Figure 7. (a) XPS survey spectrum of BCN-3, (b) SEM image, elemental mapping of (c) C, (d) N, (e) B, (f) Fe and (g) EDS spectrum of BCN-3 after constant potential electrolysis.

Lum et al[33] reported that trace levels of Cu in GO improve the catalytic activity towards CO2RR. Trace metal impurities can be introduced in the sample during the synthesis procedure or by electrodeposition during ECO2RR from the aqueous electrolyte. XPS survey spectra of the catalyst does not show presence of any trace metal impurity therefore nullifying the synthesis originated impurities (**Figure 7a**). Further, elemental analysis of BCN-3 after constant potential electrolysis was done via SEM-EDX, and any presence of trace metal impurity was not detected (**Figure 7b-g**). Moreover, if the trace metal impurities act as active sites for ECO2RR, the pure undoped activated charcoal should also reduce CO_2 which is not the case in our study.

3.5 Discussion

To understand the ECO2RR activity on the catalyst surface we need to study the steps involved during ECO2RR. ECO2RR generally follows three basic steps: (i) adsorption of CO_2 molecule, (b) transfer of electron from the catalyst to CO_2 molecule via proton coupled electron transfer reactions involving reactive intermediates and (iii) dissociation of product from the catalyst surface.

Adsorption of CO_2 on the catalyst surface was studied by the CO_2 adsorption isotherms at 195K for all the catalysts (**Figure 8a**). AC exhibits CO_2 adsorption capacity of 12.64 mmol/g and this CO_2 adsorption capacity increases with incorporating B, N in the lattice. The CO_2 adsorption capacity although decreasing with increasing B, N content is highest for the intermediate composition (BCN-3 = 14.5 mmol/g). A similar increase in gas uptake was also observed in the N_2 adsorption isotherm, where the surface area of

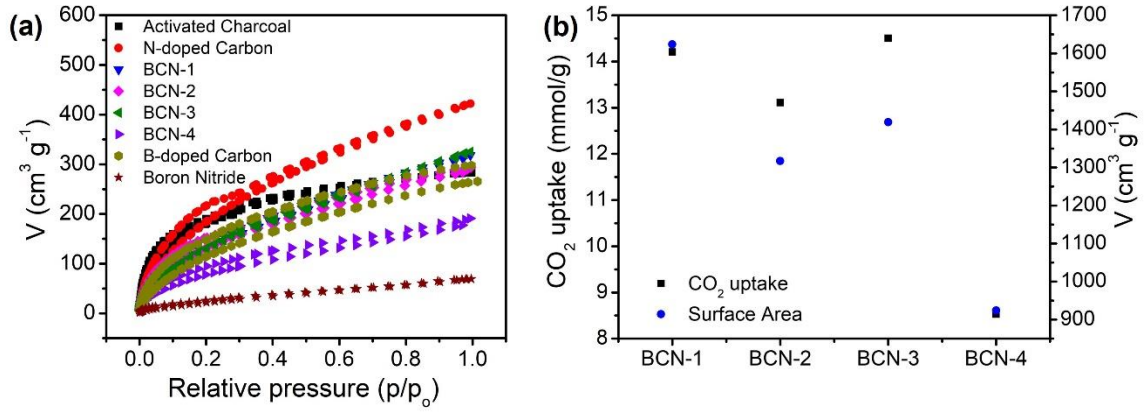

Figure 8. (a) CO_2 adsorption isotherm at 195K and (b) trend in surface area and CO_2 uptake capacity.

Table 2. Comparison of parameters of N-doped carbon, activated charcoal and various compositions of $B_xC_yN_z$.

Catalyst	**Carbon Content (%)**	**Double Layer Capacitance (mF cm^{-2})**	**BET surface area (m^{2}g^{-1})**	**Onset potential@-2 mAcm^{-2} (vs RHE)**	**CO_2 uptake (mmol/g)**
Activated charcoal	100	49.1	1118		12.64
N-doped Carbon	98.0	64.6	1672	-0.52	18.8
BCN-1	86.8	62.3	1624	-0.53	14.2
BCN-2	79.6	37.8	1317	-0.56	13.1
BCN-3	39.6	57.5	1419	-0.55	14.5
BCN-4	19.6	21.8	924	-0.59	8.5

BCN-3 increases whereas in general surface area decreases with increasing B, N content. The trend in surface area and CO_2 adsorption capacity can be clearly observed in **Figure 8b**. Interestingly, B-doped carbon also exhibits higher CO_2 uptake than AC which indicates that B-sites also assists in CO_2 adsorption (**Figure 8a**). The high CO_2 uptake capacity of BCN-3 might be responsible for its high ECO2RR selectivity.

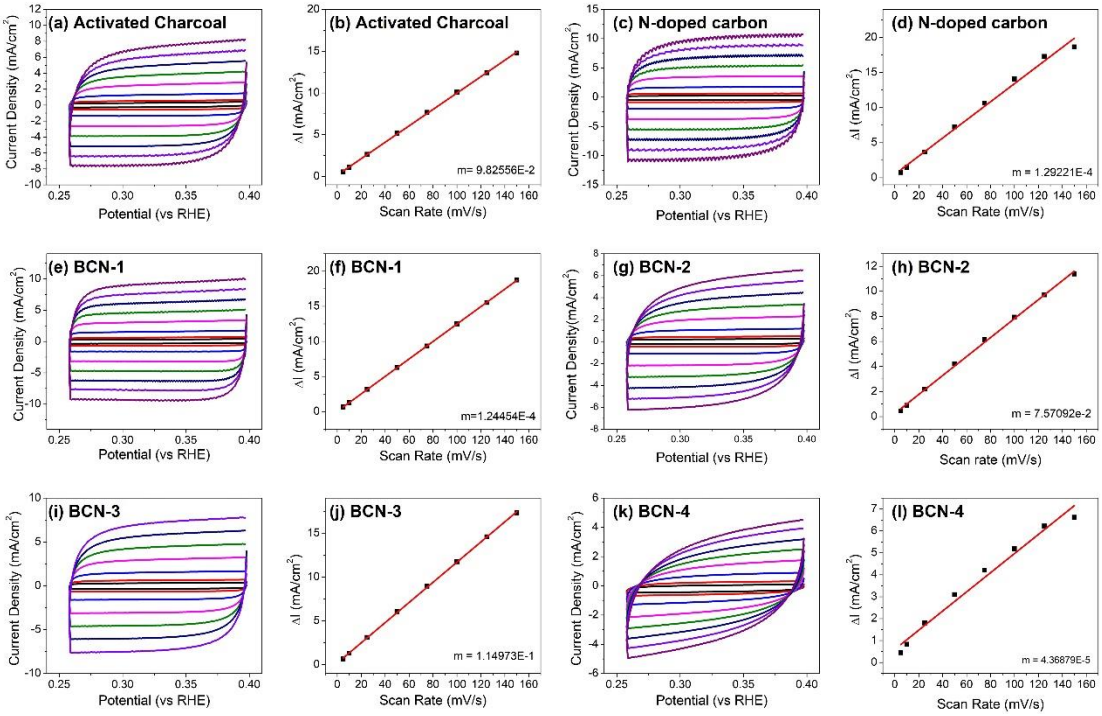

Figure 9. (a, c, e, f, g, i, k) CV curves of all BCN compositions in 0.5M H_2SO_4 at different scan rates and (b, d, f, h, j, l) corresponding difference in current density (Δi mA cm^{-2}) at 0.32 V (*vs.* RHE) plotted against scan rate to calculate double layer capacitance from the slope after linear fit.

For step two, the presence of active sites for reduction is crucial for efficient ECO2RR. To calculate the electrochemically active surface area (ECSA), double layer capacitance (C_{dl}) of the catalysts was calculated by measuring capacitive currents associated with double layer charging from the scan rate dependence of cyclic voltametric stripping and the values are tabulated in **Table 2** (**Figure 9**). BCN-1 and BCN-3 shows

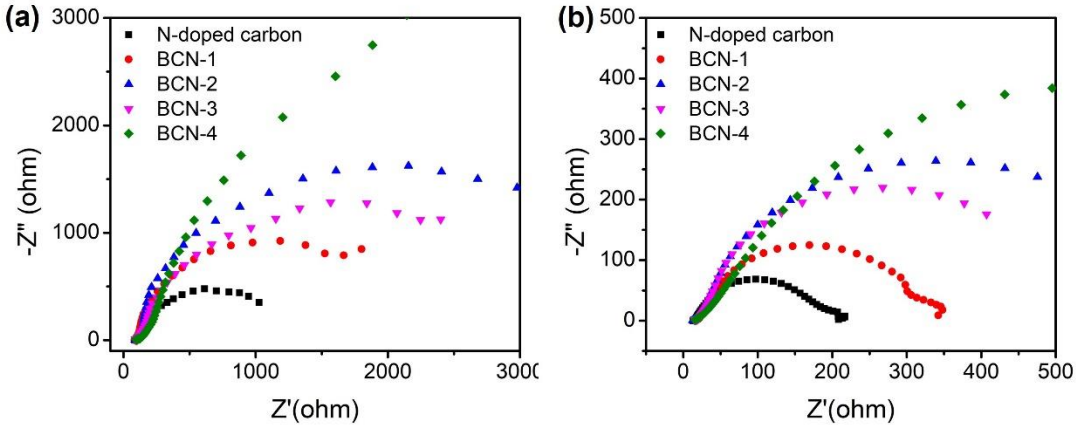

Figure 10. Nyquist plot for N-doped carbon, activated charcoal and various compositions of BCN in (a) CO_2 saturated 0.25M $NaHCO_3$ at -0.5 V and (b) 0.5M H_2SO_4. EIS measurements were done at the onset potential from 10^5 to 10^{-2} Hz with an AC voltage of 5mV.

highest and similar ECSA values. Further, to understand the electron transfer rate at the surface of catalysts, electrochemical impedance spectroscopy (EIS) was performed near the onset potential from 10^5 to 10^{-2} Hz with an AC voltage of 5mV in CO_2 saturated 0.25 M $NaHCO_3$ (**Figure 10**). Charge transfer resistance (R_{ct}) of the electron exchange between electrode and electrolyte can be qualitatively analyzed by the semi-circle formed in the Nyquist plot derived from EIS data, where a smaller circle corresponds to lower R_{ct}. Among the BCN samples, BCN-1 shows lowest R_{ct} value followed by BCN-3, BCN-2 and highest R_{ct} for BCN-4. Similarly, EIS for all the samples was carried out in 0.5 M H_2SO_4 which also shows similar trend in R_{ct} values (**Figure 10**). We observed that ECSA and R_{ct} values for BCN shows no specific relation with FE_{CO} which could be due to difference in activities of various sites present in BCN.

To investigate the role of various functionalities and defect sites on ECO2RR we calculated the relative percentages of them from core level XPS (**Table 2 and 3**) and

plotted against FE_{CO} at -0.45 V-0.5 V (vs RHE). We observed a positive correlation of FE_{CO} with total N content, with FE_{CO} increasing with N content except for BCN-4 which

Table 3. Composition of all compositions of $B_xC_yN_z$.

Catalyst	Overall composition	%C	%N	%B
NC		98.0	2.0	0
BCN-1	$BC_{12.3}N_{0.9}$	86.8	6.1	7.1
BCN-2	$BC_{6.9}N_{0.8}$	79.6	8.9	11.5
BCN-3	$BC_{1.2}N_{0.8}$	39.6	26.5	33.9
BCN-4	$BC_{0.4}N_{0.8}$	19.6	34.7	45.7

Table 4. Percentage of nitrogen and carbon functionalities of all compositions of $B_xC_yN_z$.

Catalyst	Nitrogen			Carbon			
	Pyridinic	Pyrrolic	Graphitic	oxide	C-B	C-N	C-O
NC	38.7	35.6	20.1	5.5		32.0	
BCN-1	56.5	18.6	11.8	13.2	9.8	25.0	16.9
BCN-2	66.7	17.6	9.1	6.6	8.1	26.9	16.7
BCN-3	61	22.2	12.2	4.6	3.9	35.6	21.7
BCN-4	71.3	22.6	5.1	1	4	24.5	12.9

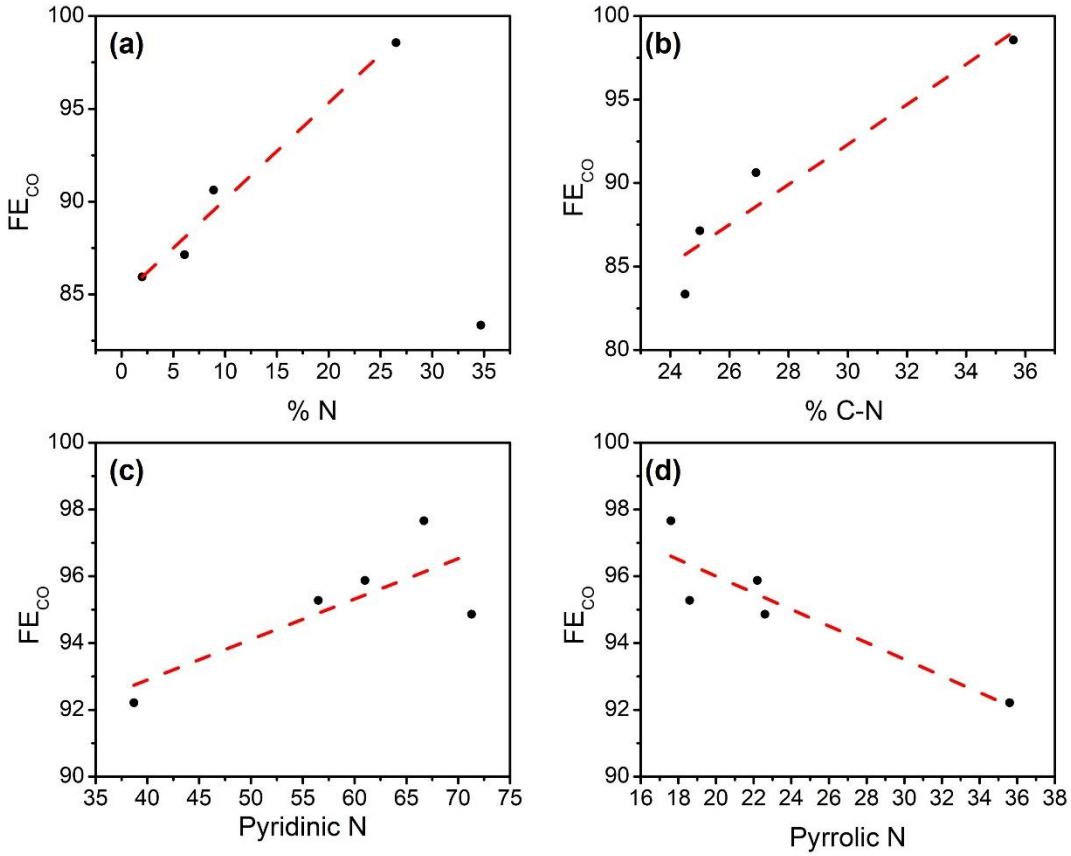

Figure 11. Correlation of CO faradaic efficiency (FE_{CO}) with (a) overall nitrogen content, (b) % N-C bonds, (c) pyridinic N content and (d) pyrrolic N content for all the studied catalysts.

has the highest N content but lowest FE_{CO} (**Figure 11a**). We envision that this deviation from linearity is because of N functionalities that have different catalytic activity. We observed that FE_{CO} correlated positively with %C-N in all the BCN catalysts implying that the N site in the carbon lattice could be the most active center (**Figure 11b**). Interestingly we observed that FE_{CO} increases linearly with pyridinic N content whereas decreases linearly with pyrrolic N content (**Figure 11c-d**). This explains the low selectivity of N-doped carbon and BCN-4 which has high pyrrolic N content and better catalytic activity of BxCyNz which has high pyridinic and low pyrrolic N content.

DFT calculations based on computational hydrogen electrode model carried out by various groups gives us an insight on role of B and N in ECO2RR activity.[34] ECO2RR on a carbon catalyst follows three elementary reaction steps:

$CO_2 + * + H^+ + e^- \rightarrow * COOH$

$*COOH + H^+ + e^- \rightarrow *CO + H_2O$

$*CO \rightarrow CO$

Where * represents an empty site for adsorption. The first step, activation of CO_2 molecule is an uphill process at 0V vs RHE involving adsorption of CO_2 and transfer of proton electron pair to the form *COOH intermediate. After the formation of *COOH, the free-energy pathway becomes thermodynamically downhill to form CO. Therefore, the potential limiting step is the formation of the *COOH intermediate.

Undoped carbon has a very large barrier for the first step as it does not have a stable state for adsorption of CO_2, whereas this barrier is reduced by incorporating N defects in the lattice [35] which breaks the electroneutrality of carbon framework and improves charge and spin densities of carbon atoms in the vicinity of dopants thereby providing more active sites for ECO2RR. For N-doped carbon, pyridinic N site is most favorable followed by pyrrolic and graphitic N.[18,21,36] Further, DOS studies show that pyridinic and pyrrolic defect sites retain a lone pair of electrons which could bind to CO_2 whereas graphitic nitrogen species the electrons are located in π^* antibonding orbital making them less accessible for CO_2 binding. *COOH tends to bind to adjacent pyridinic N site instead of pyrrolic N sites. [37,38] Moreover, it has also been predicted that N-sites does not participate

directly in ECO2RR but facilitates the transfer of *H to convert *CO_2 to *COOH, where pyridinic N shows the best capacity for facilitating *H transfer. [21,36]

Theoretical calculations have shown that BCN strongly adsorbs CO_2, predominantly on the rings which have at least two carbon atoms and at least a pair of B and N atoms.[24] For ECO2RR, B and N play a synergistic role which potentially enhances CO_2 capture, where B sites bond to the O atoms of the absorbed *CO_2 intermediate, while N-sites assists in transferring *H to the adsorbed *CO_2.[26,29,34] This synergistic effect of B and N facilitates adsorption of *COOH intermediate and is responsible for the better catalytic activity.

The present study shows that incorporation of B and N in carbon lattice enhances the selectivity for CO_2 reduction in comparison to N-doped carbon. The enhanced activity is due to stabilization of *CO_2 and *COOH intermediates on BCN rings, where B-sites assists in adsorption and the high concentration of pyridinic N-sites facilitates *H transfer. Incorporation of both B and N in carbon significantly increases the amount of N, more specifically pyridinic N, which is not possible with N-doped carbon.

Table 5. Comparison of electrochemical activity of various catalysts with the current study

Catalyst	Potential (vs RHE)	Product efficiency	Current Density($mAcm^{-2}$)	Electrolyte	Ref
$B_xC_yN_z$ nanosheets	-0.45 V	98% CO	0.15	0.25 M $NaHCO_3$	Current work
N-doped Carbon nanofiber	-0.573 V	98% CO	1.5	25mol % EMIM-BF_4-75 mol% water	[8]
3D N-doped graphene foam	-0.58V	85% CO	1.8	0.1 M $KHCO_3$	[21]
N-doped graphene nanoribbons	-0.49 V	88% CO	5	0.5 M $KHCO_3$	[36]
F-doped carbon	-0.62 V	90% CO	0.24	0.1 M $NaClO_4$	[16]
N,s-co-doped C	-0.7 V	94%	103	0.1M $KHCO_3$	[28]
B-doped graphene	-1.4 V (vs SCE)	66% HCOOH		0.1M $KHCO_3$	[20]
B, N-co-doped nanodiamond	-1 V	93.2% C2H5OH	2	0.1 M $NaHCO_3$	[26]
N,S-co doped carbon	-0.6 V	92% CO	2.63	0.1M $KHCO_3$	[27]
N,B- hierarchical carbon	-0.4V	83% CO	0.2	0.5M $KHCO_3$	[29]
B,N-co doped carbon	-0.55 V	95% CO	2.7	0.1M $KHCO_3$	[34]
Ni-N-C graphene	-0.5 V	97% CO	115	0.5 M $KHCO_3$	[39]
3D Ag foam	-0.99 V	95% CO	10.8	0.1 M $KHCO_3$	[40]
Au nanoparticles	-0.52 V	97% CO	3 Ag^{-1}	0.5 M $KHCO_3$	[41]
CdS nano needle	-1.2 V	96% CO	212	0.1M $KHCO_3$	[42]
MoS_2	-0.764V	98% CO	65	96mol% water-4 mol% EMIM-BF_4	[43]

3.6 Conclusions

In summary, incorporation of boron and nitrogen in carbon lattice to form borocarbonitrides can be an efficient strategy to tune the electrocatalytic activity towards CO_2 reduction. $B_xC_yN_z$ exhibits higher selectivity for CO_2-CO conversion than N-doped carbon. $B_xC_yN_z$ can attain high levels of doping where BCN-3 with ~26% N content exhibits maximum FE_{CO} at -0.45V of ~98%. Table 3 compares the catalytic activity of $B_xC_yN_z$ with the literature and it is evident that $B_xC_yN_z$ exhibit catalytic activity at par with the state-of-the-art catalysts. The correlation of FE_{CO} with distinct N defects reveals that pyridinic N sites are most active sites amongst all the N-species and $B_xC_yN_z$ have significantly higher content of pyridinic N sites. The enhanced catalytic activity is due to the synergistic effect of N- and B-sites which stabilizes *COOH intermediate, where N-sites enhances the *H transfer and B-site assists in the adsorption of CO_2. $B_xC_yN_z$ catalyst is stable under constant potential electrolysis retaining more than 90% of activity after 12h. Incorporation of B with N in carbon imparts structural stability to the catalyst as evident from the TEM images of BCN and NC after constant potential electrolysis.

3.7 References

[1] S. Chu, A. Majumdar, *Nature 2012 488:7411* **2012**, *488*, 294.

[2] R. Kortlever, J. Shen, K. J. P. Schouten, F. Calle-Vallejo, M. T. M. Koper, *J. Phys. Chem. Lett.* **2015**, *6*, 4073.

[3] M. M. Ayyub, C. N. R. Rao, *Mater. Horiz.* **2021**, *8*, 2420.

[4] T. E. Teeter, P. van Rysselberghe, *J. Chem. Phys.* **1954**, *22*, 759.

[5] H. Yoshio, K. Katsuhei, S. Shin, *Chem. Lett.* **1985**, *14*, 1695.

[6] H. Yoshio, K. Katsuhei, M. Akira, S. Shin, *Chem. Lett.* **1986**, *15*, 897.

[7] K. P. Kuhl, T. Hatsukade, E. R. Cave, D. N. Abram, J. Kibsgaard, T. F. Jaramillo, *J. Am. Chem. Soc.* **2014**, *136*, 14107.

[8] B. Kumar, M. Asadi, D. Pisasale, S. Sinha-Ray, B. A. Rosen, R. Haasch, J. Abiade, A. L. Yarin, A. Salehi-Khojin, *Nat. Commun. 2013 4:1* **2013**, *4*, 1.

[9] A. Vasileff, Y. Zheng, S. Z. Qiao, *Adv. Energy Mater.* **2017**, *7*, 1700759.

[10] X. Liu, L. Dai, *Nat. Rev. Mater.* **2016**, *1*, 1.

[11] H. Jiang, J. Gu, X. Zheng, M. Liu, X. Qiu, L. Wang, W. Li, Z. Chen, X. Ji, J. Li, *Energy Environ. Sci.* **2019**, *12*, 322.

[12] W. Zhou, J. Jia, J. Lu, L. Yang, D. Hou, G. Li, S. Chen, *Nano Energy* **2016**, *28*, 29.

[13] H. Wang, T. Maiyalagan, X. Wang, *ACS Catal.* **2012**, *2*, 781.

[14] K. Zhao, X. Quan, *ACS Catal.* **2021**, *11*, 2076.

[15] H. Wang, T. Maiyalagan, X. Wang, *ACS Catal.* **2012**, *2*, 781.

[16] J. Xie, X. Zhao, M. Wu, Q. Li, Y. Wang, J. Yao, *Angew. Chem.* **2018**, *130*, 9788.

[17] C. Jia, K. Dastafkan, W. Ren, W. Yang, C. Zhao, *Sustain. Energy Fuels* **2019**, *3*, 2890.

[18] J. Wu, R. M. Yadav, M. Liu, P. P. Sharma, C. S. Tiwary, L. Ma, X. Zou, X. D. Zhou, B. I. Yakobson, J. Lou, P. M. Ajayan, *ACS Nano* **2015**, *9*, 5364.

[19] G. P. Hao, W. C. Li, D. Qian, A. H. Lu, *Adv. Mater.* **2010**, *22*, 853.

[20] N. Sreekanth, M. A. Nazrulla, T. V. Vineesh, K. Sailaja, K. L. Phani, *Chem. Commun.* **2015**, *51*, 16061.

[21] J. Wu, M. Liu, P. P. Sharma, R. M. Yadav, L. Ma, Y. Yang, X. Zou, X. D. Zhou, R. Vajtai, B. I. Yakobson, J. Lou, P. M. Ajayan, *Nano Lett.* **2016**, *16*, 466.

[22] A. S. Varela, W. Ju, A. Bagger, P. Franco, J. Rossmeisl, P. Strasser, *ACS Catal.* **2019**, *9*, 7270.

[23] N. Kumar, K. S. Subrahmanyam, P. Chaturbedy, K. Raidongia, A. Govindaraj, K. P. S. S. Hembram, A. K. Mishra, U. v. Waghmare, C. N. R. Rao, *ChemSusChem* **2011**, *4*, 1662.

[24] K. Raidongia, A. Nag, K. P. S. S. Hembram, U. v. Waghmare, R. Datta, C. N. R. Rao, *Chem. Eur. J.* **2010**, *16*, 149.

[25] M. Chhetri, S. Maitra, H. Chakraborty, U. v. Waghmare, C. N. R. Rao, *Energy Environ. Sci.* **2016**, *9*, 95.

[26] Y. Liu, Y. Zhang, K. Cheng, X. Quan, X. Fan, Y. Su, S. Chen, H. Zhao, Y. Zhang, H. Yu, M. R. Hoffmann, *Angew. Chem. Int. Ed.* **2017**, *56*, 15607.

[27] F. Pan, B. Li, W. Deng, Z. Du, Y. Gang, G. Wang, Y. Li, *Appl. Catal. B. Environ.* **2019**, *252*, 240.

[28] H. Yang, Y. Wu, Q. Lin, L. Fan, X. Chai, Q. Zhang, J. Liu, C. He, Z. Lin, *Angew. Chem.* **2018**, *130*, 15702.

[29] C. Jia, W. Ren, X. Chen, W. Yang, C. Zhao, *ACS Sustain. Chem. Eng.* **2020**, *8*, 6003.

[30] H. Nozaki, S. Itoh, *J. Phys. Chem. Solids* **1996**, *57*, 41.

[31] S. Azevedo, J. R. Kaschny, *Solid State Commun.* **2013**, *168*, 11.

[32] N. Kumar, K. Moses, K. Pramoda, S. N. Shirodkar, A. K. Mishra, U. v. Waghmare, A. Sundaresan, C. N. R. Rao, *J. Mater. Chem. A* **2013**, *1*, 5806.

[33] Y. Lum, Y. Kwon, P. Lobaccaro, L. Chen, E. L. Clark, A. T. Bell, J. W. Ager, *ACS Catal.* **2016**, *6*, 202.

[34] X. Ma, J. Du, H. Sun, F. Ye, X. Wang, P. Xu, C. Hu, L. Zhang, D. Liu, *Appl. Catal. B. Environ.* **2021**, *298*, 120543.

[35] G. L. Chai, Z. X. Guo, *Chem. Sci.* **2016**, *7*, 1268.

[36] S. Liu, H. Yang, X. Huang, L. Liu, W. Cai, J. Gao, X. Li, T. Zhang, Y. Huang, B. Liu, S. Liu, L. Liu, T. Zhang, Y. Huang, H. Yang, X. Huang, W. Cai, J. Gao, X. B. Li Liu, *Adv. Funct. Mater.* **2018**, *28*, 1800499.

[37] P. P. Sharma, J. Wu, R. M. Yadav, M. Liu, C. J. Wright, C. S. Tiwary, B. I. Yakobson, J. Lou, P. M. Ajayan, X.-D. Zhou, *Angew. Chem.* **2015**, *127*, 13905.

[38] S. Ni, Z. Li, J. Yang, *Nanoscale* **2012**, *4*, 1184.

[39] H. bin Yang, S. F. Hung, S. Liu, K. Yuan, S. Miao, L. Zhang, X. Huang, H. Y. Wang, W. Cai, R. Chen, J. Gao, X. Yang, W. Chen, Y. Huang, H. M. Chen, C. M. Li, T. Zhang, B. Liu, *Nat. Energy* **2018**, *3*, 140.

[40] R. Daiyan, X. Lu, Y. H. Ng, R. Amal, *ChemistrySelect* **2017**, *2*, 879.

[41] W. Zhu, R. Michalsky, Ö. Metin, H. Lv, S. Guo, C. J. Wright, X. Sun, A. A. Peterson, S. Sun, *J. Am. Chem. Soc.* **2013**, *135*, 16833.

[42] F. Y. Gao, S. J. Hu, X. L. Zhang, Y. R. Zheng, H. J. Wang, Z. Z. Niu, P. P. Yang, R. C. Bao, T. Ma, Z. Dang, Y. Guan, X. S. Zheng, X. Zheng, J. F. Zhu, M. R. Gao, S. H. Yu, *Angew. Chem. Int. Ed.* **2020**, *59*, 8706.

[43] M. Asadi, B. Kumar, A. Behranginia, B. A. Rosen, A. Baskin, N. Repnin, D. Pisasale, P. Phillips, W. Zhu, R. Haasch, R. F. Klie, P. Král, J. Abiade, A. Salehi-Khojin, *Nat. Commun.* **2014**, *5*.

Chapter 4

Covalently Bonded MoS_2−Borocarbonitride Nanocomposites and Their Remarkable HER Activity

Summary

In the light of the recent discovery that carbon-rich borocarbonitrides show electrocatalytic activity for generating hydrogen from

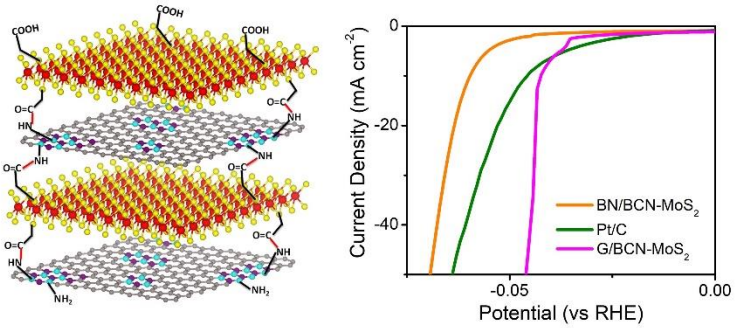

water, we have synthesized nanocomposites by covalently crosslinking BC_7N with MoS_2 sheets to explore their HER activity. In order to cross-link BC_7N and MoS_2 sheets, we have exploited the presence of different functional groups on the surface of borocarbonitride. These nanocomposites were characterized by various spectroscopic methods including fluorescence labelling and their electrochemical and photochemical HER activities were investigated. The composite where the graphene domains are cross-linked to MoS_2 nanosheets, G/BCN−MoS_2 (1:2), exhibits outstanding electrochemical HER activity with an onset potential of −30 mV (vs RHE) and a current density of 10 mA cm^{-2} at an overpotential of −35 mV. The composites also exhibit good photochemical activity. It is noteworthy that 2H-MoS_2, which does not exhibit significant catalytic activity, can be rendered highly active by cross-linking with BCN.

Paper based on this work has appeared in *J. Phys. Chem. C* **2018**, 122, 25.

4.1 Introduction

Generation of hydrogen by photochemical or electrochemical means is of great importance towards sustainable energy production. To date, no catalyst has shown better hydrogen evolution reaction (HER) performance than platinum which however suffers from issues related to stability and high cost.[1,2] In the past few years there has been an effort to replace platinum by inexpensive earth abundant materials, preferably those that are metal-free.[3,4] Some non-metallic materials such as C_3N_4,[5,6] MoS_2,[7,8] and reduced graphene oxide[9] have been used for the purpose. Among the various non-metallic materials, borocarbonitrides, $B_xC_yN_z$, deserve a special mention in the light of the recent discovery that carbon-rich borocarbonitride compositions, compare reasonably with platinum in electrochemical performance.[10] We considered it important to further investigate and possibly improve the performance of borocarbonitrides by covalently linking them with MoS_2, since both these component materials are intrinsically HER active.[9,10] What is of special interest is that BCN layers contain both graphene and boron nitride (BN) type domains possibly along with the BCN rings.[11,12] These domains contains different surface functional groups, BN domains contain amino groups while that of graphene domains contain carboxyl and other oxygen functionalities.[11]

4.2 Scope of present investigation

Making use of these different surface functionalities in the BN and graphene domains, we have cross-linked the borocarbonitride, BC_7N, with MoS_2 with specific bonding between MoS_2 and the graphene domains or with the BN domains. Carbodiimide reagents have been widely utilized for peptide synthesis due to their moderate activity.[13,14] A common reagent for the same is N-(3-

Dimethylaminopropyl)-N'-ethylcarbonate (EDC) which is used with Hydroxybenzotriazole (HOBt) as an additive. EDC in addition with HOBt activates the carboxylic acid by forming activated esters which reacts with amines to forms amide bonds with water soluble side products. We have therefore used EDC, HOBt reagent for the coupling of BC_7N and MoS_2.

Electrochemical and photochemical HER activity of these composites was studied in comparison with that of the physical mixture as well as with the individual components. Interestingly, we have found outstanding improvement in the electrochemical HER activity comparable to that of Pt in the case of the covalently cross-linked BC_7N−MoS_2 (1:2) composites where the graphene domains of BC_7N were bonded to MoS_2. It is noteworthy that the composite with high electrochemical HER activity exhibits good photochemical HER activity as well. We did not observe any meaningful HER activity with physical mixture of MoS_2 and BC_7N.

4.3 Experimental

4.3.1 Materials and Synthesis

BC_7N nanosheets were prepared by the method as reported earlier.[10,12] Boric acid (60 mg, Merck, 99.5%), activated charcoal (500 mg, SDFCL), and urea (2.4 g, SDFCL, 99%) were heated in a tubular furnace at 900 °C under a N_2 atmosphere for 10 h. The obtained black product was treated with NH_3 at 900 °C for 5 h.

Exfoliated MoS_2 (1T-MoS_2) was obtained by the Li-intercalation of bulk MoS_2(Merck, 98%) (Li_xMoS_2) with n-butyllithium reagent (Merck, 2.5 M hexane) and subsequent exfoliation using deionized water as reported elsewhere.[15] Carboxylate functionalization of MoS_2 (MoS_2−CH_2COOH) was achieved by reacting exfoliated 1T-MoS_2 solution with 10- fold excess of 2-bromoacetic acid (Merck, 99%) and allowed

to stir for 5 days at room temperature.[16] The precipitated sample was washed with water and 2-propanol to remove unreacted acid, and dried at 60 °C under vacuum. Amine functionalized MoS_2 (MoS_2− $C_6H_4NH_2$) was obtained by reacting 1T-MoS_2 with a solution of iodobenzene reagent (12 equivalent) (Merck, 98%) dissolved in N,N′-dimethylformamide (DMF; 60 mL), and the resulting mixture was allowed to stir at room temperature for 72 h.[17] The black precipitate obtained was separated by centrifugation and then washed with DMF and ethanol to remove unreacted reagents, organic by products.

4.3.2 Covalent Crosslinking

BN/BCN−MoS_2 composites were prepared by mixing BC_7N (50 mg) and MoS_2−CH_2COOH (50 mg) samples in dry DMF (5 mL) in a Schlenck flask through bath sonication. To the resultant dispersion, coupling reagents N-(3-dimethylaminopropyl) N′-ethylcarbodiimidehydrochloride (EDC.HCl, 20 mg) (Merck, 200) and 1-hydroxybenzotriazole (HOBt, 20 mg) (Merck, 98%) were added under a N_2 atmosphere and allowed to stir for 48 h. The obtained product was collected by vacuum filtration and washed several times with copious amounts of DMF and water to remove by products. For the synthesis of G/BCN− MoS_2 nanocomposites, BC_7N (50 mg) and MoS_2−$C_6H_4NH_2$ (50 mg) samples were dispersed in DMF, and the procedure was repeated. For the preparation of the physical mixture of BCN and MoS_2, BCN (50 mg) and MoS_2 (50 mg) were dispersed in aqueous solution and then filtered to get a solid product.

4.3.3 Calculation of surface functional groups

Surface concentrations of functional groups were determined by chemical tagging and photoluminescence spectroscopy. Tagging of amine groups using NHS-

Cy5 (Merck) was carried out as follows. To a 2 mg sample under study, 10 µL of 1.42 mM of NHS-Cy5 dye solution, 100 µL of triethylamine (TEA), and 6 mL of DMSO were added, and the resulting solution was stirred in the dark at room temperature for 12 h.[11] After the reaction, the obtained solutions were centrifuged, and supernatant was transferred to a flask. Fluorescence tagging of the carboxyl group using 1-bromoacetyl pyrene was carried out as follows. To a 2 mg sample, 2 mL of 1.7 mM solution of 1- (bromoacetyl)pyrene (Merck, 97%) in DMF, 1.0 mg of K_2CO_3 and 1.0 mg of KI were added. The resulting solution was stirred in dark at 50 °C for 12 h and the aforementioned procedure was repeated. The remaining sample after collection of supernatant was washed several times with DMSO/DMF to remove any physisorbed dye molecules and the washings were collected in the same flask and diluted to a known volume to record the PL. A control experiment was carried out without the sample under the same conditions. Physisorption experiments were carried out without the reagent.

4.3.4 Electrochemical and photochemical HER

The electrocatalytic hydrogen evolution activity of cross-linked composites and Pt/C (40 wt%, Sigma Aldrich) was studied by linear sweep voltammetry (LSV) technique. The measurements were done on CHI760E electrochemical workstation with conventional three electrode system –glassy carbon electrode (GCE, 3 mm in diameter) as working electrode, Ag/AgCl (Saturated KCl) as the reference electrode and a platinum coil as the counter electrode. Prior to use, the working electrode was polished sequentially with 1.0, 0.3 and 0.05 µm alumina powder until mirror shiny surface was obtained. Working electrode was prepared by drop casting 5 µL catalyst ink, prepared by dispersing 3 mg of catalyst in 300 µL of nafion solution (nafion: isopropanol: water 0.05: 1: 4 (v/v/v)), on GCE and allowed to dry in ambient conditions.

LSV measurements were done in 0.5 M H_2SO_4 (aq. solution) saturated with UHP N_2 at scan rate of 5 mV/s. The electrochemical surface area (ECSA) of catalyst was estimated using CV method as described below. We estimated the double layer capacitance (C_{dl}) using a simple CV method in non-faradaic potential region. The value of C_{dl} is linearly proportional to the electrochemically active surface area (ECSA) of the electrode. A potential range of 0.4-0.8 V (vs Ag/AgCl, sat. KCl) was selected for the capacitance measurements because in this potential window no faradic process corresponding to HER occurs and the electrode can be expected to behave as an ideally polarizable electrode (IPE). The plot of Δi (i_{anode} - $i_{cathode}$) vs scan rate will be a straight-line having slope twice the value of C_{dl}.

Electrochemical Impedance Spectroscopy (EIS) was done at the voltage corresponding to the onset potential of hydrogen evolution reaction (HER). The potential reported in this study are with respect to reversible hydrogen electrode (RHE) in accordance with the brevity of comparison with studies of HER by other catalysts. For this the potential with respect to Ag/AgCl was converted to RHE based on following equation,

$$E(RHE) = E^{o} (Ag/AgCl, sat\ KCl) + E_{expt.} (Ag/AgCl) + 0.059*pH.$$

where E^{o} is the standard reduction potential of Ag/AgCl.

For photochemical HER, catalyst (3 mg) was dispersed in aqueous solution of triethanolamine (15% v/v, 48 mL) by sonication in a glass vessel and Eosin Y dye (14 μmol) was added. This mixture was illuminated with halogen lamp (100 W) under constant stirring. A 2 mL of evolved gas was manually collected from the headspace and analysed with gas chromatograph (PerkinElmer ARNL 580C) using a thermal conductivity detector.

4.3.5 Physical Characterization

Infrared (IR) spectra were recorded using Bruker ATR-FTIR spectrometer. Morphological analysis has been performed using Nova Nano SEM 600, FEI Company while TEM imaging has been carried out with FEI TITAN3TM with an accelerating voltage of 80 kV. Raman spectra were recorded using a HORIBA LabRam HR800 at several different spots. The N_2 isotherms of covalently cross-linked composites obtained from Quantachrome Quadrasorb analyser instrument. X-ray photoelectron spectroscopy measurements were done with an Omicron spectrometer, using monochromatic Mg-K_α as X-ray source.

4.4 Results and discussion

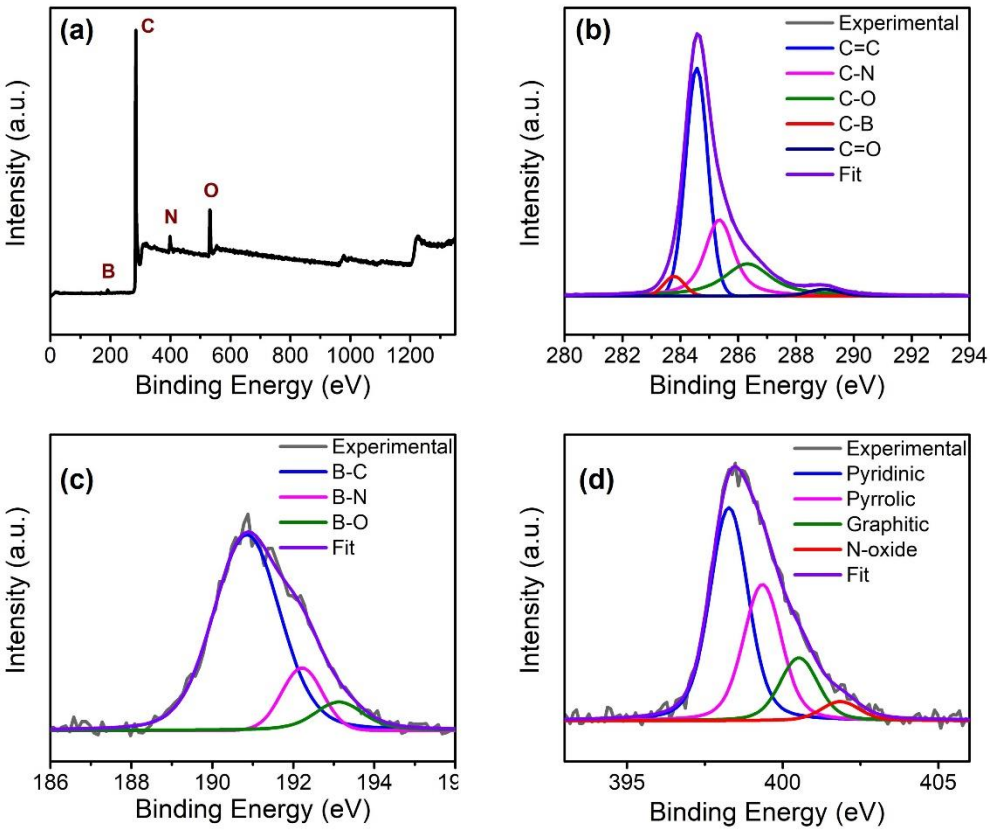

Figure 1. (a) X-ray photoelectron spectrum of BC7N, (b) to (d) showing the core level spectrum of C, N and B respectively.

Borocarbonitride of the composition BC_7N was synthesized and the nature of bonding was analysed by X-ray photoelectron spectroscopy (XPS). The B-1s signal can be deconvoluted into three peaks centred at 190.8, 192.3 and 194.0 eV attributed to B-C, B-N and B-O bonds, respectively (**Figure 1**). The C-1s signal consists of five peaks centred at 283.8, 284.6, 285.3, 286.3 and 288.9 eV which corresponds to C-B, sp^2 carbon, C-N, C-O and C=O bonds, respectively (**Figure 1b**). B1s core level spectra consist of three peaks at 190.8, 192.2, and 193.1 eV corresponding to B-C, B-N and B-

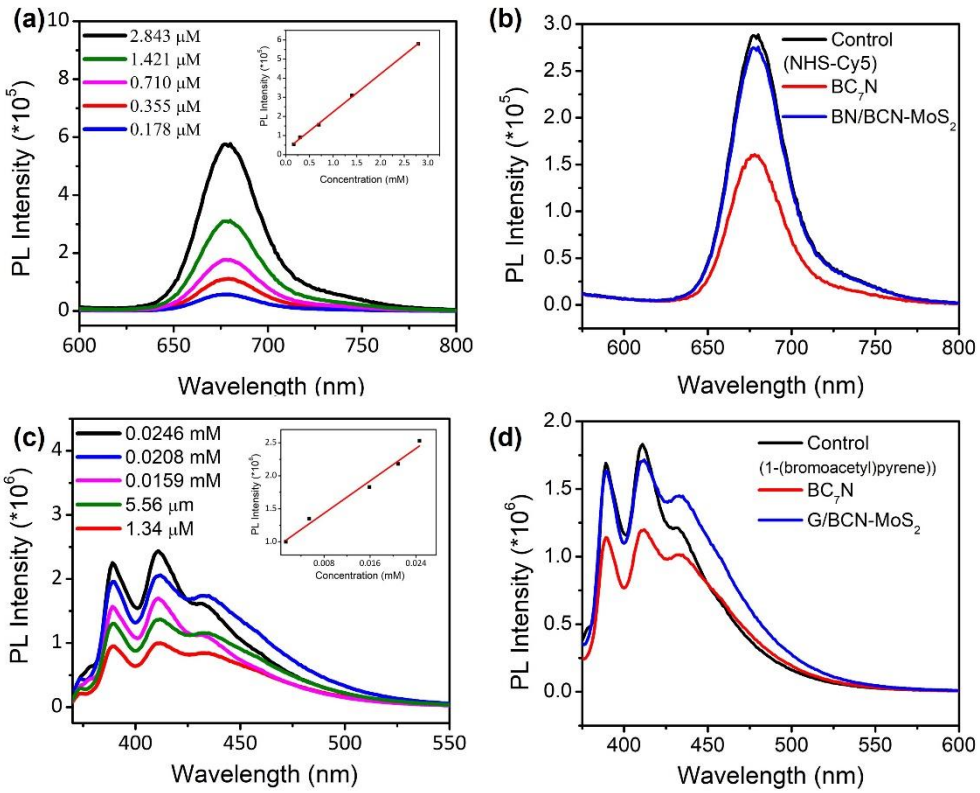

Figure 2. (a) Emission spectra of NHS-Cy5 of different concentrations (excitation wavelength 530 nm). Inset shows the calibration curve of fluorescent intensity as a function of concentration at 680 nm. (b) Emission spectra of NHS-CY5 dye after reaction with amine groups of BCN and BN/BCN-MoS_2 composite. (c) Emission spectra of 1-(bromoacetyl) pyrene of different concentrations (excitation wavelength 320 nm). Inset shows the calibration curve of fluorescent intensity as a function of concentration at 410 nm (monomeric emission). (d) Emission spectra of 1-(bromoacetyl) pyrene dye after reaction with carboxyl groups of BCN and G/BCN-MoS_2 composite.

O species, respectively (**Figure 1c**). The deconvolution of N-1s signal suggests the existence of three different kinds of N species, pyridinic (398.3 eV), pyrrolic (399.3 eV) and graphitic (400.5 eV) (**Figure 1d**). Thus, the XPS studies reveal the existence of B–C, B–N, C–N and C–C bonds in BC_7N, indicating the presence of graphene and boron nitride (BN) domains.

Quantitative estimation of the surface functionalities of BC_7N was done by the fluorescence labelling of surface species (FLOSS), employing NHS-Cy5 and 1-(bromoacetyl) pyrene dye as probes for amine and carboxyl functionalities in the BN and graphene domains, respectively.[11] The number of amine and carboxyl groups present on the BC_7N surface were estimated using calibration graph as shown in **Figure 2a and 2c**, respectively. The calibration curve of 1-(bromoacetyl) pyrene is obtained from the emission spectra by monitoring the intensity at 410 nm and plotting the intensity as a function of concentration as shown in the inset of **Figure 2c**. Quantitative estimation of surface functional groups for material under study was done by reaction with dye molecules and subsequent PL analysis of supernatant (For details refer to experimental section 4.3.3). The BC_7N sample showed surface concentrations of the amino and carboxylic groups to be 1.7×10^{19} and 8×10^{20} groups/g, respectively. On cross-linking of BC_7N with MoS_2, surface concentrations of amine and carboxylic groups of BC_7N reduced to 1.15×10^9 and 4.3×10^{12} groups/g respectively, indicating decreased number of functional groups in nanocomposites.

Scheme 1 shows the schematic of the synthetic strategy to prepare cross-linked BN/BCN−MoS_2 and G/BCN−MoS_2 nanocomposites by the carbodiimide reaction. BCN−MoS_2 composites where BN domains are cross-linked to MoS_2 sheets are named BN/BCN−MoS_2 and composites where graphene domains are cross-linked with MoS_2 sheets are named G/BCN−MoS_2. BCN was reacted with carboxyl functionalized MoS_2

(MoS_2− CH_2COOH), to prepare BN/BCN−MoS_2 while coupling of the amine functionalized MoS_2 (MoS_2− $C_6H_4NH_2$) with BCN yields G/BCN−MoS_2 nanocomposites.

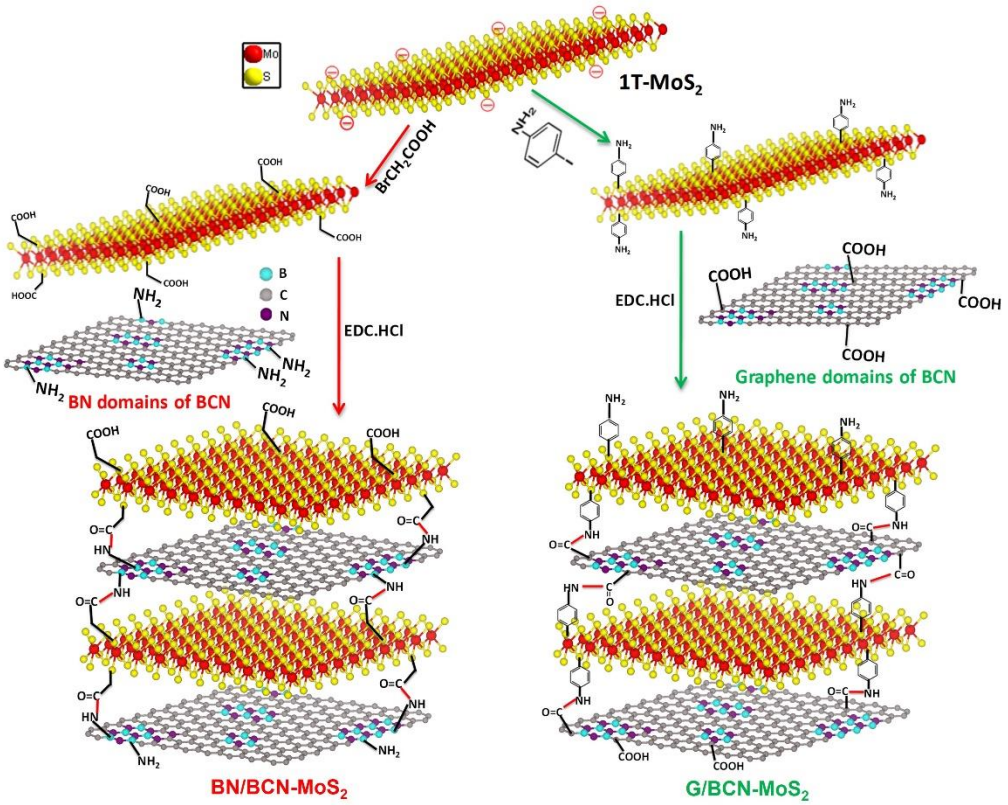

Scheme 1. Synthetic Strategy for covalently cross-Linked BN/BCN−MoS_2 and G/BCN−MoS_2 nanocomposites (EDC = 1- Ethyl-3-(3 dimethylaminopropyl) carbodiimide).

Transmission electron microscopy analysis of BCN and MoS_2 show only thin layer characteristics (**Figure 3**) while the HRTEM image of the G/BCN-MoS_2 (1:2) shows interlayer spacings (002 peaks) correspond to both BCN (0.40 nm) and MoS_2 (0.65 nm) layers, suggesting successful assembly between the heterolayers (**Figure 3**). Such layer-by-layer arrangement is facilitated by the formation of the amide bond between the amine groups of BCN and the carboxyl groups on MoS_2 and vice versa. Elemental mapping of BN/BCN−MoS_2 and G/BCN−MoS_2 nanocomposites display uniform distribution of Mo, S, B, C, and N, confirming the homogeneous nature of the nanoassemblies (**Figure 4**).

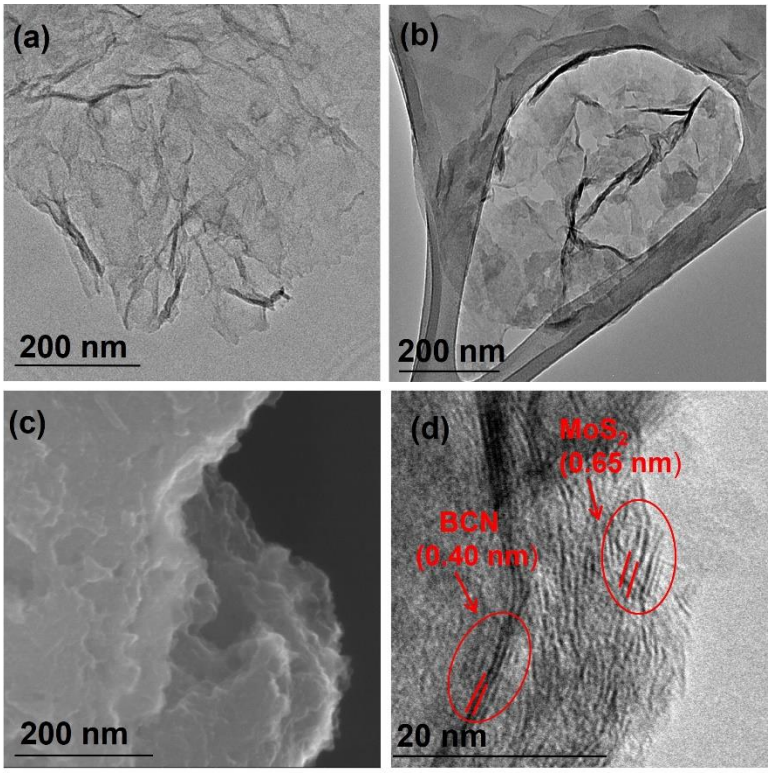

Figure 3. TEM images of (a) BCN and (b) MoS_2, (c) FESEM and (d) HRTEM image of G/BCN-MoS_2 nanocomposites.

Raman spectra of BN/BCN−MoS_2 and G/BCN−MoS_2 (1:2) nanocomposites show characteristic D and G bands of BCN at 1354 and 1596 cm^{-1}, respectively,15 along with the E^1_{2g} and A_{1g} bands due to the trigonal (2H) polytype MoS_2 at 376 and 405 cm^{-1} , respectively (**Figure 5a**).[18] Furthermore, the out of plane A_{1g} mode of BN/BCN−MoS_2 and G/BCN−MoS_2 (1:2) nanocomposite is red-shifted compared to 2H-MoS_2 probably due to the intercalation of BCN between MoS_2 nanosheets as a result of cross-linking.[19] The infrared spectrum of BCN exhibits a band at 1580 cm^{-1} due to the C=C stretching mode along with a broad band in the 2900−3100 cm^{-1} region corresponding to the residual amine groups (**Figure 5b**). MoS_2−CH_2COOH exhibits bands at 1735 and 3156 cm^{-1} assigned to −C=O and −OH stretching modes of carboxylic groups along with a C−S stretching band at 700 cm^{-1} arising from covalent functionalization. The BN/BCN−MoS_2 nanocomposite shows a carbonyl stretching

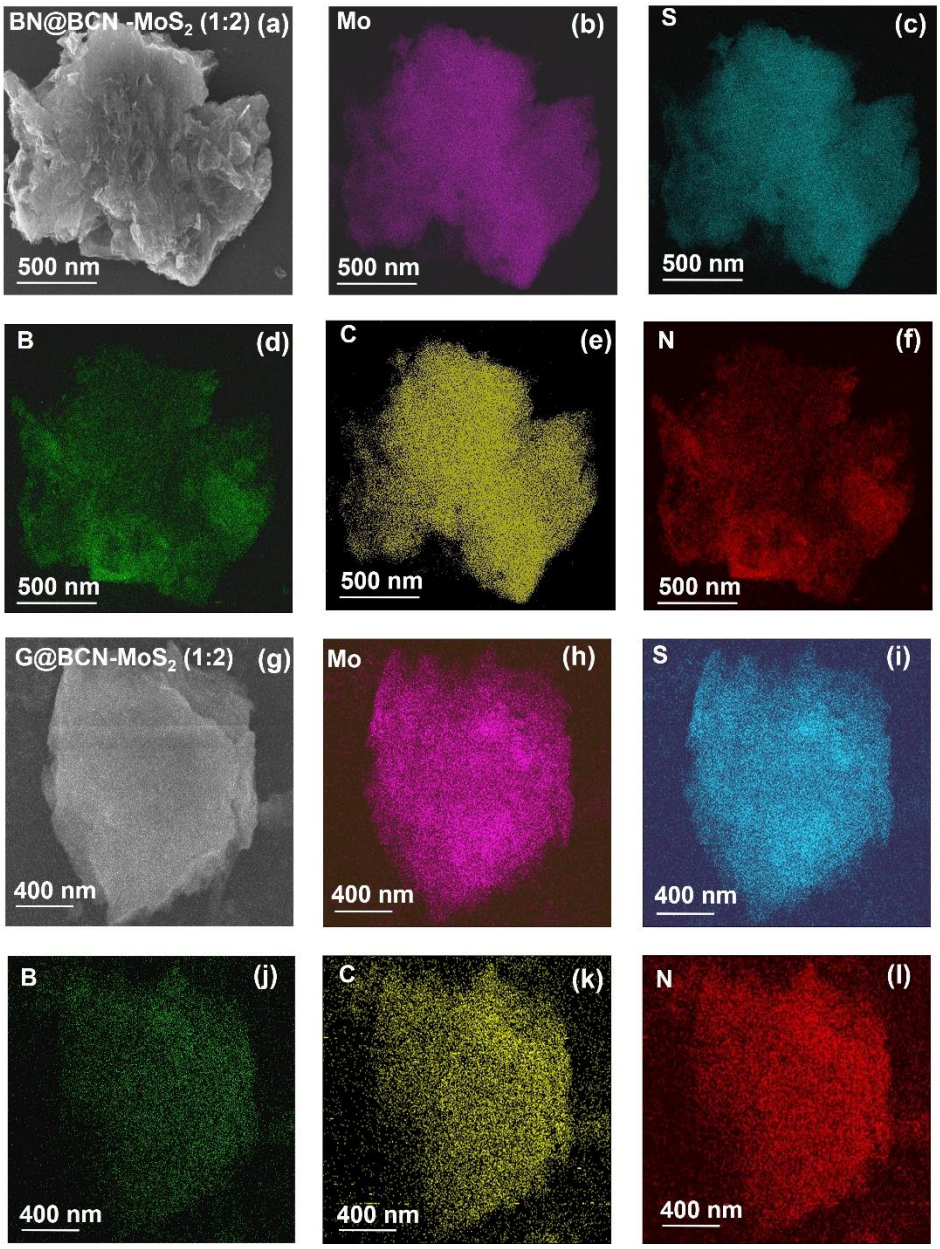

Figure 4. SEM images and elemental mapping of (a-f) BN/BCN-MoS_2 and (g-l) of G/BCN-MoS_2. (Mo- magenta; S- cyan; B- green; C- yellow; N- red)

band at ~1690 cm^{-1}, confirming crosslinking of the BCN and MoS_2 layers by the amide bond (**Figure 5b**). Similarly, G/BCN−MoS_2 exhibits a C=O stretching band at 1672 cm^{-1} due to the amide bond between the carboxyl groups of graphene domains and amine functionalized MoS_2 (MoS_2−$C_6H_4NH_2$) layers along with other characteristic vibration frequencies from amino benzene.

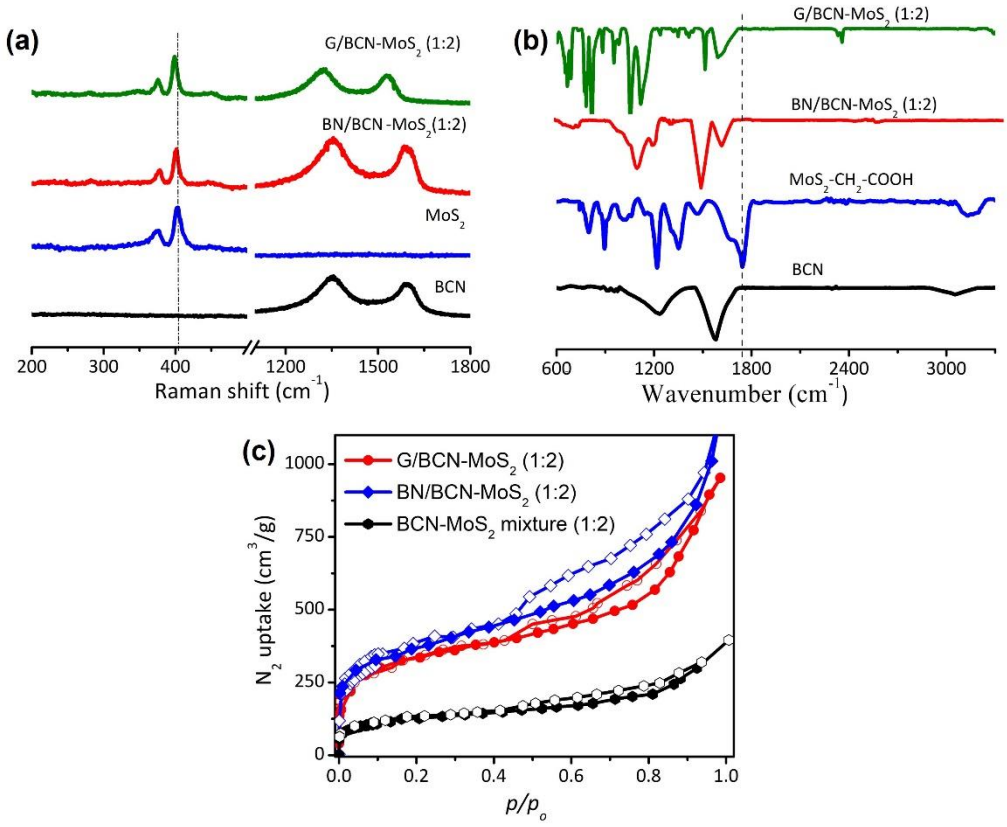

Figure 5. (a) Raman spectra and (b) IR spectra of G/BCN-MoS_2 and BN/BCN-MoS_2 nanocomposites in comparison with MoS_2 and BCN. (c) N_2 adsorption-desorption isotherms of G/BCN-MoS2 and BN/BCN-MoS_2 in comparison with physical mixture of MoS_2-BCN.

Surface area and porosity of nanocomposites obtained from N_2 adsorption−desorption isotherms at 77 K show microporous type-I features (low pressure) along with a type-H4 hysteresis loop associated with narrow slit-like pores (high pressure; **Figure 5c**).[20,21] Slit-shaped pores are formed due to cross-linking and stacking of BCN and MoS_2 layers. The Brunauer−Emmet−Teller (BET) surface area of BN/BCN−MoS_2 and G/BCN−MoS_2 (1:2) nanocomposites are 540 and 512 m^2 /g, respectively, while the physical mixture of the same overall composition shows a lower surface area of 208 m^2 /g due to non-porous nature.

Electrocatalytic HER activity of cross-linked BN/BCN−MoS_2 and G/BCN−MoS_2 nanocomposites was investigated in N_2 saturated 0.5 M H_2SO_4 solution

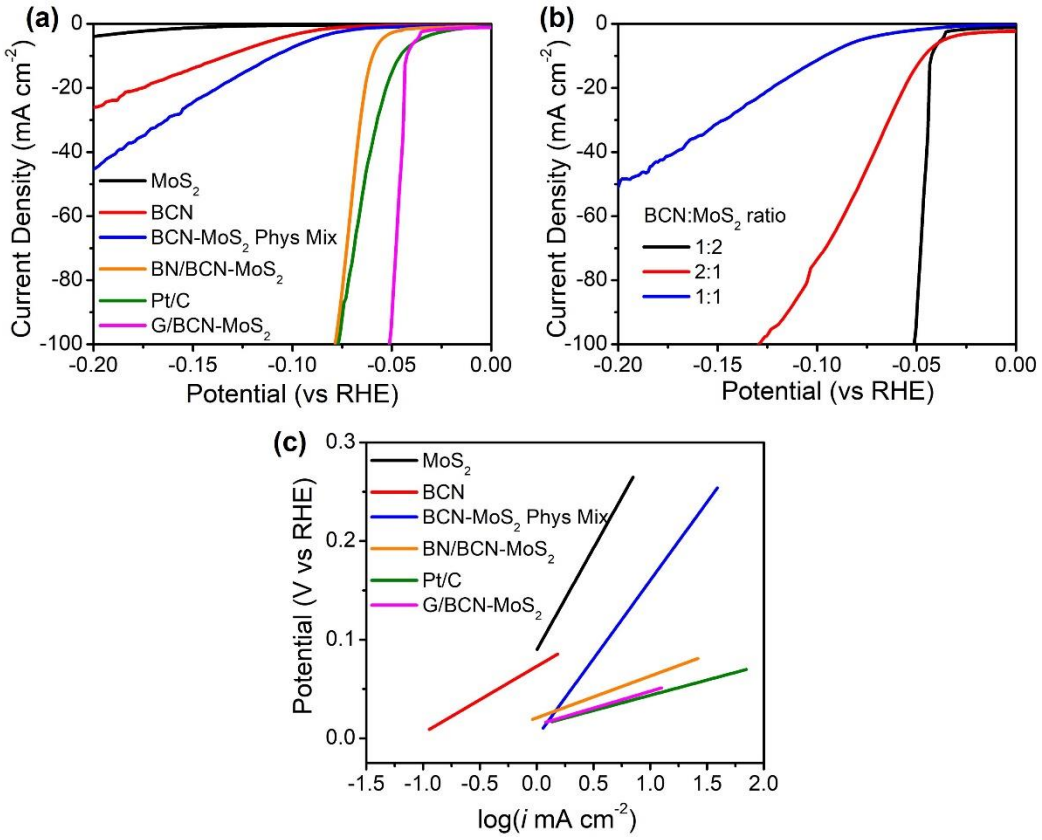

Figure 6. Electrocatalytic HER performance comparison in 0.5 M H_2SO_4. (a, b) Linear sweep voltammogram polarization curves and (c) Tafel plots of MoS_2, BCN, BCN–MoS_2 (1:2, mixture), BN/BCN–-MoS_2 (1:2, composite), G/BCN–MoS_2 (1:2, composite) and Pt/C (40 wt %). Catalyst ink (Milli-Q water: Isopropanol:5wt% nafion = 800µL:200 µL:60 µL). was dropcoated on glassy carbon electrode (0.7 mg/cm^2). Ag/AgCl (1M) and graphite rod were used as reference and counter electrode, respectively.

using a conventional three electrode cell. Polarization curves of cross-linked assemblies along with that of physical mixture of BCN and MoS_2 are presented in **Figure 6a**. It can be seen in Figure 6a that relatively lower onset potential value is obtained for the crosslinked BN/BCN−MoS_2 and G/BCN−MoS_2 catalysts compared to the physical mixture, suggesting better catalytic nature of the former. BCN and MoS_2 display onset potential (η) values of −0.08 and −0.18 V, respectively. The physical mixture of BCN and MoS_2 shows a 17mV improvement in η (−0.063 V) compared to BCN (−0.08 V),

whereas the covalently cross-linked nanocomposites show 30 and 45 mV anodic shifts in the onset potential (−0.05 and −0.035 V) for BN/BCN−MoS_2 (1:2) and G/BCN−MoS_2 (1:2), respectively.

Table 1. Electrochemical HER performance comparison of BN/BCN-MoS_2, G/BCN-MoS_2 nanocomposites and Pt/C.

Sample	**Onset (V) *vs.* RHE**	**η@10 $mAcm^{-2}$ (V) vs. RHE**	**Tafel slope (mV/dec)**
MoS_2	-0.18	-0.26	99
BCN	-0.08	-0.13	67
BN@BCN-MoS_2 (2:1, Composite)	-0.06	-0.09	58
BN@BCN-MoS_2 (1:1, Composite)	-0.05	-0.06	46
BN@BCN-MoS_2 (1:2, Composite)	-0.05	-0.06	38
G@BCN-MoS_2 (1:2, Composite)	-0.03	-0.035	34
BCN-MoS_2 (1:2, Mixture)	-0.06	-0.11	73
Pt/C (40 wt%)	-0.02	-0.04	30

To further investigate the optimum ratio BCN and MoS_2 in nanocomposites, we compared activity of cross-linked assemblies with varying BCN and MoS_2 ratios of (2:1), (1:1), and (1:2), it is interesting that the catalytic activity increases with MoS_2 content probably due to increase in number of active sites (**Figure 6b**). Cross-linked 1:1 and 1:2 BN/BCN−MoS_2 exhibit the lowest overpotential of about −0.06 V at 10

mA cm^{-2} (η_{10}) with the cathodic current density rising swiftly under more negative potential signifying the superior HER activity. To gain further insight into the kinetics of HER on the BCN−MoS_2 catalysts, Tafel slopes were explored. The Tafel slope values obtained from the Butler−Volmer equation for various catalysts are 67, 38, 34, and 30 mV dec−1 for BCN, BN/BCN−MoS_2 (1:2), G/BCN−MoS_2 (1:2), and Pt/C, respectively, while a physical mixture of BCN−MoS_2 (1:2) shows 73 mV dec^{-1}. A

Table 2. Comparison of electrochemical HER performance of BN/BCN-MoS_2 and G/BCN-MoS_2 nanocomposites with other carbon-based materials.

Catalyst	**Onset (mV) vs RHE**	**η@10 mA cm^{-2} (mV) vs RHE**	**Tafel slope (mV dec^{-1})**
G/BCN-MoS_2 (1:2)	-30±2	-35±2	33
BN/BCN-MoS_2 (1:2)	-50±3	-60±3	36
RGO-supported MoS_2[22]	-105	-150	41
MoS_2-RGO[23]	-75	-104	63
MoS_2 quantum dots-RGO[24]	-100	-150	101
MoS_2-amorphous carbon[25]	-80	-85	40
Nanostructured MoS_2-carbon cloth[26]	-100	-165	50
MoS_2-N-doped graphene aerogel[27]	-236	-261[a]	230
MoS_2-carbon aerogel[28]	-140	-190	59
MoS_2-C_3N_4[15]	-236	-320	95

[a]η@20 $mAcm^{-2}$

summary of the onset potential, overpotential of 10 mA cm^{-2} (η_{10}) and Tafel slopes of all catalysts is given in **Table 1**. The Tafel slope value of cross-linked BN/BCN−MoS_2 and G/BCN−MoS_2 (1:2) (38 and 34 mV dec^{-1}) catalysts are close to Pt/C (30 mV dec^{-1}), which suggests the efficacy of covalently bonded layers in fast electron transport to the active sites, exhibiting Volmer−Tafel mechanism. In **Table 2**, we have given a comparison of the HER activity of cross-linked assemblies with some of the MoS_2-metal free carbon-based materials reported in the literature.

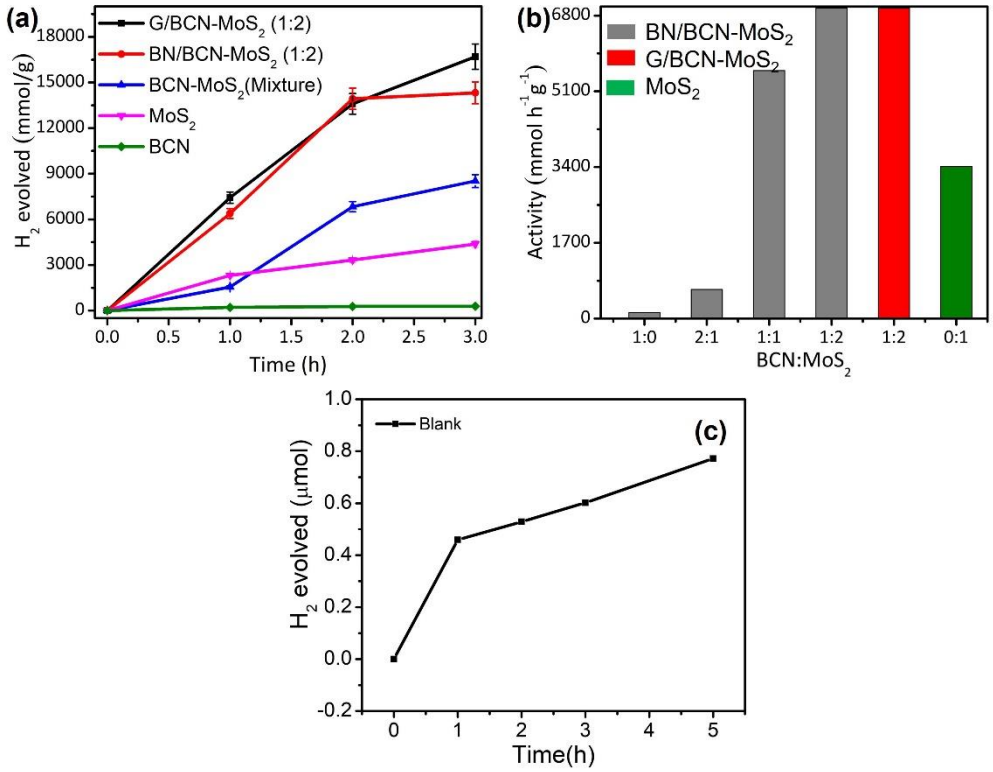

Figure 7. (a) Comparison of the photochemical HER activity of BCN, MoS_2, BCN–MoS_2 (1:2, mixture), BN/BCN–MoS_2 (1:2), and G/BCN–MoS_2; (b) Bar diagram showing the comparison of the HER activity of BN/BCN–MoS_2 with the increase in MoS_2 content along with the G/BCN–MoS_2 (1:2) composite. (c) blank experiment showing very low amount of hydrogen evolution in the absence of catalyst. For HER experiments, catalyst (3 mg) was dispersed in aqueous solution of triethanolamine (15% v/v, 48 mL) and Eosin Y dye (14 μmol). This mixture was illuminated with halogen lamp (100 W) under constant stirring.

Encouraged by the superior electrochemical HER activity of cross-linked BCN-MoS_2 nanocomposites, we have examined their performance for photochemical HER. The hydrogen evolution experiments were carried in aqueous solution of triethanolamine (TEOA, 15% (v/v)) under visible light in the presence of Eosin Y dye as a photosensitizer. Eosin Y (EY) on photoexcitation undergoes series of changes to form a highly reductive species, EY^-, which subsequently transfer electrons to the catalyst for hydrogen evolution.[9,29–31] In **Figure 7a**, we present the yield of H_2 evolved by using cross-linked BN/ BCN−MoS_2 and G/BCN−MoS_2 (1:2) and respective physical mixture as well as by using BCN and MoS_2 alone. As can be seen in Figure 7a, BCN exhibits low activity of 136 μmol h^{-1} g^{-1}, while few-layer MoS_2 has an activity of 1663 μmol h^{-1} g^{-1}, which suggests latter would be the preferred sites for HER in composites. In the case of a physical mixture of BCN and MoS_2, improvement in photochemical HER activity with respect to MoS_2 is ∼2 times, whereas the cross-linked BN/BCN− MoS_2 (1:2) and G/BCN−MoS_2 (1:2) composites show an increase by ∼5 times (**Figure 7a**). This result clearly suggests that cross-linked BCN and MoS_2 layers provides greater interaction between the two, thereby showing higher HER activity compared to the physical mixture where layers are randomly oriented. In **Figure 7b**, we present the yield of H_2 evolved by using different BN/BCN−MoS_2 (1:1, 1:2, and 2:1) assemblies. The catalytic activities of 1:1 and 1:2 BN/BCN−MoS_2 assemblies are much higher compared to few-layer MoS_2 with the 1:2 nanocomposite demonstrating the highest activity of 6965 μmol h^{-1} g^{-1}. The 2:1 BN/BCN-MoS_2 nanocomposite with more BCN content shows lower activity of 656 μmol h^{-1} g^{-1} (**Figure 7b**). A similar trend in HER activity was encountered in electrochemical studies as well. Cycling studies on BN/BCN−MoS_2 and G/BCN−MoS_2 showed stable H_2 evolution over long

periods. In **Table 3**, we compare the photochemical HER activity of cross-linked BCN−MoS_2 assemblies with that of carbon-based MoS_2 composites.

Table 3. Comparison of photochemical HER performance of BN/BCN-MoS_2 and G/BCN-MoS_2 nanocomposites with other MoS_2-carbon-based materials.

Catalyst	**Reaction Conditions**	**Activity (μmol g^{-1} h^{-1})**
BN/BCN-MoS_2 (1:2)	100 W halogen; Eosin Y-TEOA (15 v/v)	6965±348
G/BCN-MoS_2 (1:2)	100 W halogen; Eosin Y-TEOA (15 v/v)	6977±350
MoS_2-RGO[24]	300 W Xe; Eosin Y-TEOA (15 v/v)	2000
MoS_2-NRGO[9]	100 W halogen; Eosin Y-TEOA (15 v/v)	10800
MoS_2-C_3N_4[15]	400 W Xe; Eosin Y-TEOA (15 v/v)	12778

The improved HER activity in crosslinked catalysts can be understood in terms of enhanced surface area and more exposed active sites. Although BET measurements give a qualitative comparison of the geometrical surface areas (**Figure 4c**), for HER activity it is better to compare electrochemically active surface area (ECSA). Since for carbon-based materials, ECSA is directly proportional to double layer capacitance, we estimated ECSA of cross-linked catalysts by the double layer capacitance (C_{dl}) method and compared them with the physical mixture. (**Figure 8**).[10] The estimated ECSA for BN/BCN−MoS_2 (1:2), G/BCN−MoS_2 (1:2), and respective physical mixture were 0.012, 0.014, and 0.004 mF cm^{-2}, respectively, suggesting higher ECSA in crosslinked catalysts. Electrochemical impedance spectroscopy (EIS) was also used to investigate the electrochemical behaviour of composite and physical mixture (**Figure 9**). The two

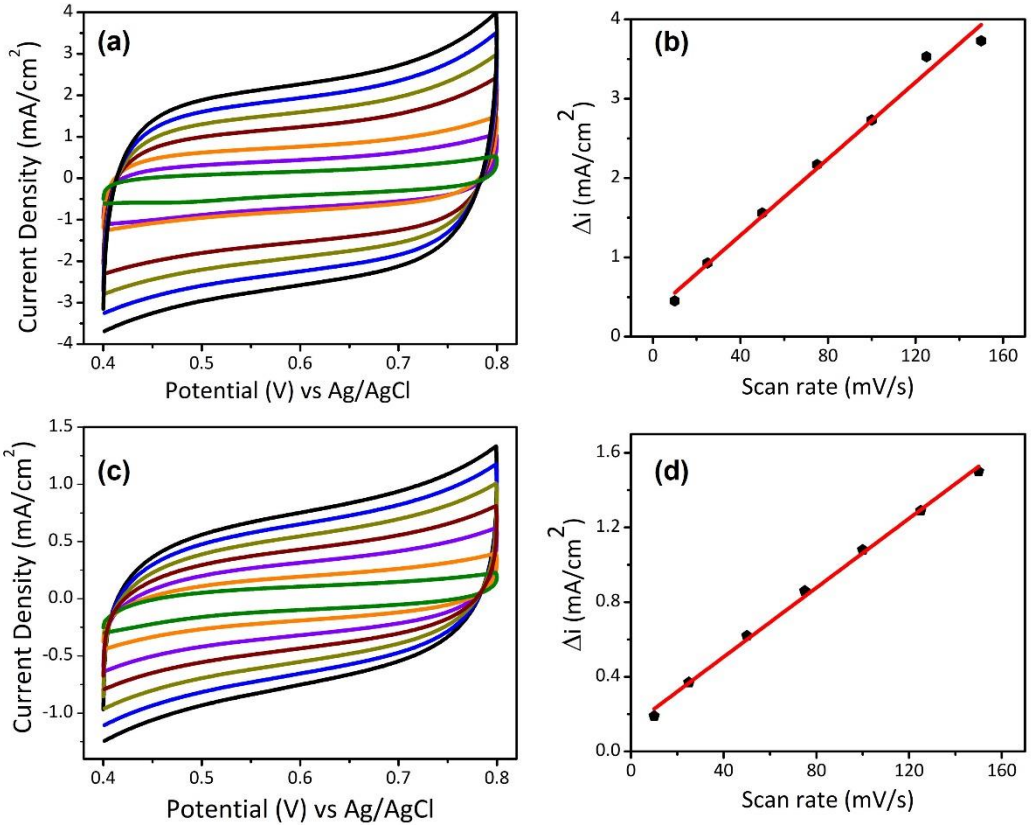

Figure 8. (a, c) are the CV curves of BN/BCN-MoS_2 (1:2) composite and relative physical mixture, respectively and (b, d) are the corresponding difference in the current density at 0.55 V plotted against scan rate to calculate the Cdl value from the slope after the linear fit in 0.5M H_2SO_4.

distinct regions in Nyquist plot corresponding to BCN and MoS_2 in case of physical mixture suggests that the two components behave independently in electrochemical process. In contrast, cross-linked BN/BCN−MoS_2 and G/BCN−MoS_2 catalysts show single region with lesser charge-transfer resistance (R_{ct}) compared to BCN or MoS_2 combined. The enhanced performance of cross-linked catalyst is attributed to the distinctive 3D heterolayer network,[32,33] as suggested by electron microscopy, along with the presence of microporous channels created in the nanocomposites due to cross-linking,[34–36] offering a high electrochemical area for the diffusion of electrolyte. Theoretical calculations on MoS_2-BC_7N nanocomposites shows that MoS_2 serves as the

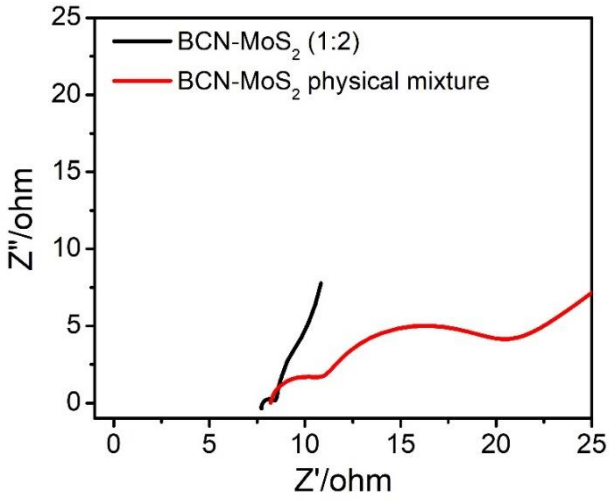

Figure 9. Nyquist plot of BCN-MoS_2 (1:2, physical mixture) and G/BCN-MoS_2 (1:2) composite at the onset potential. EIS measurements were done at the onset potential from 10^5 to 10^{-2} Hz with an AC voltage of 5mV in 0.5 M H_2SO_4.

active site for HER.[37] There is increased density of states near the Fermi level for composite with significant contribution from MoS_2. Moreover, based on the work function of MoS_2 (4.35 eV) and BCN (3.57 eV), the electrons can flow from BCN to MoS_2 upon crosslinking which results in enhanced HER activity. This corroborates with our experimental results where catalytic activity increases with increasing MoS_2 content.

The above results suggest that cross-linking of BCN layers to MoS_2 clearly enhances the catalytic activity of the latter wherein the carbon rich BCN act as channels for transferring electrons to the MoS_2 active sites across the network. The higher activity of cross-linked BCN−MoS_2 catalyst can be further attributed to the excellent intrinsic conductivity of cross-linked BCN layers which can facilitate electron transfer to the active sites in 3D network along with the possible hydrogen adsorption sites (sp^3-C, Stone−Wales defect). The high HER activity of composites is also due to enhanced charge-transfer rates, more exposed active edge sites of MoS_2 and increased surface

area due to cross-linking which further improve HER activity by providing the larger electrode/electrolyte interface area.

4.5 Conclusions

In conclusion, we have been able to synthesize two differently cross-linked nanocomposites with distinctive bonding between MoS_2 sheets and graphene domains and BN domains in BC_7N. The cross-linked assemblies show excellent hydrogen evolution activity relative to the physical mixtures. Electrochemical HER activity of the graphene domain cross-linked G/BCN−MoS_2 (1:2) assembly is noteworthy with a Tafel slope of 34 mV dec^{-1} close to that of Pt (30 mV dec^{-1}). The performance of this catalyst is best under acidic conditions (pH = 1.3). The performance of BN/BCN−MoS_2 is generally poorer than that of G/BCN−MoS_2. The present study demonstrates the advantages of cross-linking of catalytically active heterolayers BCN and MoS_2 for the HER reaction. The enhanced HER activity in cross-linked composites arises from the increased charge-transfer rates as well as from the more exposed catalytically active sites. Photochemical HER activity of the BN/BCN−MoS_2 (1:2) and G/BCN−MoS_2 (1:2) assemblies is also superior, implying that the covalent cross-linking is a valuable strategy for HER and associated catalytic reactions. Noting that pristine 2H-MoS_2 itself exhibits very poor photochemical HER activity, the present results show that the activity of 2H-MoS_2 can be vastly improved by crosslinking with BC_7N.

4.5 References

[1] D. v Esposito, S. T. Hunt, A. L. Stottlemyer, K. D. Dobson, B. E. Mccandless, R. W. Birkmire, J. G. Chen,] D v Esposito, S. T. Hunt, A. L. Stottlemyer, J. G. Chen, D. v Esposito, K. D. Dobson, B. E. Mccandless, R. W. Birkmire, *Angew. Chem. Int. Ed.* **2010**, *49*, 9859.

[2] J. Yu, L. Qi, M. Jaroniec, *J. Phys. Chem. C* **2010**, *114*, 13118.

[3] S. Min, G. Lu, *J. Phys. Chem. C* **2012**, *116*, 25415.

[4] P. C. K. Vesborg, B. Seger, I. Chorkendorff, *J. Phys. Chem. Lett.* **2015**, *6*, 951.

[5] Y. Zheng, Y. Jiao, Y. Zhu, L. H. Li, Y. Han, Y. Chen, A. Du, M. Jaroniec, S. Z. Qiao, *Nat. Commun.* **2014**, *5*, 1.

[6] K. Srinivasu, B. Modak, S. K. Ghosh, *J. Phys. Chem. C* **2014**, *118*, 26479.

[7] C. Tsai, K. Chan, F. Abild-Pedersen, J. K. Nørskov, *Phys. Chem. Chem. Phys.* **2014**, *16*, 13156.

[8] T. P. Nguyen, S. Choi, J. M. Jeon, K. C. Kwon, H. W. Jang, S. Y. Kim, *J. Phys. Chem. C* **2016**, *120*, 3929.

[9] U. Maitra, U. Gupta, M. De, R. Datta, A. Govindaraj, C. N. R. Rao, *Angew. Chem. Int. Ed.* **2013**, *52*, 13057.

[10] M. Chhetri, S. Maitra, H. Chakraborty, U. v. Waghmare, C. N. R. Rao, *Energy Environ. Sci.* **2016**, *9*, 95.

[11] M. Barua, M. B. Sreedhara, K. Pramoda, C. N. R. Rao, *Chem. Phys. Lett.* **2017**, *683*, 459.

[12] N. Kumar, K. Moses, K. Pramoda, S. N. Shirodkar, A. K. Mishra, U. v. Waghmare, A. Sundaresan, C. N. R. Rao, *J. Mater. Chem. A* **2013**, *1*, 5806.

[13] S. Y. Han, Y. A. Kim, *Tetrahedron* **2004**, *60*, 2447.

[14] D. L. Boger, S. Miyazaki, S. H. Kim, J. H. Wu, S. L. Castle, O. Loiseleur, Q. Jin, *J. Am. Chem. Soc.* **1999**, *121*, 10004.

[15] K. Pramoda, U. Gupta, M. Chhetri, A. Bandyopadhyay, S. K. Pati, C. N. R. Rao, *ACS Appl. Mater. Interf.* **2017**, *9*, 10664.

[16] D. Voiry, A. Goswami, R. Kappera, C. D. C. C. E. Silva, D. Kaplan, T. Fujita, M. Chen, T. Asefa, M. Chhowalla, *Nat. Chem.* **2014**, *7*, 45.

[17] P. Vishnoi, A. Sampath, U. v. Waghmare, C. N. R. Rao, *Chem. Eur. J.* **2017**, *23*, 886.

[18] K. C. Knirsch, N. C. Berner, H. C. Nerl, C. S. Cucinotta, Z. Gholamvand, N. McEvoy, Z. Wang, I. Abramovic, P. Vecera, M. Halik, S. Sanvito, G. S. Duesberg, V. Nicolosi, F. Hauke, A. Hirsch, J. N. Coleman, C. Backes, *ACS Nano* **2015**, *9*, 6018.

[19] S. Luo, X. Qi, L. Ren, G. Hao, Y. Fan, Y. Liu, W. Han, C. Zang, J. Li, J. Zhong, *J. Appl. Phys.* **2014**, *116*, 164304.

[20] B. Yao, C. Li, J. Ma, G. Shi, *Phys. Chem. Chem. Phys.* **2015**, *17*, 19538.

[21] K. S. W. Sing, D. H. Everett, R. A. W. Haul, L. Moscou, R. A. Pierotti, J. Rouquerol, T. Siemieniewska, *Pure Appl. Chem.* **1985**, *57*, 603.

[22] Y. Li, H. Wang, L. Xie, Y. Liang, G. Hong, H. Dai, *J. Am. Chem. Soc.* **2011**, *133*, 7296.

[23] M. Chatti, T. Gengenbach, R. King, L. Spiccia, A. N. Simonov, *Chem. Mater.* **2017**, *29*, 3092.

[24] F. Li, J. Li, Z. Cao, X. Lin, X. Li, Y. Fang, X. An, Y. Fu, J. Jin, R. Li, *J. Mater. Chem. A* **2015**, *3*, 21772.

[25] X. Zhao, H. Zhu, X. Yang, *Nanoscale* **2014**, *6*, 10680.

[26] Y. Yan, B. Xia, X. Ge, Z. Liu, J. Y. Wang, X. Wang, *ACS Appl. Mater. Interfaces* **2013**, *5*, 12794.

[27] Y. Hou, B. Zhang, Z. Wen, S. Cui, X. Guo, Z. He, J. Chen, *J. Mater. Chem. A* **2014**, *2*, 13795.

[28] Y. Zhang, L. Zuo, Y. Huang, L. Zhang, F. Lai, W. Fan, T. Liu, *ACS Sustain. Chem. Eng.* **2015**, *3*, 3140.

[29] U. Gupta, B. S. Naidu, U. Maitra, A. Singh, S. N. Shirodkar, U. v. Waghmare, C. N. R. Rao, *APL Mater.* **2014**, *2*, 092802.

[30] Shimidzu Takeo, Iyoda Tomokazu, Koide Yoshihiro, *J. Am. Chem. Soc.* **1985**, *107*, 35.

[31] S. Min, G. Lu, *J. Phys. Chem. C* **2011**, *115*, 13938.

[32] A. A. Jeffery, S. R. Rao, M. Rajamathi, *Carbon* **2017**, *112*, 8.

[33] Y. Zhao, L. Kuai, Y. Liu, P. Wang, H. Arandiyan, S. Cao, J. Zhang, F. Li, Q. Wang, B. Geng, H. Sun, *Sci. Rep. 2015 5:1* **2015**, *5*, 1.

[34] K. Pramoda, U. Gupta, I. Ahmad, R. Kumar, C. N. R. Rao, *J. Mater. Chem. A* **2016**, *4*, 8989.

[35] C. N. R. Rao, K. Pramoda, R. Kumar, *Chem. Commun.* **2017**, *53*, 10093.

[36] K. Yuan, Y. Xu, G. Brunklaus, L. Shi, *Adv. Mater.* **2015**, *27*, 6714.

[37] R. Singh, U. Gupta, S. v Kumar, M. M. Ayyub, U. v Waghmare, C. Rao, *ChemPhysChem* **2019**, *20*, 1728.

Chapter 5

Photochemical Hydrogen Generation by Splitting Seawater

Summary

Producing hydrogen from water in an efficient manner could significantly reduce consumption of fossil fuels. In this regard the abundant presence of water in oceans offers an important alternative approach for water splitting using seawater. Direct use of seawater for the generation of hydrogen is a difficult and complex process due to the presence of various ions in seawater which affect the activity of the catalysts and makes it difficult to utilise them for efficient water splitting. Herein we report various catalysts and sacrificial agents which can be utilised to efficiently reduce seawater to hydrogen under visible light irradiation. Better performance than pure water was observed in some cases and in few cases the opposite was observed, implying that with a proper approach seawater can be efficiently reduced to generate hydrogen.

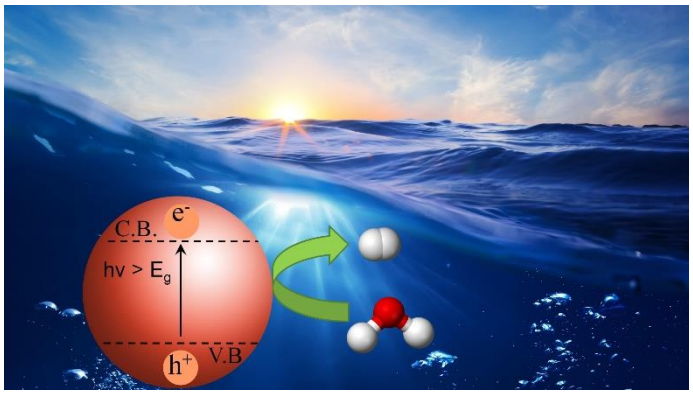

Paper based on this work has appeared in *Chem. Eur. J.* ***2018***, 24, 69, 18455-18462

5.1 Introduction

Increasing energy demands as well as environmental issues are of great concern to humankind. This has compelled scientists around the globe to look for a clean and renewable source of energy. Hydrogen has emerged as the obvious clean energy source and in this context using sunlight to split water into hydrogen and oxygen is an attractive solution.[1,2] Water can be photocatalytically or photoelectrochemically split into hydrogen and oxygen by using a suitable catalyst.[3] There has been extensive research on the hydrogen evolution reaction (HER) by water splitting and most of it has been carried out on pure water.[4–6] Considering the scarcity of fresh water and the high cost of water treatment, it is pertinent to make use of an abundant source of water without compromising with the efficiency of water splitting. About 71% of the earth is covered with water out of which 97% is present in the oceans which are saline in nature. The possible use of seawater for generating hydrogen clearly is a worthy proposition.[7,8]

In order to efficiently utilise seawater for the generation of hydrogen, it is important to examine the constituents and properties of seawater. Seawater contains various salts and the six major ions in these salts are Na^+, Mg^{2+}, Ca^{2+}, K^+, Cl^- and SO_4^{2-}, which make up >90% of the total salt content of seawater (**Figure 1**).[9] Trace amounts of iron, lead, gold, and protactinium are also found.[9] The presence of dissolved salts in the seawater affects the activity of the catalyst to some extent.[10] Direct electrolysis of seawater results in the evolution of hydrogen at the cathode and evolution of chlorine and hypochlorite at the anode. Evolution of chlorine and hypochlorite implies the competing nature of chloride oxidation with the oxidation of water.[11,12] Oxidation of chloride ions is thermodynamically less favourable than that of water (redox potential considerations: 1.36 V Cl^-/Cl_2 vs 1.23 V (H_2O/O_2)), but the former is a two-electron process and hence is kinetically more favourable (H_2O/O_2, being a 4 e^- process).[13] From the thermodynamic perspective, the presence of metal cations such as Na^+,

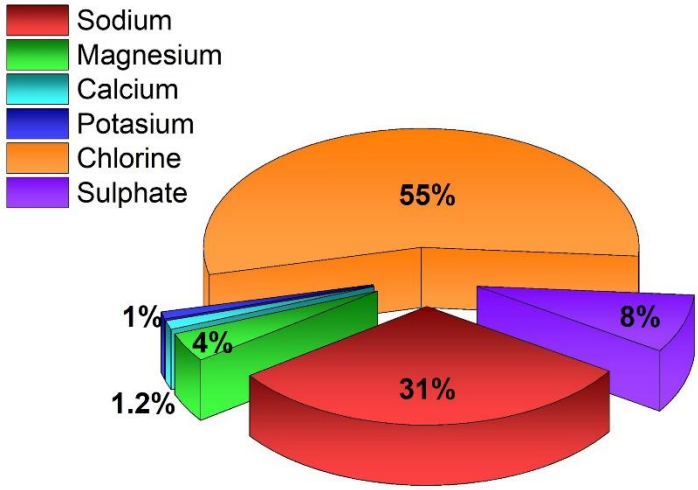

Figure 1. Composition of seawater.

Mg^{2+}, Ca^{2+} and K^{+} doesn't affect the activity because of the higher reduction potential of the cations as compared to water reduction potential. However, one issue with direct electrolysis or photoelectrolysis is the deactivation of active sites at cathode by the build-up of insoluble precipitates of the metals in the form of hydroxides. Zou *et al.*[14] have found the formation of calcium and magnesium hydroxide on the cathode during photoelectrolysis reaction in sea water.

Splitting of water photocatalytically or photoelectrochemically using semiconductor catalysts depends on the band structure of the semiconductor.[4,15] The ions present in water can get oxidised or reduced by the photogenerated electrons or holes thereby competing with water oxidation and reduction. Competition with water oxidation is more prevalent due to the comparable oxidation potential of water and chloride ion.[13] This greatly affects the efficiency of water splitting. Research on the effect of ions on splitting of water is limited and a very few studies of water splitting using seawater has been carried out.[16–19] A recent study from Maeda *et al.* reported the effect of various ions on the overall splitting of water using $Rh_{2-y}Cr_yO_{3-}$

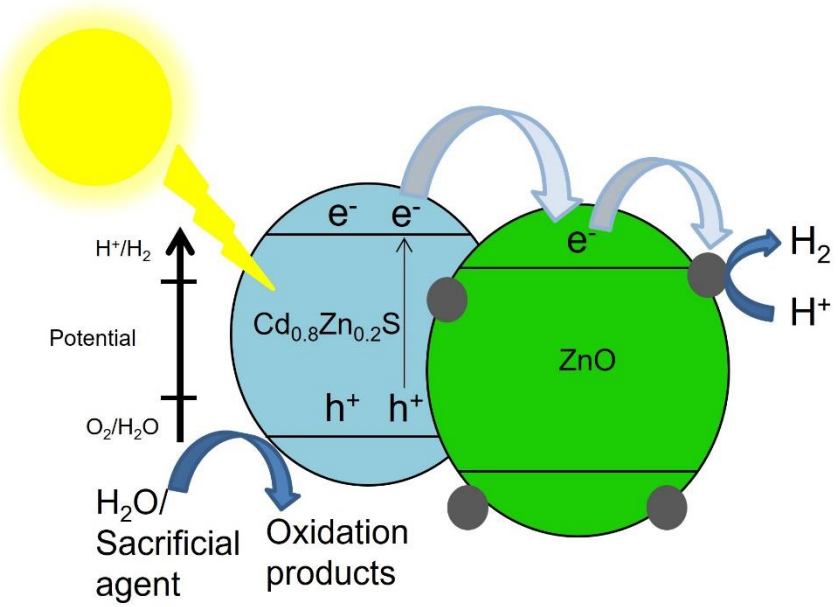

Scheme 1. Schematic representation of mechanism of photocatalytic water splitting in ZnO/Pt/$Cd_{0.8}Zn_{0.2}S$ heterostructure.

loaded ($Ga_{1-x}Zn_x$) ($N_{1-x}O_x$).[10] Seawater splitting greatly depends on the reaction conditions and is generally found to be less efficient than that of pure water.[20,21]

5.2 Scope of present investigation

In this article, we have carried out a study on generating hydrogen from seawater by using different catalysts known to be active for hydrogen generation from pure water.[22–24] The methods used in the present study is photocatalytic water splitting. Semiconductor catalysts such as CdS and $Cd_4P_2Br_3$ as well as complex heterostructures such as ZnO(NP)/Pt/$Cd_{0.8}Zn_{0.2}S$, ZnO(NR)/Pt/ $Cd_{0.8}Zn_{0.2}S$, TiO_2(NT)/Pt/ $Cd_{0.8}Zn_{0.2}S$ are used as photochemical catalysts. **Scheme 1** illustrates the mechanism of photocatalytic water splitting employing heterostructures, wherein photogenerated electrons in the conduction band of the semiconductor move to Pt nanocrystals and participate in the reduction reaction. The photogenerated holes present in the valence band of the semiconductor participates in oxidation reactions. Scavengers are used to eliminate holes, thereby reducing charge carrier

recombination and favour the reduction reaction by electrons. The detailed study with the above-mentioned catalysts has yielded interesting results. We observe better performance in seawater compared to pure water in photocatalytic hydrogen generation when an inorganic sacrificial agent (Na_2S/Na_2SO_3) is used. Decrease in activity was observed with an organic sacrificial agent. No change in performance was observed in the absence of sacrificial agent in the case of $Cd_4P_2Br_3$. An effort has been made to deduce the mechanism of water splitting in seawater.

5.3 Experimental

5.3.1 Synthesis of catalysts

CdS nanoparticles: In 10 mM aqueous solution of cadmium acetate (SD Fine chemicals 99% purity), 20 mM aqueous solution (SD Fine chemicals 52 % purity) of Na_2S was added dropwise through a burette. The nanoparticles are immediately formed on addition of Na_2S solution. The samples washed thoroughly with water followed by ethanol and dried at 80^oC in a hot air oven.

Heterostructures: The heterostructure catalysts were prepared by the method reported elsewhere[22,23]. Briefly, for the synthesis of heterostructures firstly the catalyst of desired morphology was synthesized followed by the deposition of platinum and CdZnS.

ZnO nanoparticles were synthesized in a methanolic solution of zinc acetate to which methanolic solution of KOH was added drop wise followed by stirring for 2h at 60 °C.

ZnO nanorods (NR) were prepared in an ethanolic solution of zinc acetate to which NaOH pellets were added followed by stirring for 2 h. The solution was packed in a plastic container and kept at room temperature for 6 days. Products were washed and centrifuged several times by distilled water and ethanol and dried at 70^oC in air.

TiO_2 nanotubes (NT) were prepared by adopting a method reported elsewhere.[25] In a typical synthesis procedure, TiO_2 NP (Degussa P25) was dispersed in an aqueous solution of NaOH. This dispersion was transferred to a Teflon-lined autoclave and heated at 150 °C for 45 h. The product was washed with distilled water until pH reaches close to 7. Afterwards, an aqueous solution of HCl was added to this and stirred for 6 h at room temperature. The obtained product was further washed with distilled water and ethanol to remove excess ions (pH7) and dried at 70 °C. The solid product was heated at 400 ° C for 4 h in air to obtain TiO_2 nanotubes.

After the synthesis of semiconductor catalyst, Pt (1 mol%) was photo deposited from a methanolic solution of chloroplatinic acid (H_2PtCl_6). This was followed by the deposition of $Cd_{0.8}Zn_{0.2}S$ in which required amount of zinc acetate, cadmium acetate and sodium sulphide were dropwise added to the solution.[24]

$Cd_4P_2Br_3$: In a typical synthesis of $Cd_4P_2Br_3$, 1.1:2.0:0.5 molar ratio of Cd_3P_2: $CdBr_2$: red-P was ground inside a glove box; homogeneous mixture was taken in a quartz ampule which was sealed under vacuum (2×10^{-5} mbar). The ampule was annealed at 525 °C for 16 hours.[24]

5.3.2 Photocatalytic measurements:

In a typical HER experiment with semiconductors such as CdS, CdS (5.0 mg) was dispersed in 40 mL 10% v/v lactic acid solution. In the case of heterostructure based catalysts, 10.0 mg of catalyst was dispersed in 40 mL aqueous solution containing inorganic (Na_2S-Na_2SO_3) or organic (BzOH-AcOOH) sacrificial agent. In the case of $Cd_4P_2Br_3$, 10.0 mg of catalyst was dispersed in 40 mL water. The solutions were bath sonicated for 15 min and purged with inert gas for 30 min prior to irradiation. A 400W Xe lamp fitted with a UV cut-off filter (λ> 395 nm) and IR filter was used as a light source. During irradiation 3 mL of gas was taken out at regular intervals from the headspace of the vessel using an airtight syringe and was analysed using GC (Perkin Elmer Clarus 580).

5.4 Results and Discussion

Hydrogen evolution activity of various catalysts in natural seawater (NSW) was studied. Seawater was collected from the coast of Arabian Sea and the hydrogen evolution yields of natural seawater (NSW) were compared with that of ultra-high pure water (UHP). NSW was used without any prior treatment except filtration through an activated charcoal bed. The presence of dissolved salts in the seawater affects the activity of the catalyst to some extent. Ions such as Cl^-, which are present in a high concentration in seawater, competes with the oxidation of water (1.36V (Cl^-/Cl_2) and 1.23V (H_2O/H_2)), whereas presence of metal cations such as Na^+, Mg^{2+}, Ca^{2+} and K^+ doesn't affect the activity because of the higher reduction potential of the cations as compared to water reduction potential. In order to study the effect of seawater on the photocatalytic hydrogen generation activity, we started with a simple semiconductor based CdS catalyst. The study was further extended to complex heterostructure catalysts of the type A/Pt/$Cd_{0.8}Zn_{0.2}S$ (where A= Metal oxide).

Photocatalytic hydrogen evolution using CdS: Photocatalytic hydrogen evolution of a simple photoactive single semiconductor-based system like CdS in the presence of lactic acid, as a sacrificial hole scavenger, was studied. The activity of CdS in UHP water and NSW was 134 and 207 μmol h^{-1} g^{-1} respectively (**Figure 2**). We observe an increase in activity of CdS that can be attributed to the presence of extra ions in the NSW. Although lactic acid, with a concentration higher than the total dissolved salts (TDS) and with an oxidation potential of -0.59 V, is both kinetically and thermodynamically favoured for hole scavenging, the presence of halide anions could also quench holes thereby increasing the overall activity. Control experiments in the absence of photocatalyst were done to rule out hydrogen evolution from the oxidation of sacrificial agent in seawater.

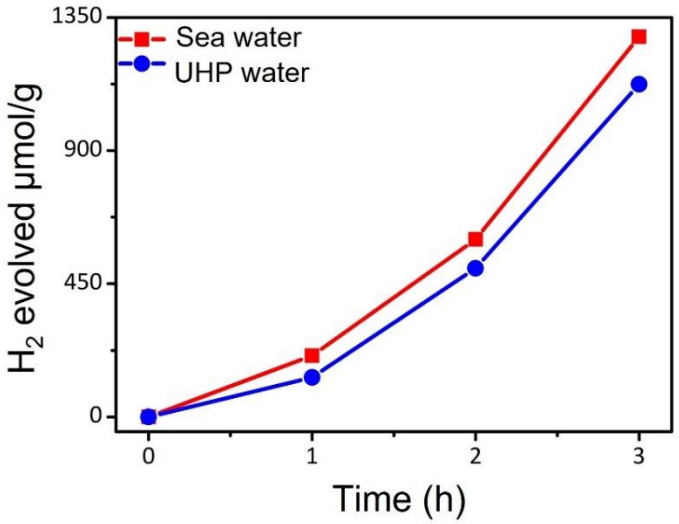

Figure 2. Time course of hydrogen evolution of CdS nanoparticles in seawater and ultra-high pure (UHP) water in lactic acid solution. CdS (5.0 mg) was dispersed in 40 mL 10% v/v lactic acid solution. A 400W Xe lamp fitted with a UV cut-off filter (λ> 395 nm) and IR filter was used as a light source.

Photocatalytic hydrogen evolution with heterostructures: After studying the effect of NSW on the activity of a simple semiconductor CdS we studied complex heterostructures of the type A/Pt/$Cd_{0.8}Zn_{0.2}S$ (where A = metal oxide such as ZnO nanoparticle (NP), ZnO nanorods (NR) and TiO_2 nanotubes (NT)) which are reported to be efficient catalysts for hydrogen evolution from UHP water.[23,24] A schematic of the mechanism of water splitting by heterostructure catalyst was illustrated in Scheme 1. Upon visible-light irradiation, $Cd_{0.8}Zn_{0.2}S$ absorbs the light to generate charge carriers. The band alignment of metal oxide-$Cd_{0.8}Zn_{0.2}S$ interface causes injection of the excited electrons from $Cd_{0.8}Zn_{0.2}S$ to metal oxide, and holes stays in the VB of $Cd_{0.8}Zn_{0.2}S$. Holes in the valence band (VB) of $Cd_{0.8}Zn_{0.2}S$ gets consumed by the sacrificial agent to yield the corresponding oxidation product and by water to yield oxygen. Metal nanoparticles catalyse the reduction of H_2O upon accepting electrons from the CB of metal oxide. The photochemical activity for the heterostructure catalysts was studied in the presence of inorganic (Na_2S/Na_2SO_3) and organic (benzyl alcohol/acetic acid) sacrificial agents (**Figures 3**). Photocatalytic activity for the catalyst $Cd_4P_2Br_3$, which is known to be active for

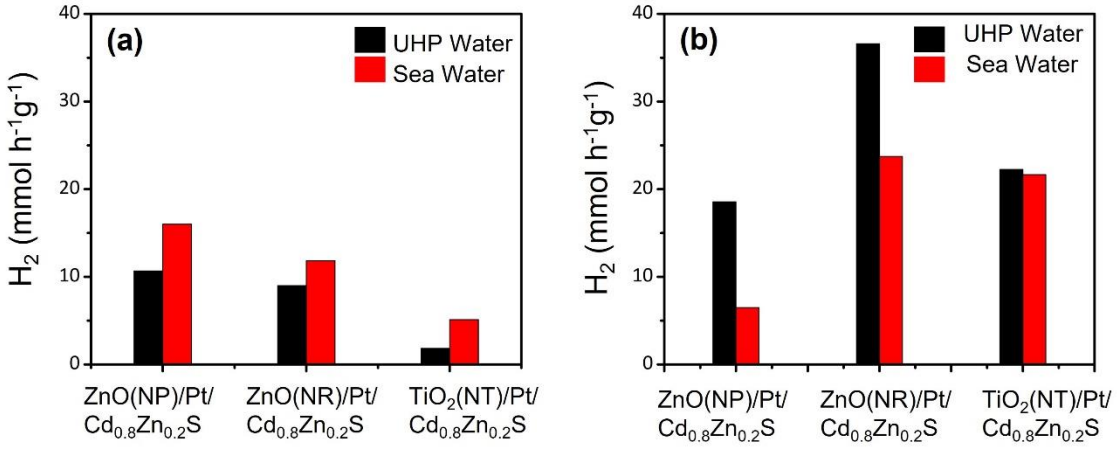

Figure 3. Photocatalytic HER activity of heterostructures with (a) sodium sulphide and sodium sulphite, and (b) benzyl alcohol as hole scavenger. 10.0 mg of catalyst was dispersed in 40 mL aqueous solution containing inorganic (Na_2S-Na_2SO_3) or organic (BzOH-AcOOH) sacrificial agent. A 400W Xe lamp fitted with a UV cut-off filter (λ> 395 nm) and IR filter was used as a light source

both water and carbon dioxide reduction, was studied in the absence of sacrificial agents.[24] The HER rate was superior in NSW than in UHP water when Na_2S-Na_2SO_3 were used as sacrificial agents. We see that the hydrogen evolution reaction in seawater shows an increase in hydrogen yields for all the three heterostructures. ZnO nanoparticle heterostructure shows a 50% increase in hydrogen evolution. The increase is less prominent when the morphology of ZnO is changed to nanorods with ZnO nanorods showing an increase of 31%. Hydrogen evolution with TiO_2 nanotubes has almost 300% increase in hydrogen yields. (**Figure 3**)

Hydrogen evolution reaction in NSW shows a decrease in hydrogen yields for all the heterostructures in the presence of organic sacrificial agents in contrast to inorganic sacrificial agents. ZnO nanoparticles show the least hydrogen evolution with a decrease of 65%. Heterostructures with the ZnO nanorods shows a decrease of 35%. TiO_2 nanotubes show nearly the same hydrogen evolution with a slight decrease of 3%. (**Figure 3**) Control experiments in the absence of photocatalyst were done to rule out hydrogen evolution from the oxidation of sacrificial agent in seawater.

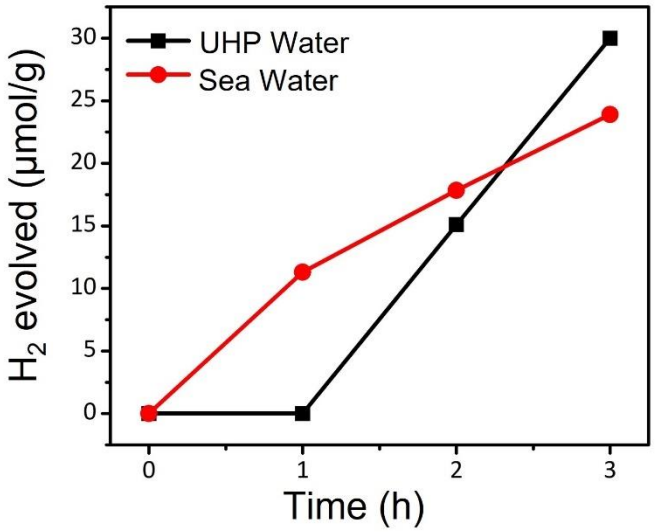

Figure 4. Sacrificial free HER using $Cd_4P_2Br_3$ in alkaline medium. 10.0 mg of catalyst was dispersed in 40 mL 3 M NaOH. A 400W Xe lamp fitted with a UV cut-off filter (λ> 395 nm) and IR filter was used as a light source.

Presence of various ions in seawater as well as the presence of sacrificial agent makes it difficult to deduce the reasons behind different activity in different cases. In order to study the effects in the absence of sacrificial agent hydrogen evolution reaction in seawater without a sacrificial agent was carried out with $Cd_4P_2Br_3$. The yields for NSW (10 μmol h^{-1} g^{-1}) and UHP water (8 μmol h^{-1} g^{-1}) were nearly the same. This implies that the presence of ions in seawater doesn't have a drastic effect on HER activity of the catalyst in the absence of sacrificial agent (**Figure 4**). The above results are summarised in **Table 1** to show how HER in seawater can be efficiently carried out with a suitable choice of catalyst and sacrificial agent.

Based on the above experimental analysis, presence of ions in seawater does not have a strong deteriorating effect on HER activity. In fact, we observed enhancement in activity in some cases. **Scheme 2** shows a schematic of seawater splitting on a semiconductor photocatalyst. The photoexcited electrons are utilised for hydrogen generation while holes are utilised for oxidation of water. However, chloride ions present in seawater can also get oxidised

to produce Cl_2 and HClO. This competing oxidation of chloride ions enhances the charge-carrier separation and might be responsible for enhanced catalytic activity.[26]

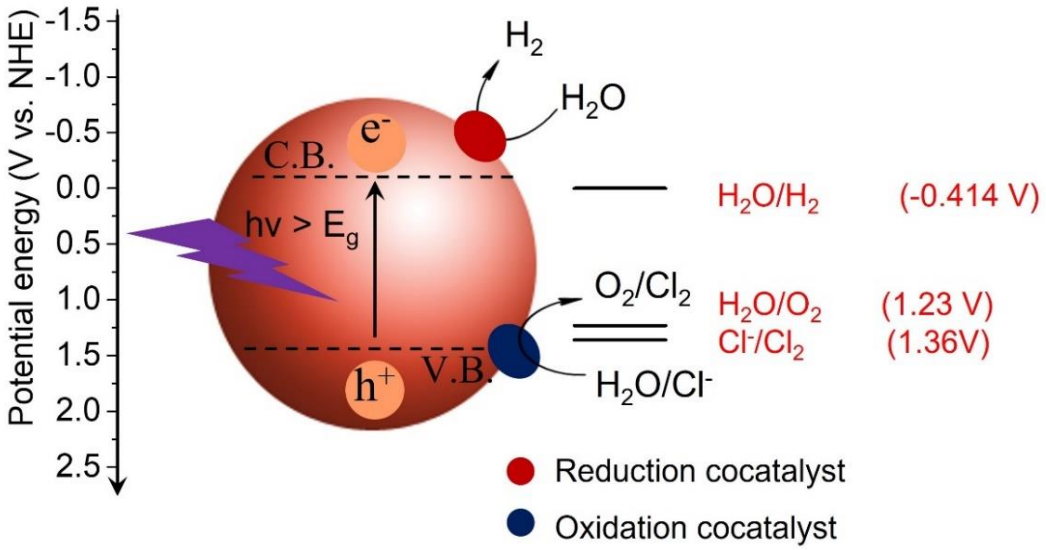

Scheme 2. Schematic illustration of photocatalytic seawater splitting on a semiconductor photocatalyst.

Table 1. Comparison of hydrogen yields of heterostructure based catalysts.

Catalyst	Hydrogen Yields (mmol h^{-1} g^{-1})			
	Na_2S/Na_2SO_3		Benzyl alcohol/acetic acid	
	UHP water	Sea water	UHP water	Sea water
ZnO/Pt/ $Cd_{0.8}Zn_{0.2}S$	10.7	16	18.6	6.5
ZnO(NR)/Pt/ $Cd_{0.8}Zn_{0.2}S$	9	11.8	36.6	23.7
TiO_2(NT)/Pt/ $Cd_{0.8}Zn_{0.2}S$	1.8	5.1	22.3	21.7

5.5 Conclusions

The present comparative study of the hydrogen generation from seawater as compared to pure water has revealed interesting results. The presence of ions in seawater doesn't seem to affect the activity of $Cd_4P_2Br_3$ in the absence of a sacrificial agent. To our surprise we find that for simple semiconductor and complex heterostructure based photocatalysts the performance

is slightly better in seawater than in pure water when we use inorganic sacrificial agents such as Na_2S/Na_2SO_3. However, the performance is affected when we use benzyl alcohol as the sacrificial agent. The above results suggest by a suitable choice of catalysts, one can split seawater without any prior treatment, and this might be very beneficial in solving the energy problem to some extent.

5.6 References

[1] M. G. Walter, E. L. Warren, J. R. McKone, S. W. Boettcher, Q. Mi, E. A. Santori, N. S. Lewis, *Chem. Rev.* **2010**, *110*, 6446.

[2] P. v. Kamat, *J. Phys. Chem. C* **2007**, *111*, 2834.

[3] A. Fujishima, K. Honda, *Nature 1972 238:5358* **1972**, *238*, 37.

[4] T. Hisatomi, J. Kubota, K. Domen, *Chem. Soc. Rev.* **2014**, *43*, 7520.

[5] K. Maeda, K. Domen, *J. Phys. Chem. Lett.* **2010**, *1*, 2655.

[6] C. N. R. Rao, S. R. Lingampalli, S. Dey, A. Roy, *Philos. Trans. Royal Soc. A* **2016**, 374.

[7] P. Hoffmann, *Forever Fuel: The Story Of Hydrogen*, Westview Press, **1981**.

[8] J. A. Turner, *Science* **2004**, *305*, 972.

[9] F. J. Millero, R. Feistel, D. G. Wright, T. J. McDougall, *Deep Sea Res., Part I* **2008**, *55*, 50.

[10] K. Maeda, H. Masuda, K. Domen, *Catal. Today* **2009**, *147*, 173.

[11] S. Trasatti, *Electrochim. Acta* **1984**, *29*, 1503.

[12] A. F. Adamson, B. G. Lever, W. F. Stones, *J. Appl. Chem.* **1963**, *13*, 483.

[13] S. Fukuzumi, Y. M. Lee, W. Nam, *ChemSusChem* **2017**, *10*, 4264.

[14] W. Luo, Z. Yang, Z. Li, J. Zhang, J. Liu, Z. Zhao, Z. Wang, S. Yan, T. Yu, Z. Zou, *Energy Environ. Sci.* **2011**, *4*, 4046.

[15] Z. Zou, J. Ye, K. Sayama, H. Arakawa, *Nature*, **2001**, *414*, 625.

[16] L. Guo, Z. Yang, K. Marcus, Z. Li, B. Luo, L. Zhou, X. Wang, Y. Du, Y. Yang, *Energy Environ. Sci.* **2018**, *11*, 106.

[17] Y. Li, R. Wang, H. Li, X. Wei, J. Feng, K. Liu, Y. Dang, A. Zhou, *J. Phys. Chem. C* **2015**, *119*, 20283.

[18] Y. Li, X. Wei, X. Yan, J. Cai, A. Zhou, M. Yang, K. Liu, *Phys. Chem. Chem. Phys.* **2016**, *18*, 10255.

[19] S. M. Ji, H. Jun, J. S. Jang, H. C. Son, P. H. Borse, J. S. Lee, *J. Photochem. Photobiol., A* **2007**, *189*, 141.

[20] Y. Li, F. He, S. Peng, D. Gao, G. Lu, S. Li, *J. Mol. Catal. A: Chem.* **2011**, *341*, 71.

[21] S. Peng, R. An, Y. Li, G. Lu, S. Li, *Int. J. Hydrogen Energy* **2012**, *37*, 1366.

[22] A. Roy, S. R. Lingampalli, S. Saha, C. N. R. Rao, *Chem. Phys. Lett.* **2015**, *637*, 137.

[23] S. R. Lingampalli, U. K. Gautam, C. N. R. Rao, *Energy Environ. Sci.* **2013**, *6*, 3589.

[24] A. Roy, M. Chhetri, S. Prasad, U. v. Waghmare, C. N. R. Rao, *ACS Appl. Mater. Interfac.* **2018**, *10*, 2526.

[25] T. Kasuga, M. Hiramatsu, A. Hoson, T. Sekino, K. Niihara, *Adv. Mater.* **1999**, 11, 15.

[26] J. Zhang, Y. Lei, S. Cao, W. Hu, L. Piao, X. Chen, *Nano Research* **2021**, *15*, 2013.

Part II

Aliovalent anion substitution: TiNF and related analogues of TiO_2

Summary

Aliovalent anion substitution in inorganic materials brings about marked changes in properties as exemplified by N, F-codoped metal oxides. In view of the important properties of TiO_2, we have attempted to prepare TiNF by employing an entirely new procedure involving the reaction of TiN with TiF_4. While the reaction at low temperature (450ºC) yields TiNF in the anatase phase, reaction at a higher temperature (600ºC) yields TiNF in the rutile phase. The lattice parameters of TiNF are close to those of the parent oxides. Partial substitution of oxygen in TiO_2 by N and F reduces the band gap, but complete substitution increases the band gap comparable to that of the oxide. We have examined properties of N, F-codoped TiO_2, and more interestingly N,F-codoped Ti_3O_5, both with lower band gaps than the parent oxides. A detailed first-principles calculations has been carried out on structural and electronic properties of N, F-TiO_2 and the TiNF phases. This has enabled us to understand the effects of N, F substitution in TiO_2 in terms of the crystal structure, electronic structure, and optical properties.

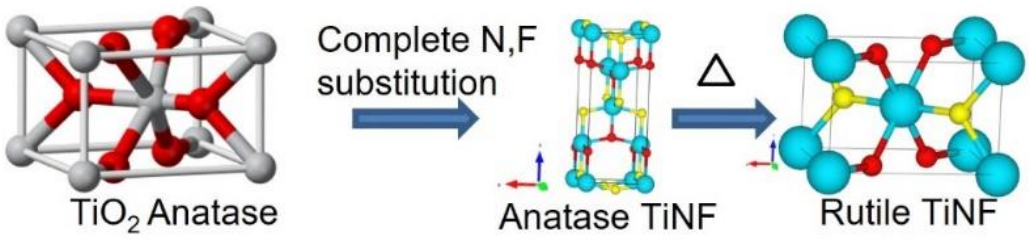

Paper based on this work has appeared in *ChemPhysChem,* **2018**, 19, 24, 3410-3417.

II.1 Introduction

Aliovalent anion substitution in inorganic compounds has profound effect on material properties.[1] For example, substitution of N^{3-} and F^{-} in metal oxides changes the electronic properties significantly.[2] N-doping alone in oxides creates oxygen vacancies in the lattice which is avoided by codoping with F. Co-doping with N and F is therefore an important way to alter the electronic as well as optical properties of oxides. It has been found recently that substitution of N^{3-} and F^{-} in ZnO affects the band gap in an interesting manner, first decreasing significantly followed by increase with higher content of N^{3-} and F^{-1}.[3,4] Especially important is the discovery of Zn_2NF in which entire O^{2-} in ZnO is substituted by N^{3-} and F^{-} equally.[5] Aliovalent anion substitution is also found to influence electronic structure of metal sulphides.[1,6] Theoretical studies on the band structure of N, F-cosubstituted oxides show that an isolated band appears at the top of the valence band which could be attributed to the N 2p states whereas F 2p states lie low in energy.[5] A decrease in band gap is observed by the substitution of N in oxides thereby rendering the oxides active in the visible spectrum whereas F doping although less explored does not affect the band structure significantly, but enhances the photocatalytic activity by creating surface oxygen vacancies.[7,8]

Since Fujishima and Honda[9] reported splitting of water by TiO_2 in 1972, it has been used widely as a photocatalyst for various applications. TiO_2 possesses excellent properties such as desirable electronic structure, photostability, chemical inertness, non-toxicity and commercial availability.[10,11] The use of TiO_2 is limited because of its activity in the ultraviolet region due to its large band gap (3.2 eV).[8] Absorption of TiO_2 has been extended to the visible region by partially substituting oxygen with nitrogen.[8,12] There

have been reports of the substitution of N^{3-} and F^{-} in TiO_2 leading to a decreased band gap and enhanced photochemical activity.[13,14] Complete substitution of O^{2-} in TiO_2 with N^{3-} and F^{-} is worthy of study as it is expected to greatly affect its electronic as well as other properties. Wöstefeld *et al.*[15] reported the synthesis of TiNF in 1988 but subsequent studies showed that the material obtained was N, F-doped TiO_2 rather than TiNF.[16,17] Nukumizu *et al.*[16] repeated the preparation and obtained $TiN_{0.13}O_{1.78}F_{0.05}$.

II.2 Scope of present investigation

In the present study, we report the full substitution of O^{2-} in TiO_2 by N^{3-} and F^{-} to generate TiNF by a new method involving the reaction of TiN and TiF_4. We have been able to obtain both the anatase and rutile forms of TiNF for the first time. In this article, we present results of our experimental efforts to synthesize TiNF as well as other N, F-substituted TiO_2 compositions, in particular N,F- substituted Ti_3O_5, the first member of the Magneli phases. More importantly we have examined the structural, electronic, and vibrational properties of TiNF in both the rutile and anatase structures by employing first-principles density functional theory calculations (DFT). Aligning the valence and conduction bands of anatase TiNF relative to the standard hydrogen electrode (SHE) potential, we assess its potential as a photocatalyst for the water splitting reaction.

III.3 Experimental

Synthesis of TiNF: Initially we attempted to synthesize TiNF by a method reported in the earlier literature which involved the reaction of $(NH_4)_2TiF_6$ and NH_4Cl followed by heating first in nitrogen and followed by ammonia.[15] We obtained an olive-green powder that was isostructural to anatase TiO_2. XPS analysis showed that the compound formed

was N, F-doped TiO_2 rather than TiNF. We have therefore employed a procedure with a reaction of TiN and TiF_4 (Merck, 100%). TiN was prepared starting with TiO_2 (Anatase, Merck 99%). TiO_2 was taken in a ceramic boat placed in a quartz tube in a tube furnace. The sample was purged with NH_3 for 2 h prior to the reaction and then temperature was raised to 800 ^oC with a rate of 5 ^oC and maintained at this temperature for 5 h. The above procedure was repeated until pure TiN was obtained.

Stoichiometric mixture of TiN and TiF_4 was ground in a mortar in an argon filled glove box and transferred to a quartz tube and sealed under vacuum (10^{-6} mbar). The sealed tube was heated in a muffle furnace at 450°C for 24 h (reaction step 1). The product obtained in this step was again sealed in a quartz tube under vacuum and heated in a muffle furnace at 450°C for 24 h (reaction step 2). This step was repeated until we obtained single phase with anatase structure (reaction step 3). The above procedure was carried out at 600 $^{\circ}$C with a 2:1 ratio of TiN and TiF_4 which gave a product with the rutile structure.

Synthesis of N,F-substituted TiO_2: N, F- substituted TiO_2 were prepared starting with TiO_2 (Anatase, Merck 99%) and NH_4F (Merck 99.99%). Mixtures of desired compositions were taken in a ceramic boat placed in a quartz tube in a tube furnace. The tube was purged with NH_3 for 1 h prior to the reaction and temperature was raised to 100 ^oC (5 ^oC/min) and maintained for 2 h. The temperature was next raised to 500 ^oC (1 ^oC/min) for 1 h. N, F-substituted Ti_3O_5 was obtained starting with amorphous TiO_2 and NH_4F (Merck 99.99%). Mixtures of these were taken in a ceramic boat placed in a quartz tube in a tube furnace. The tube was purged with NH_3 for 1 h prior to the reaction and temperature was raised to 100 ^oC (5 ^oC/min) and maintained at this temperature for 2 h. Next, the temperature was raised to 500 ^oC (1 ^oC/min) and maintained at this temperature for 1 h.

Physical Characterization: X-ray diffraction (XRD) patterns of all samples were collected in the range of 10-80^{o} (2θ) using a Bruker D8 Diffraction System with a Cu-Kα source (λ = 0.154178 nm). UV/Vis absorption spectra were recorded by using Perkin-Elmer model Lambda 900 spectrometer. X-ray photoelectron spectra were recorded using an Mg-Kα (1253.6 eV) X-ray source to calculate the elemental compositions of TiNF and N, F – substituted TiO_2 samples. EPR experiments were carried out at room temperature using a Bruker EMX XBand spectrometer working at a nominal microwave frequency of 9.4 GHz. Microwave frequency modulation of frequency 100 kHz and amplitude of 2 Gauss was used to record the power absorbed in the derivative form after phase sensitive detection. DPPH was used as field marker.

Photocatalytic hydrogen evolution and CO_2 reduction: In a typical HER experiment, catalyst (10 mg) was dispersed in 50 mL millipore water with Na_2S-Na_2SO_3 as sacrificial reagent. The solution was bath sonicated for 15 min and purged with inert gas for 30 min prior to irradiation. A 400W Xe lamp fitted with a UV cut-off filter (λ> 395 nm) and IR filter was used as a light source. During irradiation 3 mL of gas was taken out at regular intervals from the headspace of the vessel using an airtight syringe and was analysed using GC (Perkin Elmer Clarus 580 equipped with TCD and FID). Gas phase photocatalytic reduction of CO_2 experiments were performed in a reaction flask with a total volume of 160 mL. 10 mg of the photocatalyst was deposited on flat face of the cell. Glass cell was evacuated and filled with CO_2 and water vapor sequentially for five times. CO_2 was filled in the cell through a water bubbler to create humidified CO_2. The cell was irradiated with either sunlight or UV-visible light. The gas samples were collected and tested with gas-

chromatograph (Perkin Elmer Clarus 580 GC equipped with TCD and FID) for the detection of CO, CH_4 and H_2.

Computational studies: Our first-principles calculations are based on density functional theory as implemented in the Quantum ESPRESSO (QE) package.[18] We have used a local density approximation (LDA) to treat the exchange-correlation energy of electrons, and norm conserving pseudo potentials to represent the interaction between ionic cores and valence electrons. We employ an energy cut-off of 85 Ry to truncate the plane-wave basis set used in representation of Kohn-Sham wavefunctions. The structures were relaxed to minimize total energy until the Hellmann-Feynman force on each atom is less than the 0.01 eV/°A. We used uniform meshes of 4x4x4, 6x6x8, and 4x4x2 k-vectors to sample integrations over Brillouin Zones (BZ) of TiNF in anatase (primitive unit cell), rutile and N, F-doped TiO_2 respectively. We used the Heyd-Scuseria-Ernzerhof (HSE-06) hybrid functional of exchange correlation energy[19] to obtain accurate estimates of band gaps, with 2x2x2 mesh of k-points in evaluation of Hartree-Fock exchange energy. Phonon dispersion was determined with Fourier interpolation of the dynamical matrices obtained at q-points on a uniform 2x2x2 mesh with DFT linear response technique as implemented in QE. We have carried out some of the calculations with LDA ultrasoft pseudopotentials (USPP) for benchmarking through comparison with results reported elsewhere.[20] We constructed 2x2x2 supercells of the most stable chemically ordered configuration of TiNF in both anatase and rutile forms and introduced a F-vacancy by removing one F atom in the supercell. We performed LDA+U calculations using U=3.0 eV in order to include on-site correlations of Ti-3*d* orbitals. Structures were internally relaxed maintaining the lattice constant obtained with U=0 eV. For a better comparison of the structures with F-vacancy

and pristine TiNF, we repeated the calculations of pristine TiNF including the U correction. To probe the optical properties of N, F-doped TiO_2, we obtained the imaginary part of dielectric tensors as a function of frequency.

II.4 Results and Discussion

II.4.1 Experimental results

We could obtain pure TiNF by an unexpected route involving the reaction of TiN with TiF_4 at 450ºC in a sealed tube under vacuum. When we heat this mixture, we find evidence for formation of TiF_3 along with a new solid phase which we could establish to be TiNF. We propose that the following reaction occurs between TiN and TiF_4.

$$TiN + TiF_4 \rightarrow TiNF + TiF_3 \quad (1)$$

As we keep heating the sample, TiF_3 disappears as vapour, giving rise to a clean diffraction pattern corresponding to the anatase structure. As can be seen from the X-ray diffraction (XRD) patterns in **Figure 1a**, after heating the mixture of TiN and TiF_4 at 450°C for 24 h (reaction step 1) they start forming a new compound leaving some residual phases as seen from the presence of the most intense reflection of TiF_3 in the diffraction pattern (marked as red asterisk). Subsequent heating of the product leads to diminishing intensities of the reflections of both TiF_3 and TiN (reaction steps 2 and 3), giving rise to a pattern corresponding to pure anatase. It is to be noted that there is no TiF_4 in the product. The observation of reflections of TiF_3 initially substantiates occurrence of the reaction in equation 1. The structure of anatase TiNF was solved by Rietveld refinement of the powder XRD data. It crystallises in a body-centered tetragonal cell with a space group $I4_1/amd$ with lattice parameters; a = 3.793 Å and c = 9.506 Å. We observe an increase in the unit cell

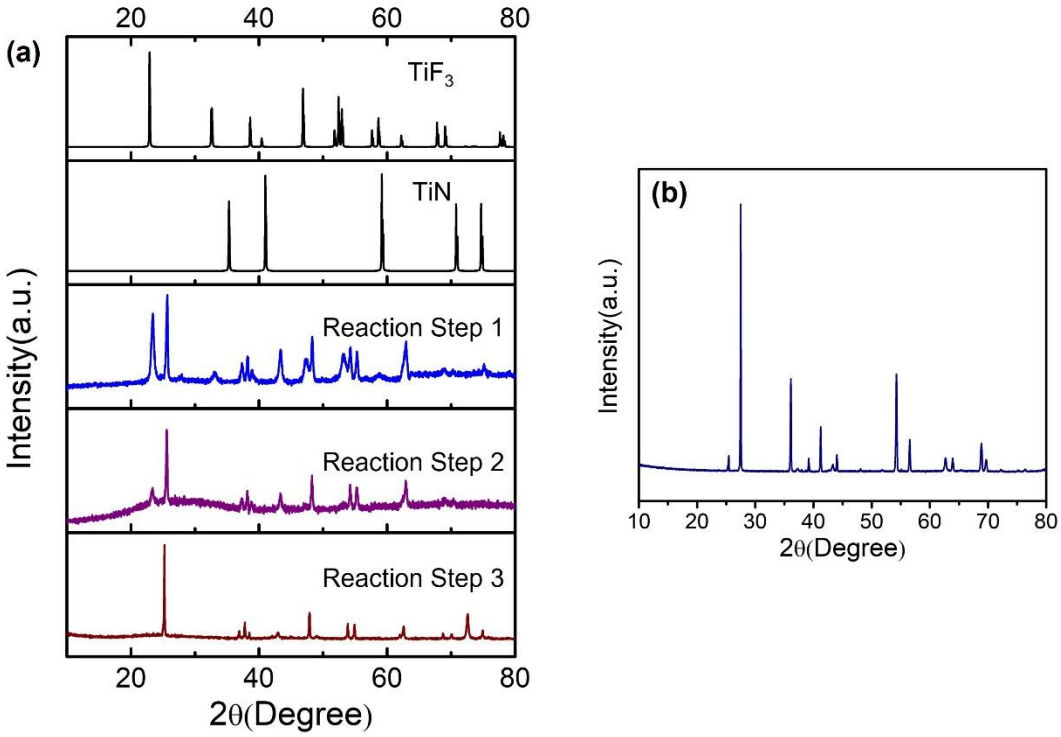

Figure 1. X-ray diffraction patterns (a) of the product of the reaction of TiN with TiF_4. Pattern obtained after reaction step three is TiNF in the anatase structure, red asterisk is the most intense reflection of TiF_3, (b) rutile TiNF.

parameter 'a' while a decrease of the parameter 'c' compared to those of anatase TiO_2 (a= 3.785 Å and c= 9.5196 Å). By following the above procedure at a higher temperature (600°C) we could obtain TiNF in the rutile structure (**Figure 1b**). We recall that anatase TiO_2 transforms to the rutile phase on heating.[21] Rutile TiNF crystallises in a tetragonal cell with a space group $P4_2/mnm$ with cell parameters a = 4.612 Å and c = 2.969 Å. There is an increase in the unit cell parameters compared to those of rutile TiO_2 (a= 4.5937 Å and c= 2.9587 Å). These values of lattice parameters for the refined structure are in good agreement with the corresponding values from the theoretically predicted structure (**Table 1**).

Table 1. Comparison of Lattice Parameters obtained using LDA Norm-Conserving Pseudo potentials with the experimental values.

	Lattice constant (Å)	
System	Experimental	**LDA-NC**
Anatase TiO_2	a=b=3.785, c=9.5196	----------
Rutile TiO_2	a=b=4.5937, c=2.9587	----------
Anatase TiNF	a=b=3.79, c=9.50	a=3.81, b=3.82, c=9.49
Rutile TiNF	a=b=4.61, c= 2.96	a=4.55, b=4.68, c=2.99
$TiO_{1.8}N_{0.1}F_{0.1}$	a=b=3.79, c=9.51	a=3.79, b=3.78, c=9.22 ($TiO_{6/4}N_{1/4}F_{1/4}$)

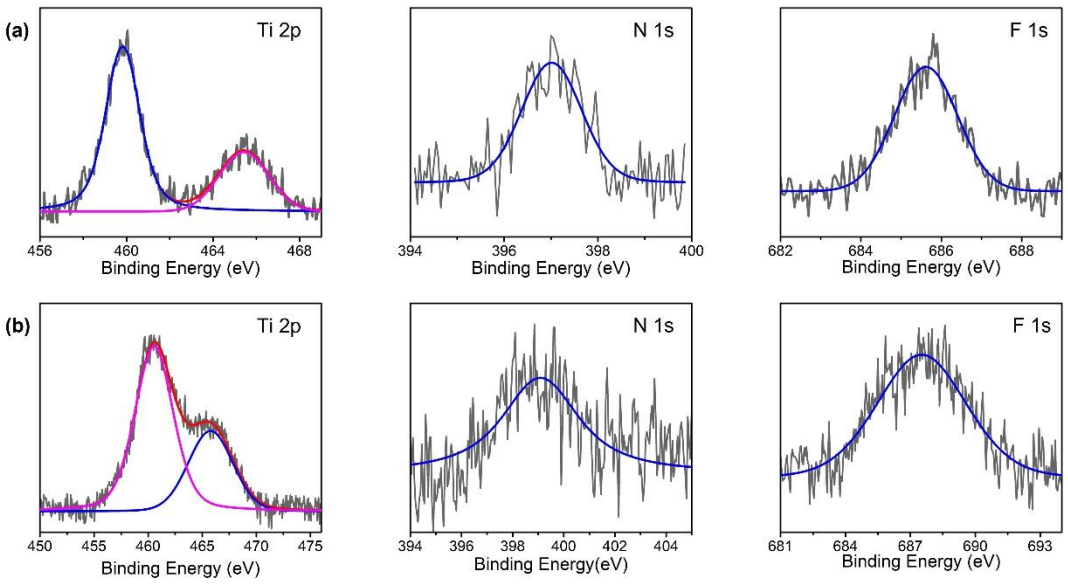

Figure 2. Core level X-ray photoelectron spectra for (a) anatase TiNF, (b) rutile TiNF.

Compositions of the anatase and rutile phases of TiNF were examined by X-ray photoelectron spectroscopy. **Figure 2** shows the core level XPS spectra of the anatase and rutile phases of TiNF. The XPS shows the presence of Ti, N and F. The XPS signals at 459.8 eV and 465.6 eV correspond to Ti ($2p_{3/2}$ and $2p_{1/2}$) which confirms the oxidation state of Ti as +4. A higher binding energy of Ti $2p_{3/2}$ at 459.8 eV in comparison with the standard value of 458.0 eV implies that the surface acidity of TiNF is higher as compared to TiO_2. The signals at 397 eV and 685.6 eV correspond to N1s and F1s respectively. Similarly for rutile TiNF, signals at 460.5 eV and 467.0 eV corresponds to Ti ($2p_{3/2}$ and $2p_{1/2}$). Signals at 399.0 eV and 687.0 eV correspond to N1s and F1s respectively. The compositions derived from the spectra were close to TiNF. Presence of Ti^{3+} could not be detected by XPS. Both anatase and rutile phases of TiNF were dark in colour, partially due to the presence of traces of Ti^{3+}, beyond the detection limit by X-ray diffraction. Reports of dark colour of such materials has been reported in the literature.[22,23] Electron paramagnetic resonance (EPR) spectra were recorded to detect the presence of Ti^{3+} in the TiNF samples. The TiNF samples (anatase and rutile) gave rise to a EPR signal with a g value of 2.191(**Figure 3**).

TiO_2 partially substituted by N and F with the composition $TiO_{1.8}N_{0.1}F_{0.1}$ was prepared by heating TiO_2 and NH_4F at 500°C in an NH_3 atmosphere. The structure of the product as revealed by XRD (**Figure 4a**), is that of the anatase with unit cell parameters a = 3.793 Å and c = 9.510 Å. We have also prepared N, F- substituted TiO_2 by the reaction of amorphous TiO_2, obtained from the hydrolysis of $TiCl_4$, with NH_4F in an ammonia atmosphere. By this method we obtained a composition $TiNF_{0.4}O_{0.3}$. XRD pattern (**Figure 4b**) shows that this composition has a structure comparable to that of Ti_3O_5. It belongs to

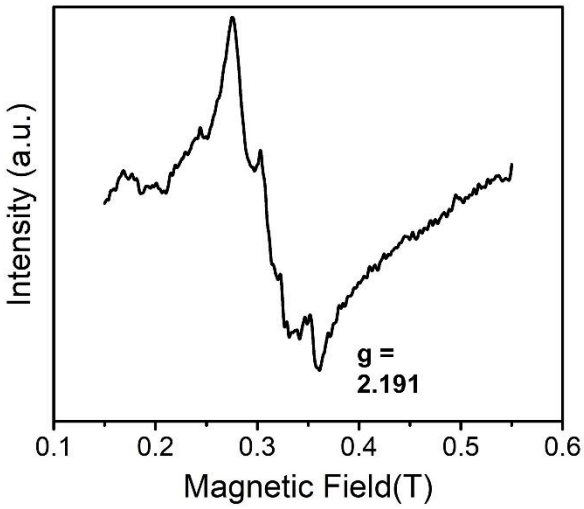

Figure 3. Electron paramagnetic resonance (EPR) spectra of TiNF.

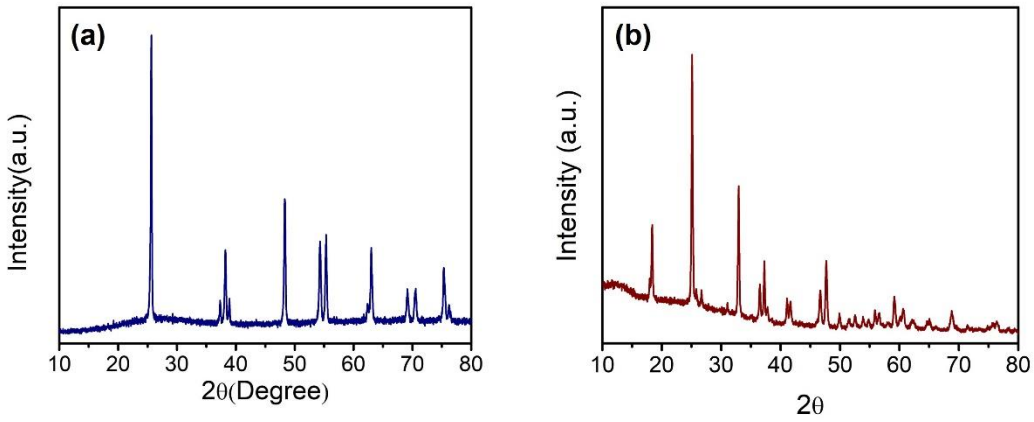

Figure 4. XRD patterns of (a)Anatase $TiO_{1.2}N_{0.1}F_{0.1}$ (b) $TiNF_{0.4}O_{0.3}$ (related to the magneli phase Ti_3O_5).

the monoclinic crystal system with the space group C2/m and unit cell parameters of a = 9.661 Å, b = 3.816 Å, c = 9.867 Å and β = 89.95º. It is interesting to get an N,F – substituted Ti_3O_5 which is the first Magneli phase in the Ti oxides (Ti_nO_{2n-1}).

Figure 5a shows optical absorption spectra of anatase and rutile phases of TiNF. Anatase TiNF shows a broad absorption band centred at 315 nm with a shoulder starting from 500 nm. This extension of the absorption to visible region is characteristic of the Ti^{3+} species in the sample which could induce a vacancy band below the conduction band[24] and could also generate anionic vacancy which forms an impurity level above valence band[25] thereby narrowing the band gap.[26] Rutile TiNF shows an absorption band centered at 365 nm. There is a feature in the absorption spectra of rutile phase TiNF originating in the infrared region which is attributed to the plasma reflectivity of the free carriers. **Figure 5b** shows the Tauc plots of TiO_2 and N,F-codoped TiO_2 of the composition $TiO_{1.8}N_{0.1}F_{0.1}$. Cosubstitution of N and F in TiO_2 confers visible absorption to TiO_2 and makes it coloured. Band gap of $TiO_{1.8}N_{0.1}F_{0.1}$ estimated from the Tauc plot is 2.6 eV with a decrease of 0.6 eV relative to TiO_2 (3.2 eV). The estimated band gap of $TiNF_{0.4}O_{0.3}$ with the Ti_3O_5 structure is 2.3 eV (Fig 5b)

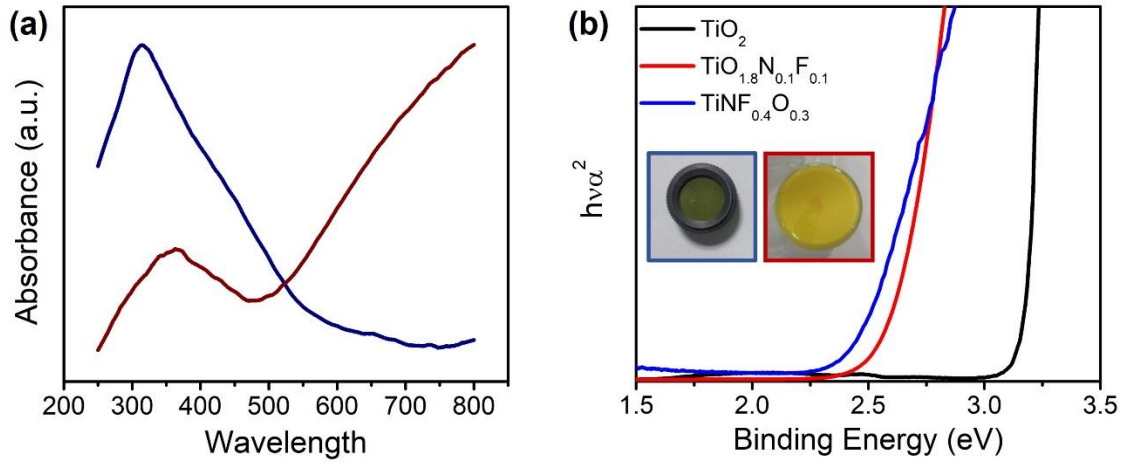

Figure 5. (a) UV-Vis absorption spectra of anatase and rutile TiNF. (b) Tauc plots of TiO_2, $TiO_{1.8}N_{0.1}F_{0.1}$ and $TiNF_{0.4}O_{0.3}$.

II.4.2 Results of First-principle calculations

Anatase TiNF crystallizes in the body-centred tetragonal (BCT) crystal structure. Since all its anion sites are symmetry equivalent, N and F atoms can be arranged in the three symmetry inequivalent configurations of the conventional unit cell ($Ti_4N_4F_4$) (**Figure 6a**). In the first configuration, alternating (001) planes are occupied entirely by N atoms and F atoms (configuration I). In the second, N and F atoms occupy the alternate atomic sites (configuration II), and in the third, N and F atoms occupy alternate sites only in (001) plane such that the diagonally opposite sites of the unit cell are occupied by the same species (configuration III). Matar[20] has reported results for electronic and structural properties of TiNF using first-principles calculations, considering the configurations I and II. As our estimates of lattice constants (**Table 2**) and the reported values obtained using USPP are different, we performed structural relaxation of configurations I and II using USPP. In TiNF in the rutile structure N and F atoms can be arranged in two symmetry inequivalent configurations. In configuration I of rutile TiNF (**Figure 6b**), N and F atoms occupy sites in alternating (001) planes, while in configuration II, N and F occupy the alternate atomic sites. The complete substitution of O by N and F leads to the elongation of lattice constants. Since the structure is disordered, we do not get $\gamma=90^o$ in configuration I and structure is orthorhombic for configuration II. For configuration II we get a lattice constant a=4.55 Å, b=4.68 Å. The lattice constants of anatase and rutile TiNF are compared to the experimental values Table 1.

We have considered the various chemical ordering of N and F atoms substituted in TiO_2 by substituting two O atoms by one N and one F atoms in the conventional unit cell of anatase TiO_2. Using site occupancy disorder (SOD)[27] technique we obtained seven

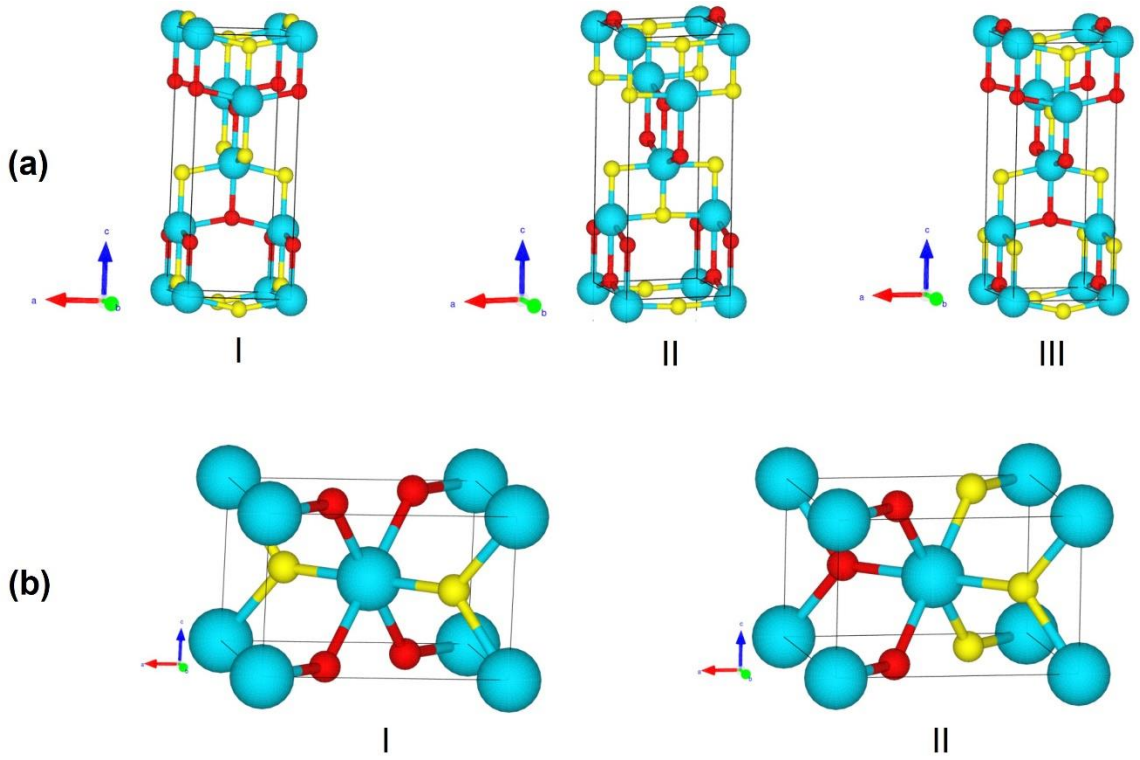

Figure 6. Various chemically ordered states of N and F in (a) anatase TiNF, (b) rutile TiNF. Ti, N and F atoms are represented by blue, yellow, and red spheres respectively.

Table 2. Lattice constants (Å) and electronic band gaps estimated within LDA and HSE calculations for anatase TiNF in the three configurations. The electronic band gaps of rutile TiNF are in parentheses.

Structural parameters	**Experimental**	**Config I**	**Config II**	**Config III**	**Config III(distorted)**
a/b	3.7891	3.84	3.81	3.86/3.80	3.80/3.82
c	9.4863	9.33	9.57	9.40	9.49
Band gap (LDA-NC)		0.68(0.28)	1.92(1.64)	1.36	2.10
Band gap (HSE)		2.17(1.89)	3.46(2.70)	2.73	3.35

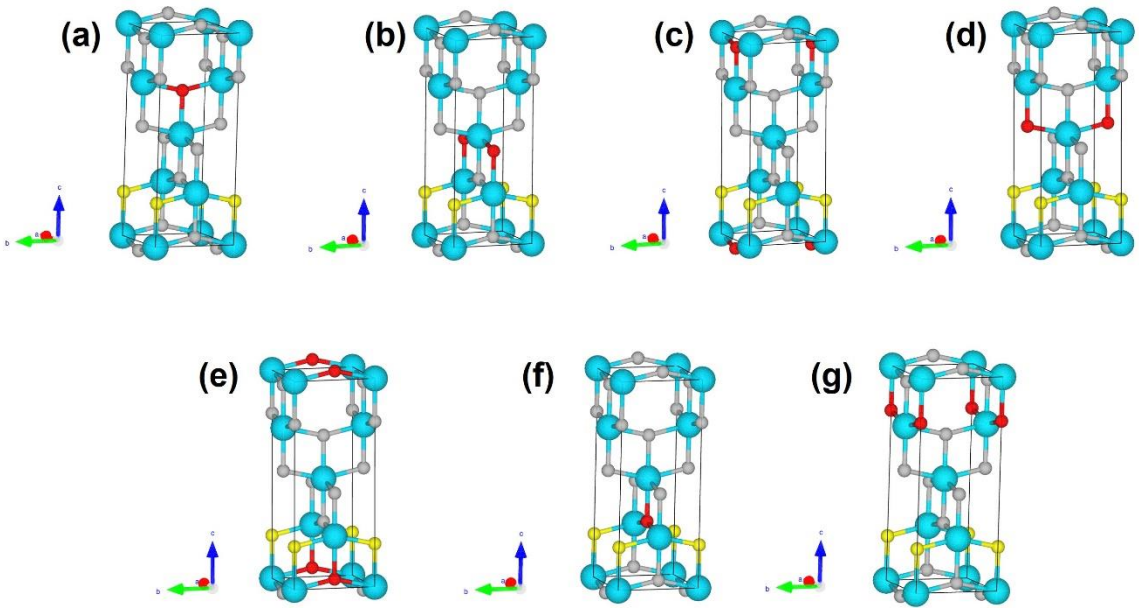

Figure 7. Various chemically ordered states of N and F substituted anatase TiO_2 ($TiO_{6/4}N_{1/4}F_{1/4}$).

inequivalent configurations of $TiO_{6/4}N_{1/4}F_{1/4}$ (**Figure 7**). Energies of these configurations, lattice constants and band gap (**Table 3**) show that the stable configuration is the one in which one plane is completely occupied by N atoms and another plane is occupied by F atoms such that N-Ti-F bonding occurs along (001) direction (**Figure 7g**). The substitution of N and F for oxygen results in expansion of the lattice of TiO_2.

We obtained formation energies of different configurations of TiNF using relation $E_{Ti_2N_2F_2} - E_{hcp}^{Ti} - E_{N_2} - E_{F_2}$, where $E_{Ti_2N_2F_2}$, E_{hcp}^{Ti} , E_{N_2} and E_{F_2} are the energies of bulk TiNF, hexagonal close packing (hcp) Ti crystal, isolated N_2 and F_2 molecules, respectively. We find that the configuration III is energetically favourable of all the considered configurations (**Figure 6a**). In TiNF in the rutile structure, configuration II with N and F atoms occupying the alternate sites is the most stable (**Figure 6b**). TiNF in its rutile structure is energetically favourable by 0.13 eV/f.u. than its anatase structure.

Table 3. Relative energies ($\Delta E=E_n-E_7$), lattice constants and associated band gaps (obtained using LDA-NC) of various chemical ordering of N and F atoms in anatase $TiO_{6/4}N_{1/4}F_{1/4}$.

Configurations	ΔE (meV/f.u.)	Lattice constants (Å)	Band gaps (eV)
1	68	a=3.75, b=3.80, c=9.26	0.95
2	47	a=3.78, b=3.79, c=9.22	0.92
3	6	a=3.74, b=3.78, c=9.27	1.80
4	60	a=3.75, b=3.81, c=9.24	0.96
5	3	a=3.75, b=3.78, c=9.32	1.38
6	17	a=3.74, b=3.79, c=9.26	1.45
7	0	a=3.79, b=3.78, c=9.22	1.01

In calculation of formation energies of $TiO_{6/4}N_{1/4}F_{1/4}$ configurations we used $E_{TiO_{\frac{6}{4}}N_{\frac{1}{4}}F_{\frac{1}{4}}}$ - $2E_{hcp}^{Ti}$- $\frac{1}{2}E_{N_2}-\frac{1}{2}E_{F_2}$-$3E_{O_2}$. E_{O_2} is the energy of gaseous oxygen molecule. The formation energy of the stable configuration (configuration VII) of N, F-doped anatase TiO_2 is -10.57 eV/f.u, indicating its formation is more favorable than that of TiNF (-7.51 eV/f.u), as expected from the generically greater stability of oxides. We find that $E_{TiO_{\frac{6}{4}}N_{\frac{1}{4}}F_{\frac{1}{4}}}< \frac{3}{2}E_{Ti_2O_4}+\frac{1}{2}E_{Ti_2N_2F_2}$ by 0.1 eV/Ti atom indicating the formation of TiNF and TiO_2 more favourable compared to $TiO_{6/4}N_{1/4}F_{1/4}$.

Electronic structure of anatase TiO_2 (**Figure 8a**) obtained along the high symmetry lines of BZ shows an indirect band gap of 2.35 eV with a dominant contribution of Ti-3d and O-2p in CBM and VBM respectively (**Figure 8b**) and is in a good agreement with

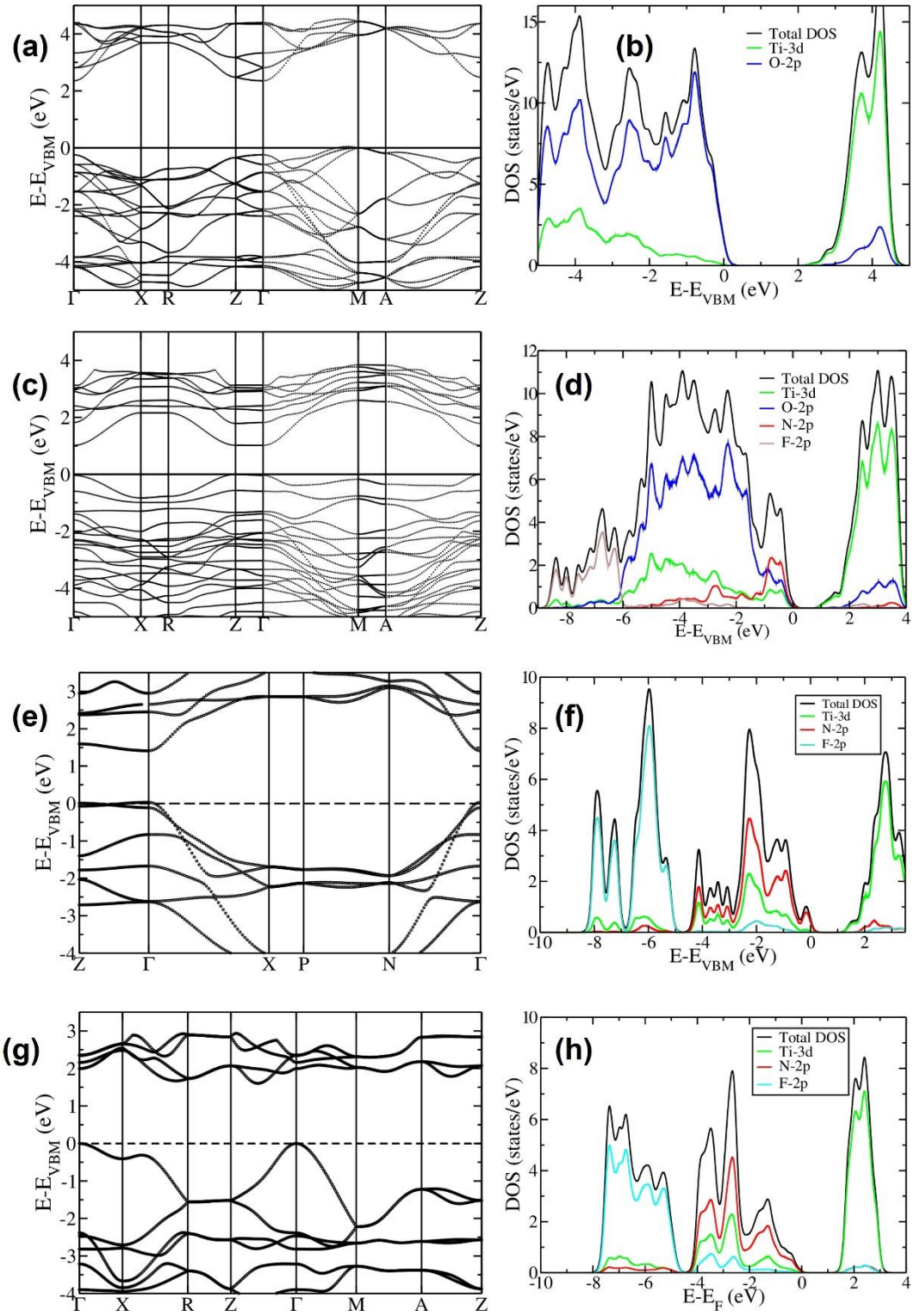

Figure 8. Electronic structure and density of states of (a) TiO_2, (b) $TiO_{6/4}N_{1/4}F_{1/4}$, (c) anatase TiNF and (d) rutile TiNF in the most stable configuration

other theoretical results.[28] Comparison of the electronic structures of anatase and rutile TiNF is depicted in **Figure 8e and 8g**. Configuration III of the anatase structure is energetically most stable with a direct band gap of 1.36 eV at the Γ-point (**Figure 8c**) and an indirect band gap of 2.73 eV using hybrid functional based calculations (**Table 2**). From the PDOS, it is clear that the states near valence band maximum (VBM) have a predominant contribution from 2p orbitals of N, with a slight mixing with Ti-3d states. Lower energy (-6 eV) valence bands are constituted primarily of F-2p orbitals. The states at the conduction band minimum (CBM) have a predominant contribution from Ti-3d orbitals (**Figure 8d**), similar to that of TiO_2, confirming the idea of valence band engineering of oxides with anion substitution.[1] Configuration II represents the most stable chemical ordering of N and F in TiNF in the rutile structure. We find an indirect band gap of 1.64 eV using LDA-NC (**Figure 8g**) and 2.70 eV using HSE calculations. Similar to TiNF in the anatase structure, we have a dominant contribution of Ti-3d orbitals in conduction bands and of N-2p orbitals in valence bands (**Figure 8h**). In $TiO_{6/4}N_{1/4}F_{1/4}$, we find an indirect band gap of 1.01 eV (**Figure 8c**) in the electronic structure obtained with LDA calculations. In the HSE band structure, the band gap is 2.37 eV. Complete substitution of O with N and F in TiO_2 increases the band gap significantly, with states at VBM having a dominant contribution from N-2p orbitals and states near the CBM mostly comprising of Ti-3d states (**Figure 8d**).

Examining the electronic structure of three chemically ordered configurations of anatase TiNF along high symmetry lines of the BZ of the primitive body centred tetragonal (BCT) unit cell (**Figure 9**). It is clear that different ordering of N and F in the lattice influences its band gaps (**Table 2**). As expected, the most stable of the configurations has

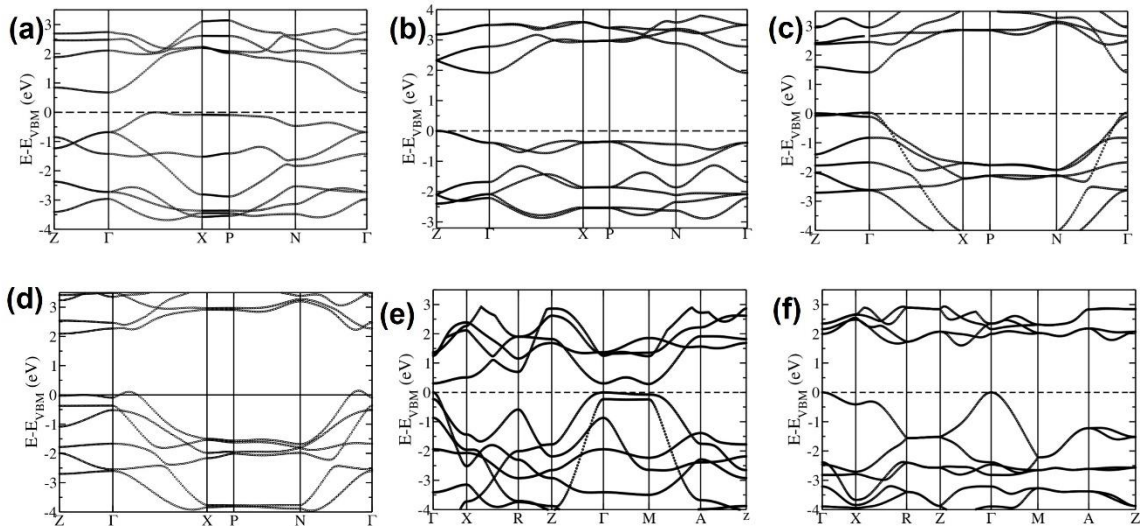

Figure 9. Electronic structure of (a-c) three configurations of anatase TiNF, (d) distorted anatase structure and (d-e) two configurations of rutile TiNF.

the widest band gap. Our LDA-based estimate of the band gap of configuration I is 0.68 eV, which was predicted to be metallic by Matar[20] In this work, the author determined the electronic nature of configuration I based on projected density of states (PDOS). In a calculation based on LDA-USPP, the band gap of configuration I is 0.12 eV which can be missed in the PDOS through use of broadening of the δ function. Electronic bands obtained along high symmetry lines of the BZ clearly show an indirect band gap of 0.68 eV (**Figure 9a**) for configuration I using LDA-NC. We find an indirect band gap of 1.92 eV for configuration II (**Figure 9b**), which is quite close to the estimate of 2.0 eV by Matar.[20]

In the phonon spectrum calculated along high symmetry lines in the BZ of configuration III of TiNF in the anatase structure, we find some modes with imaginary frequencies along Z-Γ- X lines (**Figure 10**). The mode with imaginary frequency of 255 cm^{-1} at Γ- point involves the in-plane displacements of N atoms in opposite directions. We distorted the structure by freezing these modes through displacements of atoms by 0.03 Å

and obtained a new lower energy structure upon relaxation (will be termed as the distorted structure).

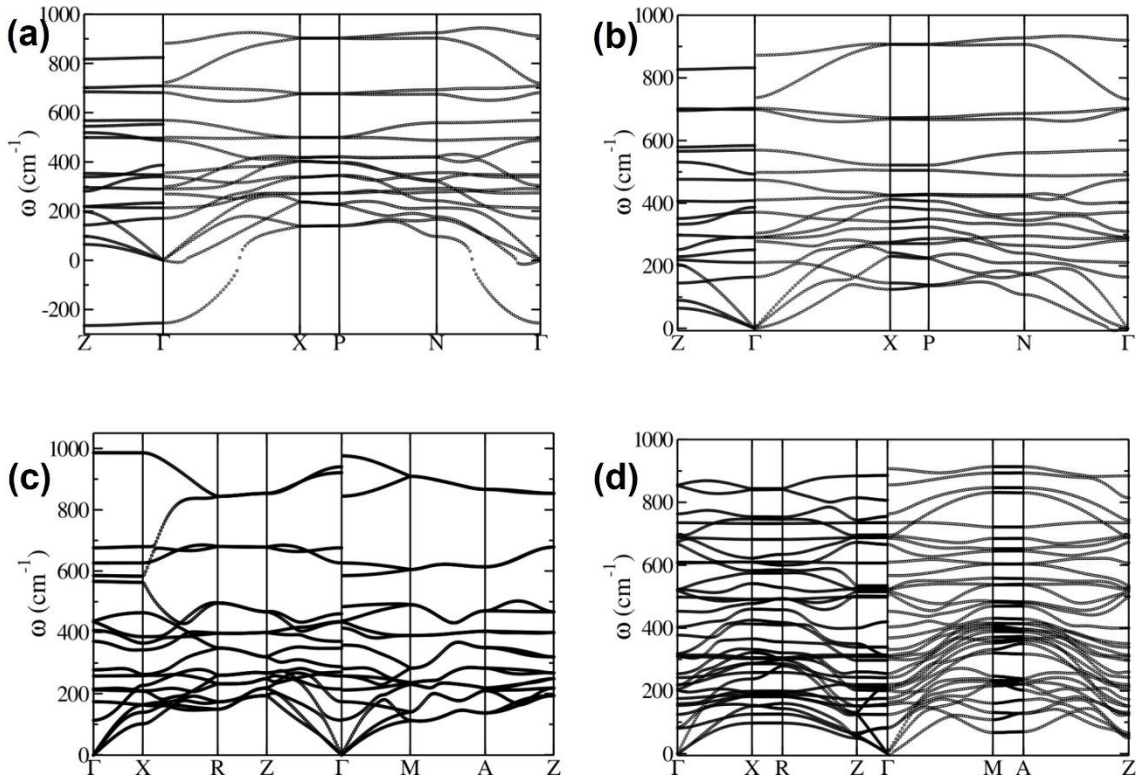

Figure 10. Phonons spectra of configuration III of TiNF in (a) undistorted and, (b) distorted anatase structure, in (c) Rutile structure and (d) N,F-doped TiO_2 in anatase structure.

The lattice constants of the distorted configuration III after freezing the mode are (a=3.81Å, b=3.82 Å and c=9.49 Å), in even better agreement with the experimental values. The energy of the relaxed structure reduces by 0.024 eV/f.u relative to the undistorted one and its band gap changes from a direct to an indirect type, and with enhancement to 2.1 eV (LDA estimate) (**Figure 9d**). Calculations with the HSE functional yields an estimate of the band gap of 3.35 eV, while the rest of the electronic structure remains qualitatively similar. We find no unstable modes ($\omega^2 < 0$) in the phonon dispersion of distorted structure

(**Figure 10b**), confirming its local stability (as an energy minimum). Phonon spectrum of TiNF in the rutile structure has no imaginary frequencies indicating its local stabiliy (**Figure 10c**). Phonon bands are more dispersed in the rutile structure compared to the anatase structure. Configuration VII of N, F-doped anatase TiO_2, has no unstable modes indicating its stability (**Figure 10d**). The polar character of the phonons of TiNF (both rutile and anatase) and N, F-doped anatase TiO_2 is clearly evident in the LO-TO splitting in their phonon spectra.

To understand the dark color of anatase and rutile phases of TiNF, we introduced Ti^{3+} defects in the rutile and anatase phases by creating a F-vacancy in the supercell. Vacany formation energy (E_v) of TiNF in the rutile and anatase phases are 3.17 eV and 4.81 eV respectively, which are comparable to anion vacancy formation energies[23], making them quite feasible in samples. From the calculated electronic structures, it is clearly evident that the band gap reduced from 1.60 eV to 1.1 eV upon introduction of F-vacancy in anatase TiNF. Similarly, there is a change in band gap from 1.75 eV to 0.92 eV due to F-vacancy in the rutile TiNF. Electronic structures (**Figure 11**) clearly show an isolated defect band just below the conduction band in both the phases of TiNF.

From the projected density of states (**Figure 11 e**), it is seen that these defect states are comprised of Ti-3*d* orbitals. Valence band maximum constitutes primarily of N-2*p* states in both the phases. The transition from N-2*p* states to Ti^{3+} defect band is very likely responsible for its black color. We notice an F-2*p* peak around -6 eV due to F-vacancy in anatase TiNF. Assuming that the hybrid functionals give similar increments in the band gap as in pristine TiNF, we predict the HSE band gaps of anatase and rutile TiNF with F-vacancy to be about 2.35 eV and 1.98 eV respectively, which belong to the green and

orange-red regions of the visible light spectrum respectively giving the sample its dark or blackish color.

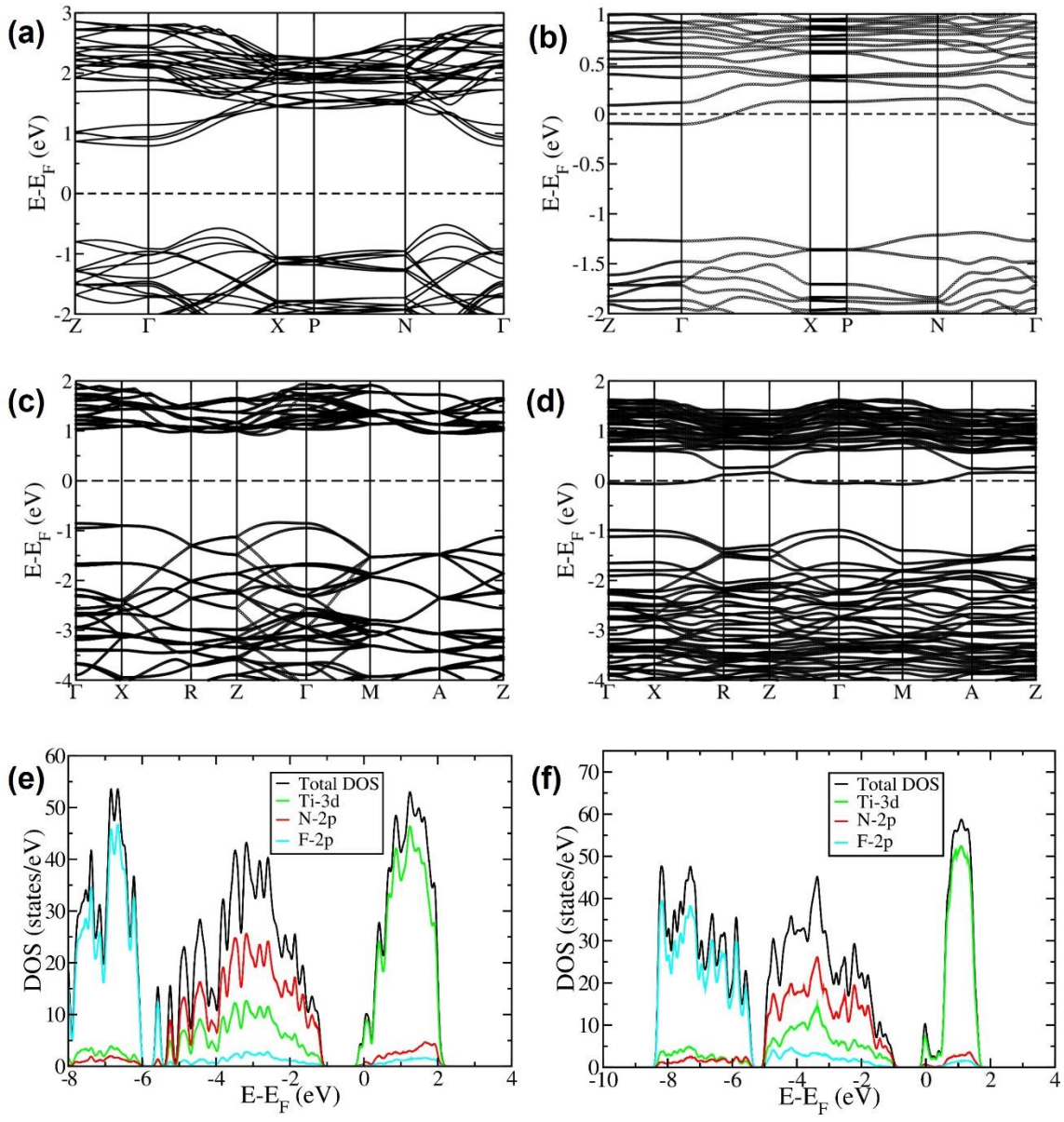

Figure 11. Electronic structure of (a) pristine anatase TiNF, (b) with F-vacancy anatase TiNF, (c) rutile TiNF, and (d) rutile TiNF with F-vacancy. Projected density of states of (e) anatase TiNF, and (f) rutile TiNF with F-vacancies.

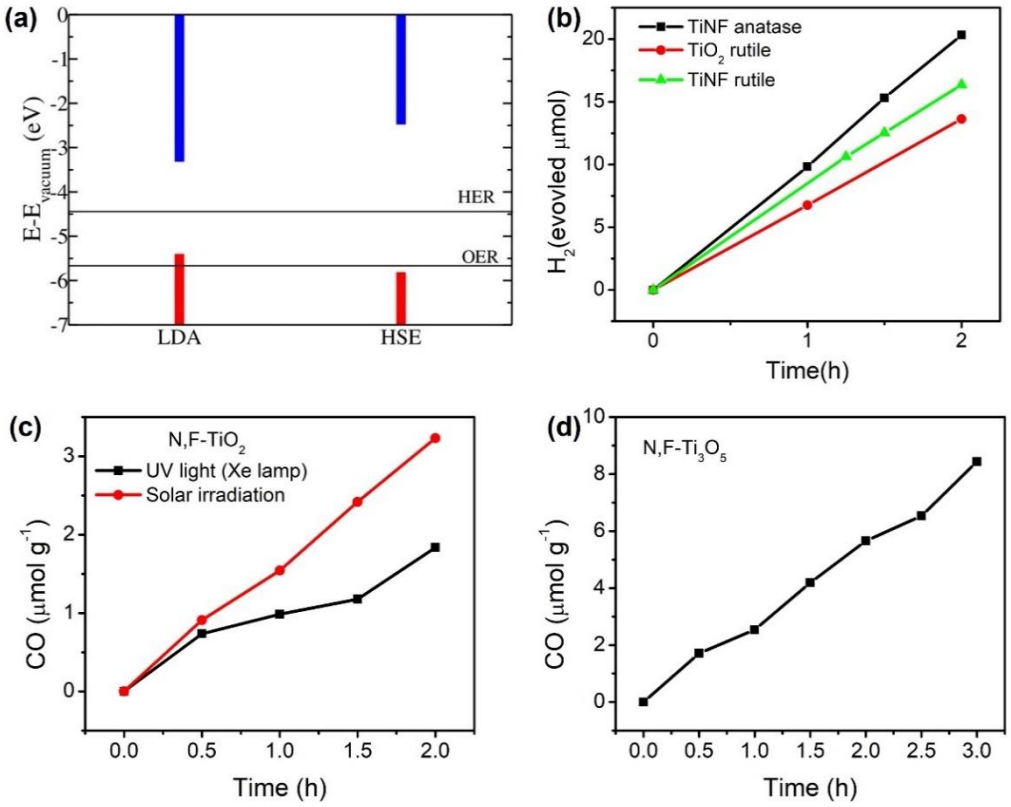

Figure 12. (a) Valence band and conduction band edges of anatase TiNF (configuration III) determined with LDA and HSE calculations, aligned with respect to vacuum potential at 0 along with the redox potentials of hydrogen evolution reaction (HER) and oxygen evolution reaction (OER). (b) Photocatalytic HER of anatase and rutile phase TiNF in comparison to TiO_2. Gas phase photocatalytic CO_2 reduction activity of (c) N,F-TiO_2 and (d) N,F-Ti_3O_5. For HER, catalyst (10 mg) was dispersed in 50 mL millipore water with Na2S-Na2SO3 as sacrificial reagent. For gas phase photocatalytic reduction of CO2 experiments,10 mg of the photocatalyst was deposited on flat face of the cell and filled with humidified CO_2. A 400W Xe lamp fitted with a UV cut-off filter (λ> 395 nm) and IR filter was used as a light source

II.4.3 Photocatalytic hydrogen evolution and CO_2 reduction

TiO_2 is known to exhibit good photocatalytic activity.[29] As 2p orbitals of N and F are similar to 2p orbitals of O, we probed the photocatalytic activity by aligning its VBM

and CBM with respect to the vacuum potential (**Figure 12**). To connect with vacuum potential, we constructed a slab with the (001) surfaces of TiNF (using relaxed bulk coordinates) and used it in a supercell with vacuum of 15 Å along z-direction. We determined the difference ΔV between the potentials in the vacuum and deep inside the bulk and find that ΔV value does not change with the number of unit cells (the difference between ΔV obtained with slabs of 1- and 2-unit cells being ~0.01 eV). Hence, we proceed further with the TiNF (001) slab consisting of just 1 unit of TiNF. We obtain the energies of bulk VBM and CBM bands relative to its macroscopic average potential in the vacuum (ΔV), and then align the bulk band edges with respect to ΔV as shown in **Figure 12a**. The VBM and CBM edges (obtained with HSE calculations) straddle the hydrogen evolution reaction (HER) and oxygen evolution reaction (OER) potentials, and we thus expect anatase TiNF to be suitable for photocatalysis of water splitting reaction. N,F-doping in TiO_2 is indeed known to enhance the photocatalytic activity.[30–33]

Preliminary experiments were performed to study the performance of anatase and rutile phases of TiO_2 towards photocatalytic hydrogen evolution activity and photocatalytic CO_2 reduction. Photocatalytic HER studies were carried out in millipore water with Na_2S and Na_2SO_3 as sacrificial agents under UV light irradiation. Interestingly, anatase and rutile phase TiNF exhibits H_2 production rate of 10 μmol h^{-1} and 9 μmol h^{-1}, respectively which higher than undoped TiO_2 (7 μmol h^{-1}) (**Figure 12b**). While both phases of TiNF did not exhibit any considerable activity towards gas phase photocatalytic CO_2 reduction, N,F-TiO_2 and N,F-Ti_3O_5 reduce CO_2 to CO under UV light and direct solar radiation (**Figure 12c and 12d**). These results are interesting since undoped TiO_2 shows very poor CO_2 reduction activity in the absence of cocatalysts.

II.5 Conclusions

It is worthy to note that we have succeeded in preparing both anatase and rutile phases of TiNF obtained by complete replacement of O by N and F. As expected, cosubstitution of N, F brings about changes in properties of oxides but the structural parameters of TiNF and other compositions are comparable to those of the oxide phases. TiNF and N, F doped anatase TiO_2 are indirect band gap semiconductors. N, F substitution in TiO_2 reduces its band gap significantly, but the band gap of TiNF is close to that of TiO_2. Based on the analysis of conduction and valence band edges, we predict TiNF to be suitable for photocatalytic water splitting reaction. Preliminary experimental results show that both anatase and rutile TiNF exhibit better photocatalytic HER activity than TiO_2. Moreover, N,F-doped TiO_2 and N,F-Ti_3O both reduces CO_2 to CO under direct solar irradiation.

II.6 References

[1] C. N. R. Rao, *J. Phys. Chem. Lett.* **2015**, *6*, 3303.

[2] C. M. Fang, K. v. Ramanujachary, H. T. Hintzen, G. de With, *J. Alloys Compd.* **2003**, *351*, 72.

[3] R. Saha, S. Revoju, V. I. Hegde, U. v. Waghmare, A. Sundaresan, C. N. R. Rao, *ChemPhysChem* **2013**, *14*, 2672.

[4] S. R. Lingampalli, C. N. R. Rao, *J. Mater. Chem. A* **2014**, *2*, 7702.

[5] S. R. Lingampalli, K. Manjunath, S. Shenoy, U. v. Waghmare, C. N. R. Rao, *J. Am. Chem. Soc.* **2016**, *138*, 8228.

[6] S. Kouser, S. R. Lingampalli, P. Chithaiah, A. Roy, S. Saha, U. v. Waghmare, C. N. R. Rao, *Angew. Chem.* **2015**, *127*, 8267.

[7] D. Li, H. Haneda, N. K. Labhsetwar, S. Hishita, N. Ohashi, *Chem. Phys. Lett.* **2005**, *401*, 579.

[8] R. Asahi, T. Morikawa, T. Ohwaki, K. Aoki, Y. Taga, *Science* **2001**, *293*, 269.

[9] A. Fujishima, K. Honda, *Nature* **1972**, *238*, 37.

[10] X. Chen, S. S. Mao, *Chem. Rev.* **2007**, *107*, 2891.

[11] T. L. Thompson, J. T. Yates, *Chem. Rev.* **2006**, *106*, 4428.

[12] Y. Cong, J. Zhang, F. Chen, M. Anpo, *J. Phys. Chem. C* **2007**, *111*, 6976.

[13] D. Li, N. Ohashi, S. Hishita, T. Kolodiazhnyi, H. Haneda, *J. Solid State Chem.* **2005**, *178*, 3293.

[14] D. Li, H. Haneda, S. Hishita, N. Ohashi, *Chem. Mater.* **2005**, *17*, 2596.

[15] C. Wüstefeld, T. Vogt, U. Löchner, J. Strähle, H. Fuess, *Angew. Chem. Int. Ed.* **1988**, *27*, 929.

[16] K. Nukumizu, J. Nunoshige, T. Takata, J. N. Kondo, M. Hara, H. Kobayashi, K. Domen, *Chem. Lett.* **2003**, *32*, 196.

[17] H. A. Seibel, P. Karen, T. R. Wagner, P. M. Woodward, *J. Mater. Chem.* **2009**, *19*, 471.

[18] P. Giannozzi, S. Baroni, N. Bonini, M. Calandra, R. Car, C. Cavazzoni, D. Ceresoli, G. L. Chiarotti, M. Cococcioni, I. Dabo, A. Dal Corso, S. de Gironcoli, S. Fabris, G. Fratesi, R. Gebauer, U. Gerstmann, C. Gougoussis, A. Kokalj, M. Lazzeri, L. Martin-Samos, N. Marzari, F. Mauri, R. Mazzarello, S. Paolini, A. Pasquarello, L. Paulatto, C. Sbraccia, S. Scandolo, G. Sclauzero, A. P. Seitsonen, A. Smogunov, P. Umari, R. M. Wentzcovitch, *J. Phys.: Condens. Matter* **2009**, *21*, 395502.

[19] J. Heyd, G. E. Scuseria, M. Ernzerhof, *J. Chem. Phys.* **2003**, *118*, 8207.

[20] S. F. Matar, *J. Solid State Chem.* **2012**, *185*, 25.

[21] S. R. Yoganarasimhan, C. N. R. Rao, *Trans. Faraday Soc.* **1962**, *58*, 1579.

[22] A. Naldoni, M. Allieta, S. Santangelo, M. Marelli, F. Fabbri, S. Cappelli, C. L. Bianchi, R. Psaro, V. Dal Santo, *J. Am. Chem. Soc.* **2012**, *134*, 7600.

[23] W. Zhou, W. Li, J. Q. Wang, Y. Qu, Y. Yang, Y. Xie, K. Zhang, L. Wang, H. Fu, D. Zhao, *J. Am. Chem. Soc.* **2014**, *136*, 9280.

[24] F. Zuo, K. Bozhilov, R. J. Dillon, L. Wang, P. Smith, X. Zhao, C. Bardeen, P. Feng, *Angew. Chem. Int. Ed.* **2012**, *51*, 6223.

[25] J. Wang, P. Zhang, X. Li, J. Zhu, H. Li, *Appl. Catal. B. Environ.* **2013**, *134–135*, 198.

[26] L. bin Xiong, J. L. Li, B. Yang, Y. Yu, *J. Nanomater.* **2012**, *2012*, 13.

[27] R. Grau-Crespo, S. Hamad, C. R. A. Catlow, N. H. de Leeuw, *J. Phys.: Condens. Matter* **2007**, *19*, 256201.

[28] M. Landmann, E. Rauls, W. G. Schmidt, *J. Phys. Condens. Matter* **2012**, *24*, 195503.

[29] J. Schneider, M. Matsuoka, M. Takeuchi, J. Zhang, Y. Horiuchi, M. Anpo, D. W. Bahnemann, *Chem. Rev.* **2014**, *114*, 9919.

[30] A. Malashevich, M. Jain, S. G. Louie, *Phys. Rev. B: Condens. Matter Mater. Phys.* **2014**, *89*, 075205.

[31] I. Tanaka, F. Oba, K. Tatsumi, M. Kunisu, M. Nakano, H. Adachi, *Mater. Trans.* **2002**, *43*, 1426.

[32] R. Bès, Y. Pipon, N. Millard-Pinard, S. Gavarini, M. Freyss, *Phys. Rev. B: Condens. Matter Mater. Phys.* **2013**, *87*, 024104.

[33] A. Paris, S. Taioli, *J. Phys. Chem. C* **2016**, *120*, 22045.

Part III

Chemical functionalization of Antimonene nanosheets

Summary

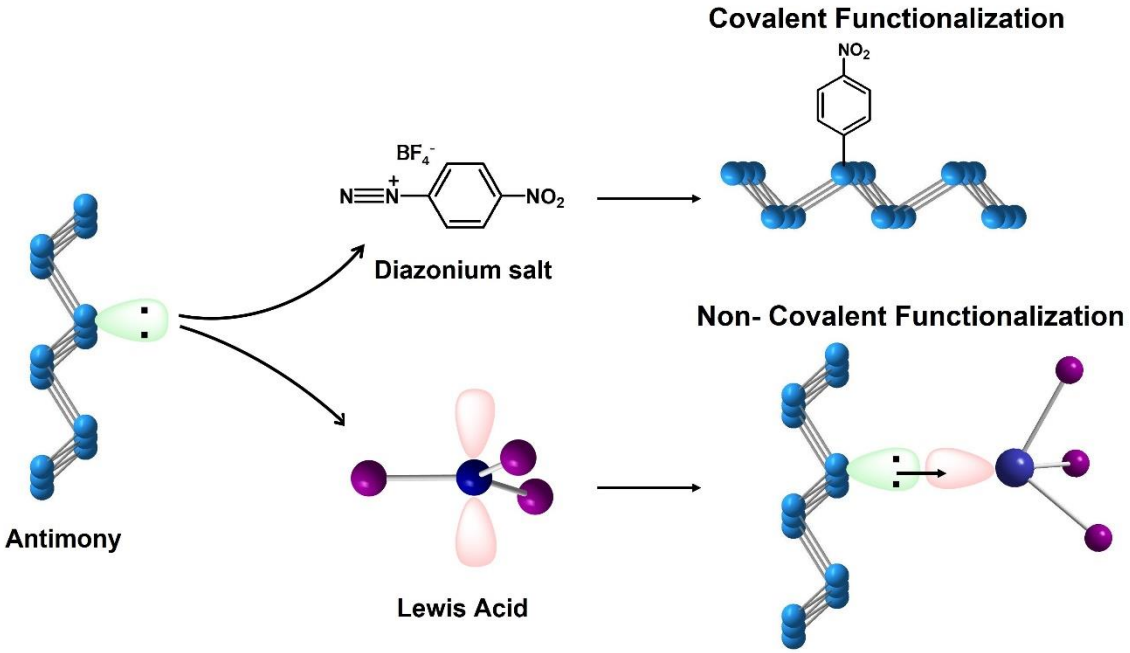

Group 15 pnictogens occupy a distinctive position among 2D materials owing to their band gaps (up to 2.5 eV). Phosphorene, the most studied pnictogen, despite its excellent electronic properties is highly unstable under ambient conditions, hence the growing interest in heavier pnictogens. Antimonene along with its ambient stability, has high electronic conductivity of up to 10^4 S m^{-1} and band gap ~2.4 eV. Antimonene crystallizes in a buckled honeycomb lattice which imparts anisotropy to the material. Bulk antimony is semi-metallic in nature but undergoes a transition to a semiconducting state in monolayer. In the work that follows, we have synthesized antimonene nanosheets of

varying thicknesses by liquid exfoliation. Interestingly, we observed band edge emission at ~2.23 eV for sheets thicker than monolayer which is due to quantum confinement and quasi-monolayer behavior due to turbostratic stacking. The presence of lone pair on antimony makes the surface reactive and susceptible to surface functionalization. Modification of antimonene by chemical functionalization can serve as a suitable approach towards tuning its electronic properties. To this effect we have studied the covalent and non-covalent functionalization of antimonene nanosheets.

Spontaneous covalent functionalization of antimonene nanosheets is achieved by reaction with diazonium salt. Non-covalent functionalization of antimonene nanosheets is achieved by reaction with group 12 and 15 Lewis acids. Interestingly, we observe a red and blue shift in emission spectra of antimonene after covalent and non-covalent functionalization, respectively. This opens the possibility of tuning the properties of antimonene and passivating the surface by functionalization.

III.1 Introduction

Two-dimensional materials exhibit fascinating physical properties owing to electron confinement in a plane.[1,2] Mechanical and chemical exfoliation of layered van der Waals materials were demonstrated by Frindt et al as early as 1966.[3,4] However, the surge in research on 2D materials was marked by the discovery of graphene in 2004.[5] Graphene possesses interesting electronic structure behaving as a semi metal with zero density of states at the Fermi level. Electronic bands cross the Fermi level at six points of a 2D hexagonal Brillouin zone and the dispersion relation is linear at these points of intersection leading to zero effective mass of electrons and holes.[6,7] These massless charge carriers impart excellent electronic properties such as high conductivity and mobility (10^5 cm^2 V^{-1} s^{-1}) to graphene.[5,8–10] The presence of strong C-C bonds and absence of dangling bonds in basal plane imparts high mechanical strength (Young's modulus ~1 TPa)[11] and chemical inertness, respectively.[2] Along with this, graphene possesses large theoretical surface area (2630 m^2 g^{-1}), high thermal conductivity (~5000 W m^{-1} K^{-1})[12] and high optical absorption.[9] However, application of graphene is limited due to its zero-band gap. Beyond graphene a wide spectrum of 2D materials such as transition metal dichalcogenides[13,14], metal halides[15], metal oxides[16,17], layered double hydroxides,[17,18] hexagonal boron nitride[19], metal carbides, group IV graphene/graphane analogues (silicene, germanane, etc.)[20–22], group V pnictogens,[23–25] are being explored for their unique electronic, mechanical, and optical properties with extraordinary potential for future technology development.[1]

III.1.1 Synthesis of 2D materials

Controllable synthesis of high-quality 2D materials is essential for their large-scale applications.[1,26] Synthesis of 2D material can be done by top-down approach involving separation of nanosheets from bulk solids or bottom-up synthesis (**Figure 1**). Separation from bulk material can be done by mechanical exfoliation[5] and chemical exfoliation.[27–29] Bottom-up approach requires pristine conditions and precise control over layer thickness which can be achieved by deposition techniques such as chemical vapor deposition, pulsed laser deposition and atomic layer deposition.[30] Mechanical exfoliation of layered bulk material can achieve high quality flakes but has low efficiency. Liquid reactions such as liquid phase exfoliation, chemical exfoliation and hydrothermal reactions produce smaller and low-quality sheets but with high efficiency. Vapor deposition techniques provides a balance between quality and efficiency but requires strict growth conditions such as high vacuum and high temperatures. Further transfer of deposited films to desired substrates introduces defects that depreciates their performance.

Top-down approach involving exfoliation of nanosheet from bulk layered material is feasible since layered materials have strong in-plane interaction and weak out-of-plane interactions, namely van der Waals interaction. Liquid phase exfoliation method is generally the most scalable top-down route to synthesize atomically thin sheet with controlled dimensions.[27,29] Dispersions of exfoliated nanosheets are beneficial since it allows deposition of films on surfaces, enables formation of heterostructures/composites by mixing dispersions of different materials and fabrication of electronic devices by techniques such as inkjet printing and roll-to-roll coating. There are four main liquid

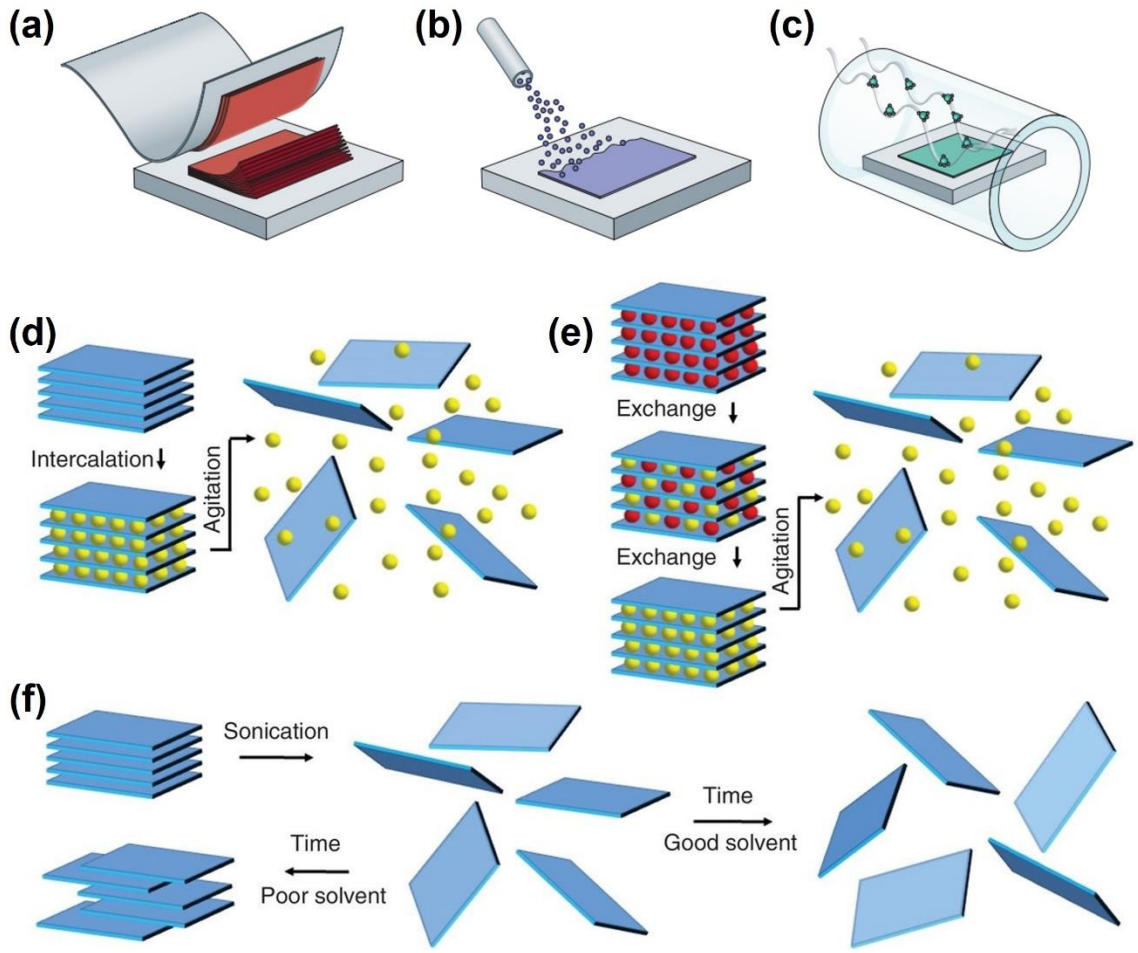

Figure 1. Schematic representation of synthesis methods of two-dimensional materials (a) micromechanical exfoliation, (b) physical vapor deposition, (c) chemical vapor deposition and (d-f) liquid phase exfoliation; (d) ion intercalation, (e) ion exchange, and (f) sonication assisted exfoliation. Reprinted with permission from Nature ref 2, Copyright 2017.

exfoliation techniques. First involves oxidation of layered material with oxidizers such as sulphuric acid and potassium permanganate followed by ultrasonication in a suitable solvent.[31,32] Second involves intercalation of ionic species such as n-butyllithium between layers, which weakens the interlayer interaction and reduces the energy barrier for exfoliation, followed by exfoliation by thermal shock or ultrasonication (**Figure 1d**).[3,33,34] Third, similar to second method, involves intercalation of ions by exchange of ions already

present in materials (LDHs, clays and metal oxides) followed by exfoliation by ultrasonication (**Figure 1e**).[17,35] Fourth, the most recent method involves exfoliation by ultrasonic waves in a suitable solvent (**Figure 1f**).[27,36,37] Ultrasonic waves generate cavitation bubbles that collapse into high-energy jets, splitting up the layered crystallites and producing exfoliated nanosheets. Interaction of solvent reduces the potential energy barrier and overcomes van der Waals interaction. Stability of exfoliated dispersions against reaggregation is ensured by choosing a suitable solvent with surface energy similar to the layered material which decreases the energy difference between exfoliated and reaggregated states.

III.1.2 Pnictogens

Among 2D materials, group 15 pnictogens have received significant attention due to their interesting electronic and optoelectronic properties. In contrast to graphene which has planar hexagonal structure, monolayer pnictogens have puckered structure with each atom bonded to two in-plane atoms and one out-of-plane atom along with one lone pair which imparts anisotropic properties and surface reactivity to the layers, respectively.[24] Zero-band gap of graphene and limited band gap range of transition metal dichalcogenides (1.5-2.5 eV)[38] limits their electronics and optoelectronic applications. In this respect pnictogens have band gaps in the range of 0.36 to 2.62 eV with carrier mobilities of several thousand $cm^2\ V^{-1}\ s^{-1}$, which makes them promising class of material.[25,39,40] Among pnictogens, phosphorene the most widely studied member of the group is susceptible to oxidation under ambient conditions, which limits its application.[41] Compared to this, heavy pnictogen (As, Sb and Bi) monolayers are stable under ambient conditions. While phosphorene crystallizes in orthorhombic structure, heavy pnictogens are most stable in

rhombohedral structure.[24,42] The rhombohedral structure of layered As, Sb and Bi is similar to honeycomb lattice of graphite, however these are not true van der Waals materials. Thus, the interaction between two buckled layers is stronger, making their exfoliation difficult.[23,24] In the work that follows we have focused on the synthesis of antimonene nanosheets of varying thickness by liquid phase exfoliation and their subsequent functionalization to tailor the properties.

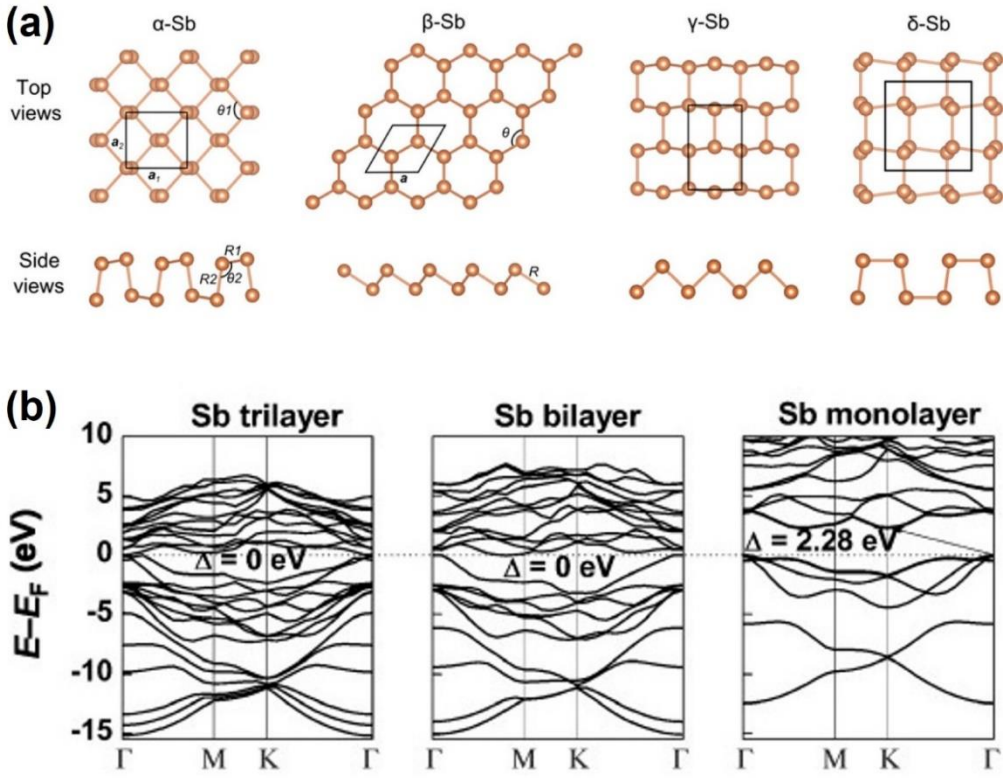

Figure 2. (a) Structural configurations of various allotropes of antimonene. (b) Electronic band structure of antimony trilayer, bilayer and monolayer. Adapted with permission from ref 42, Copyright 2015 American Chemical Society. Reprinted with permission from ref 40, Copyright 2015 John Wiley and Sons.

Bulk antimony crystallizes in a rhombohedral layered structure with $R\bar{3}$m space group (β-phase). Monolayer antimony, known as antimonene, has a buckled hexagonal

lattice and can exist in four phases, with the β-phase being the thermodynamically most stable (**Figure 2a**).[24,43] Antimonene is more stable than phosphorene under ambient conditions and has been theoretically predicted to have high carrier mobility,[44] thickness-dependent electronic properties,[45] and size-dependent thermal conductivity.[46] Antimony is semi-metallic in nature however when thinned down to monolayer exhibits an indirect band gap of 2.28 eV which further transitions into a direct band gap under tensile strain (**Figure 2b**).[45] Theoretical calculations reveal that a 22-layer Sb behaves as a topological insulator, an 8-layered Sb attains a quantum spin hall phase and under three layers, Sb behaves as a semiconductor.[47] Surface oxidation of antimonene has been shown to induce a variable band gap in the range 0 to 2.28 eV.[48] Experimentally, antimonene band gap between 0.8 – 1.44 eV has been observed by UV-Vis spectroscopy.[49] Moreover, monolayer antimonene photoluminescence (PL) emission has been observed between 500-600 nm under 470 nm laser excitation[50]. The presence of band gap only in monolayer limits the applications of antimonene for optoelectronics. However, PL of multilayer antimonene nanoribbons on InSe is reported to have a maxima at 610 nm[51] and antimonene quantum dots show excitation dependent PL emission between 350-500 nm.[52] The presence of PL emission from multilayer antimony could be due to quantum confinement and therefore opens up the possibility for utilization in electronic and optoelectronic applications. Furthermore, modification of antimonene can serve as a suitable approach towards tuning its electronic properties.

III.1.3 Chemical functionalization of two-dimensional materials

Materials at atomic scale thicknesses are extremely sensitive to local environment. Chemical functionalization is one way to passivate the surface from surrounding and

simultaneously tailor the inherent properties. Modification of material properties involving traditional doping methods is not suitable for atomically thin 2D materials since it involves inevitable structural damage during the synthesis.[53] Chemical functionalization of 2D materials with organic and inorganic moieties is a simple approach to modify the properties of materials such as inhibition of reaggregation, improved wettability and dispersibility, tunable physicochemical, electronic, and optical properties along with enhanced stability and introduction of novel properties.[54] According to the nature of interaction, chemical functionalization can be of two distinct types; firstly covalent functionalization involving formation of covalent bond between the parent material and foreign species, secondly, non-covalent functionalization which can happen through electrostatic or π-π interactions.[55]

Covalent functionalization: Covalent functionalization of 2D materials involves formation of covalent bond at the surface of the materials involving changes in the hybridization leading to modification of electronic band structure.[56] Covalent functionalization of graphene involving interaction of π-system with organic groups such as phenyl radicals,[57,58] diazonium salts, carbene, nitrene, aryne, etc have been studied.[59,60] Covalent functionalization of graphene suffers from low degree of functionalization due to inertness/neutrality of graphene. Negatively charged graphene is therefore employed for covalent functionalization which involves; electron transfer to the reactant forming radicals followed by addition reaction or nucleophilic reaction to suitable electrophiles.[61–65] Covalent functionalization of transition metal dichalcogenides with organic moieties have been shown to alter the properties involving a metallic to semiconducting transition for 1T-MoS_2 with tunable photoluminescence.[66] Pnictogens

with the unique puckered structure and lone pair of electrons can be functionalized by organic moieties leading to surface passivation and tunable electronic properties.[67]

A common method of covalent functionalization is reaction with aryl diazonium salts leading to the formation of covalent bonded organic moieties on the surface and has been extensively studied for metal surfaces.[41,68–72] Surface of black phosphorus can be spontaneously functionalized with aryl diazonium salt yielding phosphorus-carbon bonds.[41] This chemical functionalization passivates black phosphorus and alters the electronic properties by yielding a strong, tunable p-type doping that enhances the field-effect transistor mobility and on/off ratios. A similar spontaneous grafting of aryl diazonium salt on graphene forming C-C bonds has been shown to alter the electronic properties.[73–75] Functionalization with diazonium salt can be done by spontaneous grafting or electrochemical methods.[76,77] For the spontaneous grafting method, depending on the reduction potentials of reactants, the electron transfer from the material to diazonium salt can be spontaneous. One of the most studied diazonium salt is p-nitrobenzene diazonium salt (p-NBD) which has a reduction potential of 0.03V in acetonitrile and all the materials with reduction potentials $E^o < 0.6$ V will spontaneously reduce p-NBD.[69,70]

Non-covalent functionalization: Non-covalent functionalization influences the electronic band structure of material while preserving the lattice structure.[78] The presence of π-electron cloud on graphene allows non-covalent interaction of molecules.[79,80] Interaction of solvents with graphene layers helps in exfoliation with solvents of similar surface energy.[37] Non-covalent functionalization of graphene with organic and metal-organic species causes doping and modulation of work function of graphene which improves its performance in electronic devices.[81] Graphene can also be decorated with conjugated

molecules via pi-pi interactions.[79,80] Surface atoms of 2D metal chalcogenides terminate with lone pair of electrons which acts as Lewis bases and therefore can interact with Lewis acids. Interaction of lone pairs of InSe with Lewis acid $TiCl_4$ can effectively modify the Fermi level leading to p-type doping.[82]

Non-covalent functionalization of black phosphorus and antimonene utilizes the presence of lone pairs on the surface for the interaction with electron deficient and polarizable aromatic molecules such as perylene bisimide and tetracyanoquinodimethane (TCNQ) which leads to surface passivation of black phosphorus[83] and induces a band gap of 1.05 eV in antimonene.[84] Interaction with electron donor/acceptor organic molecules leads to doping of the materials with decrease in band gap due to formation of dopant levels and also affects their optical properties.[78] Non-covalent functionalization of pnictogens has been mainly focused to black phosphorus and only a few reports of antimonene.

III.1.4 Scope of present investigation

Evident from the above discussion, antimonene possess excellent electronic and optoelectronic properties, although its properties are limited due to its band gap in monolayer regime only. In the work that follows we have synthesized antimonene nanosheets with varying thicknesses by liquid phase exfoliation and studied its optical properties. Antimonene has a puckered structure with 3 sigma bonds and a lone of pair of electrons which makes the surface susceptible to various reactions. Chemical functionalization of antimonene nanosheets involving participation of lone pair with electrophilic species was carried out to alter its properties. **Figure 3** shows an illustration of functionalization strategy for Sb involving covalent and non-covalent interactions with a diazonium salt and a Lewis acids, respectively.

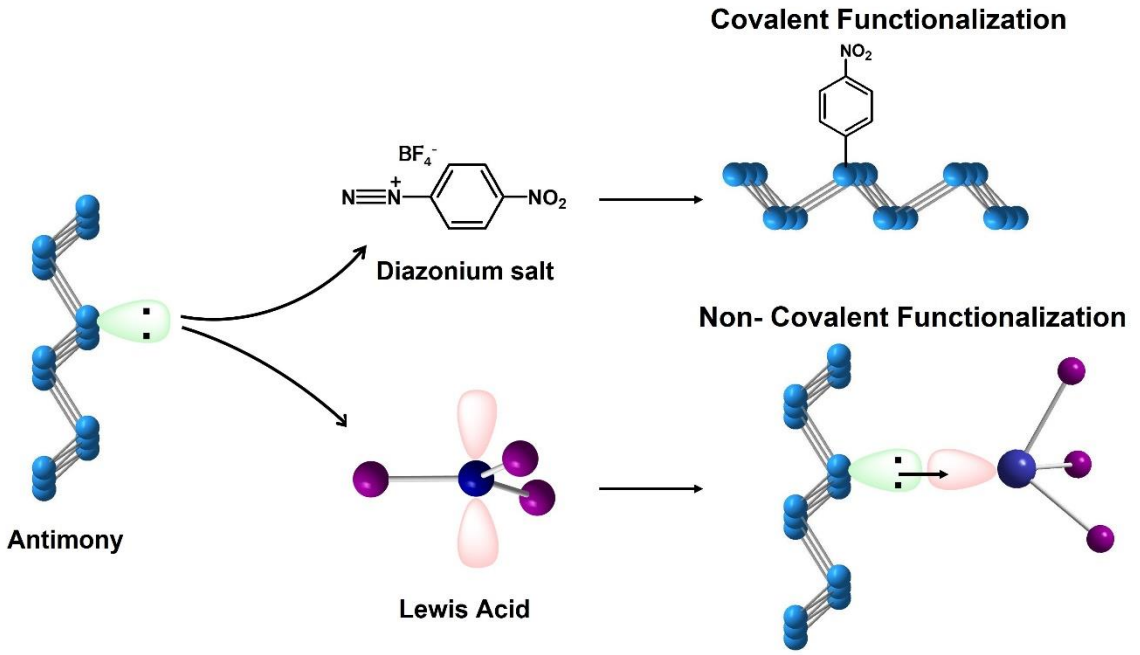

Figure 3. Schematic illustration of covalent and non-covalent functionalization strategy for Antimony.

Covalent functionalization of antimonene nanosheets was achieved by spontaneous reaction with aryl diazonium salt, p-nitrobenzene diazonium salt (p-NBD) which has a reduction potential of 0.03V in acetonitrile and all the materials with reduction potentials $E^o < 0.6$ V will spontaneously reduce p-NBD.[69,70] Sb has a reduction potential of 0.212 V and hence we expect a spontaneous reaction with p-NBD. Non-covalent functionalization of antimonene nanosheets was achieved by the spontaneous reaction with Lewis acids. Antimonene, due to the presence of lone pairs, behaves as a Lewis base and therefore can interact with Lewis acids to form Lewis acid-base adducts. A series of group 13 Lewis acids, BCl_3, $AlCl_3$, $GaCl_3$, $InCl_3$, $AlCl_3$ and group 12 Lewis acids $ZnCl_2$ and $CdCl_2$ were employed and the effect of non-covalent functionalization on its properties was studied. In depth analysis of reaction mechanism and effects of functionalization was carried out.

III.1.5 Experimental

Materials: Antimony crystals (Smart Elements, 99.99995%), N-Methyl-2-pyrrolidone (NMP) (Spectrochem, 99%), acetonitrile (ACN) (Spectrochem, dry solvent, 99.5%), p-nitrobenzene diazonium tetrafluoroborate (Merck, 97%), Si substrate (University wafer, <100>, thickness 525±25 μm, ρ = 0.1-100 Ω cm). Prior to synthesis, NMP and acetonitrile solvents were degassed by purging inert gas (Ar) for 30 minutes with continuous stirring.

Synthesis of Antimony nanosheets: Antimony crystals were ground in a mortar pestle to obtain to fine powder. Sb powder (400 mg) was transferred to a round bottom centrifuge tube and filled with degassed N-methyl-2-pyrrolidone (17.5 mL). The tube was closed with a cap fitted with the sonicator probe and packed under inert atmosphere. Probe sonication was carried out for 4 hours with a pulse sequence of 4 s on and off at 25% amplitude. The resulting dispersion of exfoliated Sb was centrifuged at 2500 rpm (3935 *g*) to separate the unexfoliated Sb. Further centrifugation at higher speeds was done to separate two grades of Sb, Sb nanosheets (sediment at 14500 rpm) and few-layered Sb (supernatant at 15500 rpm).

Covalent functionalization of Antimony nanosheets: Sb nanosheets (Sb-NS) obtained as solid by centrifugation at 14500 rpm were separated and washed multiple times with acetonitrile to remove residual NMP. Finally, Sb-NS were dispersed in acetonitrile and sonicated for 15 minutes to get a uniform dispersion in a round bottom flask. p-nitrobenzene diazonium tetrafluoroborate (100 mg) was added to the above dispersion and sonicated for another 5 minutes to completely dissolve the salt. This reaction mixture was kept stirring continuously for 48 hours under ambient condition in light. After 48 hours,

the reaction mixture was washed multiple times with acetonitrile to remove any unreacted diazonium salt. The obtained black solid was named as Sb-NS-NO_2.

Non-covalent functionalization of Antimony nanosheets: Reaction solvents were selected based on the solubility of Lewis acids. Tetrahydrofuran (THF) was used for BCl_3, $GaCl_3$, $InCl_3$ and $ZnCl_2$; toluene was used for $AlCl_3$; methanol was used for $CdCl_2$. Prior to the reaction, Sb nanosheets (Sb-NS) were washed multiple times with solvent appropriate for the Lewis acid. Sb-NS dispersion in dry solvent and inert atmosphere was kept in a Schlenk flask and molar ratio of Lewis acid were added to this dispersion. The solutions were kept stirring under inert atmosphere and were observed over a period. BCl_3 and $GaCl_3$ reacted vigorously and formed a colorless solution instantaneously. $AlCl_3$ reacted relatively mildly but formed a colorless solution after 1 hour. Reactions with $InCl_3$ and $CdCl_2$ were considerably slower and didn't corrode the material. After optimization, reaction with $AlCl_3$ was done for 15 min, $CdCl_2$ for 10 days and $InCl_3$ for 14 days. The solid products obtained were washed multiple times with solvents and utilized for further characterizations.

Covalent and non-covalent functionalization of few-layered Sb (Sb-FL): Sb-FL was obtained as supernatant on centrifugation at 15500 rpm for 1 hour. The dispersion in NMP was drop coated on Si substrate and vacuum dried for further characterizations and reaction with p-NBD and Lewis acids. For covalent functionalization, Si substrate with Sb-FL sample was dipped in a solution of p-NBD (100 mg) in acetonitrile (5 mL) and left undisturbed for 48 hours under ambient conditions in light. After 48 hours, the substrate was removed and washed multiple times with acetonitrile to remove unreacted p-NBD from the surface. For non-covalent functionalization, Sb-FL substrate was dipped in a

solution of Lewis acid in desired solvent under inert atmosphere. After the reaction, the substrate was washed multiple times with solvent to remove any unreacted Lewis acid.

Cleaning Si substrate: Si substrates were first dipped in acetone and heated to 50°C for 10 mins. After this the substrates were rinsed with methanol and dried under N_2 gun. The dried substrates were dipped in Piranha solution for 10 mins and washed rigorously with water afterwards. In the final step, the substrates were dipped in 2% HF solution for 10 minutes, washed rigorously with water and then dried under N_2 gun.

Physical Characterization

Liquid phase exfoliation was carried out with a Sonics Vibracell probe sonicator (750 W) equipped with a titanium alloy (Ti-6Al-4V) based tapered probe (tip diameter = 6 mm). The probe sonicator assembly was maintained at 5°C by circulating cold water to avoid overheating of the probe. Raman spectra were recorded on a Horiba-Jobin Yvon LabRAM HR 800 Raman spectrometer equipped with Ar^+ laser with 514 nm notch filter with a spectral resolution of 1.5 cm^{-1}. Samples for Raman measurements were prepared by drop coating the dispersion on a glass slide and dried under vacuum. Bright-field transmission electron microscopy images were recorded on a JEOL 300kV HRTEM instrument. AFM analyses were carried in contact mode on a Bruker Innova AFM instrument. Sb nanosheets separated at different centrifugation speeds were drop coated on Si substrate and dried under vacuum. Nanoscope analysis software was used to analyze the data.

X-ray photoelectron spectroscopy studies were carried out on a Thermo K-alpha+ spectrometer using micro focused and mono chromated Al K_α radiation (1486.6 eV),

400μm spot size, pass energy of 50 eV and a step size of 0.1 eV and resolution of 0.6 eV. Samples for XPS were prepared by drop coating a thick layer of Sb-NS or Sb-NS-NO_2 samples on Si substrate and dried under vacuum. XPS analysis of core level spectra were done on fityk software using VoigtA function for peak fitting with a linear background. Photoluminescence measurements were performed on Edinburgh Instruments FLS 1000 spectrometer equipped with a Xe arc lamp (450 W) and a visible photomultiplier tube detector (PMT-900) (sensitivity > 35000:1). FESEM images were recorded on Thermofisher FEI Quanta 3D instrument equipped with field emission gun and EDS detector. Cathodoluminescence images and spectra were recorded with a Gatan MonoCL4 accessory with standard photomultiplier tube (PMT) detector (185-850 nm) attached with FESEM instrument. Samples for FESEM-EDX-CL analysis were prepared by drop coating dispersion of Sb-FL on Si substrate. FT-IR measurements were done with a Perkin Elmer frontier IR instrument equipped with a DTGS detector. Samples were prepared by grinding the sample dispersions with heated KBr and pressed into pellets. Spectra were recorded in transmittance mode with 64 scans and a spectral resolution of 4 cm^{-1}.

III.2 Results and Discussion

III.2.1 Synthesis and Characterization of Antimonene Nanosheets

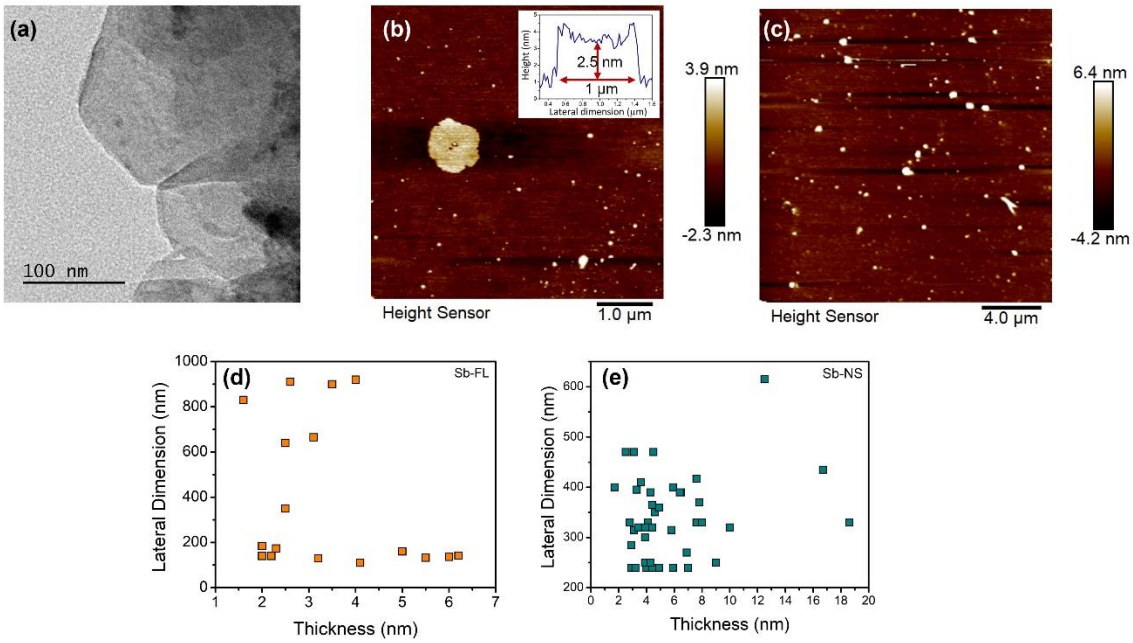

Figure 4. (a) Transmission electron microscopy image of few-layered antimonene (Sb-FL). (b, c) AFM image of Sb-FL and Sb-NS. Particle size distribution of (d) Sb-FL and (e) Sb-NS.

Liquid phase exfoliation of Sb crystals was carried out by probe sonication of ground Sb crystals in N-methyl-2-pyrrolidone (NMP).[85] The exfoliated dispersion was separated from the unexfoliated solid material by centrifugation. We have prepared two grades of Sb with different thicknesses and labelled them as Antimonene nanosheets (Sb NS) and few-layered antimonene (Sb FL). Exfoliated products were analyzed by transmission electron microscopy (TEM) which confirms the nanosheet morphology (**Figure 2**). Further analysis was carried out by atomic force microscopy. AFM studies shows that Sb-NS consists of nanosheets with lateral dimensions ~500 nm and thickness

below 10 nm (**Figure 2**) while Sb-FL consists of thinner nanosheets with thicknesses under 5 nm. **Figure 2b** shows a typical AFM image of Sb FL with one big sheet of thickness 2.5 nm and lateral dimension 1 µm with several smaller sheets with lateral dimension less than 300 nm and thickness under 5 nm. It is well known that for liquid exfoliated materials, height of layers will be overestimated due to the presence of residual solvent and contributions from capillary forces and adhesion,[85–88] hence we expect that Sb-FL is primarily 3-4 layer thick.

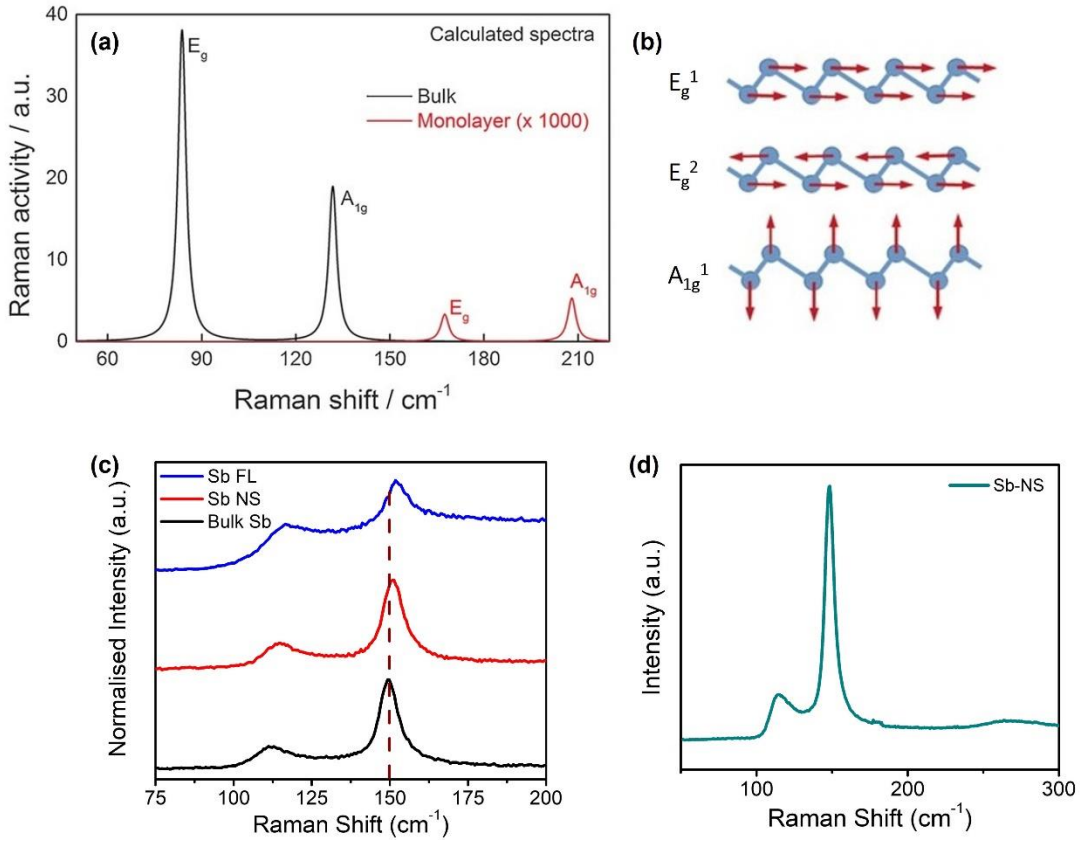

Figure 5. (a) Calculated Raman spectra of bulk antimony and monolayer antimonene and (b) the corresponding vibrational modes. Reproduced with permission from ref 84, John Wiley and sons. (c) Raman spectra of Sb bulk, Sb-NS and Sb-FL. (d) Raman spectra of Sb-NS kept under vacuum for 1 year.

To confirm the chemical nature of exfoliated Sb, Raman spectra were recorded. Theoretically, Bulk β-phase Sb has three Raman active optical modes, a pair of degenerate E_g modes (88 cm^{-1}) corresponding to in-plane transversal and longitudinal vibrations in opposite directions and an A_{1g} mode (137 cm^{-1}) corresponding to opposite-in-phase out-of-plane vibrations (**Figure 5**).[85] For monolayer antimonene, the Raman modes are blue shifted (E_g 167 cm^{-1} and A_{1g} 208 cm^{-1}) due to strong contraction of in-plane lattice constant (Figure 4).[85]

Experimentally, bulk antimony exhibits two phonon modes, E_g (112cm^{-1}) and A_{1g} (149.8 cm^{-1}). Sb NS and Sb FL exhibits a slight blue shift in the two phonon modes at 114 cm^{-1} and 150.8 cm^{-1}; 116.7 and 152 cm^{-1} respectively (**Figure 5c**).[89] Decreasing the thickness leads to the contraction of in-plane lattice constant, resulting in a blue shift of Raman signals. The blue shift is less for A_{1g} mode due to the lower sensitivity of out-of-plane vibrations to the in-plane lattice constant.[85] Antimony oxides were not detected in Raman spectra, proving the chemical purity of the exfoliated samples. These samples were found to be stable for more than 1 year, as confirmed by Raman studies (**Figure 5d**).

III.2.2 Covalent Functionalization of Antimonene Nanosheets

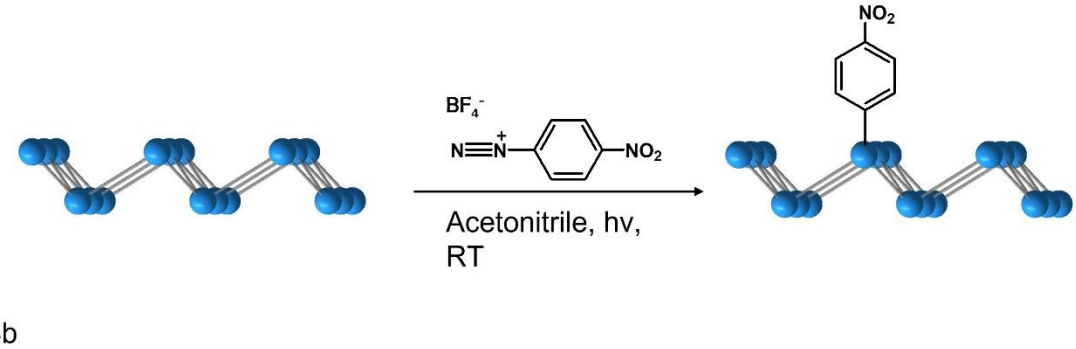

Scheme 1. Schematic illustration of covalent functionalization of antimonene with p-nitrobenzene diazonium tetrafluoroborate (p-NBD).

For covalent functionalization, we have initially focused on Sb-NS because of its higher concentration compared to Sb-FL. Sb-NS were functionalized with 4-Nitrobenzenediazonium tetrafluoroborate salt (p-NBD) under ambient conditions. A basic scheme for this reaction is as shown (**Scheme 1**); a more detailed scheme is discussed later in **Scheme 2**.

Functionalization of the Sb-NS sample was verified by vibrational spectroscopy. **Figure 6** shows the FT-IR spectra of the functionalized Sb-NS sample (denoted by Sb-NS-NO_2) and 4-Nitrobenzenediazonium tetrafluoroborate salt (p-NBD). For the diazonium salt (p-NBD), the peaks at 1540 and 1356 cm^{-1} are assigned to the asymmetric and symmetric stretching modes of -NO_2, along with a sharp peak at 1314 cm^{-1} corresponding to C-N stretching mode. For Sb-NS-NO_2, we observe stretching modes of -NO_2 which are shifted to 1516 and 1346 cm^{-1}, which could be due to change in the bonding environment. p-NBD has a signature sharp peak at 2302 cm^{-1} corresponding to stretching mode of N_2^+ species, which is missing in Sb-NS-NO_2 sample, implying absence of unreacted diazo species. For

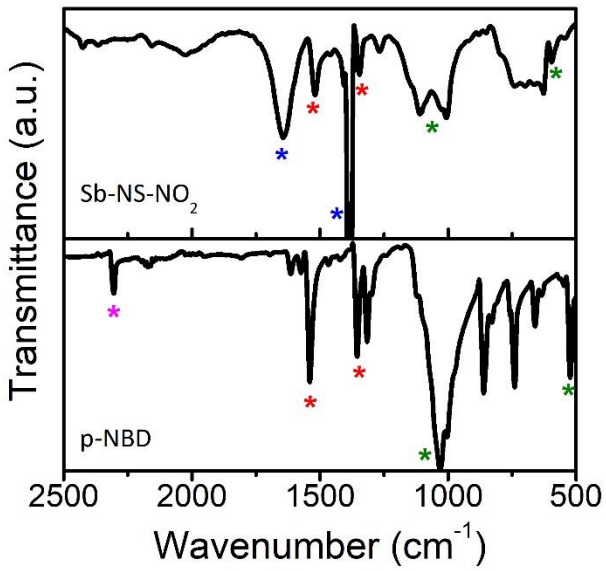

Figure 6. FT-IR spectra of p-nitrobenzene diazonium tetrafluoroborate (p-NBD) and functionalized antimonene nanosheets (Sb-NS-NO_2). Peaks corresponding to symmetric and asymmetric stretching modes of -NO_2 are highlighted by (*). Stretching mode of N_2^+ species (*). Peaks corresponding to BF_4^- (*). KBr impurity (*).

the diazonium salt (p-NBD) we observed asymmetric and symmetric stretching modes corresponding to BF_4^- near 1118-1030 cm^{-1} along with the bending mode at 522cm^{-1}. BF_4^- species was observed in Sb-NS-NO_2 around 1136-1005 cm^{-1} along with a bending mode at 592 cm^{-1} which was interesting since its presence could be important to understand the reaction mechanism.

To understand the nature of bonding, we have heated the Sb-NS-NO_2 samples at 200°C and 500°C and analyzed the corresponding FT-IR spectra.[60] We observe that the peaks corresponding to -NO_2 and BF_4^- group remain intact after heating the sample at 200°C, while they disappear after heating at 500°C (**Figure 7**). On heating we expect that any physiosorbed nitrobenzene/diazonium species if present will be removed.[60] On comparing

FTIR of heated sample with the parent sample, we observed that the -NO_2 and BF_4^- signatures are still prominent, signifying that the bonding involved with this functionalization is covalent in nature.

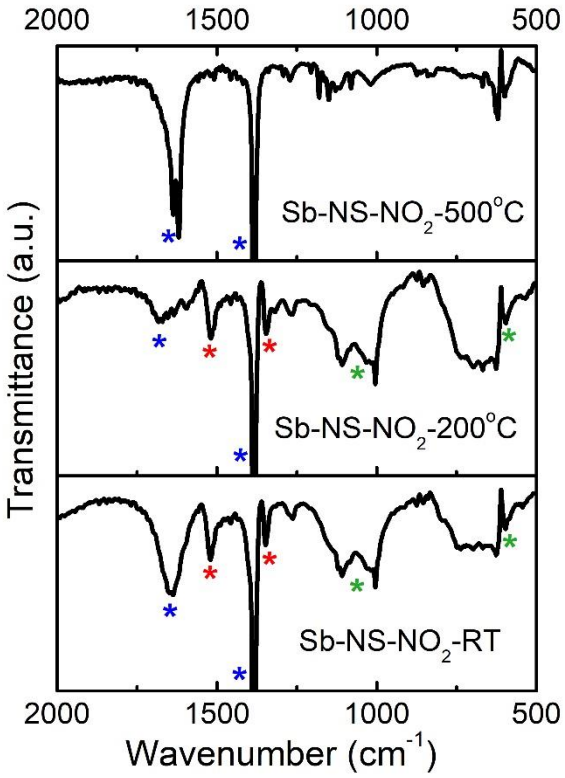

Figure 7. FT-IR spectra of Sb-NS-NO_2 at (a) room temperature, (b) 200 C and (c) 500 C. (d) Blank KBr. Peaks corresponding to symmetric and asymmetric stretching modes of -NO_2 are highlighted by (*). Peaks corresponding to BF_4^- (*). KBr impurity (*).

Surface functionalization was further confirmed by X-ray Photoelectron spectroscopy (XPS) (**Figure 8**). N1s- spectra of p-NBD exhibits peaks at 400.6, 403.9 and 405.9 eV corresponding to reduced nitrogen species, N_2^+ species and -NO_2, respectively. The presence of reduced nitrogen species could be due to reduction of N_2^+ species by X-ray or during storage.[69] Sb-NS shows a N1s peak at 398.9eV which was assigned to residual solvent.[90,91] In Sb-NS-NO_2, a peak is observed at 405.2 eV corresponding to -NO_2 species,

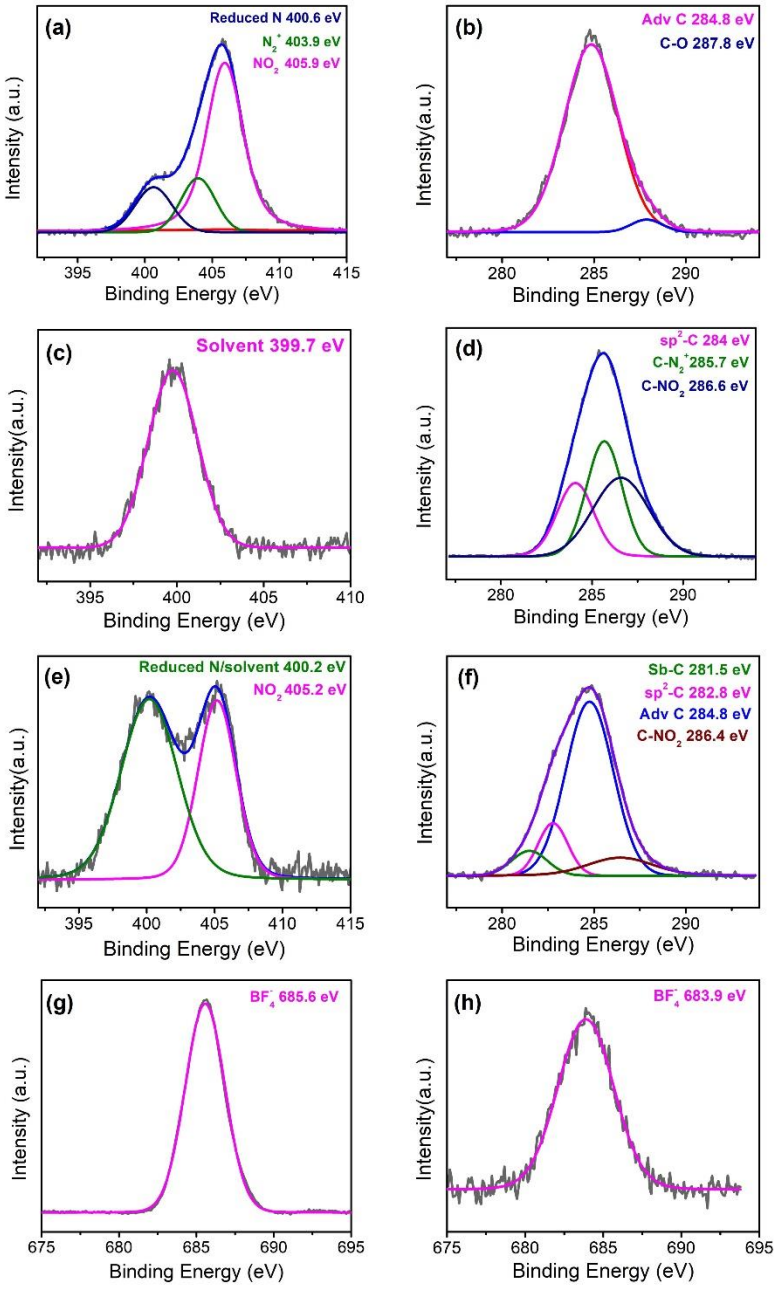

Figure 8. N1s and C1s core-level XPS of (a, b) p-NBD, (c, d) Sb-NS and (e, f) Sb-NS-NO_2; and F1s core level spectra of (g) p-NBD and (h) Sb-NS-NO_2 Numbers in legend represent peak positions.

which wasn't observed in Sb-NS sample. This confirms that after functionalization -NO_2 group has been incorporated in the sample. Along with this, a peak is observed at 400.2 eV

which can similarly be assigned to solvent, -NH_2 group or -N=N- linkages (discussed in Scheme B). C1s core level spectra of p-NBD show peaks at 284, 285.7 and 286.6 eV corresponding to sp^2 carbon, C- N_2^+ species and C-NO_2. C1s core level spectra of Sb-NS-NO_2 shows peaks at 281.5, 282.8, 284.8 and 286.4 eV assigned to Sb-C, aromatic sp^2 C, adventitious C and C-NO_2. The presence of Sb-C linkage further verifies covalent bonding of nitrobenzene on Sb. Quantitative analysis of XPS peak areas reveals ~22% functionalization of Sb.

Mechanism: A proper knowledge of reaction mechanism is crucial for a widespread understanding of the nature of bonding and for tuning the extent of reaction with varying nature of organic moieties. To this effect, we have done detailed analysis of FT-IR and XPS spectra of the products and reaction medium. Reaction of Sb-NS with p-NBD is carried out for 48 hours and the FT-IR of supernatant obtained after centrifugation shows

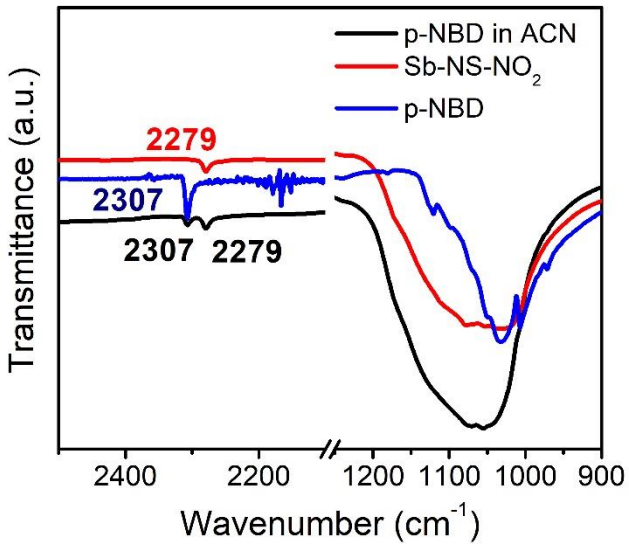

Figure 9. FTIR spectra of diazonium salt, diazonium salt in acetonitrile and supernatant after reaction from Sb-NS-NO_2 (after 48 hours).

a peak at 2280 cm^{-1} corresponding to solvated p-NBD species in acetonitrile (ACN) (**Figure 9**).[92,93] This shows that the diazonium salt is stable under the reaction conditions.

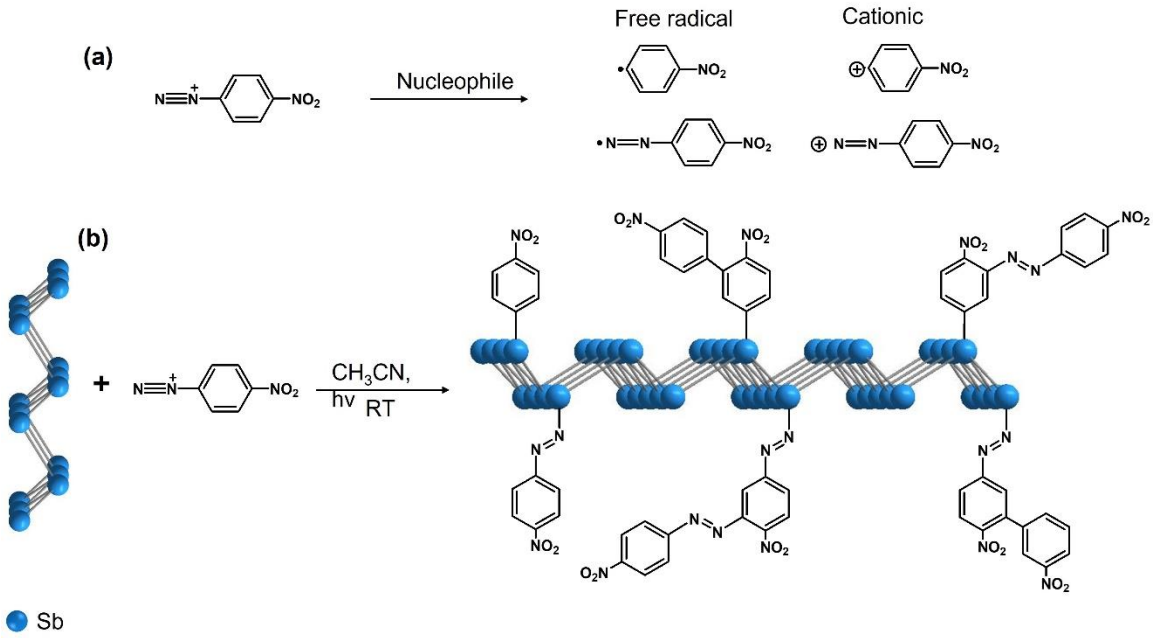

Scheme 2. Schematic illustration of (a) possible reaction intermediates of p-NBD and (b) corresponding products on covalent functionalization of antimonene with p-nitrobenzene diazonium tetrafluoroborate.

Scheme 2 gives a pictorial representation of the possible products. Reaction of diazonium salt with a nucleophile can follow either cationic or free-radical mechanism.[68,69,94] For the diazonium salt, the possible reactive intermediates are shown in Scheme B(a). The electron rich Sb has a lone pair which can act as a nucleophile and react with p-NBD to form a range of products (**Scheme 2b**). Initially, nitrobenzene-like species can attach to Sb via a Sb-C linkage or Sb-N=N linkage.[41,69] There is also a possibility that Sb might have some surface oxygen species which can also react with diazonium salt forming Sb-O-C linkages. Moreover, the reactive intermediates can further react with these moieties to form longer carbon species.

The presence of -NO_2 species in the Sb-NS-NO_2 heated at 200^{o}C confirms that majority of the nitrobenzene species are attached via Sb-C linkage since -N=N- linkage is unstable above 100^{o}C (**Figure 7**).[95] Moreover, deconvolution of N1s XPS spectra of Sb-NS-NO_2 around 398-401 eV is controversial because peak corresponding to azo linkage will overlap with residual solvent peak (**Figure 8**). FTIR and XPS spectra of Sb-NS-NO_2 shows a blue shift in position of BF_4^- and F1s core level, in comparison to p-NBD, suggesting interaction with a different counter ion (**Figure 6** and **Figure 8**).[96] We hypothesize that the lone pair on Sb will participate in the reaction with p-NBD leading to the formation of quaternary Sb^+ species which is probably the counter ion balanced by BF_4^-.[90] This reduces the possibility of Sb-O-C linkages as these form neutral species.[90]

Surface modification of graphene/Cu/Ag/Au with diazonium salt involves a single electron transfer from metal surface and hence is expected to preferentially follow a free radical mechanism.[41,60,68,69,71,94] In the case of Sb, electron lone pairs are transferred to diazonium salt and hence cationic mechanism might dominate with the formation of Sb-C linkage. A more dedicated study could lead to a better understanding of nature of bonding in similar systems.

Effects of functionalization: After functionalization we observe a blue-shift in Raman peaks suggesting a distortion in Sb-lattice (**Figure 10a**). Since blue shift in A_{1g} (2.2 cm^{-1}) is more pronounced compared E_g mode the local distortion brings about a greater change in the out-of-plane lattice constant rather than the in-plane lattice constant.[85] Nearest neighbor Sb atoms contribute to the out of plane lattice constant while next nearest neighbors contribute to in-plane lattice constant. On functionalization, with the formation of quaternary species with a partial positive charge on Sb, we expect that the nearest Sb

atoms will be more affected than the next nearest Sb. Hence, we expect that the A_{1g} mode will be more affected than E_g mode.

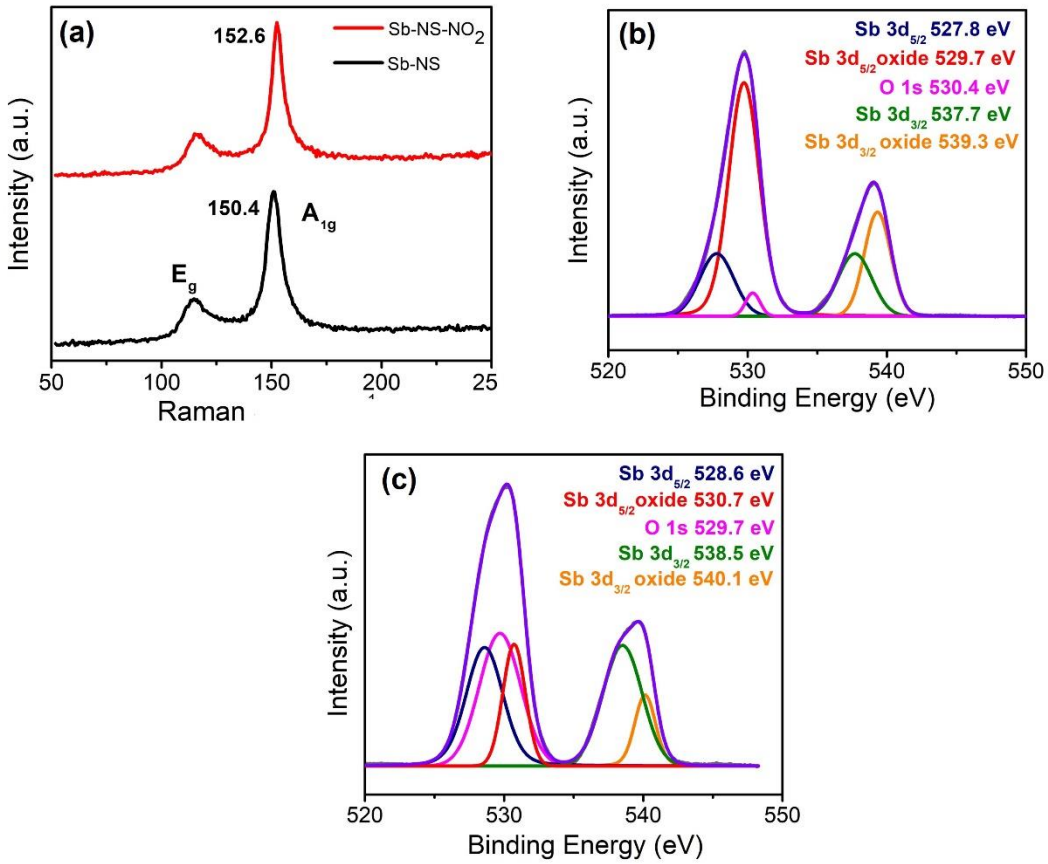

Figure 10. (a) Raman spectra of Sb-NS and Sb-NS-NO2and Sb 3d core level spectra of (b) Sb-NS and (c) Sb-NS-NO_2.

Sb 3d core level spectra of Sb-NS shows two peaks at 527.8 and 537.7 eV corresponding to Sb $3d_{5/2}$ and Sb $3d_{3/2}$, respectively (**Figure 10b**). After functionalization there is a slight blue shift in Sb 3d peaks to 528.6 and 538.5 eV which indicates a charge transfer from Sb to diazonium salt (**Figure 10c)**. Sb-NS has a considerable contribution from Sb-oxide species which could result from surface oxidation during sample storage

and measurement conditions. Interestingly, the contribution from Sb-oxide decreases relatively after functionalization indicating surface passivation by nitrobenzene layers.

Bulk Sb is semi-metallic in nature and exhibits thickness dependent transition to semiconductor.[40] This transition to a semiconducting state can be probed by photoluminescence (PL) spectroscopy. From AFM analysis, we can assume that Sb-NS still lies in the semi-metallic state and accordingly did not show any emission in PL which also rules out emission due to any impurities (**Figure 11a).** Interestingly, for Sb-FL exhibits a broad feature centered around 650 nm (**Figure 11b**). The band gap of nano sized materials is sensitive to its dimensions; hence the broad feature could be due to cumulative emissions from Sb nanosheets of different sizes and thicknesses.

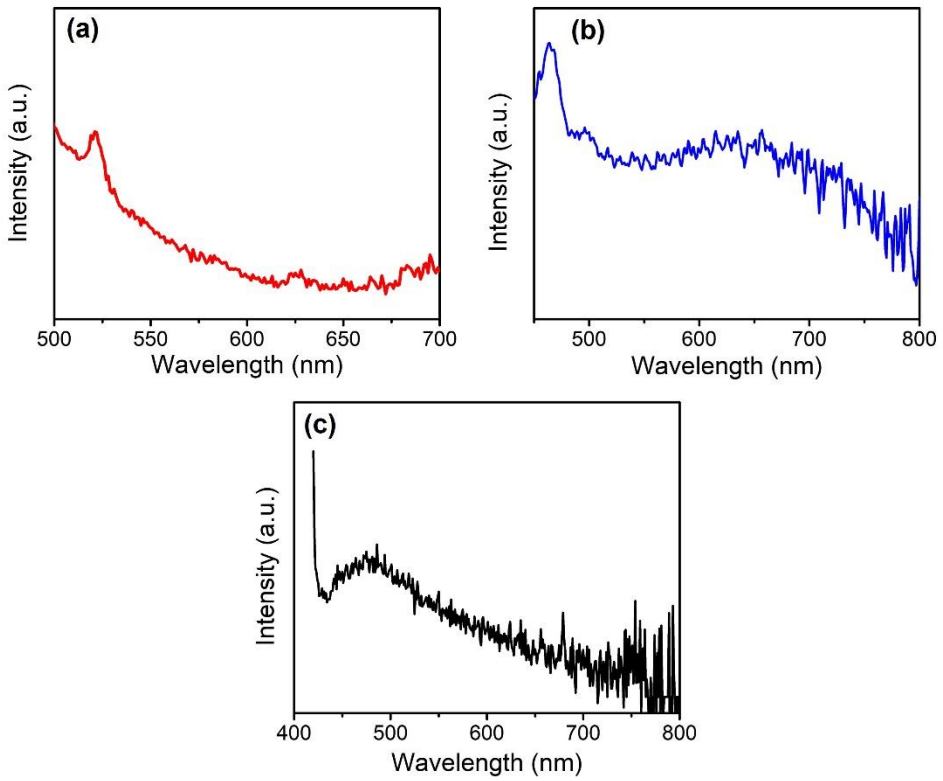

Figure 11. Photoluminescence spectra of (a) Sb-NS, (b) Sb-FL and (c) NMP (after sonication).

To confirm the origin of this broad emission, a control PL spectrum was acquired of the solvent (N-methyl pyrrolidone (NMP)) which was subjected to similar probe sonication conditions. PL spectrum of NMP shows a broad peak around 475 nm (**Figure 11c**). NMP is known to show fluorescence around 420 nm. Moreover, on being subjected to sonication NMP is known to polymerize and show emission in the range of 350-450 nm.[97,98] Since, the contribution from NMP lies below 500 nm, the presence of PL emission band centered at 650 nm should be from Sb-FL.

Since the broad PL emission from Sb-FL can originate from the cumulative emission of Sb-FL of different dimensions, drawing out any conclusions from functionalizing these samples via PL might be inaccurate. Hence, we studied the emission properties of these nanosheets using FESEM cathodoluminescence spectroscopy (CL) wherein we have studied the emission properties of a particular marked nanosheet before and after functionalization.

CL spectra was acquired on various nanosheets of Sb-FL and it was observed that majority of the nanosheets exhibit weak emission in the range of 450 – 800 nm with some nanosheets exhibiting strong CL emission with sharp peaks in the range of 250-800 nm (**Figure 12**). Interestingly, CL spectra of the bright Sb nanosheets exhibit very sharp peaks at 290 nm, 430 nm, 560 nm, 650 nm, and 750 nm (**Figure 12**). And these peaks were used as the basis to deconvolute the broad CL spectra of the less-emissive sheets. For functionalization study, only these less emissive sheets were taken into consideration as these give a better representation of the sample.

Moreover, CL measurements were done on sonicated NMP to rule out the solvent contribution. On most regions CL mapping of NMP sample does not show any emission

which is cross checked by the corresponding CL spectra (**Figure 12 g-i**). However, in some places we could observe some bright regions which according to literature could be due to polymerized NMP and we observe a sharp emission at around 475 nm (like PL) with a shoulder at around 425 nm.

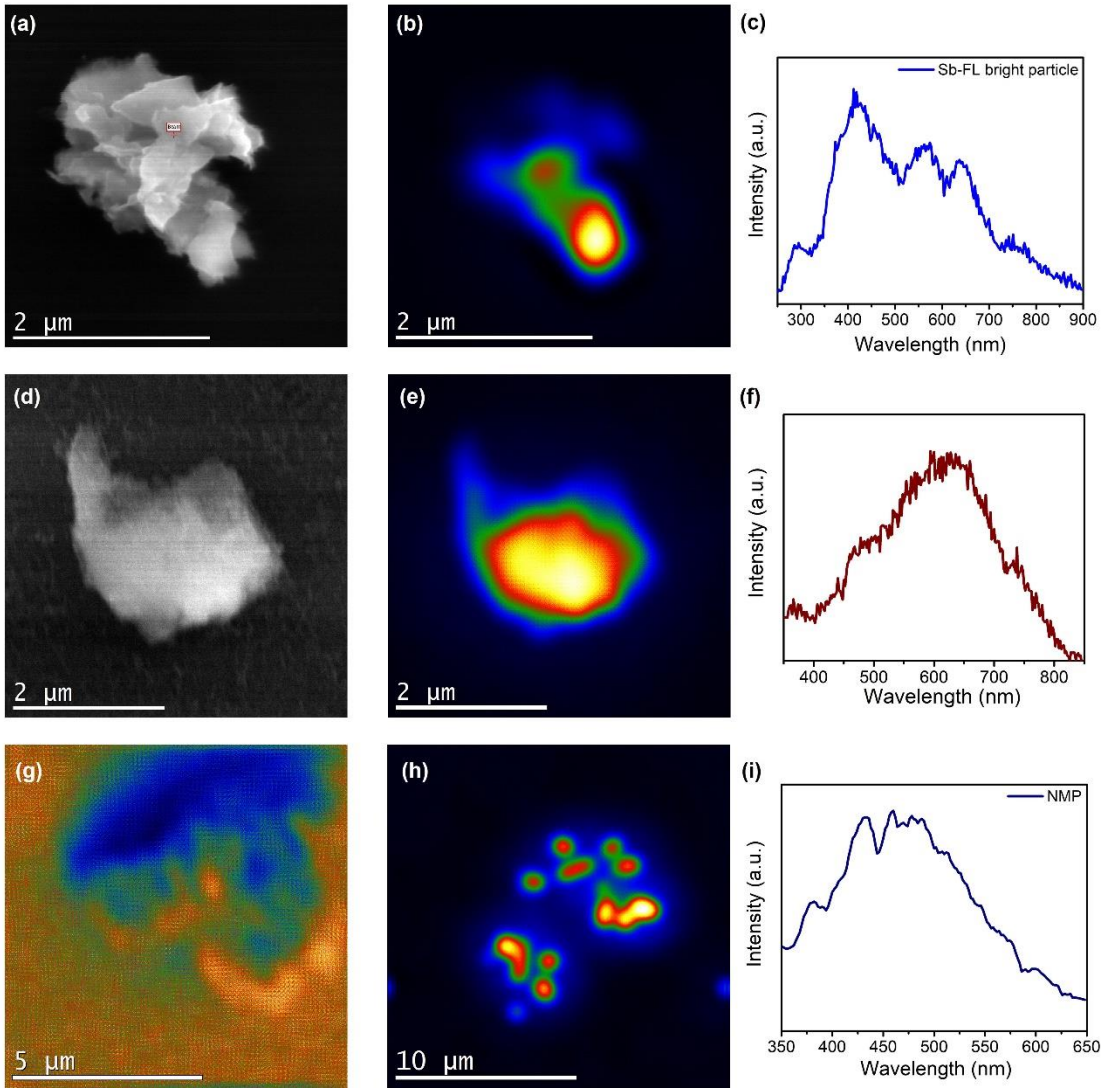

Figure 12. (a) FESEM image, (b) CL mapping and (c) corresponding CL spectrum of an Sb-FL bright particle. (d) FESEM image, (e) CL mapping and (f) corresponding CL spectrum of an Sb-FL representing majority of nanosheets. (g, h) CL mapping and (f) corresponding CL spectrum of an NMP

Based on the above CL spectra analysis, deconvolution of CL spectra of Sb-FL was carried out. CL spectra of Sb-FL show peaks at 557, 638, and 720 nm corresponding to band edge and defects, along with a broad feature below 500 nm corresponding to solvent residues (**Figure 13c**).[97,98] The presence of band edge emission in Sb-FL at ~557 nm (~2.2 eV, emission A) is due to band opening on account of quantum confinement. Along with this, dispersions of liquid exfoliated materials undergo turbostratic stacking which have weaker interlayer interaction compared to bulk, thereby behaving as quasi-monolayers.[99,100] This will also be a contributing factor behind having band gaps in comparatively thicker sheets. Emission B (~ 638nm or 1.94 eV) and C (720nm or 1.72 eV) could be due to formation of defects in Sb lattice during liquid exfoliation.[101]

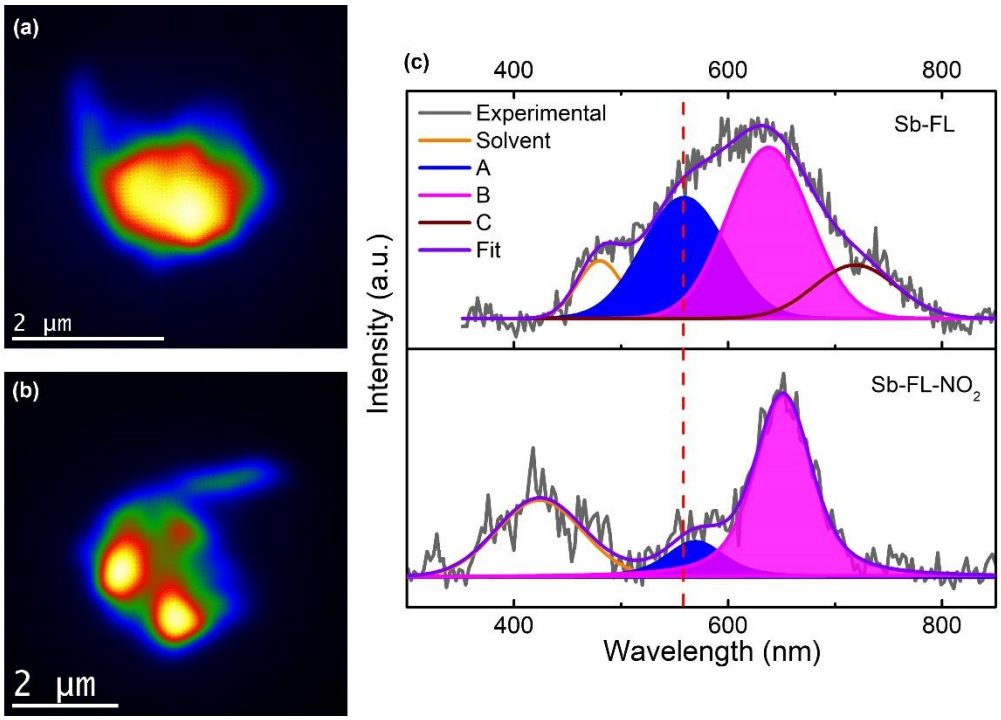

Figure 13. CL mapping of (a) Sb-FL and (b) Sb-FL-NO_2. (c) Comparison of CL spectra of Sb-FL and Sb-FL-NO_2.

The Sb-FL sheet under study was subjected to covalent functionalization by immersing the substrate in a solution of p-NBD for 48 hours. After functionalization we observe that the nanosheet under study retains its structural integrity. There is a slight decrease in overall intensity of CL mapping which could be due to presence of nitrobenzene type groups on the surface (**Figure 13b**). Interestingly, after functionalization we observe a red shift in emissions (A and B) which could be due to change in the positions of VBM and CBM with the introduction of nitrobenzene species into the lattice (**Figure 13c**). A similar change in antimonene band structure have been reported for antimonene oxides.[48] Along with this we expect more defect states to form after functionalization which might be the reason for increase in relative intensity of emission B. A detailed theoretical investigation on similar system will lead to a better understanding of antimonene and emission in 2D materials in general.

III.2.3 Non-Covalent Functionalization of Antimonene Nanosheets

Non- covalent chemical functionalization of pnictogens is an interesting method to tune optical properties for various applications.[78] Pnictogens with lone pair on each atom, behaves as a Lewis base and can interact with Lewis acids to form Lewis acid-base adducts (LABA) (**Scheme 3**).[78,102] Strength of an acid/base depends on two factors: Lewis acidity/basicity and hard-soft nature. In group 15, Lewis basicity decreases down the group with Sb being more Lewis basic than Bi. According to hard-soft acid base (HSAB) principle,[103] soft bases have low electronegativity, are highly polarizable and easily undergoes oxidation. The strength/stability of the Lewis acid-base adduct depends on the inherent Lewis acidity/basicity of the two involved species along with their hard-soft nature with the strongest adducts formed between species with similar nature.

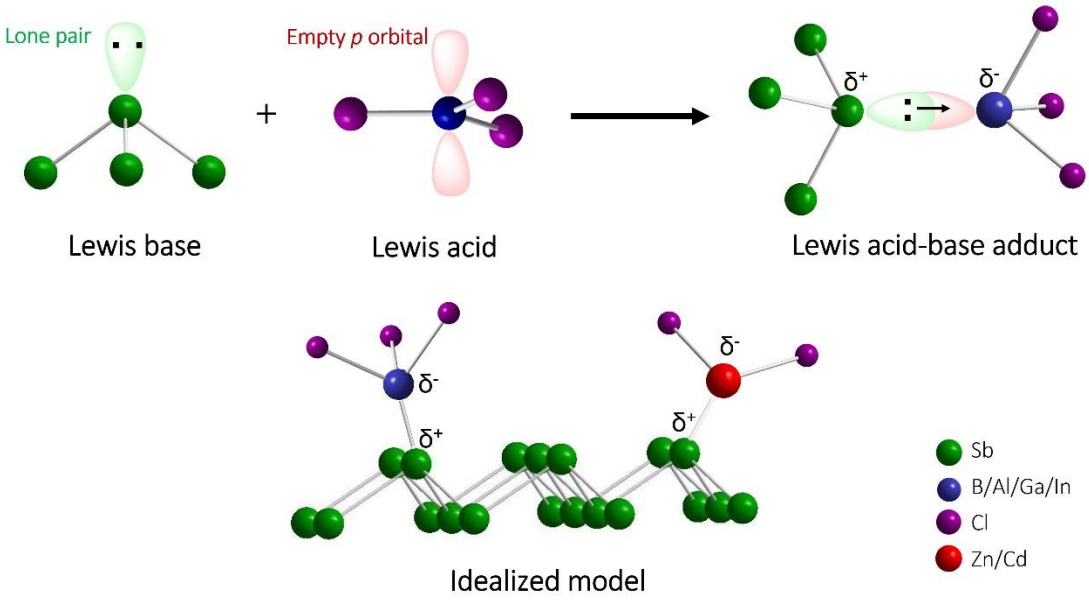

Scheme 3. Schematic illustration of Lewis acid-base adduct formation

Non-covalent functionalization of antimonene nanosheets (Sb-NS) was carried out with group 13 halides with Lewis acidity order BCl_3>$AlCl_3$≥$GaCl_3$>$InCl_3$. BCl_3 reacted instantaneously with a crackling sound and did not yield a solid product implying complete oxidation/corrosion of Sb lattice. Reaction with $AlCl_3$ and $InCl_3$ yielded a solid product, wherein reaction with $AlCl_3$ was faster than $InCl_3$ while $GaCl_3$ gave a colorless solution. This observation is not in line with the Lewis acidity order of group 13 halides which predicts $GaCl_3$ to be of similar Lewis acidity to $AlCl_3$. This anomalous behavior is due to increased softness of $GaCl_3$ which results in corrosive reaction with Sb. $InCl_3$ being the softest and weakest Lewis acid of the group forms the most stable adduct with Sb. To validate this observation, functionalization of Sb was carried out with group 12 halides: $ZnCl_2$ and $CdCl_2$. Like $GaCl_3$, $ZnCl_2$ did not yield a solid product while $CdCl_2$ forms a stable adduct since its Lewis acidity and softness is similar to $InCl_3$.

Successful functionalization of Sb-NS was confirmed by X-ray photoelectron spectroscopy (XPS) and energy dispersive spectroscopy (EDS) mapping. EDS mapping of functionalized materials show uniform distribution of all the elements giving an initial indication of functionalization (**Figure 14**). Core level XPS shows presence of Al:Cl, In:Cl and Cd:Cl in the expected stoichiometry (with an exception of Sb-$AlCl_3$) indicating functionalization without complexation (**Figure 15**). Moreover, shifts in Sb core level spectra indicates electron transfer from Sb to Lewis acid, which further substantiates formation of LABA.

Charge transfer on functionalization was probed by Raman spectroscopy. Significant shift in Raman modes were observed in functionalized Sb (**Figure 16**). A_{1g} mode of Sb-NS (151 cm^{-1}) is red shifted to 149.9, 147.7 and 146.1 cm^{-1} for $AlCl_3$, $CdCl_2$

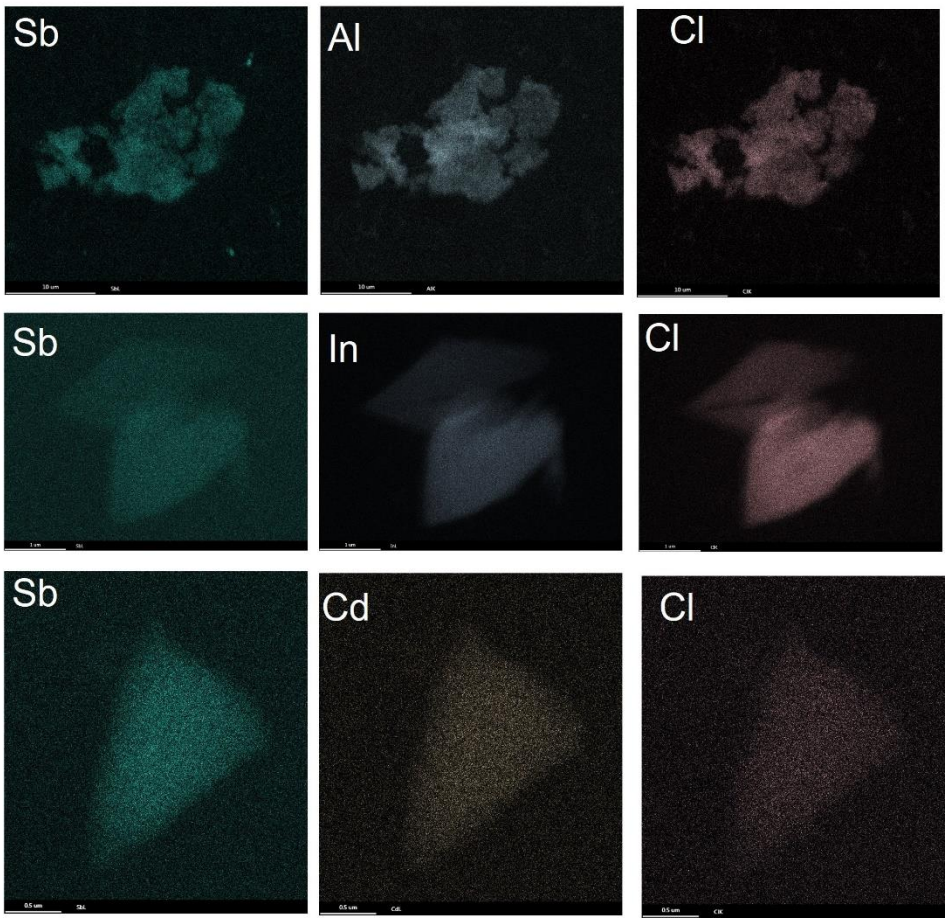

Figure 14. EDS mapping of functionalized Sb; Sb-$AlCl_3$, Sb-$InCl_3$ and Sb-$CdCl_2$.

and $InCl_3$, respectively. Red shift in the Sb A_{1g} vibrational mode is due to strain introduced in the lattice on functionalization which affects the out of plane lattice constant more strongly compared to in plane lattice constant.[104] This distortion of lattice is due to charge transfer and steric repulsions leading to expansion of out-of-plane lattice constant and is highly localized since we do not observe any measurable shift in E_g mode.

Red shift of Raman peaks on functionalization with Lewis acid has been previously reported for InSe-$TiCl_4$ wherein the strain introduced on interaction with $TiCl_4$ forces Se out of its lattice.[82] A similar red shift of Raman peaks due to strain are also reported for

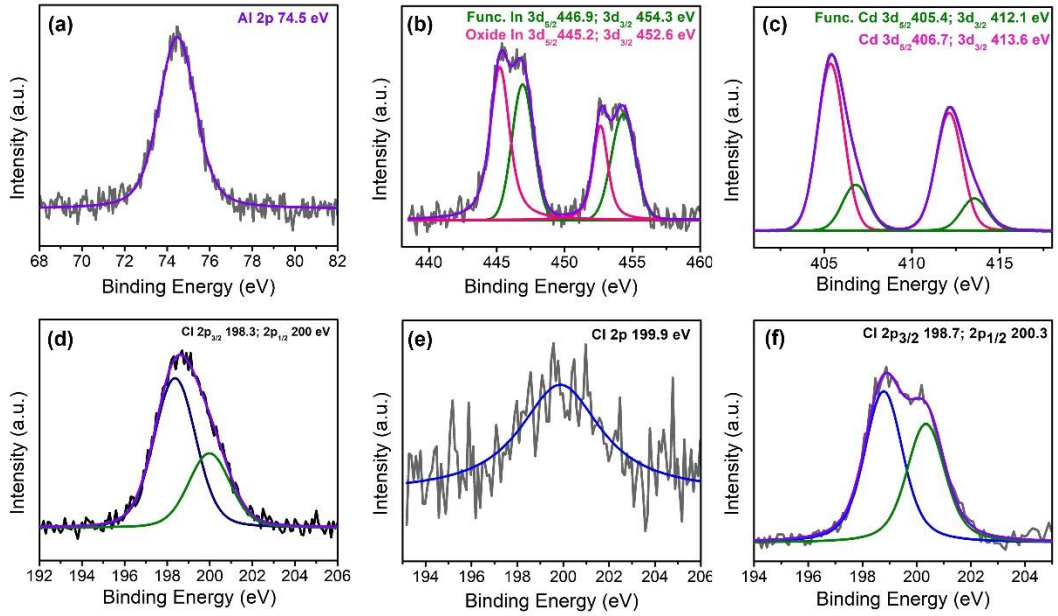

Figure 15. XPS core level spectra of (a, c) Al2p and Cl2p, (b, e) In 3d and Cl 2p, (c, f) Cd 3d and Cl 2p for Sb-$AlCl_3$, Sb-$InCl_3$ and Sb-$CdCl_2$, respectively.

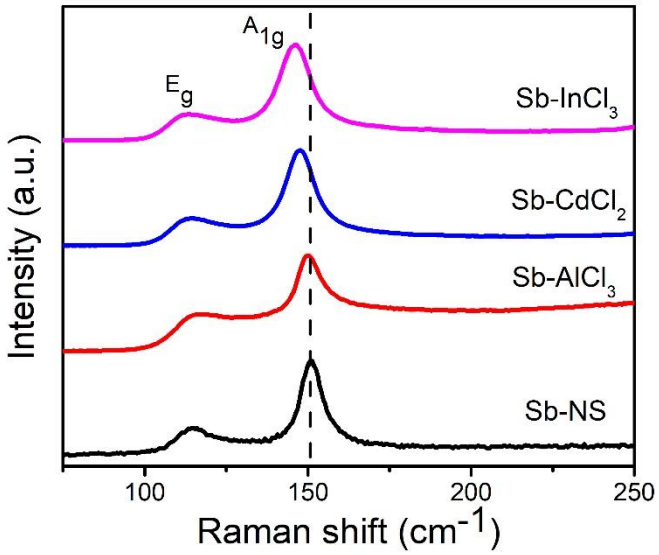

Figure 16. Raman spectra of Sb-NS and functionalized Sb-NS.

graphene, phosphorene, and other materials.[105,106] The extent of red shift on interaction with Lewis acids depends upon the Lewis acidity/basicity and nature. From our study, we

observe highest red shift for $InCl_3$ signifying stronger charge transfer and steric repulsion in $InCl_3$ followed by $CdCl_2$ and negligible shifts in $AlCl_3$. Raman modes corresponding to Lewis acids were not observed in any functionalized sample.

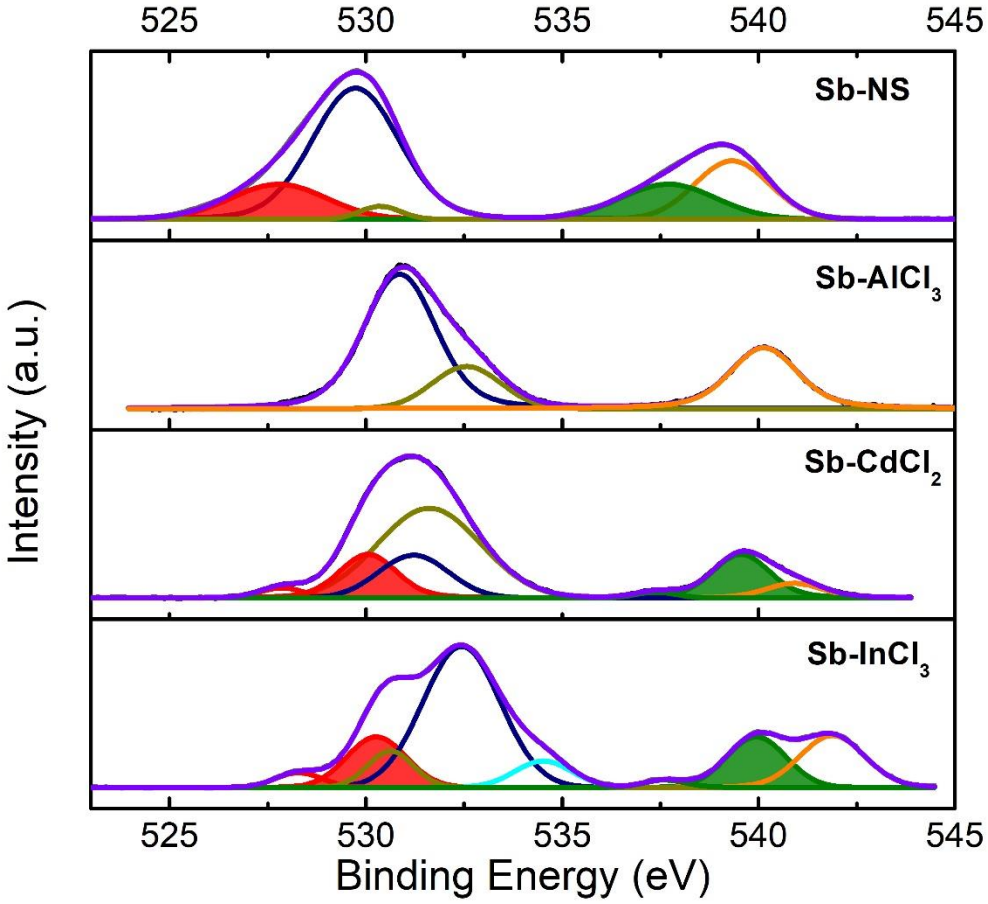

Figure 17. XPS core level spectra of Sb-NS and functionalized Sb-NS.

To gain further insights into the bonding nature, core level XPS were deconvoluted and thoroughly analyzed (**Figure 17**). Sb core level XPS consists of Sb $3d_{5/2}$ peak, O1s and Sb $3d_{3/2}$. Sb $3d_{5/2}$ peak overlaps with O1s peak and was deconvoluted based on the peak position and area of Sb $3d_{3/2}$. Sb $3d_{3/2}$ peak for Sb-NS can be deconvoluted in two peaks at 537.7 eV and 539.3 eV corresponding to Sb(0) and Sb oxide, with high oxide content.

Upon functionalization, the Sb $3d_{3/2}$ peak can be deconvoluted into three peaks corresponding to unreacted Sb(0), functionalized Sb and functionalized Sb-oxide. There is a considerable blue shift in functionalized Sb $3d_{3/2}$ indicating electron transfer to the Lewis acid. Sb $3d_{3/2}$ peak is blue shifted by 2.5 eV and 1.9 eV for $InCl_3$ and $CdCl_2$, respectively. This shift gives an indication of extent of electron transfer/ strength of adduct formation, where $InCl_3$ forms the most stable adduct. However, in the case of Sb-$AlCl_3$ we observed a complete oxidation of Sb due to a corrosive reaction with $AlCl_3$. Moreover, there is a decrease of Sb-oxide after functionalization indicating surface passivation. Blue shift in core level XPS of Sb along with red shift in Raman modes proves effective functionalization of Sb with Lewis acids, wherein $InCl_3$ forms the most stable adduct followed by $CdCl_2$ and $AlCl_3$ completely oxidizes Sb.

To understand the effects of functionalization on the band structure, FESEM-cathodoluminescence (CL) studies were carried out. CL spectra of Sb-FL can be deconvoluted into three emissions (A, B and C), along with a broad band below 500 nm corresponding to solvent emission, where emission A (~2.2 eV) is due to band edge while B and C are defect related emissions (**Figure 18**). Interestingly, we observe a blue shift in band edge emission to 2.27, 2.30 and 2.40 eV for $AlCl_3$, $InCl_3$ and $CdCl_2$, respectively (**Figure 18**). A similar blue shift is also observed in the defect bands with an increase in intensity for peak B which could be due to introduction of new defect states in the lattice. It is interesting to note that Sb-FL retains its structural integrity and emission after functionalization with $AlCl_3$ which could be due to a more controlled experimental procedure.

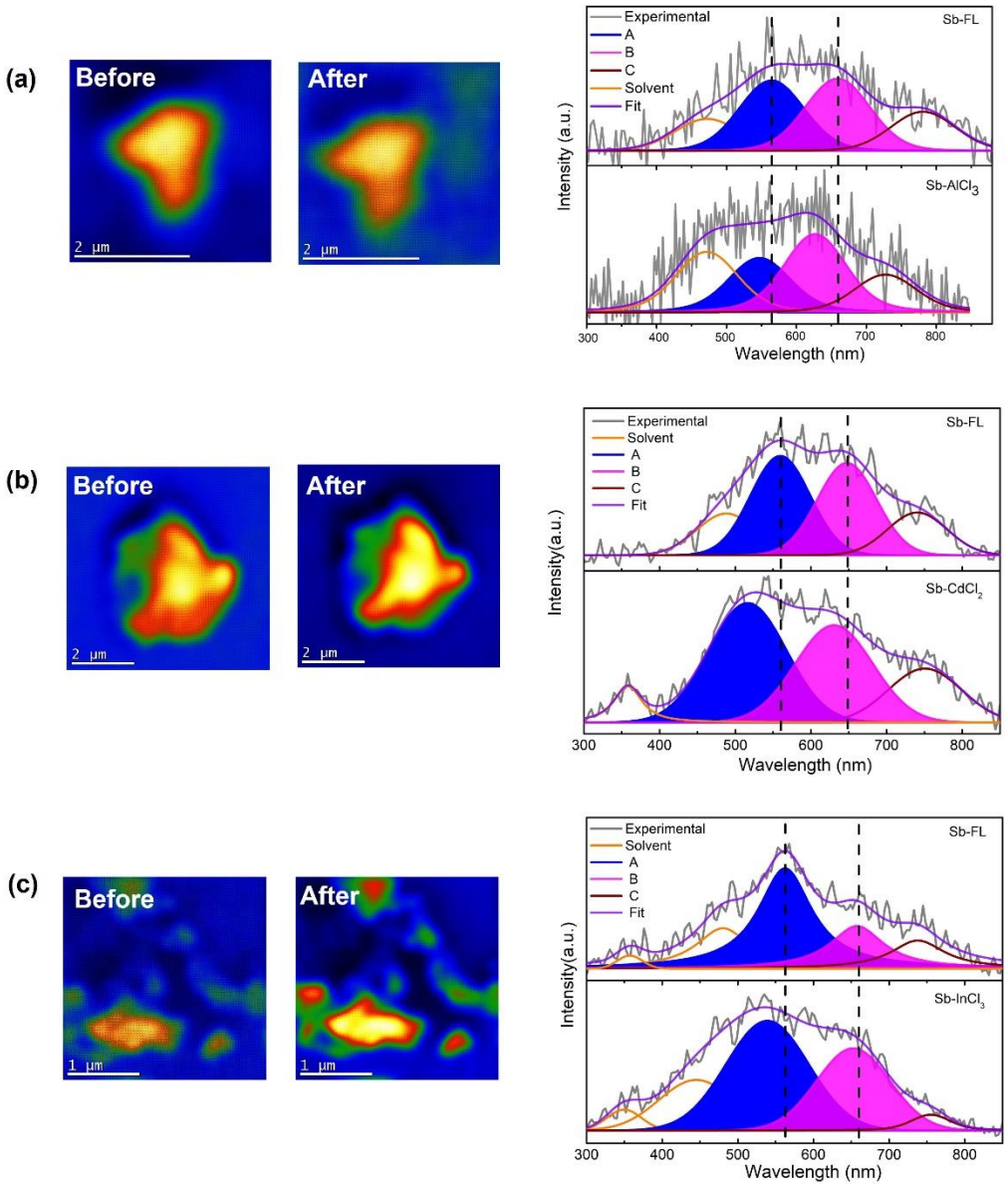

Figure 18. CL mapping and spectra of (a) Sb-$AlCl_3$, (b) Sb-$CdCl_2$ and (c) Sb-$InCl_3$.

The extent of shifts in band edge cannot be directly correlated with the extent of shifts in XPS or Raman as the changes in band structure are dominated by the incorporation of Lewis acid metal bands in the band structure of antimonene. A similar behavior was also observed on functionalization of phosphorene with Lewis acids.[107]

III.3 Conclusions

In conclusion, we have synthesized antimonene nanosheets by liquid exfoliation and studied their emission properties. Interestingly, we observe band edge emission in antimonene nanosheets at ~2.23eV along with defect emission at ~1.94 eV. Theoretically, the transition from semi-metal to semiconductor occurs at monolayer regime, however, band edge emission in relatively thicker sheets (~ 3-4 layers) was observed which is due to quantum confinement and turbostratic stacking.

These emissive antimonene nanosheets were functionalized with diazonium salt and we could successfully tune the band edge emission to 2.18 eV. To our knowledge, this is the first report on covalent functionalization of antimonene nanosheets. Covalent functionalization of antimonene nanosheets involves charge transfer from antimonene lone pairs to diazonium salt which was confirmed by Raman, FT-IR and XPS along with detection of Sb-C linkage.

Non-covalent functionalization of antimonene was achieved by the formation of Lewis acid-base adducts with multiple Lewis acids. The strength/stability of the adduct and the corresponding tunability in its band structure depends on the Lewis acidity and basicity of the interacting materials and there hard-soft nature. Based on these two parameters, different Lewis acids can be used to achieve desirable tunability and surface passivation for various applications. Interestingly, band edge emission of antimonene could be tailored by non-covalent functionalization.

This work demonstrates the possibility of tuning the electronic structure of antimonene by chemical functionalization; covalent and non-covalent. The choice of organic moiety,

Lewis acid and extent of functionalization can be tuned to achieve desired change in electronic and optical properties of the material which could be beneficial for various applications. Moreover, these functionalization strategies stabilizes the material from surface oxidation which will also be beneficial for various applications.

III.4 References

[1] S. Z. Butler, S. M. Hollen, L. Cao, Y. Cui, J. A. Gupta, H. R. Gutiérrez, T. F. Heinz, S. S. Hong, J. Huang, A. F. Ismach, E. Johnston-Halperin, M. Kuno, V. v. Plashnitsa, R. D. Robinson, R. S. Ruoff, S. Salahuddin, J. Shan, L. Shi, M. G. Spencer, M. Terrones, W. Windl, J. E. Goldberger, *ACS Nano* **2013**, *7*, 2898.

[2] A. J. Mannix, B. Kiraly, M. C. Hersam, N. P. Guisinger, *Nat. Rev. Chem.* **2017**, *1*, 1.

[3] P. Joensen, R. F. Frindt, S. R. Morrison, *Mater. Res. Bull.* **1986**, *21*, 457.

[4] R. F. Frindt, *J. Appl. Phys.* **2004**, *37*, 1928.

[5] K. S. Novoselov, A. K. Geim, S. v. Morozov, D. Jiang, Y. Zhang, S. v. Dubonos, I. v. Grigorieva, A. A. Firsov, *Science* **2004**, *306*, 666.

[6] P. Miró, M. Audiffred, T. Heine, *Chem. Soc. Rev.* **2014**, *43*, 6537.

[7] C. N. R. Rao, A. K. Sood, K. S. Subrahmanyam, A. Govindaraj, *Angew. Chem. Int. Ed.* **2009**, *48*, 7752.

[8] K. S. Novoselov, A. K. Geim, S. v. Morozov, D. Jiang, M. I. Katsnelson, I. v. Grigorieva, S. v. Dubonos, A. A. Firsov, *Nature* **2005**, *438*, 197.

[9] A. K. Geim, K. S. Novoselov, *Nat. Mater.* **2007**, *6*, 183.

[10] K. I. Bolotin, K. J. Sikes, Z. Jiang, M. Klima, G. Fudenberg, J. Hone, P. Kim, H. L. Stormer, *Solid State Commun.* **2008**, *146*, 351.

[11] C. Lee, X. Wei, J. W. Kysar, J. Hone, *Science* **2008**, *321*, 385.

[12] A. A. Balandin, S. Ghosh, W. Bao, I. Calizo, D. Teweldebrhan, F. Miao, C. N. Lau, *Nano Lett.* **2008**, *8*, 902.

[13] J. A. Wilson, A. D. Yoffe, *Adv. Phys.* **2006**, *18*, 193.

[14] Q. H. Wang, K. Kalantar-Zadeh, A. Kis, J. N. Coleman, M. S. Strano, *Nat. Nanotechnol.* **2012**, *7*, 699.

[15] C. C. Coleman, H. Goldwhite, W. Tikkanen, *Chem. Mater.* **1998**, *10*, 2794.

[16] M. Osada, T. Sasaki, *J. Mater. Chem.* **2009**, *19*, 2503.

[17] R. Ma, T. Sasaki, *Adv. Mater.* **2010**, *22*, 5082.

[18] P. Nalawade, B. Aware, V. J. Kadam, R. S. Hirlekar, *J. Sci. Ind. Res.* **2009**, *68*, 267.

[19] D. Golberg, Y. Bando, Y. Huang, T. Terao, M. Mitome, C. Tang, C. Zhi, *ACS Nano* **2010**, *4*, 2979.

[20] E. Bianco, S. Butler, S. Jiang, O. D. Restrepo, W. Windl, J. E. Goldberger, *ACS Nano* **2013**, *7*, 4414.

[21] B. Lalmi, H. Oughaddou, H. Enriquez, A. Kara, Ś. Vizzini, B. Ealet, B. Aufray, *Appl. Phys.Lett.* **2010**, *97*, 223109.

[22] B. Aufray, A. Kara, Ś. Vizzini, H. Oughaddou, C. Ĺandri, B. Ealet, G. le Lay, *Appl. Phys. Lett.* **2010**, *96*, 183102.

[23] M. Pumera, Z. Sofer, *Adv. Mater.* **2017**, *29.*

[24] S. Zhang, S. Guo, Z. Chen, Y. Wang, H. Gao, J. Gómez-Herrero, P. Ares, F. Zamora, Z. Zhu, H. Zeng, *Chem. Soc. Rev.* **2018**, *47*, 982.

[25] S. Zhang, M. Xie, F. Li, Z. Yan, Y. Li, E. Kan, W. Liu, Z. Chen, H. Zeng, *Angew. Chem.* **2016**, *128*, 1698.

[26] L. Niu, J. N. Coleman, H. Zhang, H. Shin, M. Chhowalla, Z. Zheng, *Small* **2016**, *12*, 272.

[27] J. N. Coleman, M. Lotya, A. O'Neill, S. D. Bergin, P. J. King, U. Khan, K. Young, A. Gaucher, S. De, R. J. Smith, I. v. Shvets, S. K. Arora, G. Stanton, H. Y. Kim, K. Lee, G. T. Kim, G. S. Duesberg, T. Hallam, J. J. Boland, J. J. Wang, J. F. Donegan, J. C. Grunlan, G. Moriarty, A. Shmeliov, R. J. Nicholls, J. M. Perkins, E. M. Grieveson, K. Theuwissen, D. W. McComb, P. D. Nellist, V. Nicolosi, *Science* **2011**, *331*, 568.

[28] J. Kang, J. W. T. Seo, D. Alducin, A. Ponce, M. J. Yacaman, M. C. Hersam, *Nat. Commun.* **2014**, *5*, 1.

[29] V. Nicolosi, M. Chhowalla, M. G. Kanatzidis, M. S. Strano, J. N. Coleman, *Science* **2013**, *340*, 6139..

[30] J. Yu, J. Li, W. Zhang, H. Chang, *Chem. Sci.* **2015**, *6*, 6705.

[31] W. S. Hummers, R. E. Offeman, *J. Am. Chem. Soc.* **2002**, *80*, 1339.

[32] D. R. Dreyer, S. Park, C. W. Bielawski, R. S. Ruoff, *Chem. Soc. Rev.* **2009**, *39*, 228.

[33] G. Eda, H. Yamaguchi, D. Voiry, T. Fujita, M. Chen, M. Chhowalla, *Nano Lett.* **2011**, *11*, 5111.

[34] C. J. Shih, A. Vijayaraghavan, R. Krishnan, R. Sharma, J. H. Han, M. H. Ham, Z. Jin, S. Lin, G. L. C. Paulus, N. F. Reuel, Q. H. Wang, D. Blankschtein, M. S. Strano, *Nat. Nanotechnol. 2011 6:7* **2011**, *6*, 439.

[35] G. F. Walker, W. G. Garrett, *Science* **1967**, *156*, 385.

[36] M. Lotya, Y. Hernandez, P. J. King, R. J. Smith, V. Nicolosi, L. S. Karlsson, F. M. Blighe, S. De, W. Zhiming, I. T. McGovern, G. S. Duesberg, J. N. Coleman, *J. Am. Chem. Soc.* **2009**, *131*, 3611.

[37] J. N. Coleman, *Acc. Chem. Res.* **2013**, *46*, 14.

[38] Q. H. Wang, K. Kalantar-Zadeh, A. Kis, J. N. Coleman, M. S. Strano, *Nat. Nanotechnol.* **2012**, *7*, 699.

[39] J. Gusakova, X. Wang, L. L. Shiau, A. Krivosheeva, V. Shaposhnikov, V. Borisenko, V. Gusakov, B. K. Tay, *Phys. Status Solidi A* **2017**, *214*, 12.

[40] S. Zhang, Z. Yan, Y. Li, Z. Chen, H. Zeng, *Angewv Chemv Intv Edv* **2015**, *54*, 3112.

[41] C. R. Ryder, J. D. Wood, S. A. Wells, Y. Yang, D. Jariwala, T. J. Marks, G. C. Schatz, M. C. Hersam, *Nat. Chemv* **2016**, *8*, 597.

[42] G. Wang, R. Pandey, S. P. Karna, *ACS Appl. Mater. Interfaces* **2015**, *7*, 11490.

[43] Z. Xie, B. Zhang, Y. Ge, Y. Zhu, G. Nie, Y. F. Song, C. K. Lim, H. Zhang, P. N. Prasad, *Chem. Rev.* **2022**, *122*, 1.

[44] Y. Wang, P. Huang, M. Ye, R. Quhe, Y. Pan, H. Zhang, H. Zhong, J. Shi, J. Lu, *Chem. Mater.* **2017**, *29*, 2191.

[45] S. Zhang, Z. Yan, Y. Li, Z. Chen, H. Zeng, *Angew. Int. Ed.* **2015**, *54*, 3112.

[46] S. K. Gupta, Y. Sonvane, G. Wang, R. Pandey, *Chem. Phys. Lett.* **2015**, *641*, 169.

[47] P. Zhang, Z. Liu, W. Duan, F. Liu, J. Wu, *Phys. Rev. B: Condens. Matter Mater. Phys.* **2012**, *85*, 201410.

[48] S. Zhang, W. Zhou, Y. Ma, J. Ji, B. Cai, S. A. Yang, Z. Zhu, Z. Chen, H. Zeng, *Nano Lett.* **2017**, *17*, 3434.

[49] X. Wang, J. He, B. Zhou, Y. Zhang, J. Wu, R. Hu, L. Liu, J. Song, J. Qu, *Angew. Chem.* **2018**, *130*, 8804.

[50] F. Zhang, J. He, Y. Xiang, K. Zheng, B. Xue, S. Ye, X. Peng, Y. Hao, J. Lian, P. Zeng, J. Qu, J. Song, *Adv. Mater.* **2018**, *30*, 38.

[51] H. S. Tsai, C. W. Chen, C. H. Hsiao, H. Ouyang, J. H. Liang, *Chem. Commun.* **2016**, *52*, 8409.

[52] Y. Liu, Y. Xiao, M. Yu, Y. Cao, Y. Zhang, T. Zhe, H. Zhang, L. Wang, *Small* **2020**, *16*, 42.

[53] G. R. Bhimanapati, Z. Lin, V. Meunier, Y. Jung, J. Cha, S. Das, D. Xiao, Y. Son, M. S. Strano, V. R. Cooper, L. Liang, S. G. Louie, E. Ringe, W. Zhou, S. S. Kim, R. R. Naik, B. G. Sumpter, H. Terrones, F. Xia, Y. Wang, J. Zhu, D. Akinwande, N. Alem, J. A. Schuller, R. E. Schaak, M. Terrones, J. A. Robinson, *ACS Nano* **2015**, *9*, 11509.

[54] R. Balog, B. Jørgensen, L. Nilsson, M. Andersen, E. Rienks, M. Bianchi, M. Fanetti, E. Lægsgaard, A. Baraldi, S. Lizzit, Z. Sljivancanin, F. Besenbacher, B. Hammer, T. G. Pedersen, P. Hofmann, L. Hornekær, *Nat. Mater.***2010**, *9*, 315.

[55] N. Martín, N. Tagmatarchis, Q. H. Wang, X. Zhang, *Chem. Eur. J.* **2020**, *26*, 6292.

[56] G. Bottari, M. Ángeles Herranz, L. Wibmer, M. Volland, L. Rodríguez-Pérez, D. M. Guldi, A. Hirsch, N. Martín, F. D'Souza, T. Torres, *Chem. Soc. Rev.* **2017**, *46*, 4464.

[57] J. Chattopadhyay, A. Mukherjee, S. Chakraborty, J. H. Kang, P. J. Loos, K. F. Kelly, H. K. Schmidt, W. E. Billups, *Carbon* **2009**, *47*, 2945.

[58] K. F. Kelly, W. E. Billups, *Acc. Chem. Res.* **2012**, *46*, 4.

[59] J. Park, M. Yan, *Acc. Chem. Res.* **2012**, *46*, 181.

[60] J. M. Englert, C. Dotzer, G. Yang, M. Schmid, C. Papp, J. M. Gottfried, H. P. Steinrück, E. Spiecker, F. Hauke, A. Hirsch, *Nat. Chem.* **2011**, *3*, 279.

[61] G. Abellán, M. Schirowski, K. F. Edelthalhammer, M. Fickert, K. Werbach, H. Peterlik, F. Hauke, A. Hirsch, *J. Am. Chem. Soc.* **2017**, *139*, 5175.

[62] F. Hof, R. A. Schäfer, C. Weiss, F. Hauke, A. Hirsch, *Chem. Eur. J.* **2014**, *20*, 16644.

[63] J. M. Englert, P. Vecera, K. C. Knirsch, R. A. Schäfer, F. Hauke, A. Hirsch, *ACS Nano* **2013**, *7*, 5472.

[64] H. G. Kulvlla, F. v DIStefano, J. Organomet, N. L. Allinger, T. Tribble, M. A. Miller, D. H. Wertz, J. Am Chem, *J. Am. Chem. Soc.* **2002**, *100*, 2126.

[65] A. Pénicaud, C. Drummond, *Acc. Chem. Res.* **2012**, *46*, 129.

[66] D. Voiry, A. Goswami, R. Kappera, C. D. C. C. E. Silva, D. Kaplan, T. Fujita, M. Chen, T. Asefa, M. Chhowalla, *Nat. Chem.* **2014**, *7*, 45.

[67] A. Hirsch, F. Hauke, *Angew. Chem. Int. Ed.* **2018**, *57*, 4338.

[68] B. L. Hurley, R. L. McCreery, *J. Electrochem. Soc.* **2004**, *151*, B252.

[69] A. Mesnage, X. Lefèvre, P. Jégou, G. Deniau, S. Palacin, *Langmuir* **2012**, *28*, 11767.

[70] A. Adenier, N. Barré, E. Cabet-Deliry, A. Chaussé, S. Griveau, F. Mercier, J. Pinson, C. Vautrin-Ul, *Surf. Sci.* **2006**, *600*, 4801.

[71] S. Betelu, I. Tijunelyte, L. Boubekeur-Lecaque, I. Ignatiadis, J. Ibrahim, S. Gaboreau, C. Berho, T. Toury, E. Guenin, N. Lidgi-Guigui, N. Félidj, E. Rinnert, M. L. D. la Chapelle, *J. Phys. Chem. C* **2016**, *120*, 18158.

[72] M. P. Stewart, F. Maya, D. v. Kosynkin, S. M. Dirk, J. J. Stapleton, C. L. McGuiness, D. L. Allara, J. M. Tour, *J. Am. Chem. Soc.* **2004**, *126*, 370.

[73] P. Huang, H. Zhu, L. Jing, Y. Zhao, X. Gao, *ACS Nano* **2011**, *5*, 7945.

[74] E. Bekyarova, M. E. Itkis, P. Ramesh, C. Berger, M. Sprinkle, W. A. de Heer, R. C. Haddon, *J. Am. Chem. Soc.* **2009**, *131*, 1336.

[75] H. Zhang, E. Bekyarova, J. W. Huang, Z. Zhao, W. Bao, F. Wang, R. C. Haddon, C. N. Lau, *Nano Lett.* **2011**, *11*, 4047.

[76] F. Barrière, A. J. Downard, *J. Solid State Electrochem.* **2008**, *12*, 1231.

[77] J. Pinson, F. Podvorica, *Chem. Soc. Rev.* **2005**, *34*, 429.

[78] H. Ghodrati, N. Antonatos, Z. Sofer, *Small* **2019**, *15*, 43.

[79] V. Georgakilas, M. Otyepka, A. B. Bourlinos, V. Chandra, N. Kim, K. C. Kemp, P. Hobza, R. Zboril, K. S. Kim, *Chem. Rev.* **2012**, *112*, 6156.

[80] V. Georgakilas, J. N. Tiwari, K. C. Kemp, J. A. Perman, A. B. Bourlinos, K. S. Kim, R. Zboril, *Chem. Rev.* **2016**, *116*, 5464.

[81] A. E. Mansour, M. M. Said, S. Dey, H. Hu, S. Zhang, R. Munir, Y. Zhang, K. Moudgil, S. Barlow, S. R. Marder, A. Amassian, *Adv. Func. Mater.* **2017**, *27*, 1602004.

[82] S. Lei, X. Wang, B. Li, J. Kang, Y. He, A. George, L. Ge, Y. Gong, P. Dong, Z. Jin, G. Brunetto, W. Chen, Z. T. Lin, R. Baines, D. S. Galv'o, J. Lou, E. Barrera, K. Banerjee, R. Vajtai, P. Ajayan, *Nat. Nanotechnol.* **2016**, *11*, 465.

[83] G. Abellán, V. Lloret, U. Mundloch, M. Marcia, C. Neiss, A. Görling, M. Varela, F. Hauke, A. Hirsch, *Angew. Chem. Int. Ed.* **2016**, *55*, 14557.

[84] G. Abellán, P. Ares, S. Wild, E. Nuin, C. Neiss, D. R.-S. Miguel, P. Segovia, C. Gibaja, E. G. Michel, A. Görling, F. Hauke, J. Gómez-Herrero, A. Hirsch, F. Zamora, *Angew. Chem.* **2017**, *129*, 14581.

[85] C. Gibaja, D. Rodriguez-San-Miguel, P. Ares, J. Gómez-Herrero, M. Varela, R. Gillen, J. Maultzsch, F. Hauke, A. Hirsch, G. Abellán, F. Zamora, *Angew. Chem.* **2016**, *128*, 14557.

[86] P. Nemes-Incze, Z. Osváth, K. Kamarás, L. P. Biró, *Carbon* **2008**, *46*, 1435.

[87] C. Backes, R. J. Smith, N. Mcevoy, N. C. Berner, D. Mccloskey, H. C. Nerl, A. O'neill, P. J. King, T. Higgins, D. Hanlon, N. Scheuschner, J. Maultzsch, L. Houben, G. S. Duesberg, J. F. Donegan, V. Nicolosi, J. N. Coleman, *Nat. Commun.s* **2014**, *5*, 1.

[88] D. Hanlon, C. Backes, E. Doherty, C. S. Cucinotta, N. C. Berner, C. Boland, K. Lee, A. Harvey, P. Lynch, Z. Gholamvand, S. Zhang, K. Wang, G. Moynihan, A. Pokle, Q. M. Ramasse, N. McEvoy, W. J. Blau, J. Wang, G. Abellan, F. Hauke, A. Hirsch, S. Sanvito, D. D. O'Regan, G. S. Duesberg, V. Nicolosi, J. N. Coleman, *Nat. Commun.* **2015**, *6*, 1.

[89] L. Peng, S. Ye, J. Song, J. Qu, *Angew. Chem.* **2019**, *131*, 9996.

[90] M. van Druenen, F. Davitt, T. Collins, C. Glynn, C. O'Dwyer, J. D. Holmes, G. Collins, *Chem. Mater.* **2018**, *30*, 4667.

[91] J. Debgupta, B. A. Kakade, V. K. Pillai, *Phys. Chem. Chem. Phys.* **2011**, *13*, 14668.

[92] Y. M. Lopatkin, P. A. Kondratenko, *J. Appl. Spectros.* **2007**, *74*, 472.

[93] L. A. Kazitsyna, B. S. Kikot', O. A. Reutov, *Bull. Acad. Sci. USSR., Div. Chem. Sci.* **1964**, *13*, 894.

[94] G. L. C. Paulus, Q. H. Wang, M. S. Strano, *Acc. Chem. Res.* **2013**, *46*, 160.

[95] P. Saint-Cricq, S. Deshayes, J. I. Zink, A. M. Kasko, *Nanoscale* **2015**, *7*, 13168.

[96] R. L. Hunt, B. S. Ault, *Spectrochim. Acta* **1980**, *37A*, 63.

[97] G. Song, Y. Lin, Z. Zhu, H. Zheng, J. Qiao, C. He, H. Wang, *Macromol. Rapid Commun.* **2015**, *36*, 278.

[98] S. P. Ogilvie, M. J. Large, G. Fratta, M. Meloni, R. Canton-Vitoria, N. Tagmatarchis, F. Massuyeau, C. P. Ewels, A. A. K. King, A. B. Dalton, *Sci. Rep.* **2017**, *7*, 1.

[99] S. Latil, V. Meunier, L. Henrard, *Phys. Rev. B: Condens. Matter Mater. Phys.* **2007**, *76*, 201402.

[100] R. Negishi, C. Wei, Y. Yao, Y. Ogawa, M. Akabori, Y. Kanai, K. Matsumoto, Y. Taniyasu, Y. Kobayashi, *Phys. Status Solidi B* **2020**, *257*, 2.

[101] J. N. Coleman, M. Lotya, A. O'Neill, S. D. Bergin, P. J. King, U. Khan, K. Young, A. Gaucher, S. De, R. J. Smith, I. v. Shvets, S. K. Arora, G. Stanton, H. Y. Kim, K. Lee, G. T. Kim, G. S. Duesberg, T. Hallam, J. J. Boland, J. J. Wang, J. F. Donegan, J. C. Grunlan, G. Moriarty, A. Shmeliov, R. J. Nicholls, J. M. Perkins, E. M. Grieveson, K. Theuwissen, D. W. McComb, P. D. Nellist, V. Nicolosi, *Science* **2011**, *331*, 568.

[102] D. Tofan, Y. ukako Sakazaki, K. L. endahl Walz Mitra, R. Peng, S. Lee, M. Li, A. Velian, *Angew. Chem.* **2021**, *133*, 8410.

[103] R. G. Pearson, *J. Chem. Ed.* **1968**, *45*, 581.

[104] S. B. Pillai, H. R. Soni, P. K. Jha, *Springer Proc. Phys.* **2019**, *236*, 379.

[105] Z. H. Ni, T. Yu, Y. H. Lu, Y. Y. Wang, Y. P. Feng, Z. X. Shen, *ACS Nano* **2008**, *2*, 2301.

[106] R. Fei, L. Yang, *Appl. Phys. Lett* **2014**, *105*, 83120.

[107] A. Ienco, G. Manca, M. Peruzzini, C. Mealli, *Dalt. Trans.* **2018**, *47*, 17243.